REPORT DOCUMENTATION PAGE		READ INSTRUCTIONS BEFORE COMPLETING FORM
1. REPORT NUMBER 85-14	2. GOVT ACCESSION NO.	3. RECIPIENT'S CATALOG NUMBER
4. TITLE (and Subtitle) HUB EFFECTS IN PROPELLER DESIGN AND ANALYSIS		5. TYPE OF REPORT & PERIOD COVERED TECHNICAL REPORT
		6. PERFORMING ORG. REPORT NUMBER
7. AUTHOR(s) MO-HWA WANG		8. CONTRACT OR GRANT NUMBER(s) N00014-82-K-0198
9. PERFORMING ORGANIZATION NAME AND ADDRESS DEPARTMENT OF OCEAN ENGINEERING MASSACHUSETTS INSTITUTE OF TECHNOLOGY 77 MASSACHUSETTS AVENUE, CAMBRIDGE, MA 02139		10. PROGRAM ELEMENT, PROJECT, TASK AREA & WORK UNIT NUMBERS
11. CONTROLLING OFFICE NAME AND ADDRESS OFFICE OF NAVAL RESEARCH DEPARTMENT OF THE NAVY ARLINGTON, VA 22217		12. REPORT DATE JULY 1985
		13. NUMBER OF PAGES 191
14. MONITORING AGENCY NAME & ADDRESS(if different from Controlling Office)		15. SECURITY CLASS. (of this report) UNCLASSIFIED
		15a. DECLASSIFICATION/DOWNGRADING SCHEDULE

16. DISTRIBUTION STATEMENT (of this Report)

APPROVED FOR PUBLIC RELEASE: DISTRIBUTION UNLIMITED

17. DISTRIBUTION STATEMENT (of the abstract entered in Block 20, if different from Report)

18. SUPPLEMENTARY NOTES

19. KEY WORDS (Continue on reverse side if necessary and identify by block number)

PROPELLER   LASER DOPPLER ANEMOMETRY
HUB   HUB VORTEX
STEADY FLOW
VORTEX LATTICE

20. ABSTRACT (Continue on reverse side if necessary and identify by block number)

A numerical model is established for the design of propeller blade shape for a prescribed circulation distribution and a given hub geometry. The vortex lattice approach is adapted for blades and their wakes. The hub is represented by a distribution of dipoles which ends at the hub apex. It is shown that consideration of the hub results in a lower pitch and lower camber at the inner radii.

(continued)

DD FORM 1473 EDITION OF 1 NOV 65 IS OBSOLETE
1 JAN 73
S/N 0102-014-6601

20. (continued)

An iterative method is developed for analyzing the interference between the blades and the hub. It is shown that the circulation at the root of a propeller with a hub is larger than the circulation at the root of a propeller without a hub. Two examples show that the increase in thrust due to hub effects has the same order of magnitude as the drag force effects on the hub for propellers which are moderately loaded at the hub.

Experiments are carried out for comparison with the numerical results. Excellent agreement is obtained in the circulation distribution for a conventional propeller, and fair agreement for a controllable pitch propeller. Experimental results show that the circulation is, roughly speaking, conserved. A method for estimating the drag force on the hub due to the hub vortex is established by assuming that the circulation is conserved.

HUB EFFECTS IN PROPELLER
DESIGN AND ANALYSIS

Mo-Hwa Wang

Report 85-14

Massachusetts Institute of Technology
Department of Ocean Engineering
Cambridge, MA 02139

MASSACHUSETTS INSTITUTE OF TECHNOLOGY
DEPARTMENT OF OCEAN ENGINEERING
CAMBRIDGE, MASSACHUSETTS 02139

Report 85-14

HUB EFFECTS IN PROPELLER

DESIGN AND ANALYSIS

by

Mo-Hwa Wang

July 1985

HUB EFFECTS IN PROPELLER DESIGN AND ANALYSIS

by

Mo-Hwa Wang

ABSTRACT

A numerical model is established for the design of propeller blade shape for a prescribed circulation distribution and a given hub geometry. The vortex lattice approach is adapted for blades and their wakes. The hub is represented by a distribution of dipoles which ends at the hub apex. It is shown that consideration of the hub results in a lower pitch and lower camber at the inner radii.

An iterative method is developed for analyzing the interference between the blades and the hub. It is shown that the circulation at the root of a propeller with a hub is larger than the circulation at the root of a propeller without a hub. Two examples show that the increase in thrust due to hub effects has the same order of magnitude as the drag force effects on the hub for propellers which are moderately loaded at the hub.

Experiments are carried out for comparison with the numerical results. Excellent agreement is obtained in the circulation distribution for a conventional propeller, and fair agreement for a controllable pitch propeller. Experimental results show that the circulation is, roughly speaking, conserved. A method for estimating the drag force on the hub due to the hub vortex is established by assuming that the circulation is conserved.

TABLE OF CONTENTS

CHAPTER 1

INTRODUCTION AND BACKGROUND

Current trends in propeller design have led to extremely complex blade shapes, e.g., highly skewed propellers. This means that empirical methods of design or analysis may be less useful due to the shortage of data. As digital computers become more powerful, the calculation of fluid problems becomes faster and new techniques for improving the accuracy of numerical schemes become feasible and necessary.

Several lifting surface design and analysis methods have been developed, for instance, MIT's PBD10 (propeller blade design) and PSF2 (propeller steady force analysis) [Greeley and Kerwin, 1982]. Three assumptions were made in these methods: the hull, the propeller hub, and the free surface were ignored.

Vorus [1976] investigated the problem of propeller-induced vibrations at very high and very low frequency, which simplifies the free surface condition, by modeling the ship stern as a semi-infinite flat plate. Breslin [1978] studied the propeller-induced hull forces by a source distribution on the hull. Huang and Cox [1977] showed that thrust deduction can be predicted by inviscid flow analysis. Breslin, Van Houten, Kerwin, and Johnsson [1982] studied the prediction of vibratory pressures, forces, and moments induced on ship hulls by intermittently cavitating propellers. The presence of the hull and the free surface will be ignored in this thesis.

The interference between the propeller blade and the hub will be considered in this thesis. The hub effects may be important especially for the propeller with a large hub such as a controllable pitch propeller. In

August 1974, after 2000 hours of service, the USS Barbey, a destroyer escort, lost all five blades from the hub during a crash in an astern maneuver [Wind, 1978]. Wind developed a minimum hub size criterion from a structural safety point of view. He recommended increasing the hub size for Barbey from 1320 mm to 1500 mm and estimated a loss of efficiency roughly proportional to the loss of disc area. From a hydrodynamic point of view, a larger hub has a larger influence on the blade, so it is necessary to modify the design procedure by considering the hub effect. The comparison of efficiency between these two designs will then become meaningful.

The force on the hub may be an important factor for propeller design, especially for those propellers with a non-zero circulation at the hub. A good example is an early torpedo propeller design which resulted in unusually heavy loading at the hub [McCormick, Eisenhuth, and Lynn, 1956]. It was found experimentally that the thrust was reduced by 45% due to a very strong vortex core shed from the hub on the afterbody of the hub. In order to calculate the force on the hub, study should be made of propeller design/analysis with hub effects considered.

This thesis has three parts. The first part develops a numerical model for designing a propeller blade under the effects of a prescribed hub geometry. The second part modifies this model in order to analyze combinations of blades and hub under off-design conditions. The third part presents experiments to verify the accuracy of the numerical model. Also, the structure of the hub vortex, and the force generated by it, will be experimentally investigated. Because the form of the hub vortex depends on the viscous interaction between a complicated external flow and a rotating body -- the hub, there is no attempt to predict the size or strength of the

hub vortex theoretically. A method of estimating the force generated by the hub vortex is the goal of this thesis.

Some background on research into interactions between blades and hub will be presented here. Although the hub effect is not considered in recent lifting surface theory, e.g., Greeley and Kerwin [1982], the hub was considered in early years when the propeller was designed roughly by lifting line theory. Lerbs' [1952] induction factor method had a finite or zero hub in optimum or non-optimum propellers. The hub was treated as an infinitely long cylinder of radius r_H with two boundary conditions, namely, the circulation and the radial velocity component are both zero at the hub. For small r_H, the influence of the latter boundary condition was small and was neglected. As for the bound circulation on the hub, Lerbs argued that the circulation was zero at the hub when approaching r_H from inside the hub. When approaching r_H from outside, the circulation approached zero continuously because the pressures tended to be equalized by a flow from the pressure side of one blade to the suction side of the adjacent blade.

After Lerbs, there were several authors who treated the optimum propeller with a large hub as an infinitely long cylinder (e.g., McCormick, [1955]; Tachmindji, [1956]; Tachmindji and Milam, [1957]; Thorsen, [1962]; and Kerwin and Leopold, [1964]).

McCormick [1955] extended Goldstein's [1929] zero hub solution to the finite hub with infinite length. He formulated the potential problem for lightly loaded lifting line with vanished normal velocity conditions on the hub and on the trailers. The solution for velocity potential was an infinite series of modified Bessel functions and Lommel's function. The bound circulation was given by the jump in the velocity potential at the trailing vortex sheets. He found that the circulation was not zero at the

hub. The slope of the circulation at the hub was almost zero in his results, although this was not pointed out in the paper. The hub effect was significant near the blade root. As an example, the circulation increased by a factor of 1.56 (of the zero hub case) for a hub with a radius one-fifth that of a two-bladed propeller. The hub effect was not as pronounced for a propeller with a larger number of blades.

Kerwin and Leopold [1964] used a vortex lattice to represent the trailing vortex. They, assumed that the slope of the bound circulation at the hub was zero and used an image system for the vortex in the hub in order to satisfy the normal velocity boundary conditions at the hub. This was based upon the assumption that the 2-D vortex image theory is approximately valid for the 3-D case provided the pitch angle is sufficiently high. Table 2 in their paper showed that this approximation was excellent for vortices near the hub, but not for the distant elements. However, the latter was very small, so that perfect cancellation was unimportant. Since the image system may not be sufficiently accurate in all cases, a scheme employing a source-sink distribution on the surface of the hub cylinder was considered. The optimum circulation at the hub from their results was not zero.

Wald [1964] pointed out that the treatment of the optimum propeller with a large hub as an infinitely long cylinder was not correct because this did not correspond to the wake condition. The problem was restated as one of finding a distribution of circulation surrounding a hub which was transformed into true helicoidal sheets following the deformation which occurs at the apex of the hub. A solution was given for the infinite-bladed propeller. The circulation at the hub of an optimum propeller was zero. However, according to Wald, the optimum circulation on the blade

would not decrease to zero at the hub when there was a long hub vortex cavity.

Andrews and Cummings [1972] adapted Wald's fictitious propeller concept plus Kerwin's image vortex concept. The hub shape was represented by a line sink of constant strength. The strength, length, and position of the line sink were determined in order to satisfy boundary conditions of the hub at three points: hub radius at infinity upstream, hub radius at the propeller, and a stagnation point at the hub end. The boundary streamline at the propeller tip is then followed back into the wake to find the radius of the fictitious zero-hub propeller. The thrust and torque versus rpm calculations were performed using a lifting line model of this fictitious zero-hub optimum propeller (Lerbs' method), assuming that two propellers which generate the same wake have the same thrust and torque characteristics as Wald's ideal. The circulation distribution from the zero-hub propeller was moved up to corresponding locations at the actual propeller plane. Images of the trailing vortices were then added in the hub to approximate the hub surface boundary condition as was done by Kerwin and Leopold. These image vortices end at the hub apex. An iterative procedure was used to determine the hydrodynamic pitch angle and the induced velocity. Then the actual shape of the blades was determined by Kerwin's lifting surface. Figure 7 in their paper showed the pitch and camber reduced very much.

Ludolph [1977] represented the hub by a series of constant ring sources. The strength of each of these rings was determined in such a way that the average normal velocity vanished on the hub. He calculated the lift by two methods: one ignored the hub, the other accounted for the hub. He found that the difference between the two methods was more pronounced if

the bound circulation at the hub was zero than if it was not. He also found that, for the case when the bound circulation was zero, the hub effect was smaller when the point of maximum circulation was moved radially outward. Figures 12 and 16 in his paper showed some problems: the lifting line result was quite different from the lifting surface result. Probably, the constant strength source ring was not appropriate.

Recently, Hess and Valarezo [1985] used surface panel methods to model the propeller blade with sources and dipoles and to model the hub with sources. The sides of the panels on the hub were either parallel or perpendicular to the axis of rotation. This led to panels with irregular size on the hub near the blades or the trailing vortices. The trailing vortices had a pure helical wake. A lift "carry over" was used from the blade-hub intersection to the axis of rotation, implying that the bound circulation was finite but with zero slope at the hub. The "carry over" [see Hess, 1972] meant that an extra strip, from hub surface to hub center, carried a dipole with constant strength which equaled the strength of a dipole of the first strip on the blade. A concentrated vortex -- a hub vortex -- was formed along the axis of rotation. The strength of the hub vortex equaled the sum of all the carried-dipole strengths of all the blades.

Concerning the formation of the hub vortex, Saunders [1957] said that there were two theories. One theory held that the flow close to the hub surface did not have concentrated root vortices. Instead, the flow of the field was uniform. When the water particles moved toward the hub apex, the tangential velocity became faster and a hub vortex was formed at the hub apex. The other theory held that there were root vortices coming off the trailing edges of the blades just as the tip vortices were. The hub vortex was formed by the coalescence of those root vortices.

CHAPTER 2

AXISYMMETRIC BODY

Before studying the interference of blades and hub, it is necessary to investigate an axisymmetric body. A real marine propeller always has a long shaft linking it to the ship stern. In order to isolate the propeller from the ship, an axisymmetric body for modeling the hub is easier to handle than a semi-infinite long shaft. This artificial hub may produce different results of blade shape if the hub has different length in the forebody -- the artificial shaft. In short, a study on the bared hub is just a start for a more complex problem.

2.1 Vortex Rings

In potential flow, a surface singularity distribution method is always suitable for modeling an arbitrary body shape. For an axisymmetric body, vortex rings or source rings may be a reasonable choice. Since we plan to use a vortex lattice to represent the combination of the blades and hub, vortex rings will be used to represent the axisymmetric body.

From the Biot-Savart law

$$d\vec{V} = -\frac{\Gamma}{4\pi} \frac{\vec{r} \times d\hat{s}}{|\hat{r}|^3} \tag{2.1}$$

the induced velocities due to a vortex ring with center at the origin are derived [Kuchemann and Weber, 1953].

The axial velocity v_x is

$$v_x\left[\frac{x}{r_0}, \frac{r}{r_0}\right] = \frac{\Gamma}{2\pi r_0} \frac{1}{\sqrt{\left[\frac{x}{r_0}\right]^2 + \left[\frac{r}{r_0} + 1\right]^2}} \left[K(k) - \left[1 + \frac{2\left[\frac{r}{r_0} - 1\right]}{\left[\frac{x}{r_0}\right]^2 + \left[\frac{r}{r_0} - 1\right]^2}\right] E(k)\right]$$

(2.2)

and the radial velocity v_r is

$$v_r\left[\frac{x}{r_0}, \frac{r}{r_0}\right] = \frac{\Gamma}{2\pi r_0} \frac{-\frac{x}{r_0}}{\frac{r}{r_0} \sqrt{\left[\frac{x}{r_0}\right]^2 + \left[\frac{r}{r_0} + 1\right]^2}} \left[K(k) - \left[1 + \frac{2\frac{r}{r_0}}{\left[\frac{x}{r_0}\right]^2 + \left[\frac{r}{r_0} - 1\right]^2}\right] E(k)\right]$$

(2.3)

where

$$k^2 = \frac{4\frac{r}{r_0}}{\left[\frac{x}{r_0}\right]^2 + \left[\frac{r}{r_0} + 1\right]^2}$$

$$K(k) = \int_0^{\pi/2} \frac{1}{\sqrt{1 - k^2\sin^2\alpha}} \, d\alpha$$

(2.4)

$$E(k) = \int_0^{\pi/2} \sqrt{1 - k^2\sin^2\alpha} \, d\alpha$$

r_0 = vortex ring radius

Γ = vortex ring strength -- its sense is defined in Figure 2.1

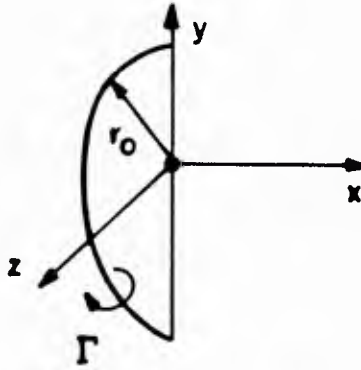r = radial distance from x-axis to field point

Figure 2.1   Vortex Ring Notation

v_x is an even function of x, while v_r is an odd function of x. There is a table of v_x and v_r in [Küchemann and Weber, 1953]. K(k) and E(k) are complete elliptic integrals which may be found in IMSL subroutines.

2.2 Modeling an Axisymmetric Body by Vortex Rings

    In order to solve the problem of an axisymmetric body in a uniform flow with the inflow parallel to the body axis, a finite number of vortex rings are spaced equally over the length of the body. The radius of each ring is equal to the local body radius. The strengths of the vortex rings are unknowns to be determined by solving a boundary value problem. Control points, equal in number to the vortex rings, are located on the body surface with one control point at the middle of any two adjacent rings.

The last control point, the most downstream one, is at the middle of the last ring and the body apex. The boundary condition at each control point is that the total velocities at these points have zero normal velocity components. Thus, there is a set of simultaneous linear algebraic equations for unknown vortex ring strengths.

Once the vortex ring strengths are solved, the velocity at any point can be calculated by superimposing the velocities induced by vortex rings to the inflow. As for the surface velocities, an additional jump velocity by vortex sheet should be imposed as well.

For demonstration, five vortex rings are chosen to represent an axisymmetric body as shown in Figure 2.2. Only half of the body is shown.
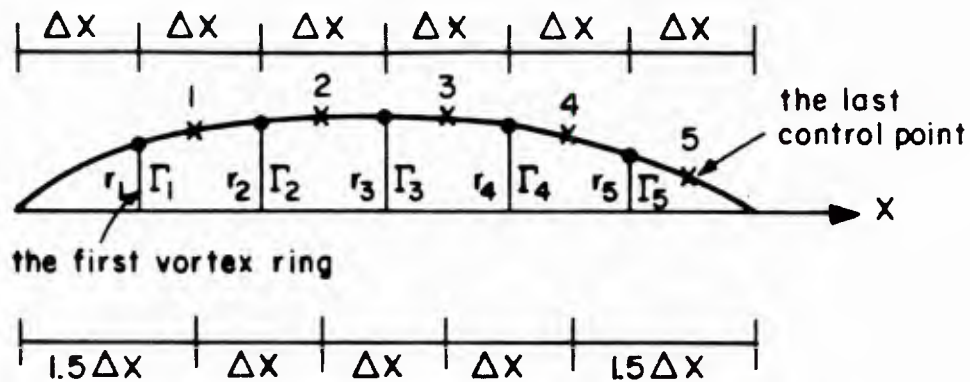

Figure 2.2   Vortex Rings Representing a Half Axisymmetric Body

The concentrated vortex rings are redistributed into constant vortex sheets as follows:

$$\gamma_1 = \frac{\Gamma_1}{\frac{3}{2} \Delta x} = \frac{2}{3} \frac{\Gamma_1}{\Delta x}$$

$$\gamma_2 = \frac{\Gamma_2}{\Delta x} \qquad \gamma_3 = \frac{\Gamma_3}{\Delta x} \qquad \gamma_4 = \frac{\Gamma_4}{\Delta x} \qquad (2.5)$$

$$\gamma_5 = \frac{2}{3} \frac{\Gamma_5}{\Delta x}$$

The jump velocity u_s is tangential to the surface and has a magnitude one half that of the vortex sheet. At the first control point, for example,

$$u_s = \frac{1}{2} \left[\frac{\gamma_1 + \gamma_2}{2} \right] \qquad (2.6)$$

2.3 Rankine Ovoid

A Rankine ovoid is a good example of an axisymmetric body with exact solutions. It is a superposition of a source with strength m located at (-a,0,0) and a sink with strength -m located at (a,0,0), and a uniform inflow U [Newman, 1977].

The body shape is controlled by the following equation

$$\frac{2\pi U R^2}{m} - \frac{x + a}{[(x + a)^2 + R^2]^{1/2}} + \frac{x - a}{[(x - a)^2 + R^2]^{1/2}} = 0 \qquad (2.7)$$

where R(x) is the radius of the body at x.

2.4 Comparison Axisymmetric Body Using Vortex Rings with Exact Solution
from Rankine Ovoid

Two Rankine ovoids using the vortex ring approximation are studied.

One has a slenderness ratio of 1:5 and the other has a slenderness ratio

of 1:2.22. The nondimensional vortex ring strengths, $\Gamma/2\pi U$, and the

surface velocity errors in percent of uniform inflow velocity are shown in

Figure 2.3 and Figure 2.4 for these two ovoids respectively. There are 48

vortex rings for each body. The errors are smaller in a long body than in

a fat body. The errors are smaller in the middle of the body than at the

ends for either body.

A modification was made to improve the accuracy of velocities by

adding a central source/sink line along the body axis, with source/sink

strengths determined by slender body theory, i.e.,

$$\frac{Q}{2\pi} = -\frac{dA(x)}{dx} \qquad (2.8)$$

where $A(x)$ is the cross sectional area at x.

The improvement is immediately seen in Figure 2.5 and Figure 2.6.

The prediction of field point velocities has opposite results. The

errors from the model with vortex rings are smaller than from the model

with vortex rings plus central source/sink lines. These comparisons are

shown in Table 2.1 and Table 2.2.

FIG. 2.3 VORTEX RING STRENGTHS AND ERRORS OF SURFACE
VELOCITY IN PERCENT OF FREE STREAM. SLENDERNESS RATIO
1:5; 48 VORTEX RINGS ONLY. a=2.8, (2 PI U)/m=5.0.
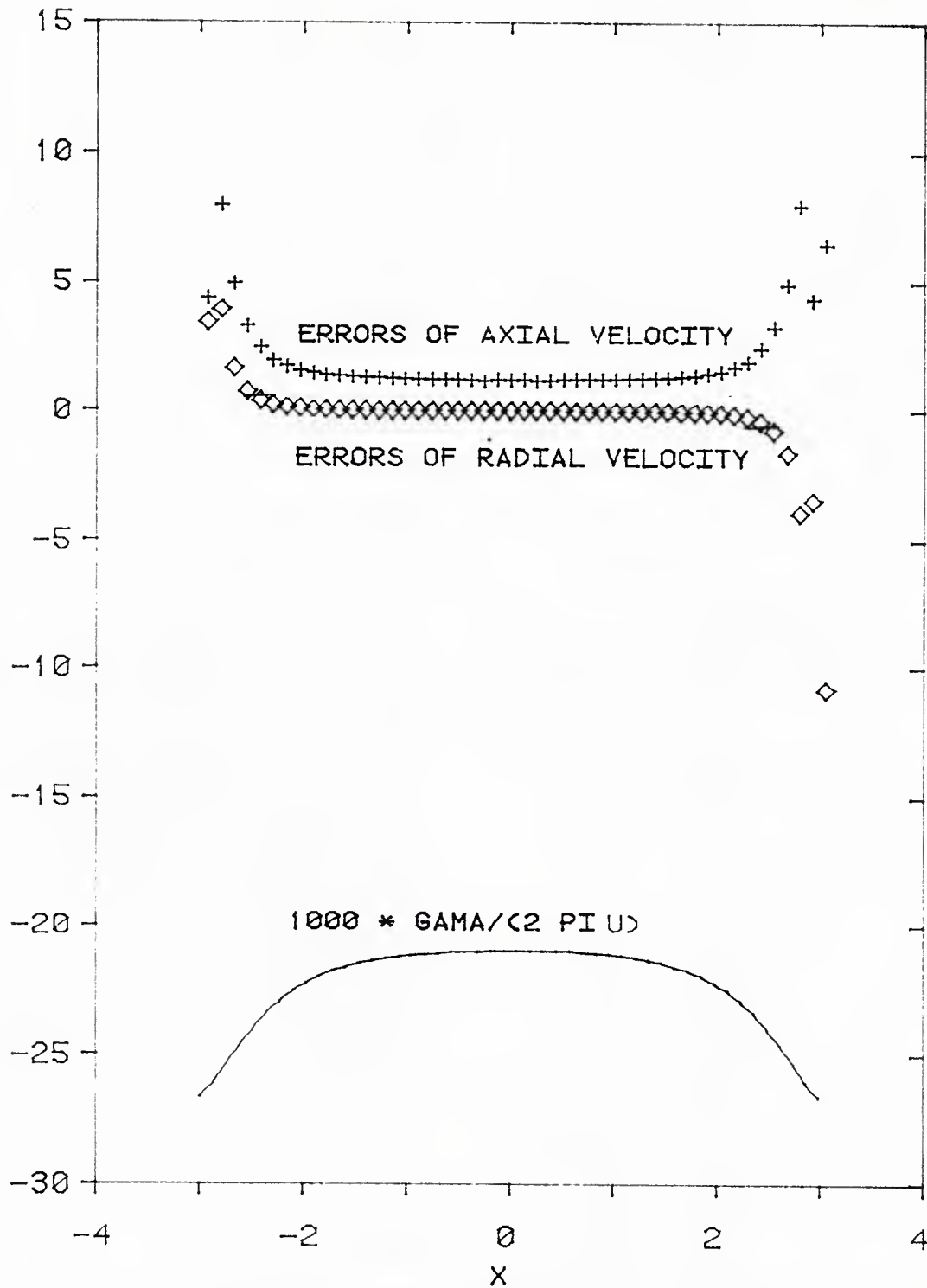
FIG. 2.4 VORTEX RING STRENGTHS AND ERRORS OF SURFACE VELOCITY IN PERCENT OF FREE STREAM. SLENDERNESS RATIO 1:2.22; 48 VORTEX RINGS ONLY; a=1.4,(2 PI U)/m=2.5

FIG. 2.5 VORTEX RING STRENGTHS AND ERRORS OF SURFACE
VELOCITY IN PERCENT OF FREE STREAM. SLENDERNESS RATIO
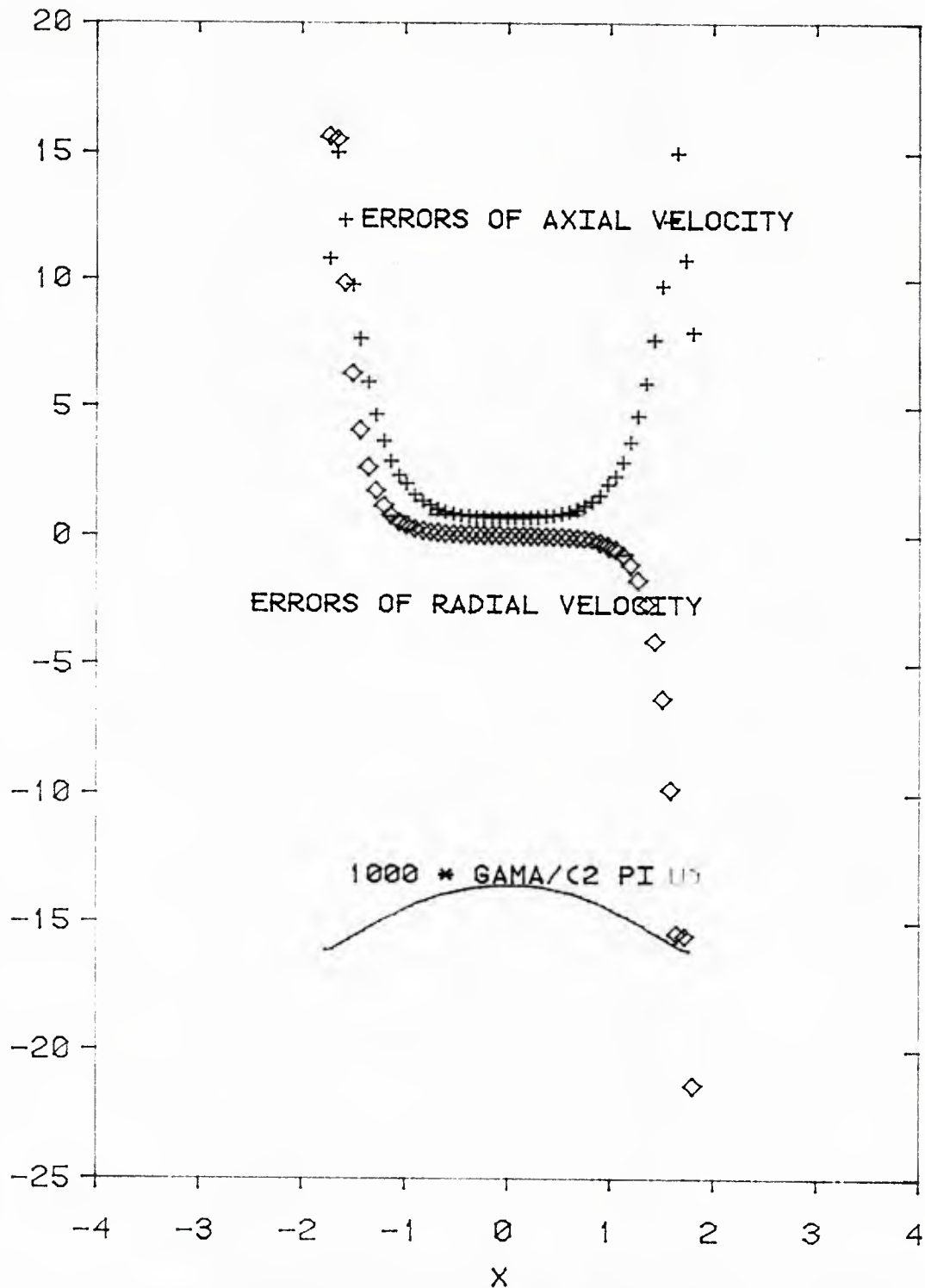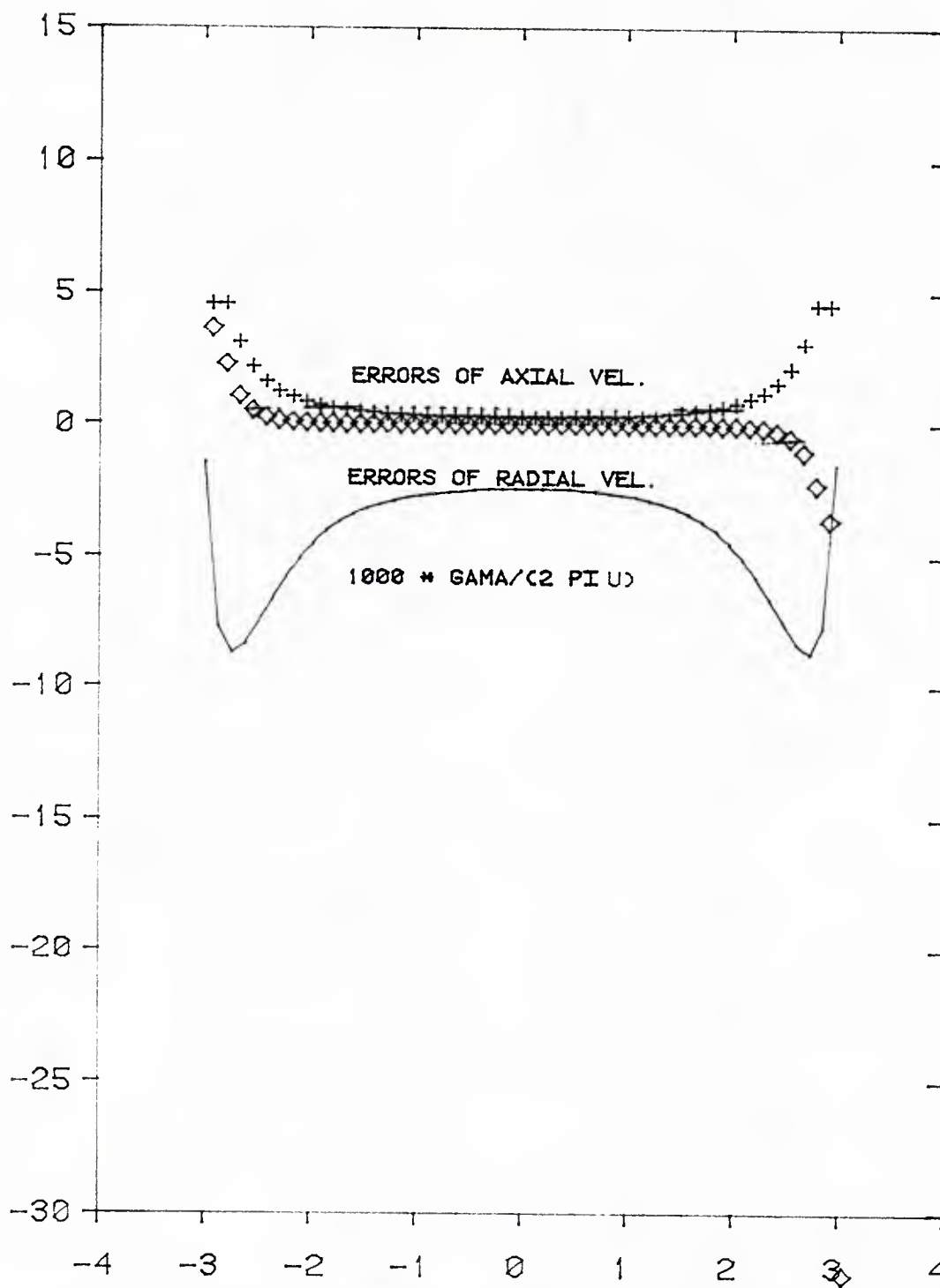1:5; 48 VORTEX RINGS AND CENTRAL LINE SOURCES.
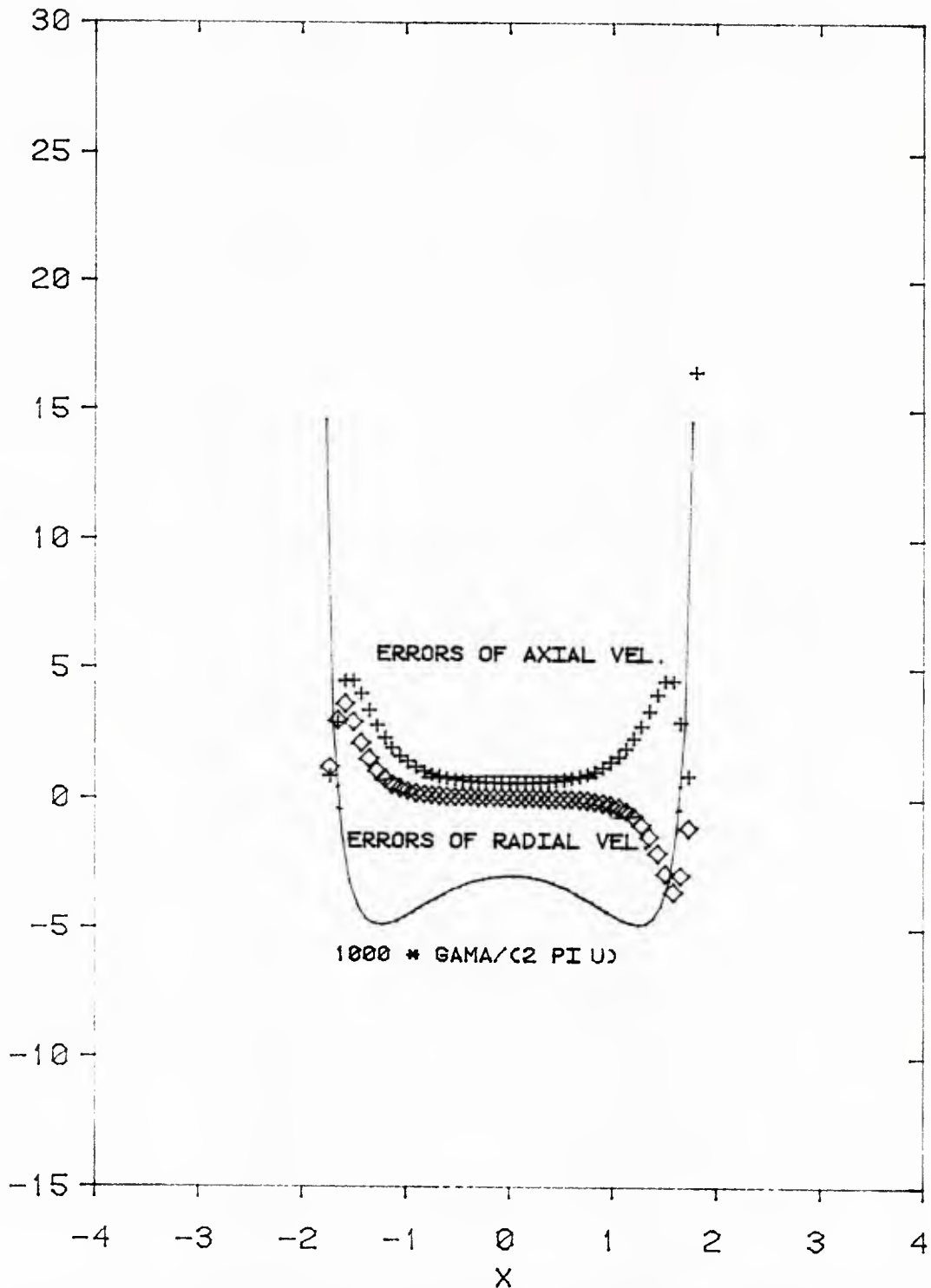a=2.8,(2 PI U)/m=5.0.

FIG. 2.6 VORTEX RING STRENGTHS AND ERRORS OF SURFACE
VELOCITY IN PERCENT OF FREE STREAM. SLENDERNESS RATIO
1:2.22; 48 VORTEX RINGS PLUS CENTRAL LINE SOURCES.
$a=1.4, (2 PI U)/m=2.5$.

No.	r	$(u/U)_{Rankine}$	Model of Vortex Rings		Model of Vortex Rings Plus Central Source/Sink Line	
			u/U	Errors in % of Free Stream U	u/U	Errors in % of Free Stream U
1	0.7	1.02329	1.00061	-2.268	1.02204	-0.125
2	0.8	1.02268	1.02280	0.012	1.02405	0.136
3	0.9	1.02201	1.02229	0.028	1.02339	0.136
4	1.0	1.02131	1.02158	0.027	1.02267	0.136
5	1.1	1.02057	1.02083	0.026	1.02190	0.133
6	1.2	1.01981	1.02006	0.025	1.02112	0.131
7	1.3	1.01903	1.01927	0.024	1.02032	0.129
8	1.4	1.01825	1.01848	0.023	1.01950	0.125
9	1.5	1.01747	1.01769	0.022	1.01869	0.122
10	1.6	1.01670	1.01690	0.020	1.01787	0.117
11	1.7	1.01593	1.01613	0.020	1.01707	0.114
12	1.8	1.01518	1.01537	0.019	1.01629	0.111
13	1.9	1.01445	1.01463	0.018	1.01552	0.107
14	2.0	1.01375	1.01391	0.016	1.01477	0.102

Table 2.1 Comparison of field point velocities (at x = 0, r as specified) of two models of axisymmetric bodies with the exact solution of the Rankine ovoid of slenderness ratio 1:5 and half thickness 0.62. Each model has 48 rings.

No.	r	$(u/U)_{Rankine}$	Model of Vortex Rings		Model of Vortex Rings Plus Central Source/Sink Line	
			u/U	Errors in % of Free Stream U	u/U	Errors in % of Free Stream U
1	0.9	1.12147	1.11927	-0.220	1.12486	0.339
2	0.95	1.11563	1.11642	0.079	1.11964	0.401
3	1.0	1.10996	1.11076	0.080	1.11392	0.396
4	1.1	1.09922	1.09995	0.073	1.10305	0.383
5	1.2	1.08932	1.08999	0.067	1.09299	0.367
6	1.3	1.08031	1.08091	0.060	1.08379	0.348
7	1.4	1.07215	1.07269	0.054	1.07545	0.330
8	1.5	1.06483	1.06532	0.049	1.06794	0.311
9	1.6	1.05827	1.05871	0.044	1.06120	0.293
10	1.7	1.05243	1.05283	0.040	1.05517	0.274
11	1.8	1.04723	1.04758	0.035	1.04979	0.256
12	1.9	1.04260	1.04292	0.032	1.04500	0.240
13	2.0	1.03849	1.03878	0.029	1.04072	0.223

Table 2.2 Comparison of field point velocities (at x = 0, r as specified) of two models of axisymmetric bodies with the exact solution of the Rankine ovoid of slenderness ratio 1:2.22 and half thickness 0.83. Each model has 48 rings.

CHAPTER 3

PROPELLER BLADE DESIGN WITH HUB EFFECT

3.1 The Mixed Design and Analysis Problem

The task is to design the mean line shape of a propeller blade when the load distribution, the advance coefficient J, and the circumferential mean effective wake are given. The choice of other propeller parameters such as number of blades, blades rank and skew, section thickness ratio, and chord length ratio are assumed to be determined by other methods [Eckhardt and Morgan, 1955; Morgan and Wrench, 1965; and Brockett et al., 1981]

The geometry of the hub, including the fairwater, is assumed to be given as well. The afterbody of the hub is assumed to be prescribed as a cubic function. The traditional hub with blunt end is not adopted in this thesis since such a configuration would result in flow separation, which is not considered in the present study. Another modification of the hub is that the forebody of the hub is a closed body and also has the shape of a cubic function. In order to model upstream flow conditions, the influence of the artificial forebody will be investigated later on.

The interference between the blades and hub is anticipated to be strong, especially near the intersection points. The trailing vortex sheets shed from the blades also interact with the hub. The task is to account for these interferences in the design of the blade shape.

The source/vortex lattices are distributed on the blade mean surface [Greeley and Kerwin, 1982]. As for the hub, the vortex lattices are distributed over the hub surface.

The procedure is to first assume a blade geometry with source and vortex lattices of prescribed strengths on its mean surface. This is an initial guess of the blade shape. It may not fulfill the boundary conditions on the blade surface, on the trailing vortex sheets, or on the hub surface. The objective of the design procedure is to align the blade shape so that all the boundary conditions are fulfilled. This procedure will include the determination of the unknown hub surface vortices. Thus, this is a mixed design and analysis problem.

3.2 Basic Assumptions

The propeller runs in an unbound, inviscid, and incompressible fluid with constant advance coefficient J (= V_S/nD), where V_S is the ship speed, n is the number of revolutions per unit time, and D is the propeller diameter. There is no free surface -- no solid boundary except the hub.

The hub is an axisymmetric football-like body with a forebody, an afterbody, and a parallel midbody where K blades are located symmetrically.

The inflow is assumed to be symmetrical about the rotation axis and to be steady with respect to a coordinate rotating with the propeller.

The flow is irrotational everywhere except in the trailing vortex sheet, or tip and hub vortex tube. The trailing vortex sheet is assumed to be thin, and the tip and hub vortex tube is assumed to be small in diameter.

The blades are assumed to be thin and operate at a small angle of attack.

3.3 The Coordinates

Two coordinate systems (Figure 3.1) will be adapted in this thesis. One is a Cartesian coordinate system with x-axis coincident with the rotation axis, pointing in the downstream direction; the y-axis points upward and coincides with one of the K blades (called the key blade hereafter) at the middle chord of the root section. Vectors $\hat{i}$, $\hat{j}$, and $\hat{k}$ are unit vectors corresponding to the x-, y-, and z-axes. The other coordinate system is a cylindrical coordinate system: x, r, and θ with x-axis coincident with the x-axis of the Cartesian system. θ is measured from the positive y-axis toward the positive z-axis. r is the radial distance from the origin in the y-z plane.

The propeller is rotating opposite to the θ direction at constant angular velocity ω or $-\omega\hat{i}$, in vector notation. Both coordinate systems are rotating with the propeller so that the flow is steady in those systems.

3.4 Field Equations

Because of the assumption of inviscid, irrotational, and incompressible flow outside the blade, hub, and vortex sheet and vortex tube, the governing equation is the Laplace equation

$$\nabla^2\phi = 0 \qquad\qquad (3.1)$$

It is known that the solutions to this equation and their spatial derivatives are finite and continuous at all points, except possibly at some points on the boundary where a singularity of some kind -- for
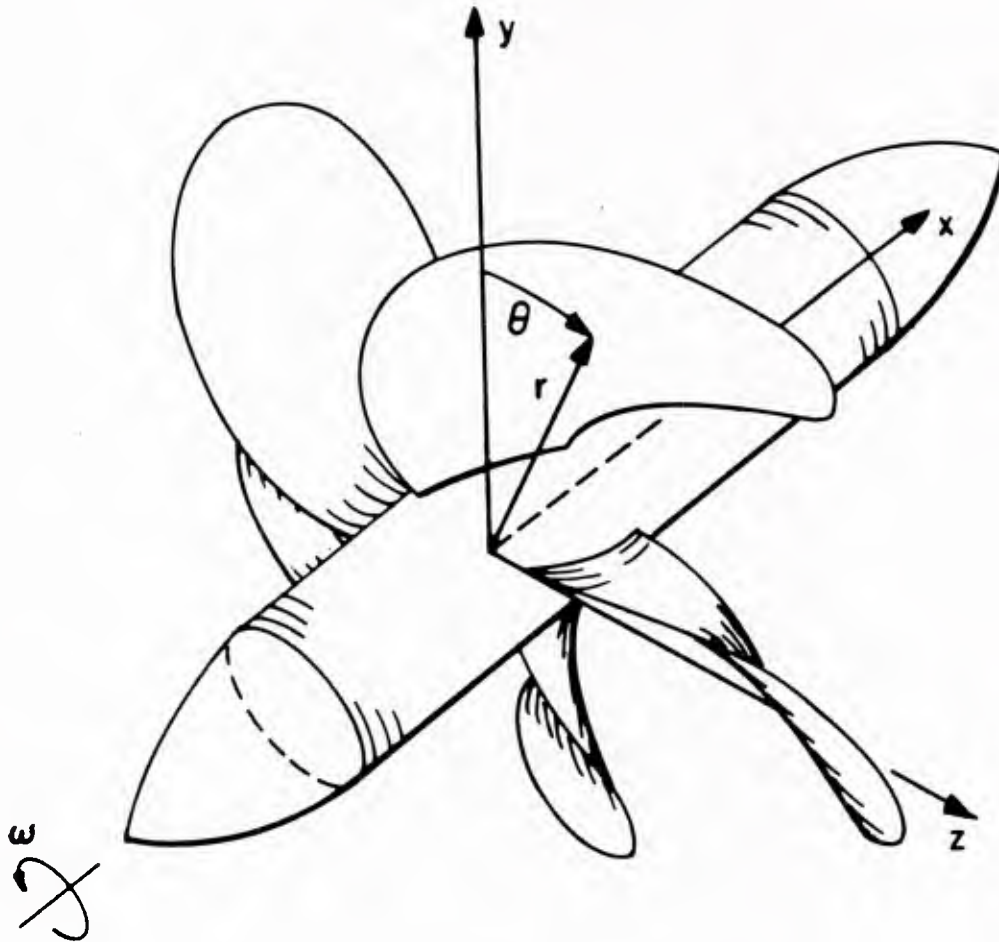
Figure 3.1 Coordinates

example, an abrupt change of the tangential velocity at the boundary -- may exist (see Batchelor, p. 101).

3.5 Boundary Conditions

(a) The normal velocities on the blades and hub should vanish in the blade fixed coordinate system.

(b) The flow is finite at the blade trailing edge (Kutta condition).

(c) The trailing vortex sheets should be force-free and coincident with the local flow streamlines.

(d) Circulation should be conserved.

(e) The perturbation velocity must vanish at infinity.

3.6 The Solution Algorithm

The algorithm for solving this mixed design and analysis problem is to proceed with the design and analysis alternatively.

Vortex lattices and source lattices are distributed over the blade camber surface. Vortices are responsible for the lifting force while sources represent the blade thickness from linear theory. The trailing vortices shed from the blade trailing edge are paneled as vortex lattices which should obey Kelvin's circulation conservation theory.

Since the hub is a non-lifting element, it is represented by a distribution of dipoles which ends at the hub apex. The hub surface is paneled as quadrilateral elements for most of the hub except the place right next to the hub apex where triangular elements are used. Each panel is given a constant dipole sheet with unknown strength which is to be determined later. Mathematically, a constant dipole sheet is equivalent to constant vortex segments along the sheet boundary [Hess, 1972]. So, again the hub surface is paneled as vortex lattices.

The flow diagram in Figure 3.2 is for determination of the blade shape while a hub analysis is embedded in it.
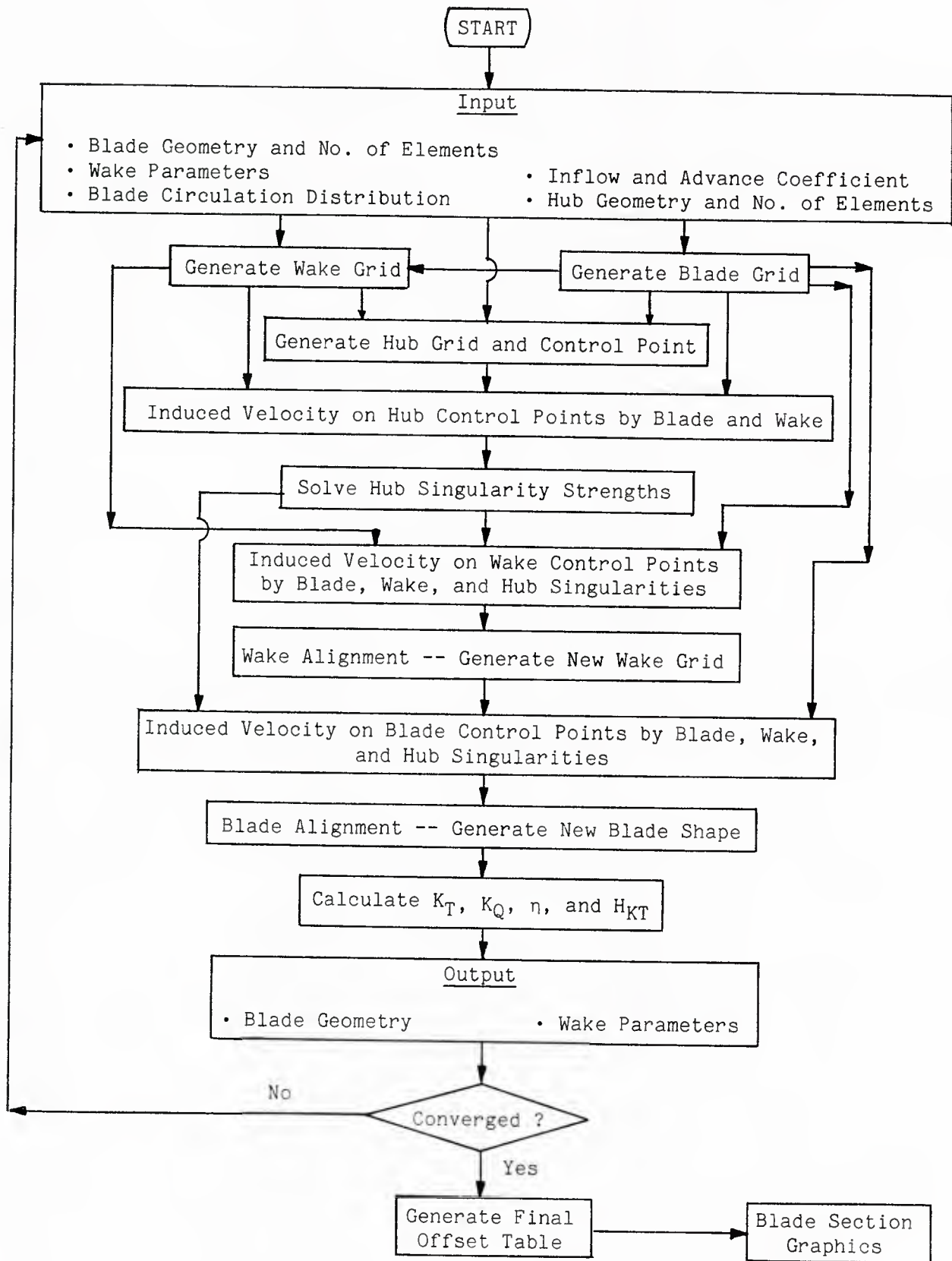
Figure 3.2   Flow Diagram of Blade Shape Design with Hub Effects

3.7 Details of the Method of Solution

3.7.1 Blade Panels

The blades are represented by camber surfaces which are discretized as spanwise and chordwise vortex lattices and spanwise source lattices. The details of the arrangement of these singularities is presented in Greeley and Kerwin [1982] and will not be repeated here. The only change is the location of spanwise elements. The endpoints of the discrete vortices are located at radii

$$\rho_m = \frac{(R - r_H)(4m - 4)}{4M + 1} + r_H, \quad m = 1,2,\dots,M + 1 \tag{3.2}$$

This divides the radial interval from the hub r_H to tip R into M equal intervals. The first spanwise element has one end at the hub surface while the last spanwise element has its far end inset one quarter element from the tip. The first chordwise element will then have its end on the hub surface and will coincide with the hub element which will be defined later.

3.7.2 Trailing Vortex Panels

The wakes are modeled the same way as those modeled by Greeley and Kerwin [1982], except the inner radius of the so-called transition wake should be exactly the same as the hub geometry. The hub geometry will be modeled as a cubic function (see the next section), as will the transition wake.

Usually the transition wake extends further downstream than the hub, which means that the hub boundary disappears before the transition wake terminates. Thus, transition wakes are undefined beyond the hub. This will be compensated by simply assuming a parameter $x = x_5$ (less than x_4, the hub apex -- see the next section on hub geometry), beyond which the first transition wake has a constant radius, like that at $x = x_5$. This transition wake maximum radius replaces the radius of the hub vortex at the end of the transition wake in Greeley and Kerwin [1982].

The so-called ultimate wakes include the hub vortex and K tip vortices. The hub vortex originates at the end of the transition wake and extends downstream to a distant point on the x-axis, as in Greeley and Kerwin [1982].

The change in this new wake model will make the wake more realistic.

3.7.3 Hub Geometry

The hub, in this thesis, is the general term for the assembly of the propeller shaft, hub, and fairing. The geometry of the hub is simplified and represented by the following equations

$$r_h(x) = a(x - b)^3 + r_H$$

where

$$\text{(i)} \quad a = \frac{r_H}{(x_2 - x_1)^3} \qquad b = x_2 \qquad x_1 \leq x \leq x_2$$

(ii) $a = 0$ and $r_h = r_H = $ constant $x_2 \leqq x \leqq x_3$ (3.3)

(iii) $a = -\dfrac{r_H}{(x_4 - x_3)^3}$ $b = x_3$ $x_3 \leqq x \leqq x_4$

The **geometry** of the hub defined by these equations is controlled by five parameters, namely, r_H, x_1, x_2, x_3, and x_4. r_H is the hub maximum radius. The interval between $x = x_2$ and $x = x_3$ has constant radius equal to r_H. The interval between $x = x_3$ and $x = x_4$ is a cubic function which is best fit with real hub fairing. The interval between $x = x_1$ and $x = x_2$ is an artificial forebody to make this hub a closed body. The length of this nose will be proved numerically in one example to have little effect on the blade shape.

3.7.4 Hub Panels

Though there are many ways to panel the hub surface, the hub panels should be compatible with their neighbors, namely, the blades and the wakes. The natural way is to let the hub panel boundaries follow the blade and wake panel boundaries where they meet together. In this way, a set of hub helical vortex lattices is defined. As for the portion between the hub nose and the blades leading edge, the hub helical vortex may follow a helical line along the hub surface with a pitch angle exactly the same as that of the blade section.

There will be another set of vortices on the hub called vortex rings, although they are really polygons due to discretization. The x-position of these vortex rings will be the same as that of the end points of the first

blade spanwise elements in the blade region, and will be the same as that of the end points of the first transition wake in the wake region. As for the region between the hub nose and the blade leading edges, the vortex rings are equally spaced. There are NN1 vortex rings from $x = x_1$ (the end of the forebody) to the blade leading edge.

Thus these two sets of vortex lattices make up the panels for the hub. The number of panels is the number of unknowns which are going to be solved if we have the same number of equations. Before doing so, the reduction of unknowns from symmetry should be pointed out.

The inflow is assumed to be axisymmetric; the hub geometry is axisymmetric too. The blades and their wakes are not axisymmetric, but they are similar to each other. So, they are periodic in space in a blade-fixed coordinate system. Once 1/K portions of the hub panels are solved, all the hub singularities are known from periodicity. Thus, the unknowns are reduced K times, where K is the number of blades.

From the above argument and following the concept of key blade, a "key hub" is defined as the smallest portion of the hub which contains all the unknowns that need to be solved in the axisymmetric flow. From this definition, the key hub is not unique. However, the one that will be chosen in this thesis is the following. The key hub is, roughly speaking, the portion of the hub between the key blade and the second blade and between the first wake and the second wake.

The first hub helical vortex coincides with the key blade chordwise vortices and coincides with the key blade trailing vortices. From the key blade leading edge toward the hub nose, this first helical vortex follows the same pitch angle as that of the key blade root section. Once the first

helical vortex is generated, the rest of the helical vortices are parallel
to the first one with equal angle spacing between each other.

Suppose there are NH helical vortices in the key hub. Then the angle
between any two adjacent helical vortex elements will be

$$\Delta\theta = \frac{2\pi}{K \cdot NH} \tag{3.4}$$

Figure 3.3 shows an arrangement of NH = 4 and K = 5. Notice that the
M = 5 helical vortex is on the second blade, so it has identical strength
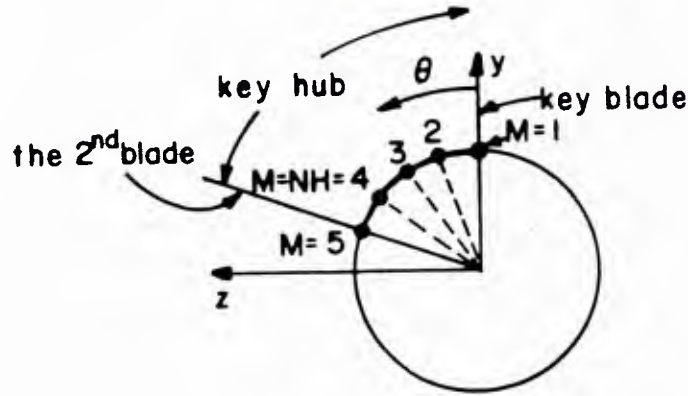as the one at M = 1 on the key blade from periodicity.

Figure 3.3 Cross Section of a Key Hub

Figure 3.3 shows a plane perpendicular to the x-axis, so one vortex
ring is also seen here as a portion of a polygon with 20 sides.

The first ring vortex (N = 1) is the one closest to the hub nose; the
last vortex ring (N = NR) is the one closest to the hub apex. The total
number of vortex rings NR is equal to the sum of NN1, NN, and NN2.

$$NR = NN1 + NN + NN2 \tag{3.5}$$

NN1 is the number of vortex rings between the hub nose and the blade leading edge. As mentioned before, these NN1 vortex rings are equally spaced in x between the hub nose and the blade leading edge. NN is the number of rings between the blade leading edge and the blade trailing edge. NN, by definition, equals the number of spanwise vortices on the key blade. NN2 is the number of vortex rings between the blade trailing edge and the hub apex. This number is dynamically adjusted with wake alignment. It will be explained in the wake alignment section.

The total number of panels is NT = NR·NH. Each panel consists of two helical vortex elements and two vortex ring elements. The control points upon which the normal velocity vanishes are chosen as the centroid of each panel.

The normal vector of each panel is constructed by forming the cross-product of the two diagonal vectors of the panel. The normal vector is defined as positive if it points into the hub.

The sense of positive vortex panels is counterclockwise when looking in the positive normal vector direction. The sense of helical vortices is positive if it points downstream. The sense of vortex rings is positive if it points in the positive θ direction.

A typical I^{th} hub vortex panel, a quadrilateral element, is shown in Figure 3.4a.

Notice that the relationship between I and N and M is

$$I = (M - 1)NR + N \tag{3.6}$$

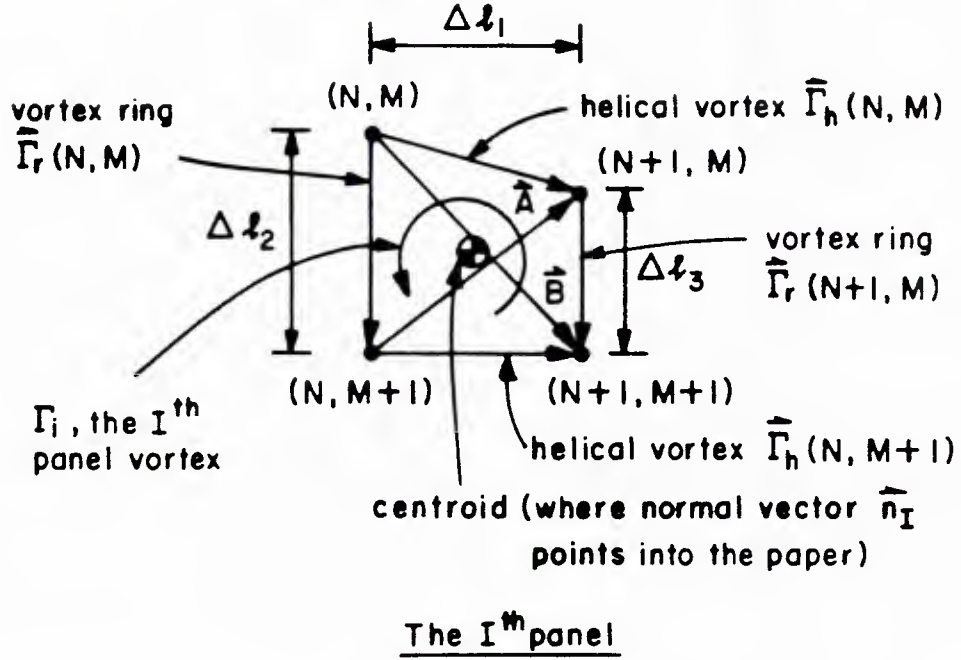The normal vector of the Ith panel is defined as

Figure 3.4a   A Typical Quadrilateral Panel on the Hub

$$\hat{n}_I = \frac{\vec{A} \times \vec{B}}{|\vec{A} \times \vec{B}|} \qquad (3.7)$$

where $\vec{A}$ and $\vec{B}$ are diagonal vectors of the panel I.   The panel area is

$$A_I = \frac{1}{2} |\vec{A} \times \vec{B}|$$

The (N,M + 1) helical vortex will have the same strength as that of (N,1) if M equals NH.   From the definition of vortex panel, vortex ring, and helical vortex, the (N,M) vortex ring and the (N,M+1) helical vortex are equal in strength to the Ith vortex panel, while the (N,M) helical vortex and the (N+1,M) vortex ring are equal in strength to the negative value of the Ith vortex panel.

A typical I^{th} hub vortex panel right next to the hub apex is a triangle as shown in Figure 3.4b.
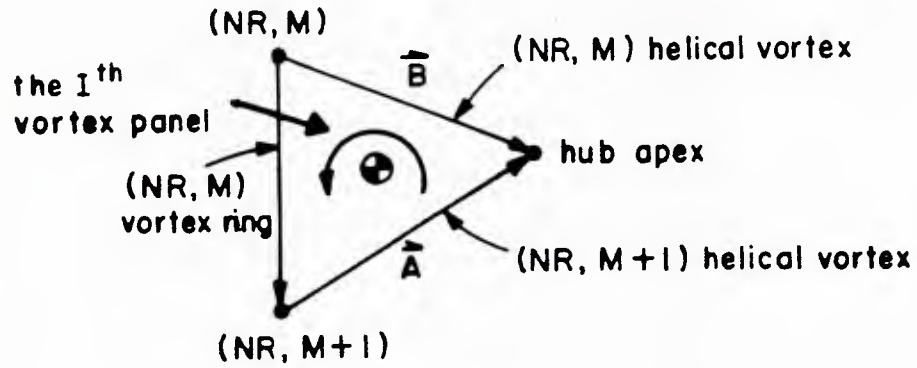

Figure 3.4b A Typical Triangular Panel on the Hub

All the properties of the quadrilateral panel apply for the triangular panel also. A triangular panel can be treated as a quadrilateral panel with one vortex ring with zero length.

3.7.5 The Solution for Hub Singularities

The boundary conditions on hub control points in vector form are

$$(\vec{V} \cdot \vec{n})_i = 0 \qquad i = 1,2,\ldots,NT \tag{3.8}$$

The total velocity vector $\vec{V}$ is

$$\vec{V} = \vec{V}_I + \vec{V}_B + \vec{V}_W + \vec{V}_H \tag{3.9}$$

where $\tilde{V}_I$ is the inflow velocity, and $\tilde{V}_B$, $\tilde{V}_W$, and $\tilde{V}_H$ are the velocities induced by blade singularities, trailing vortex wakes, and hub singularities respectively.

$\tilde{V}_B$ and $\tilde{V}_W$ can be calculated if the blade singularities and wake geometries are known, so that

$$[\tilde{V}_H \cdot \tilde{n} = - (\tilde{V}_I + \tilde{V}_B + \tilde{V}_W) \cdot \tilde{n}]_i \qquad i = 1,2,\ldots,NT \qquad (3.10)$$

$\tilde{V}_{H_i}$, $\tilde{V}_H$ at the ith control point, is the summation of all the velocities induced by hub singularities, i.e.,

$$\tilde{V}_{H_i} = \sum_{j=1}^{NT} \tilde{V}_{ij} \Gamma_j \qquad (3.11)$$

where $\tilde{V}_{ij}$ is the velocity induced at the ith control point by the jth panel (and all panels equivalent to the jth panel in the rest of the hub) of unit strength singularity, and Γ_j is the unknown strength of the jth panel singularity. At this stage, some readers may be interested in looking at the Appendix to see the power of reducing the number of unknowns by the concept of key hub.

Substituting (3.11) into (3.10) and carry out the inner product, we obtain simultaneous linear algebraic equations for Γ_j.

$$\sum_{j=1}^{NT} (\tilde{V}_{ij} \cdot \tilde{n}_i) \Gamma_j = [- (\tilde{V}_I + \tilde{V}_B + \tilde{V}_W) \cdot \tilde{n}]_i \qquad i = 1,2,\ldots,NT \quad (3.12)$$

or

$$A \ \Gamma = B \qquad\qquad (3.13)$$

in matrix form.

A is an NT by NT matrix; Γ and B are vectors of NT elements.

Matrix A's element a_{ij} and vector B's element b_i are defined as

$$a_{ij} = \tilde{V}_{ij} \cdot \tilde{n}_i \qquad\qquad (3.14)$$

$$b_i = [- \ (\tilde{V}_I + \tilde{V}_B + \tilde{V}_W) \cdot \tilde{n}]_i \qquad\qquad (3.15)$$

In order to save computer time, but without losing any accuracy in calculating b_i, the lattices on the key blade and the second blade (they are the boundaries of the key hub) have fine grids while the other blades may have coarse grids.

Once the hub panel strengths are solved, the decomposition of these panel strengths into hub helical vortices and hub ring vortices is straightforward. Taking the Ith panel and its four adjacent panels,
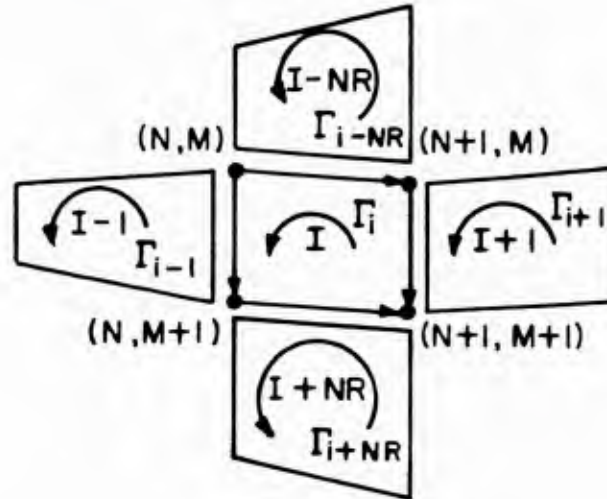

Figure 3.5 Decomposition of Panel Strengths

namely, the $(I - 1)^{th}$, $(I + 1)^{th}$, $(I - NR)^{th}$, and $(I + NR)^{th}$ panels (Figure 3.5), for example, the helical vortices $\Gamma_h(N,M)$ and $\Gamma_h(N,M + 1)$ and the vortex rings $\Gamma_r(N,M)$ and $\Gamma_r(N + 1,M)$ are

$$\Gamma_h(N,M) = \Gamma_{i-NR} - \Gamma_i$$
$$\Gamma_h(N,M + 1) = \Gamma_i - \Gamma_{i+NR}$$
$$\Gamma_r(N,M) = \Gamma_i - \Gamma_{i-1}$$
$$\Gamma_r(N + 1,M) = \Gamma_{i+1} - \Gamma_i$$

$$(3.16)$$

where $i = (M - 1)NR + N$

3.7.6 Wake Alignment and Blade Alignment

The wake alignment and blade alignment will follow the same scheme as in Greeley and Kerwin [1982], except that the induced velocities on wake control points or on blade control points will be added contributions from the hub helical/ring vortex system.

3.7.7 Force Calculation

The blade forces are computed in the same way as in Greeley and Kerwin [1982], i.e., by determining the forces acting on the line singularities representing the key blade by applying the Kutta-Joukowsky law for the vortices and Lagally theory for the sources.

The force calculation on the hub will be done by integrating the pressure at the hub control points instead of on the singularities. The advantage of doing so is to save computer time. Because the velocities

induced on the hub control points by blade and wake singularities have already been found in solving the hub boundary value problem, the velocities induced by the hub panels with unit strength have also already been done at the same time. The former plus the latter, times the hub panel strength, plus inflow will be the total velocity at the control points except for the vortex sheet jumping velocities which will be introduced next.

The concentrated vortex element (vortex lattice) can be regarded as a lumped vortex sheet. The influence function of the vortex lattice is easier to calculate than that of the vortex sheet. This is the reason to choose the vortex lattice instead of the vortex sheet. The most important thing is that it does not give rise to errors, as far as the normal velocity is concerned, in calculating to solve the boundary value problem.

The situation is changed when the tangential velocity is considered. The vortex sheet in a panel produces a tangential velocity equal to one half of its strength at its control point, while the vortex lattices along that panel produce zero tangential velocity at that control point and lead to the wrong result.

The solution is to redistribute the concentrated vortex lattices into a vortex sheet [Kim and Kobayashi, 1984]. A typical quadrilateral panel is shown in Figure 3.4a with two vortex rings $\vec{\Gamma}_r(N,M)$ and $\vec{\Gamma}_r(N + 1,M)$ and two helical vortex lattices $\vec{\Gamma}_h(N,M)$ and $\vec{\Gamma}_h(N,M + 1)$. The vortex sheet $\vec{\gamma}(I)$ in the Ith panel has two components -- $\vec{\gamma}_r(I)$ comes from averaged vortex rings and $\vec{\gamma}_h(I)$ comes from averaged helical vortices. Notice that the two vortex rings are parallel to each other while the helical vortices may have an arbitrary angle to each other.

$$\vec{\gamma}(I) = \vec{\gamma}_r(I) + \vec{\gamma}_h(I)$$

$$\vec{\gamma}_r(I) = \frac{\vec{\Gamma}_r(N,M) + \vec{\Gamma}_r(N + 1,M)}{2(\Delta l_1)} \qquad (3.17)$$

$$\vec{\gamma}_h(I) = \frac{\vec{\Gamma}_h(N,M) + \vec{\Gamma}_h(N,M + 1)}{\Delta l_2 + \Delta l_3}$$

For a triangular panel, $\vec{\Gamma}_r(N + 1,M)$ and Δl_3 are both zero in the above equations.

The jump velocity is $\gamma/2$ with a direction normal to $\vec{\gamma}(I)$ and tangential to the panel.

The pressure on a body rotating at constant angular velocity, $-\omega\vec{i}$, in a uniform onset flow with only an axial component can be expressed as [Kim and Kobayashi, 1984]

$$p = -\frac{1}{2}\rho[\vec{V}\cdot\vec{V} - V_x^2 - r^2\omega^2] + p_\infty \qquad (3.18)$$

where

$$\vec{V} = \text{total velocity} = v_x\vec{i} + r\omega\hat{e}_\theta + \vec{V}_p$$

and p_∞ is the pressure far upstream. $\vec{V}_p$ is the perturbation velocity due to the propeller blades, wakes, and hub.

$$\vec{V}_p = \vec{V}_B + \vec{V}_W + \vec{V}_H \qquad (3.19)$$

3.7.8 Termination of Design Iteration Procedure

If the new blade shape, namely pitch and camber distribution, is nearly the same as the old one, then the design of the blade shape is done. Otherwise this new blade shape will be the input data for another run.

3.8 Design Example

A design example will be given in the following section.

3.8.1 Input Data of Blades

This is a five-bladed propeller with a hub ratio of 0.3 running in an axial shear flow with advance coefficient $J = V_s/nD = 1.016$, where V_s is the ship speed. The blade geometry (except the pitch and camber which will be determined) as well as inflow information is given in Table 3.1.

Radius r/R	Rake/Diameter x_s/D	Skew Angle in Degrees	Chord/ Diameter C/D	Thickness/ Diameter t_o/D	Inflow/ Ship Velocity V_x/V_s
0.3000	0.0060	1.420	0.1868	0.0464	0.9575
0.3438	-0.0070	-2.340	0.2142	0.0415	0.9455
0.3875	-0.0200	-6.100	0.2416	0.0366	0.9335
0.4750	-0.0340	-9.530	0.2961	0.0285	0.9159
0.5625	-0.0340	-8.980	0.3473	0.0230	0.9021
0.6500	-0.0220	-5.850	0.3875	0.0194	0.8954
0.7375	-0.0035	-0.940	0.4108	0.0171	0.8899
0.8250	0.0240	6.650	0.4020	0.0148	0.8831
0.9125	0.0480	14.620	0.3577	0.0127	0.8693
0.9563	0.0620	19.620	0.2956	0.0103	0.8642
1.0000	0.0760	24.620	0.0700	0.0079	0.8591

Table 3.1 Blade Geometry for the Design Example

The load is given in the form of a radial curculation distribution

$$\Gamma_b(r) = 2\pi R V_s \sum_{l=1}^{L} a_l \sin(\tilde{r} \cdot l) \tag{3.20}$$

where L is the number of series coefficients retained, 5 for this case, and $\tilde{r}$ is the transformed radial coordinate

$$\tilde{r} = \cos^{-1}\left[\frac{1 - r_H - 2r}{1 - r_H}\right] \qquad 0 \leq \tilde{r} \leq \pi \tag{3.21}$$

and

$$a_1 = 0.036716$$

$$a_2 = -0.004519$$

$$a_3 = -0.004184$$

$$a_4 = 0.000125$$

$$a_5 = 0.000031$$

A plot of circulation distribution is shown in Figure 3.6.

3.8.2 Hub Geometry and Hub Modeling

Real hub geometry, as well as a best fit hub geometry with $r_H = 0.3$, $x_3 = 0.012$, and $x_4 = 0.761$, and the equation (3.3) are given in Table 3.2.
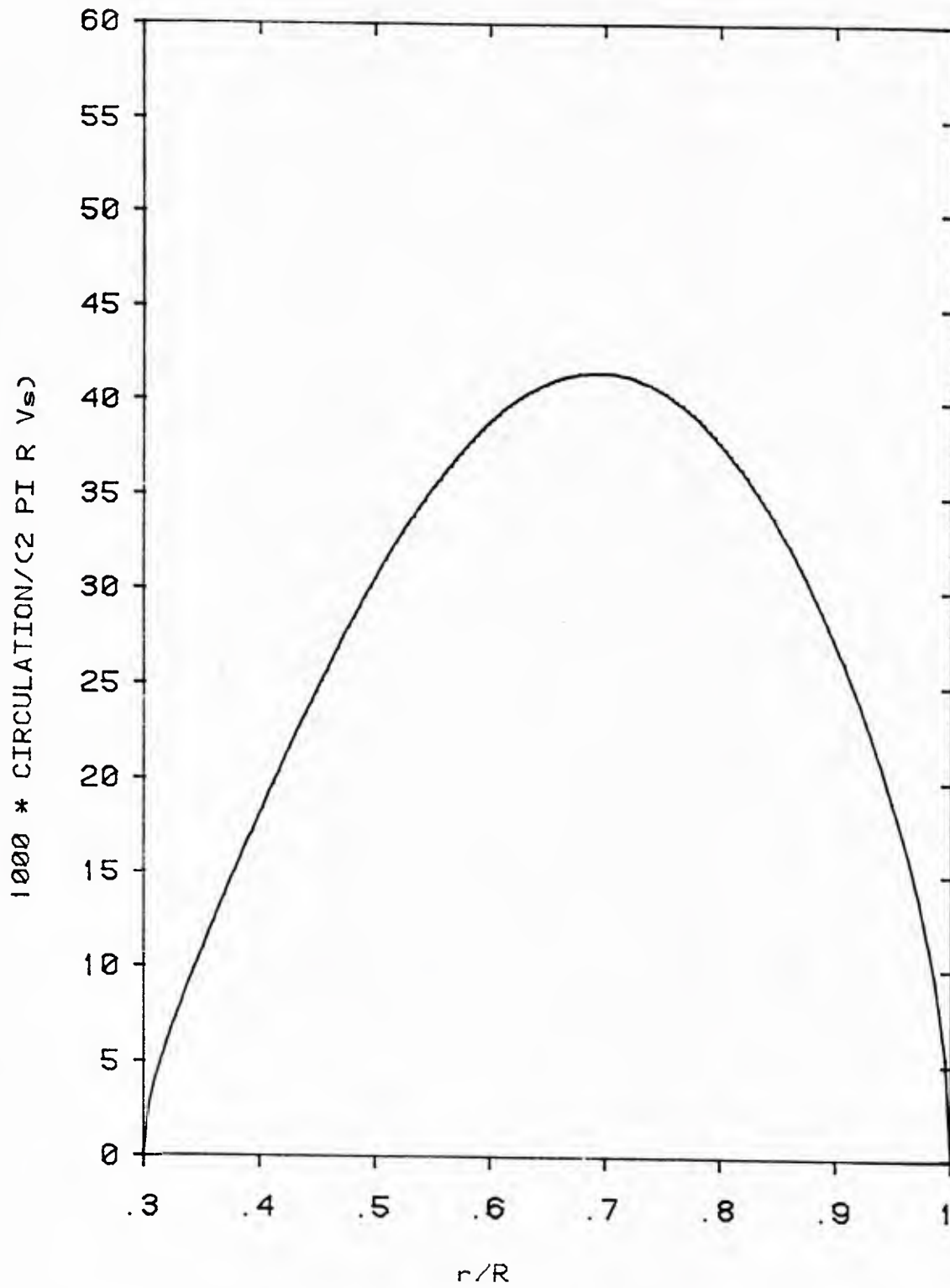
FIG. 3.6 CIRCULATION DISTRIBUTION FOR DESIGN EXAMPLE

$\frac{x}{R}$	-0.284	-0.185	-0.086	0.012	0.111	0.210	0.309	0.407	0.556	0.761
$\frac{r}{R}$	0.3	0.3	0.3	0.3	0.299	0.298	0.296	0.247	0.185	--
$\frac{r'}{R}$	0.3	0.3	0.3	0.3	0.299	0.294	0.281	0.256	0.185	0.0

Table 3.2   Real Hub Geometry r/R and Fitted Hub Geometry r'/R

As for the other two hub parameters, x_1 and x_2 are arbitrary at this stage and their influence on blade shape design will be investigated. That is, three different sets of x_1 and x_2 are chosen to represent three different lengths of hub, and the blade shape will be designed three times, each design corresponding to one hub. Those hubs will be called short hub, medium hub, and long hub. Their x_1 and x_2 values, and a hub fatness to hub total length ratio are shown in Table 3.3.

	Short Hub	Medium Hub	Long Hub
x_1	-0.60	-1.0	-1.5
x_2	-0.284	-0.284	-0.3
Fatness/Length	1:4.54	1:5.87	1:7.54

Table 3.3 x_1 and x_2 Values of Three Hubs

3.8.3 Inflow Modification

Because the hub is modeled as a closed body, the flow will be accelerated by it in the mid part of the hub. The nose (x_1 value) is arbitrarily chosen and the flow depends on the body shape. This results in

an arbitrary flow pattern which deviates from the real inflow, and a
x_1-dependency blade shape is anticipated.

The solution to this is to reduce the inflow in such a way that after
being accelerated by the hub, the flow at the propeller plane will recover
the given inflow approximately. The propeller is designed in an
axisymmetric shear flow, although potential flow is assumed. If the inflow
is uniform (a special case of an axisymmetric flow), the flow field around
an axisymmetric body has already been solved in Chapter 2. As for an
axisymmetric shear flow, three-dimensional Navier-Stokes equations have to
be solved, which is beyond the scope of this thesis.

In order to solve the problem, an approximate method is adapted as
follows. First, solve the problem of a bare hub (dummy hub) in a uniform
flow by the method of Chapter 2. Then, calculate the ratio of the
disturbance velocities at the propeller plane (x = 0) to uniform flow.
Finally, deduct an amount of velocity equal to the product of the above
ratio and the given inflow from the given inflow. Table 3.4 shows the
given inflow as well as the modified inflow for three dummy hubs introduced
in 3.8.2 by these approximate methods. Recall that in Chapter 2 two models
are introduced; one is an axisymmetric body represented by vortex rings,
and the other one is an axisymmetric body represented by vortex rings plus
a central source line. Because the former predicts the field point
velocities more accurately than the latter, the former is adapted here for
calculating the modified inflow.

r/R	Given Inflow/V_S	Modified Inflow/Vs		
		Short Hub	Medium Hub	Long Hub
0.3	0.9575	0.8503	0.8659	0.8774
0.3438	0.9455	0.8505	0.8666	0.8741
0.3875	0.9335	0.8458	0.8610	0.8683
0.475	0.9159	0.8448	0.8566	0.8638
0.5625	0.9021	0.8462	0.8545	0.8607
0.65	0.8954	0.8517	0.8571	0.8621
0.7375	0.8899	0.8557	0.8591	0.8629
0.8250	0.8831	0.8563	0.8582	0.8610
0.9125	0.8693	0.8482	0.8492	0.8512
0.9563	0.8642	0.8453	0.8460	0.8477
1.0	0.8591	0.8423	0.8427	0.8441

Table 3.4   Given Inflow and Modified Inflow

3.8.4   The Effect of Hub-Nose Length

The pitch and camber distribution of three designs corresponding to three different lengths of hub nose are shown in Table 3.5. The results are good; the difference between the medium hub case and the long hub case is quite small (about 2% for camber and 0.6% for pitch) while the difference between the short hub case and either the medium hub case or the long hub case is about 19% for camber and 5% for pitch. Too short a nose may make the blade shape depend on hub-nose length, while a reasonably long $(x_1 \leq -1.0)$ hub-nose length can result in a unique blade shape.

The K_T, K_Q, and η values and H_{KT} (the axial force on the hub) are summarized in Table 3.6 for these three designs. H_{KT} is the drag on the hub nondimensionalized with respect to $\rho n^2 D^4$, the same as for K_T. It is observed that H_{KT} is also x_1-independent if x_1 is large enough. H_{KT} is about 2% of K_T for this design case. Two-dimensional plots of the

r/R$_0$	Short Hub ($x_1 = -0.6$)		Medium Hub ($x_1 = -1.0$)		Long Hub ($x_1 = -1.5$)	
	P/D	f$_0$/C	P/D	f$_0$/C	P/D	f$_0$/C
0.3	0.8803	-0.0410	0.9218	-0.0497	0.9277	-0.0508
0.3438	1.1128	0.0041	1.1246	0.0046	1.1234	0.0052
0.3875	1.2997	0.0260	1.2923	0.0303	1.2865	0.0316
0.4750	1.4970	0.0330	1.4886	0.0357	1.4825	0.0367
0.5625	1.5428	0.0409	1.5416	0.0415	1.5386	0.0421
0.6500	1.5581	0.0404	1.5596	0.0404	1.5595	0.0406
0.7375	1.4584	0.0346	1.4601	0.0343	1.4607	0.0341
0.8250	1.2987	0.0325	1.2988	0.0324	1.2989	0.0323
0.9125	1.1086	0.0251	1.1096	0.0250	1.1102	0.0249
0.9563	0.9275	0.0245	0.9283	0.0243	0.9290	0.0241
1.0	0.6418	0.0288	0.6412	0.0283	0.6414	0.0279

Table 3.5 Comparison of pitch and camber distribution among three cases of hub-nose length. NH = 4 and NN1 = 8 for all three designs.

	Short Hub	Medium Hub	Long Hub
K$_T$	0.351	0.352	0.352
K$_Q$	0.0699	0.0700	0.0700
η	0.813	0.813	0.813
H$_{KT}$	-0.01539	-0.00796	-0.00743

Table 3.6 Force Coefficients for Three Designs

discretized key hub and key blade are shown in Figure 3.7, Figure 3.8, and Figure 3.9 for the cases of short hub, medium hub, and long hub respectively. In the long hub case, the plot is for NH = 5, which is for studying the convergence of blade shape due to NH and will be discussed in the next section.
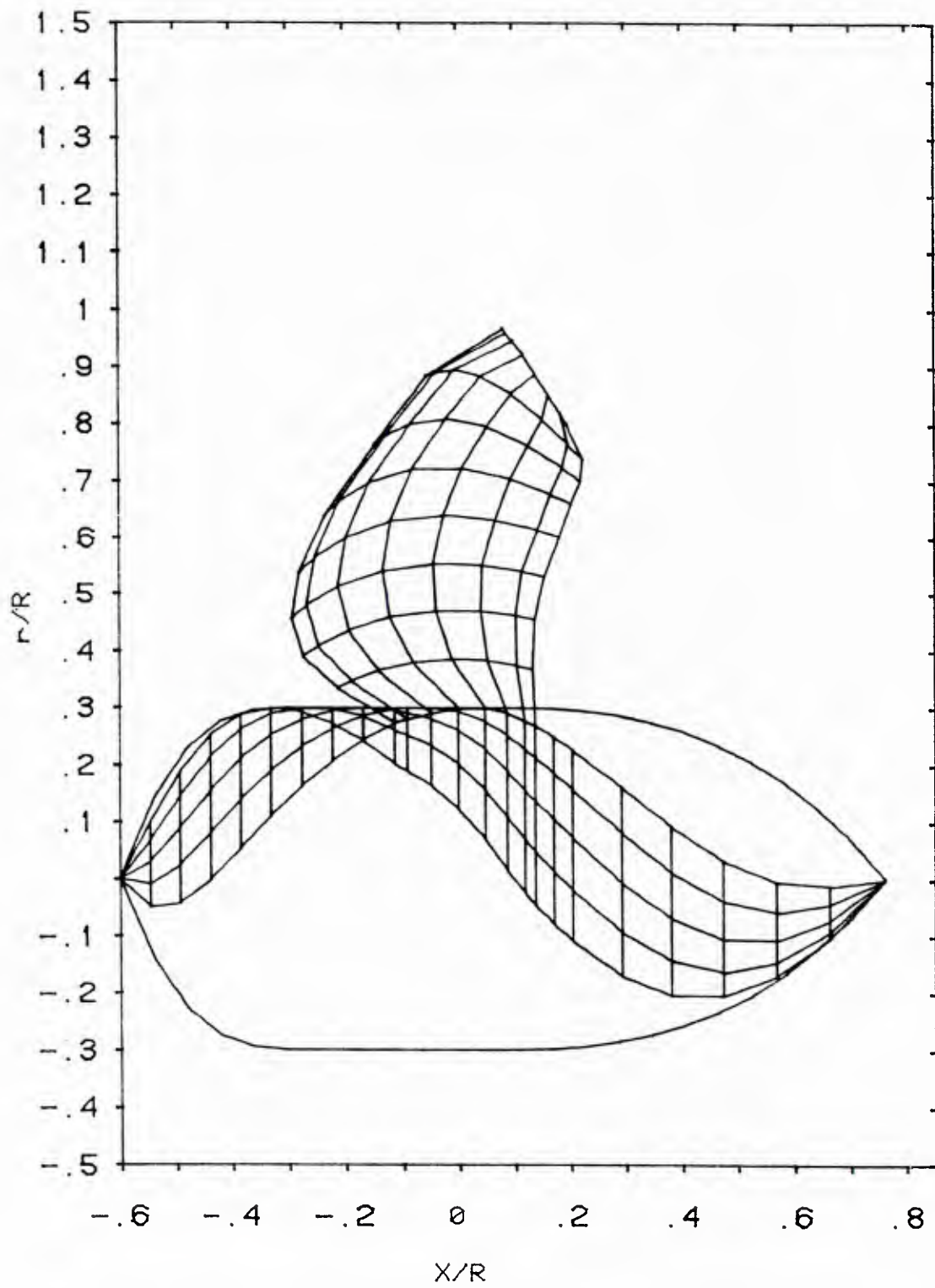
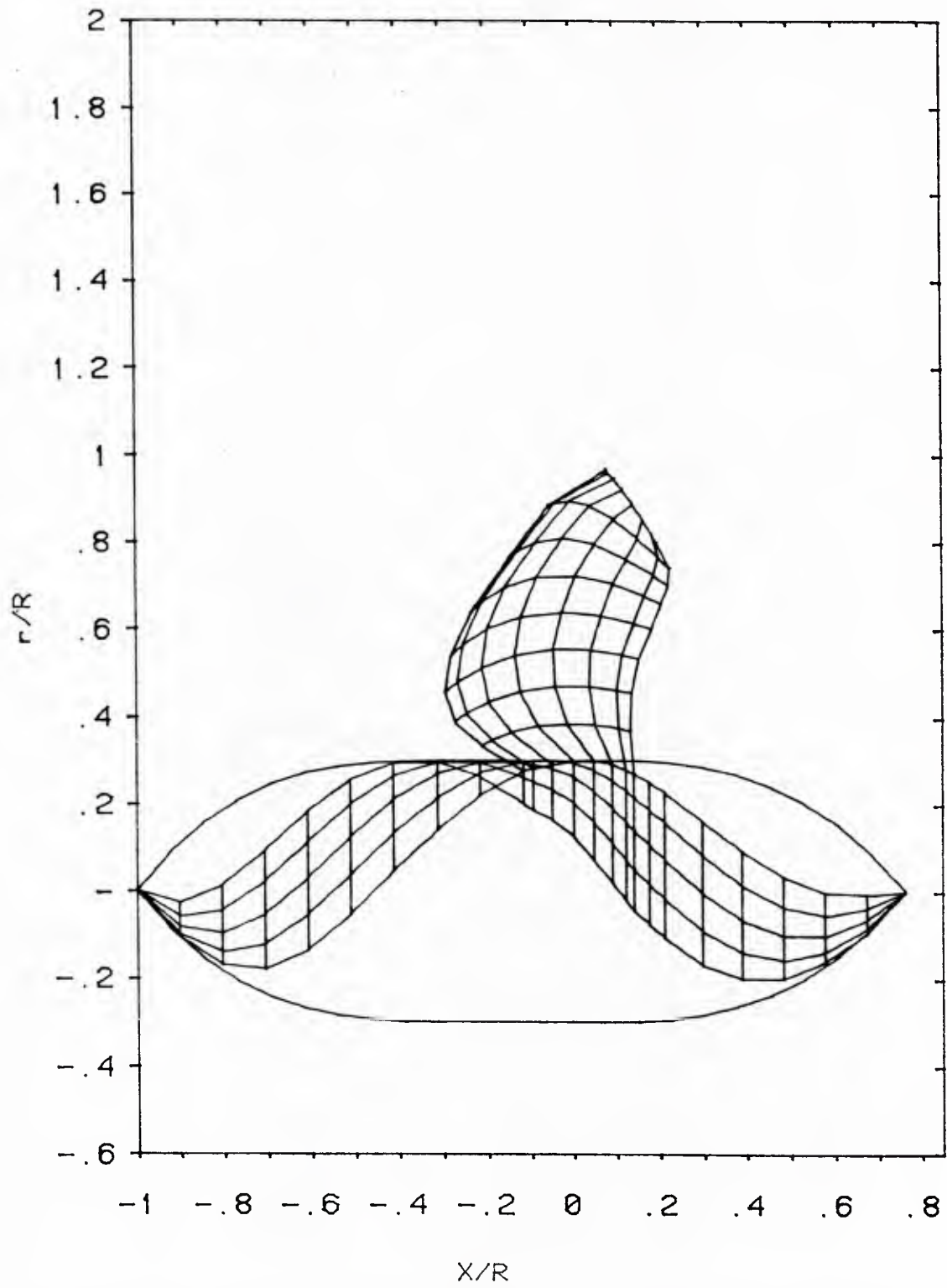FIG. 3.7 DISCRITIZED KEY BLADE AND SHORT KEY HUB
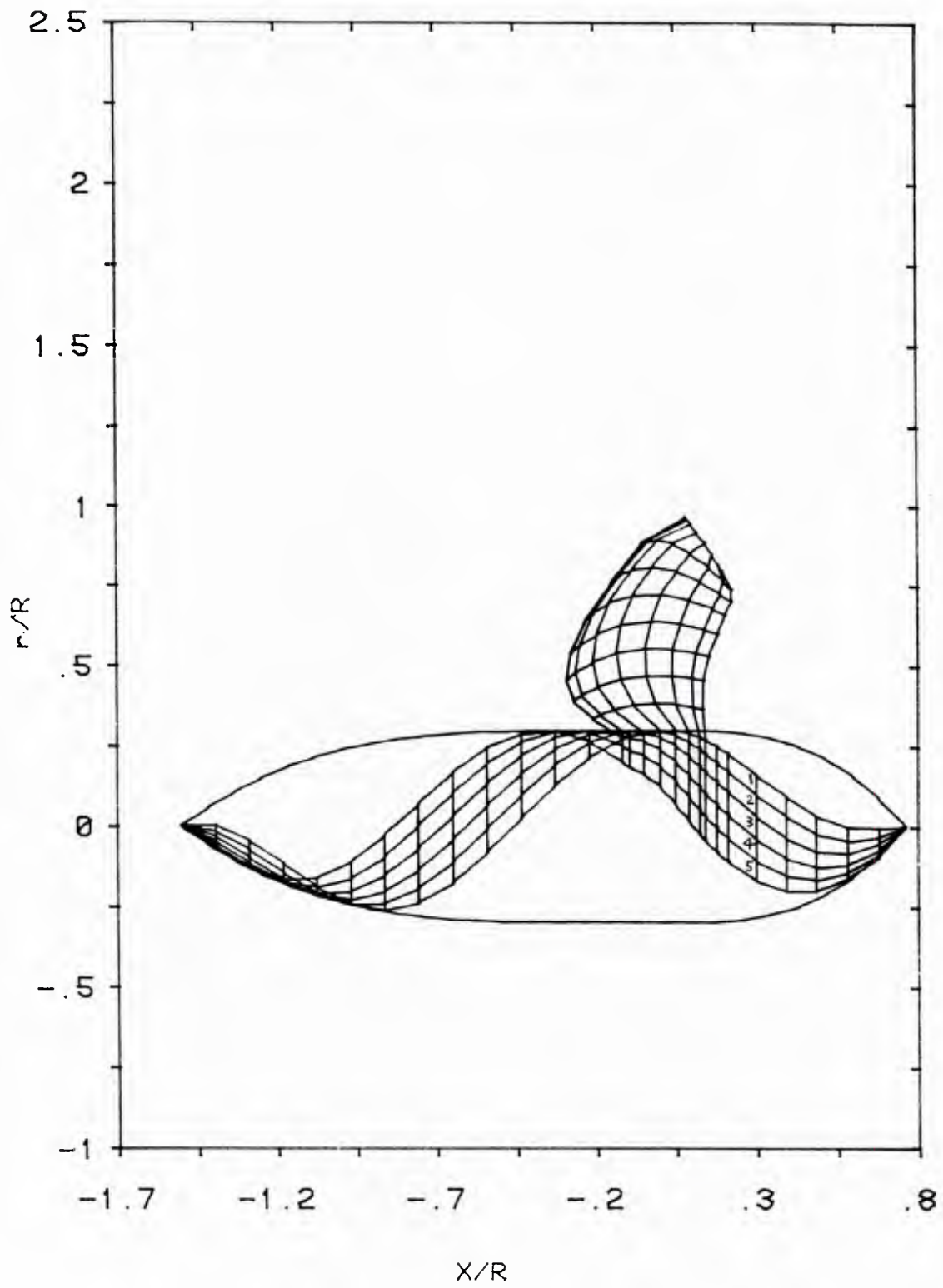
FIG. 3.8 DISCRITIZED KEY BLADE AND MEDIUM KEY HUB

FIG. 3.9 DISCRITIZED KEY BLADE AND LONG KEY HUB

3.8.5 The Influence of Number of Helical Vortices on Blade Shape and Force

If the case of the long hub is regarded as a convergent result for changing the hub-nose length while NH is fixed (equals 4), the sensitivity of NH to blade shape is next to be studied while the hub length is fixed for the long hub.

In additon to NH = 4, two cases of NH = 3 and NH = 5 are studied. The results of pitch and camber distribution as well as the force coefficients are shown in Table 3.7.

	NH = 3		NH = 4		NH = 5	
r/R	P/D	f_o/C	P/D	f_o/C	P/D	f_o/C
0.3	0.9332	-0.0500	0.9277	-0.0508	0.9241	-0.0519
0.3438	1.1272	0.0059	1.1234	0.0052	1.1210	0.0049
0.3875	1.2887	0.0320	1.2865	0.0316	1.2852	0.0316
0.4750	1.4830	0.0368	1.4825	0.0367	1.4827	0.0368
0.5625	1.5388	0.0421	1.5386	0.0421	1.5388	0.0422
0.6500	1.5603	0.0406	1.5595	0.0406	1.5602	0.0406
0.7375	1.4611	0.0340	1.4607	0.0341	1.4613	0.0341
0.8250	1.2988	0.0322	1.2989	0.0323	1.2993	0.0323
0.9125	1.1105	0.0249	1.1102	0.0249	1.1107	0.0249
0.9563	0.9292	0.0240	0.9290	0.0241	0.9294	0.0241
1.0	0.6413	0.0278	0.6414	0.0279	0.6413	0.0279
K_T	0.352		0.352		0.352	
K_Q	0.700		0.700		0.701	
η	0.813		0.813		0.813	
H_{KT}	-0.00705		-0.00743		-0.00788	

Table 3.7   The Sensitivities of NH Values to Blade Shape and
            Force Coefficients

3.8.6 Summary of Results of Design Example

The case of a long hub with NH = 5 is regarded as the final result for the design example. The blade shape as well as the a = 0.8 mean line with the same camber ratio are plotted at ten radial sections in Figure 3.10. Except for the first two sections, the blade shape is very close to a = 0.8 mean line.

The discretized key hub, key blade, and its transition wakes and ultimate wakes are shown in Figure 3.11. The blowup of the three-dimensional views of key hub, key blade, and its transition wakes are shown in Figure 3.12(a). All five discretized blades are shown in Figure 3.12(b).

The strengths of the hub vortex sheet redistributed from the discretized vortex rings are plotted in Figures 3.13(a) and 3.13(b). The symbols numbered from 1 to 5 in Figure 3.13(a) represent the strengths corresponding to the vortex ring segments in Figure 3.9. It is seen that the strengths of vortex ring segments are almost constant for the rings far ahead of the blade leading edges (about $x = - 0.2 R$). This suggests that for those lattices far away from the blade leading edges a simple vortex ring is sufficient to represent the hub. A reduction in the number of unknowns for those lattices has a factor of NH. A solid line in Figure 3.13(a) indicates vortex sheet strengths of the dummy hub in a uniform stream which equals the ship speed V_s.

The jump velocities raised by these vortex sheets is just one half of the vortex sheet strengths. The negative signs mean these jump velocities point downstream because of the definition of the positive sense of the
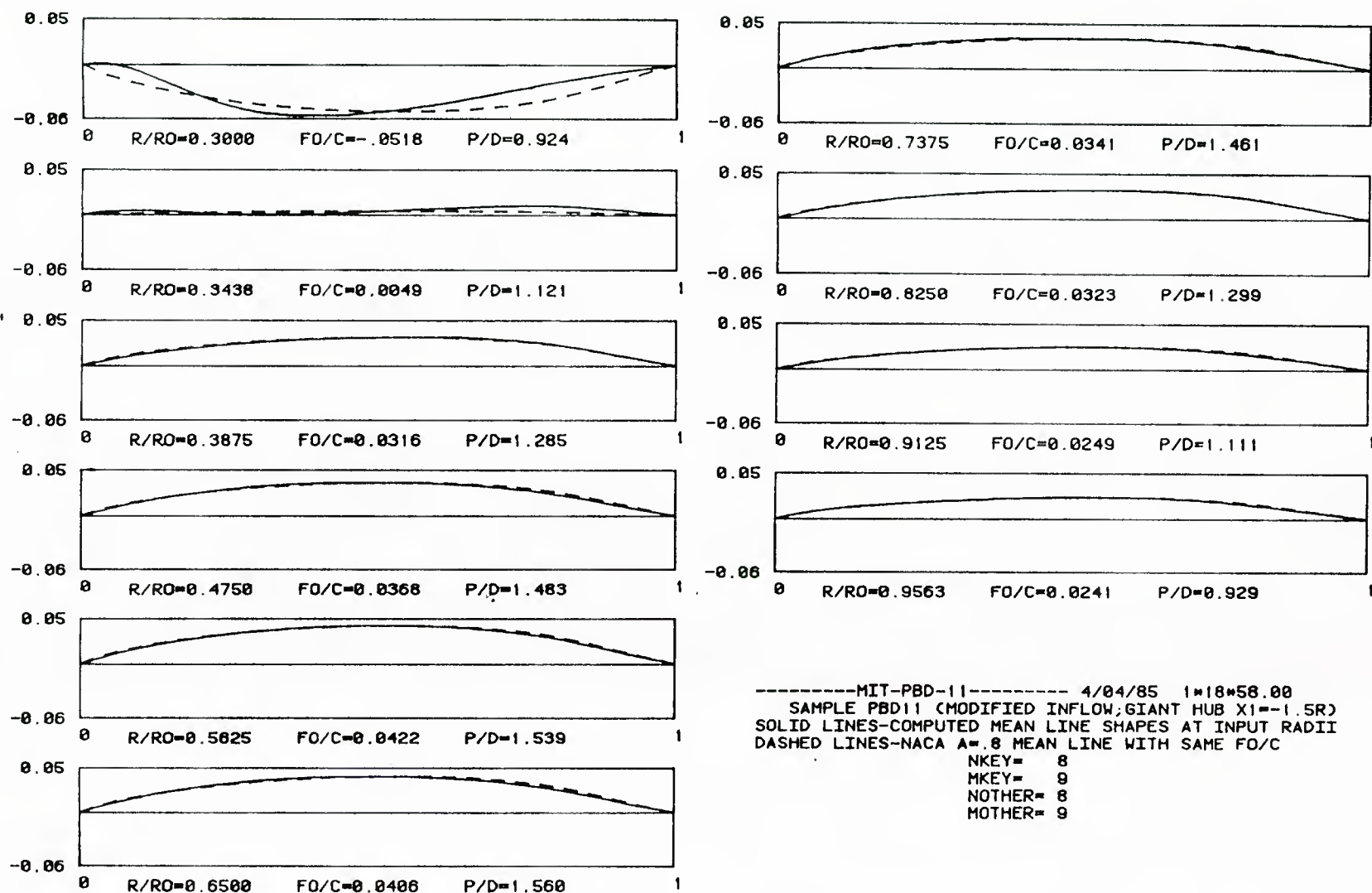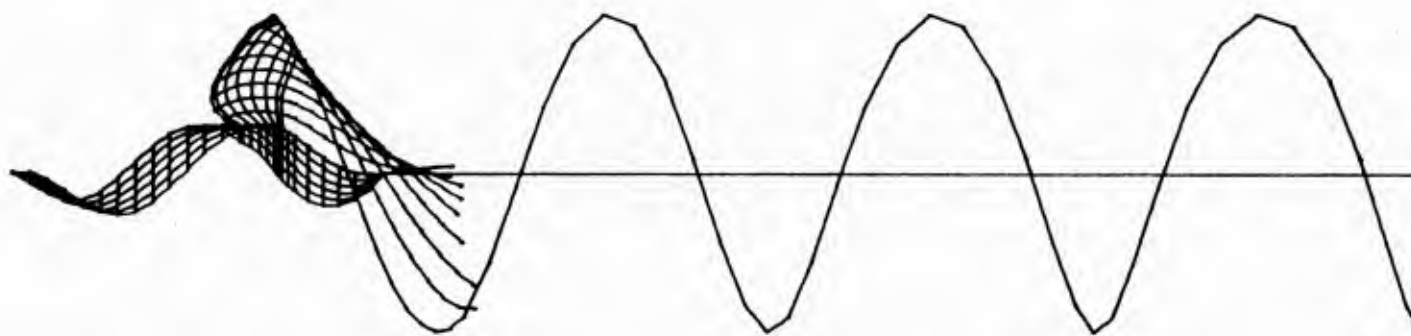
FIG. 3.10 BLADE MEAN LINE SHAPES AT 10 SECTIONS

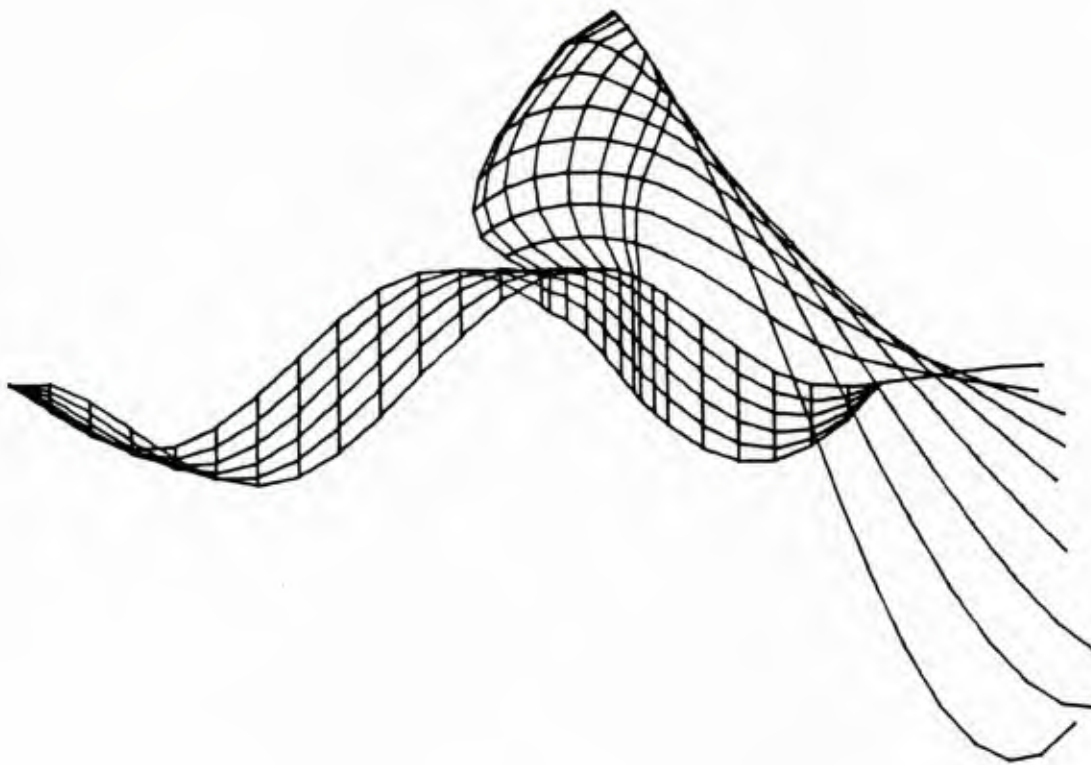FIG. 3.11 DISCRETIZED KEY HUB, KEY BLADE, TRANSITION AND ULTIMATE WAKES

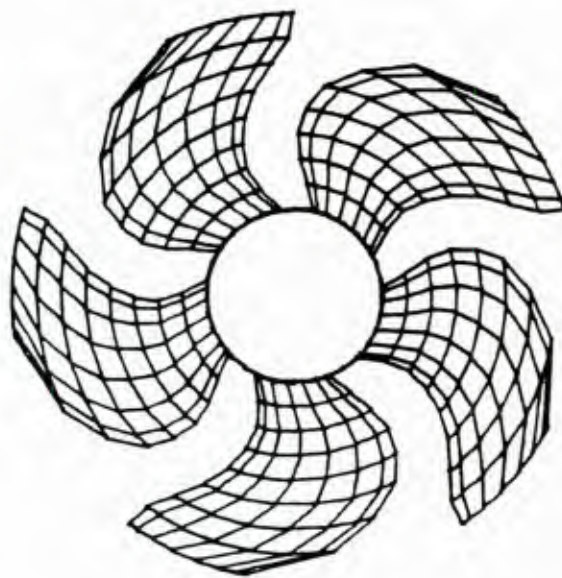FIG. 3.12(a) KEY HUB, KEY BLADE AND ITS TRANSITION WAKES
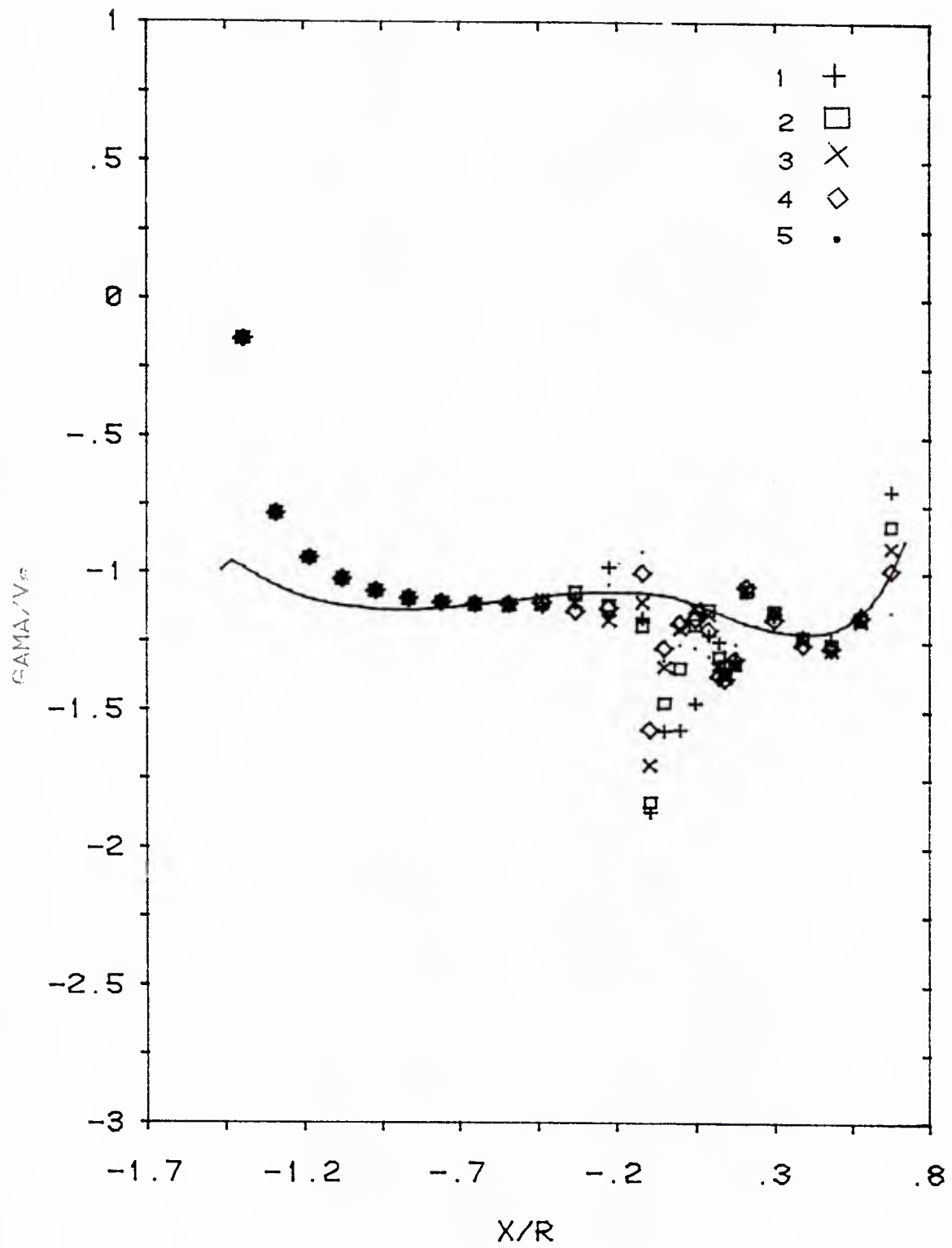

FIG. 3.12(b) DISCRETIZED BLADES

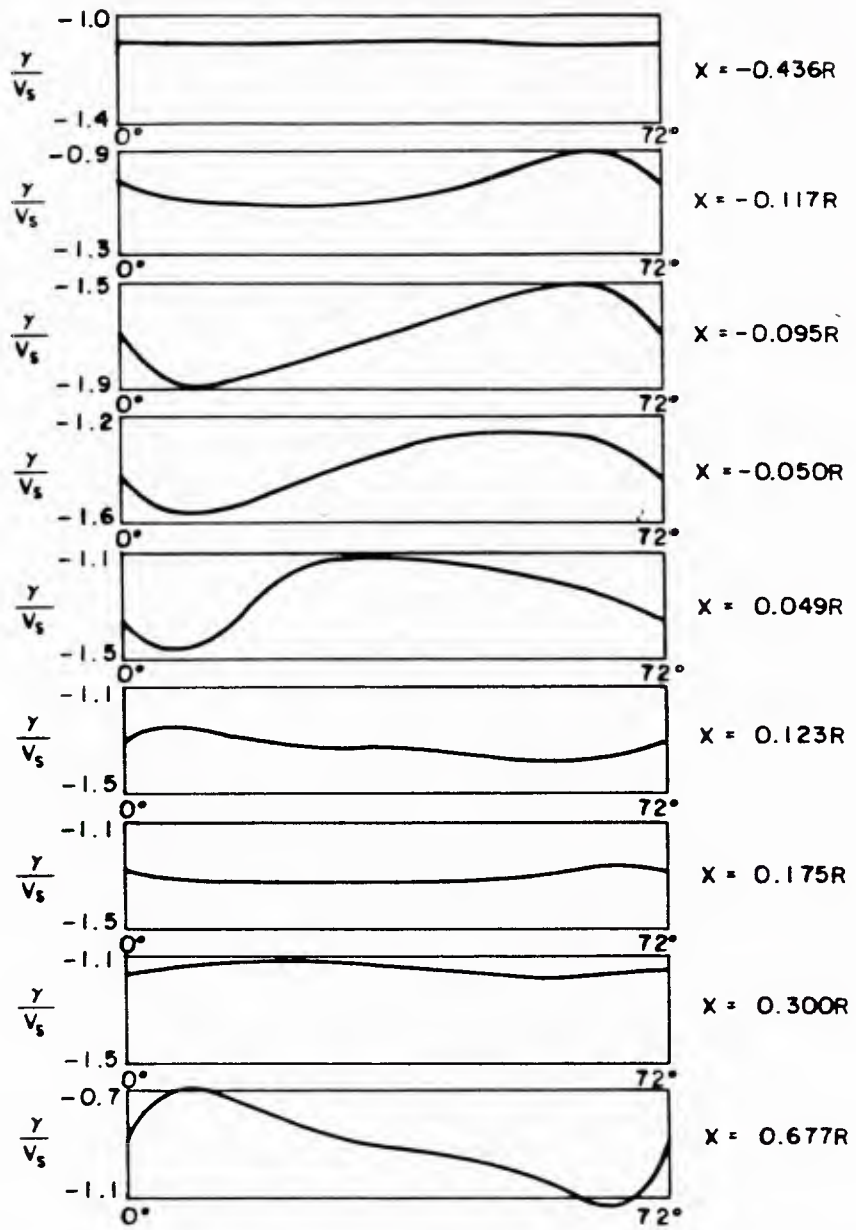FIG. 3.13(a) STRENGTHS OF HUB-VORTEX-RING SHEETS

Fig. 3.13b Ring - Vortex - Sheet Strength at Different Location

vortex rings. The acceleration of axial velocities are as high as ship speed in some regions between blades.

3.8.7 Comparison between Design with Hub Effects and Design without Hub Effects

It is interesting to investigate the hub effects by comparing the design with the hub case with the design without the hub case. Figure 3.14 shows the section shape of mean lines for both designs. The hub effects are important at sections close to the hub. The hub effects are supplying a solid boundary to lifting surfaces (blades) which attach to it. Thus, they will increase the lift force if the blades remain the same shape, or reduce the camber and/or angle of attack (pitch) if the required lift (load) is fixed. The pitch and camber distribution in the radial direction are also replotted in Figure 3.15 and Figure 3.16 for both cases, with the hub and without the hub.
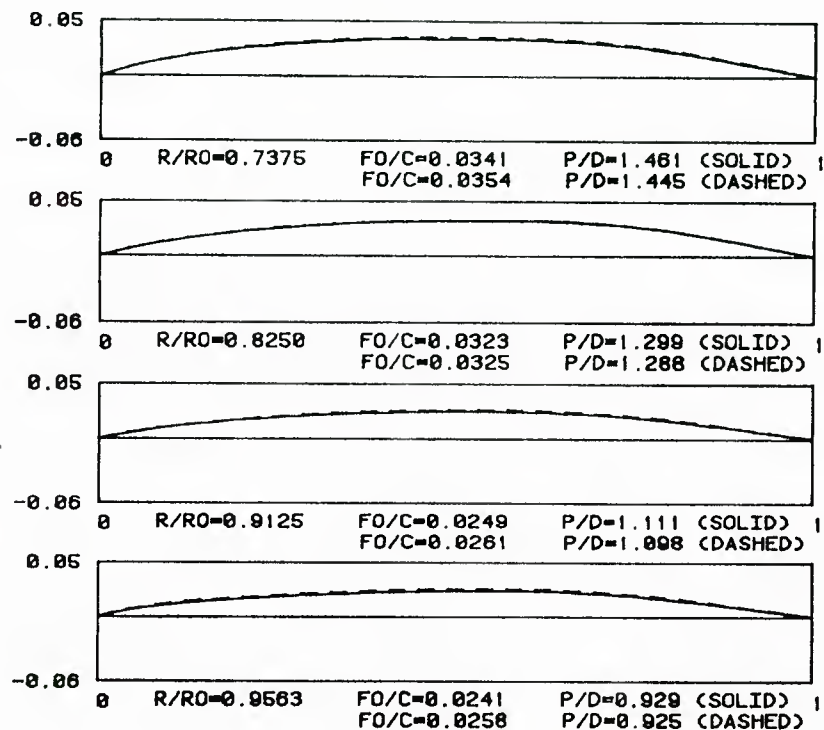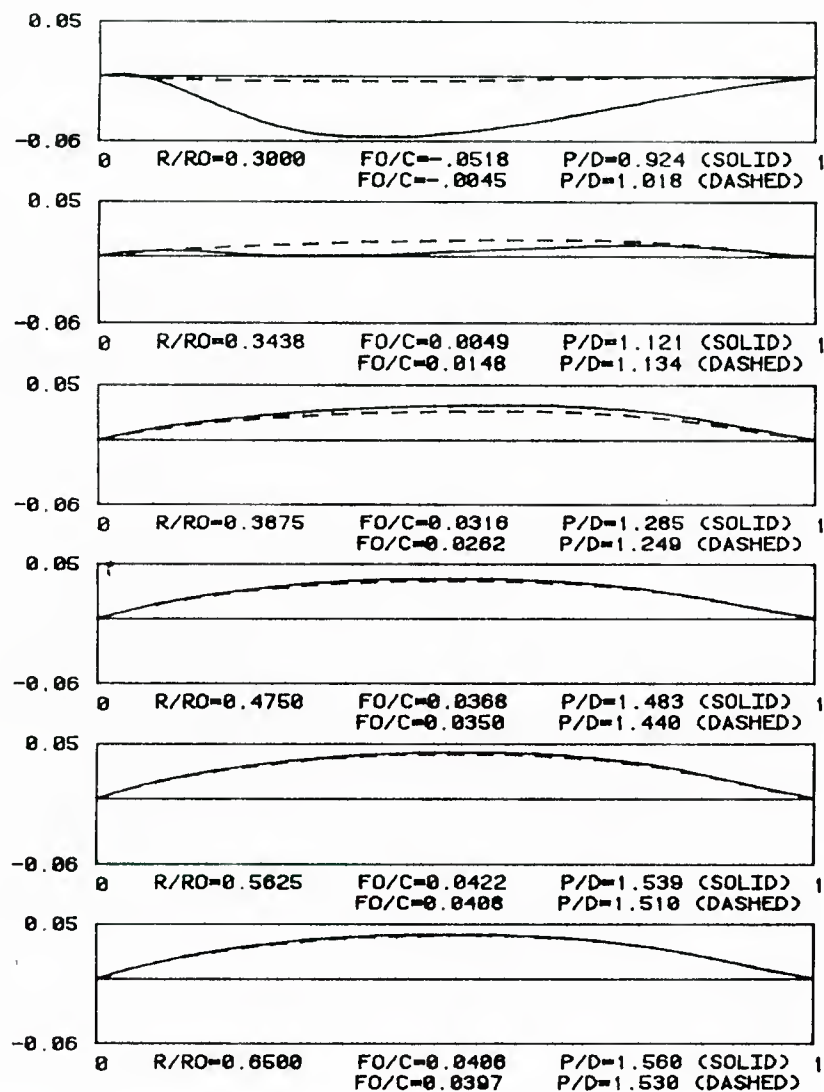
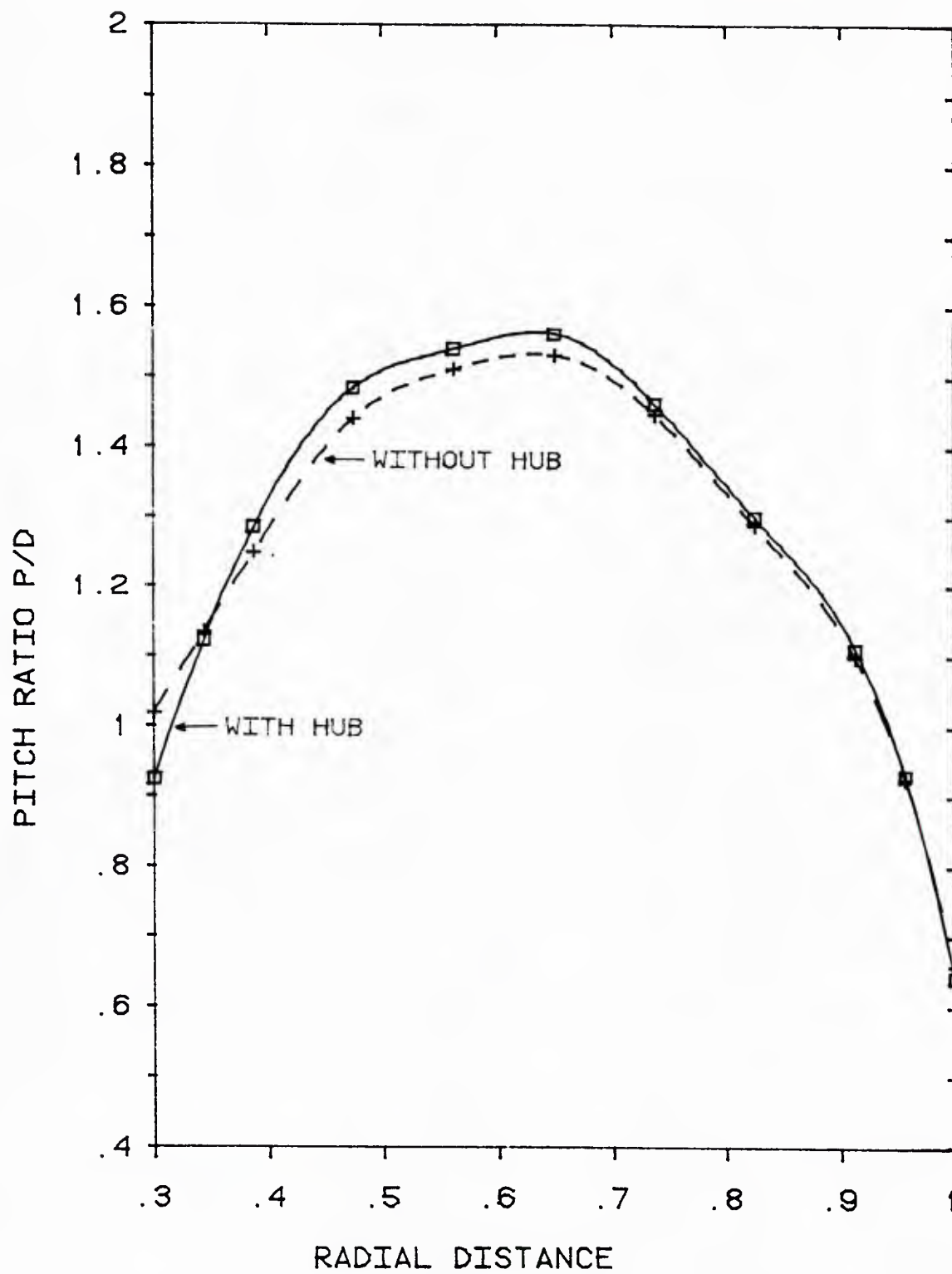FIG. 3.14 MEAN LINE SHAPES: DESIGN WITH HUB EFFECTS AND WITHOUT
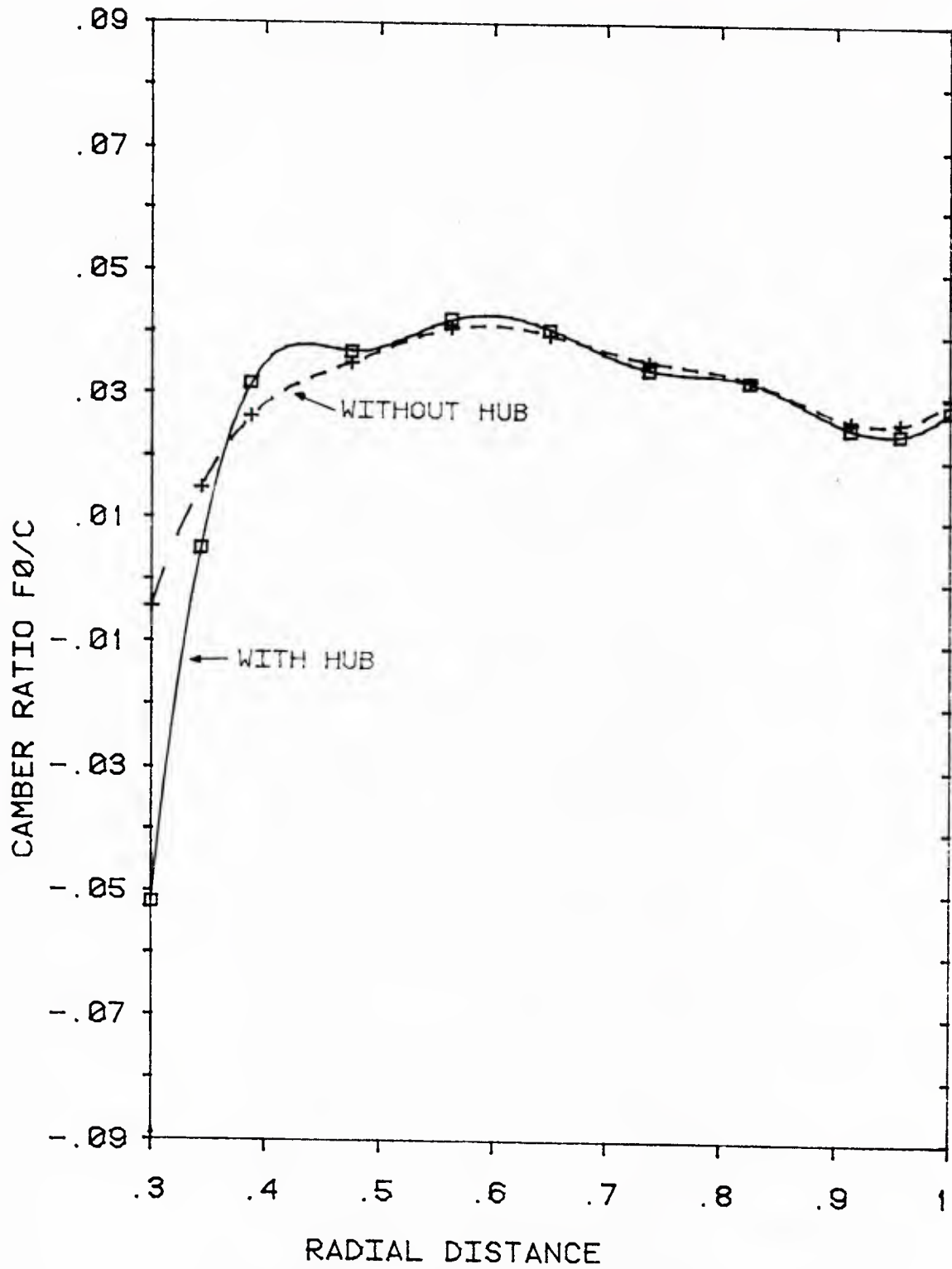
FIG. 3.15 PITCH DISTRIBUTION

FIG. 3.16 CAMBER DISTRIBUTION

CHAPTER 4

PROPELLER ANALYSIS WITH HUB EFFECTS

4.1 The Relationship between Analysis and Design

For the design problem, the load is given, while the blade shape is to be determined. For the analysis problem the situation is opposite, that is, the blade shape is given while the load is to be determined. As mentioned before, a blade shape design with hub effects is a mixed design and analysis problem, namely, design the blade shape and analyze the hub. Because the blade load problem is a pure analysis problem, both the singularities on the blades and on the hub need to be solved.

It is immediately found that the hub analysis part is common to both problems. So, the concept of solving the blade analysis problem with hub effects may be that a separate hub analysis part joins the blade analysis part which has been done by Greeley and Kerwin [1982]. Iterative procedures are needed.

4.2 The Analysis Algorithm

4.2.1 Two Methods of Solving the Analysis Problem

There are two ways to solve the blades-hub interference problem. One is to solve all the singularities (blades and hub) once and for all. The other way is to do it iteratively as mentioned above.

The first method is straightforward. First, establish a set of simultaneous linear equations with a big influence matrix, including the influence between blade-blade, blade-hub, and hub-hub. Then solve these equations.

The second method is to first solve the blade singularities by totally ignoring the hub as in Greeley and Kerwin [1982], then solve the hub singularities by assuming the blade singularities remain the same. The next step is to solve for the blade again assuming the hub remains the same. This time, the hub influence on the blade can be calculated and certainly will not be ignored anymore. So, the procedure is to analyze the blade and hub iteratively until the strengths of all the singularities converge.

4.2.2 Comparison of the Two Methods

If the number of unknowns on the key hub and on the key blade has the same order of magnitude, N say, then the total operation has about $8 N^3$ for the first method, less than $8 N^3$ for the second method if the number of iterations is less than four. The storage of the matrix of the first method is about $4N^2$, but only about N^2 for the second method.

After the design problem has been solved, the advantage of using the second method is obvious. This method will be adopted in this thesis.

4.2.3 The Iterative Method

The basic assumptions, the field equations, and the boundary conditions are all the same as those for the design problem. The

panelization for the blades, wakes, and hub are also the same as those for the design problem. The flow diagram for analyzing this problem by the iterative method is shown in Figure 4.1.

It is seen from this flow diagram that the matrices of influence coefficient for both the blades and for the hub will depend on the wake geometry. Only after the wakes have been aligned will the wake geometry be fixed and these two matrices will remain constant.

4.3 Two Examples of Analysis

There will be two examples of propellor analysis with hub effects, as well as propeller analysis without hub effects.

Also, there will be experimental work (see Chapter 5) in order to compare with the theoretical predictions.

Details of the results of the analysis and the comparisons between theoretical predictions and experimental results will be given in Chapter 6.
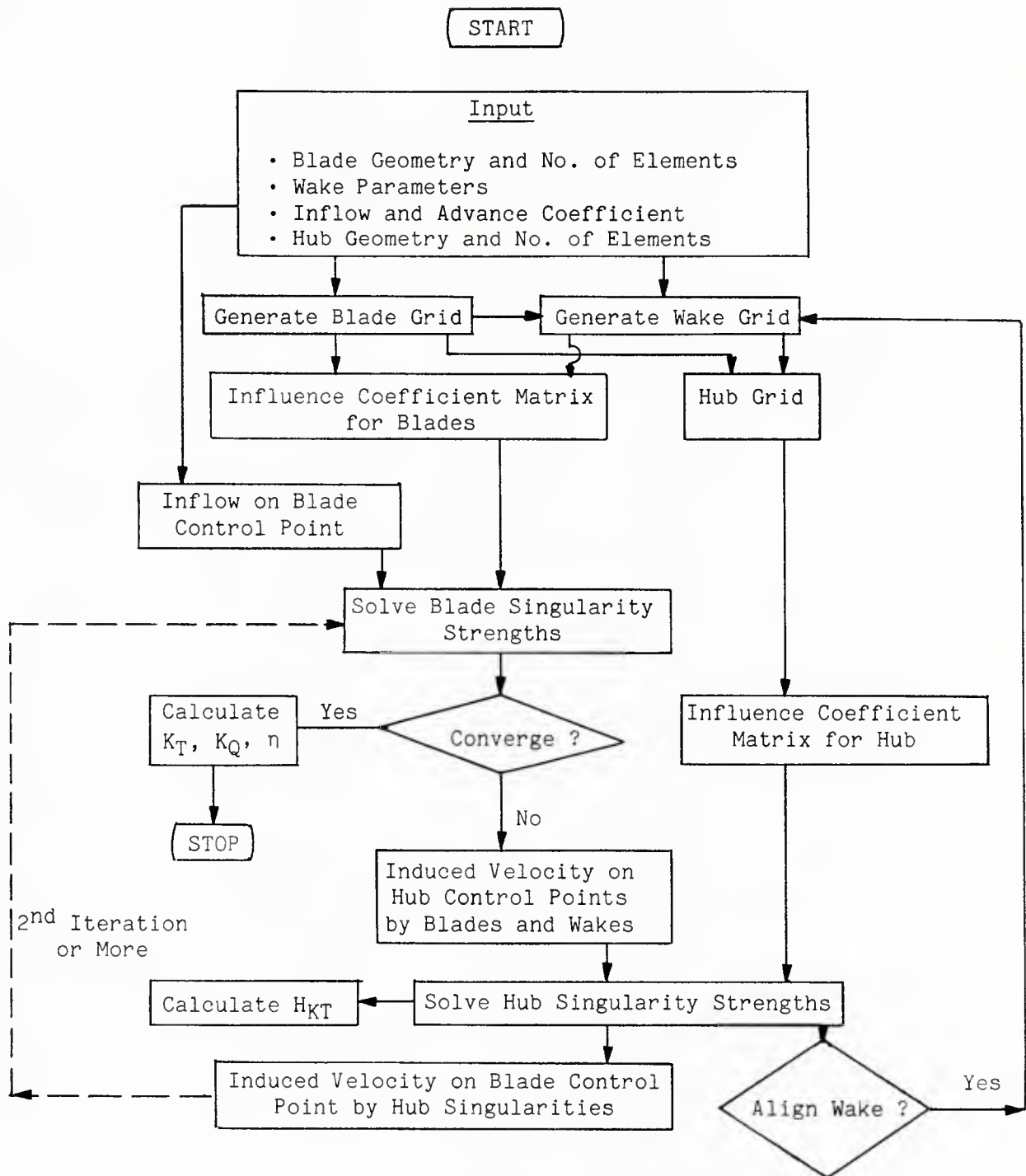
Figure 4.1 Flow Diagram for Blade Analysis with Hub Interference

CHAPTER 5

EXPERIMENT

5.1 Purposes

There are three goals for testing models in this thesis. First, there is the search for evidence of the circulation conservation law by experiment. Second, there is the comparison of the forces and circulation distribution predicted by numerical models with those measured from physical models. Third, there is the study of the cause of the hub vortex and its structure.

Circulation is certainly conserved in an inviscid fluid. But, in a real fluid, the energy is dissipated -- the question is: how fast is it dissipating? Is it slow enough that the circulation conservation law can still be applied in the domain close to the propeller disk?

If circulation is conserved or is dissipating very slowly if at all, it may provide the opportunity to check the numerical model predictions -- either the circulation distribution or the forces -- with experimental data.

As mentioned before, the hub vortex produces a cavity and low pressure at the hub apex, so drag is produced. The cause of the hub vortex is still controversial, and the structure of the hub vortex still needs to be confirmed as a Rankine vortex.

5.2 Propeller Models

There were two propeller models tested in this thesis. One was a CP (controllable pitch) propeller from the DD-963 class destroyer, model 4660 [Jessup, Boswell, and Nelka, 1977], and the other was a research propeller 4498. P4660 has a larger hub ratio (0.3) than P4498 (0.2). P4660 has a lower pitch and camber at sections near the root than P4498. The geometry of both propellers is tabulated in Table 5.1 and Table 5.2, and the pitch and camber distribution are plotted in Figure 5.1 and Figure 5.2.

5.3 Hub Models

P4660 has three different fairings with different lengths. P4498 has one fairing. These fairings are shown in Figure 5.3.

r/R	P/D	x_i/D	Skew	C/D	f_0/C	t_0/D
0.30	1.165	0.0091	2.985	0.178	0.0000	0.0420
0.35	1.296	0.0103	3.481	0.210	0.0050	0.0372
0.45	1.480	0.0103	4.810	0.271	0.0209	0.0290
0.55	1.566	0.0103	6.631	0.327	0.0267	0.0226
0.65	1.566	0.0103	8.978	0.374	0.0256	0.0178
0.75	1.498	0.0103	11.895	0.406	0.0209	0.0146
0.85	1.381	0.0103	15.410	0.409	0.0151	0.0122
0.90	1.306	0.0102	17.403	0.387	0.0122	0.0110
0.95	1.222	0.0103	19.557	0.326	0.0094	0.0091
1.00	1.128	0.0102	21.876	0.000	0.0000	0.0000

Table 5.1 Geometry of Propeller 4660 -- design J = 1.038, propeller diameter = 1 ft
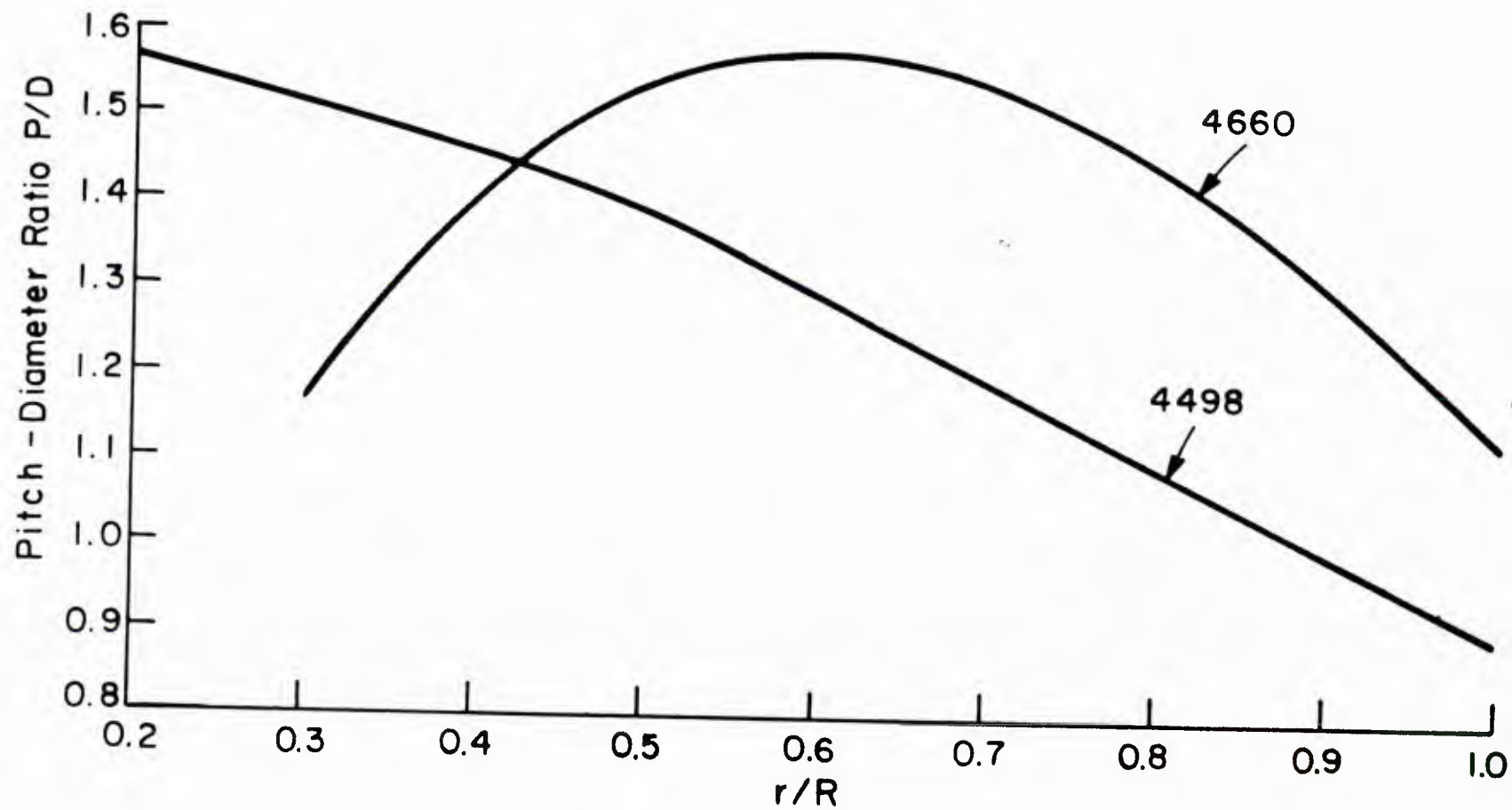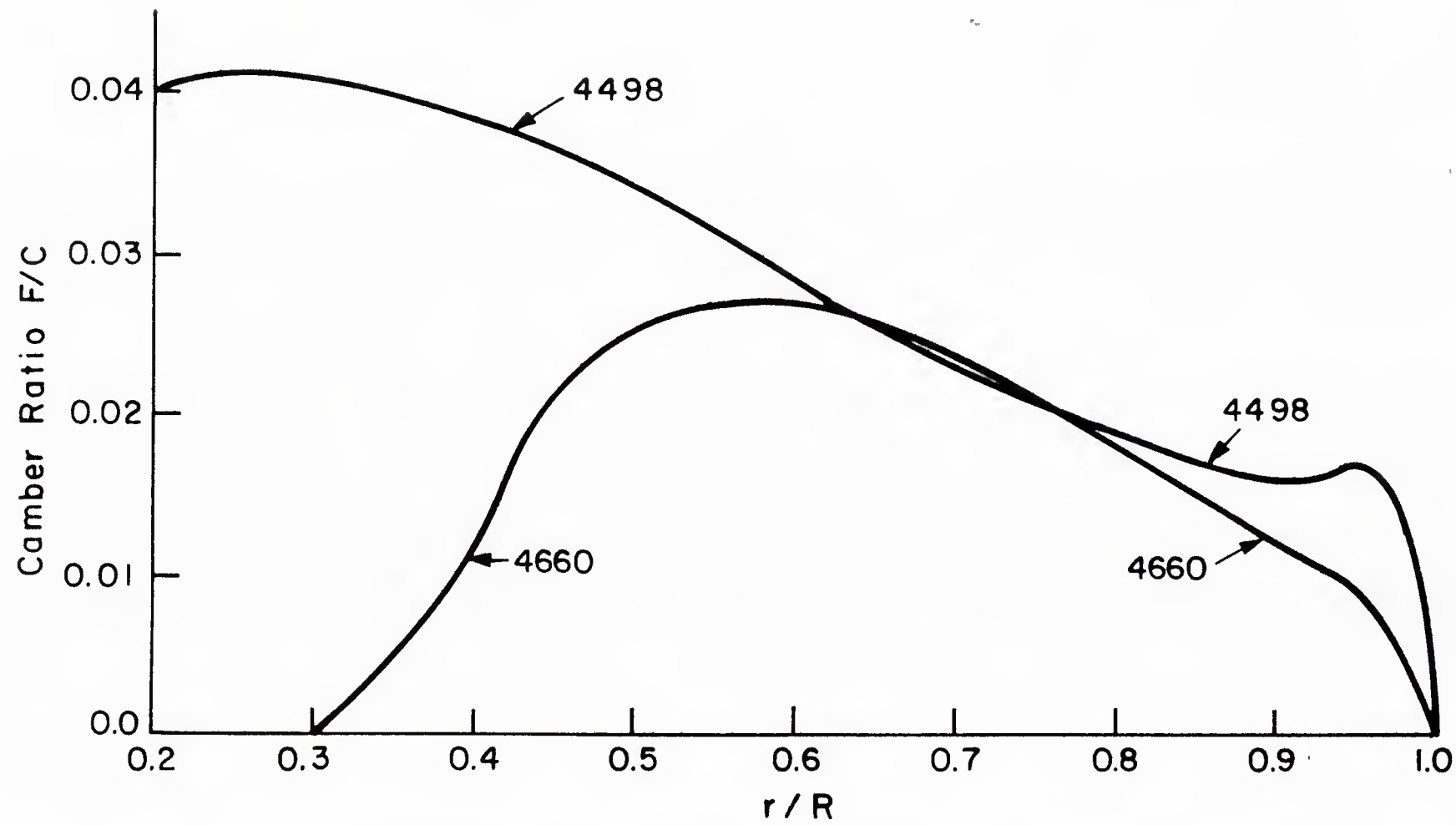
Fig. 5.1 Pitch Distribution For Propeller 4660 and 4498
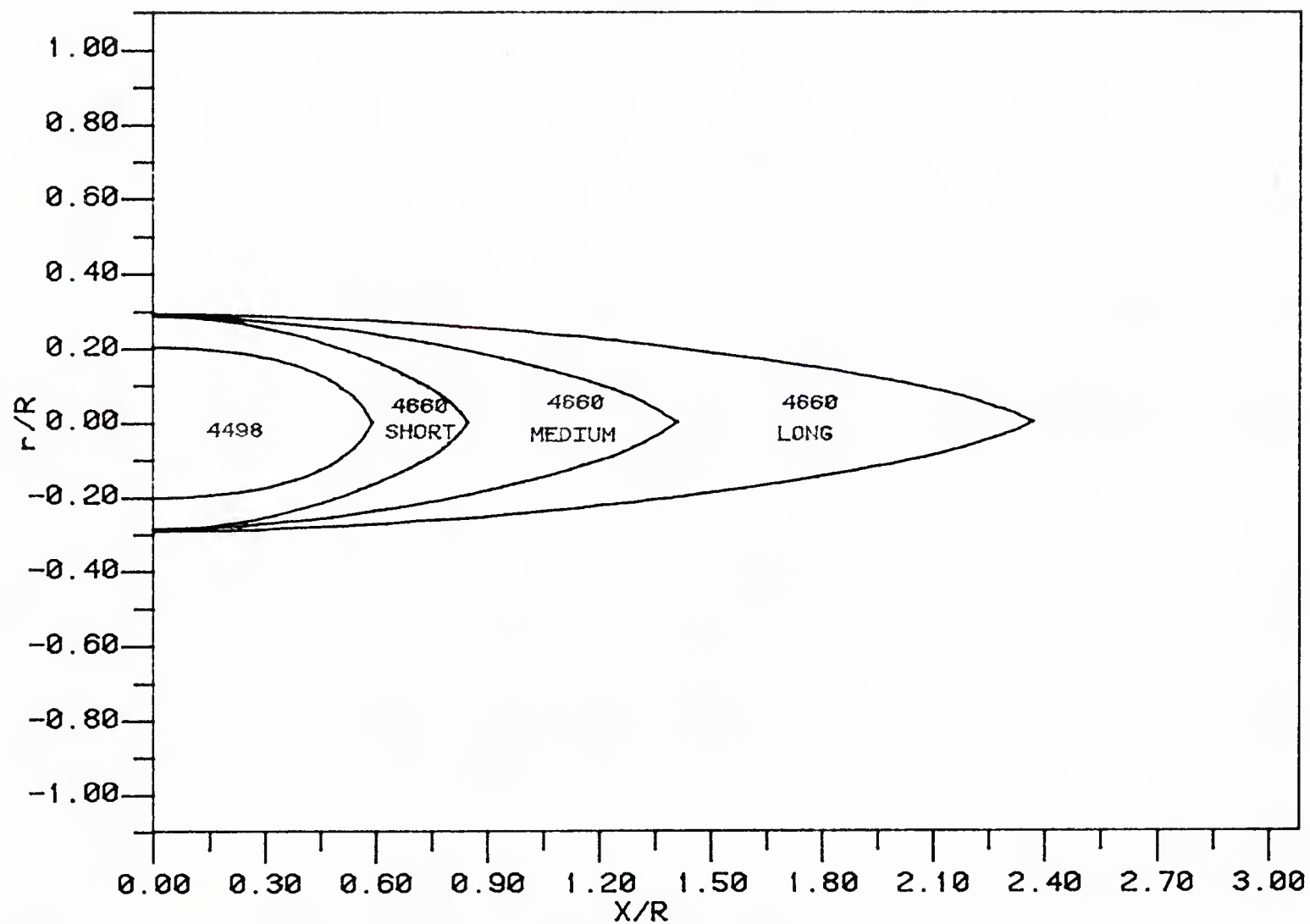
Fig. 5.2 Camber Distribution For Propeller 4660 and 4498

FIG. 5.3 3 HUB GEOMETRY OF PROPELLER 4660 &
1 HUB GEOMETRY OF PROPELLER 4498

r/R	P/D	x_i/D	Skew	C/D	f_o/C	t_o/D
0.20	1.566	0.0	0.0	0.174	0.0402	0.0434
0.25	1.539	0.0	4.647	0.202	0.0408	0.0396
0.30	1.512	0.0	9.293	0.229	0.0407	0.0358
0.40	1.459	0.0	18.816	0.275	0.0385	0.0294
0.50	1.386	0.0	27.991	0.312	0.0342	0.0240
0.60	1.296	0.0	36.770	0.337	0.0281	0.0191
0.70	1.198	0.0	45.453	0.347	0.0230	0.0146
0.80	1.096	0.0	54.245	0.334	0.0189	0.0105
0.90	0.996	0.0	63.102	0.280	0.0159	0.0067
0.95	0.945	0.0	67.531	0.210	0.0168	0.0048
1.00	0.895	0.0	72.000	0.000	0.0001	0.0029

Table 5.2   Geometry of Propeller 4498 -- design J = 0.889, propeller
diameter = 1 ft

5.4   Water Tunnel

All the tests were carried out in the MIT Marine Hydrodynamics

Laboratory (MHL) Variable Pressure Water Tunnel.   The tunnel has a square

test section with four plexiglass viewing windows 44" × 16" × 2".   The

inside dimension of the test section is 20" × 20" which is large enough for

a propeller of 12" diameter, with little interference with the wall.   The

free stream velocity range is from 0 to 30 ft/sec.   A movable propeller

drive shaft extending from far upstream to the test section can rotate up

to 2000 rpm.   The impeller speed is manually controlled with an error of

about 0.5%.   The propeller speed is also manually controlled with an error

of about 0.2%.

5.5 Instrumentation

5.5.1 Laser Doppler Anemometry Systems

The LDA system in MHL is a Thermo Systems, Inc. (TSI) 9000 series model utilizing a 15 mW He-Ne laser. The system may operate either in dual beam forward scatter mode or dual beam backscatter mode. It is easy to shift from one mode to the other by moving the receiving optics from one side of the test section to the other. The LDA mounts on a carriage which can move in three perpendicular directions. With a Bausch and Lomb electronic position measuring system, the laser beam position can be read as accurately as 0.0005" using the Accurite II counter of this system.

The details of the set up of the LDA system as well as its connection to the data processing system are shown schematically in Figure 5.4. This system has been continuously improved since Min [1977]. Trial and error and the effort of many people have been put in since then.

The functions of each component in the LDA system are all well explained [TSI]. An abstract of the description is presented below to provide an understanding of the system -- this turns out to be crucial to having good data.

- Beam Collimator: To insure that the two beams focus and cross at the same point. This is especially necessary in large systems and where beam expansion is used.
- Rotating Mounts: There are two rotating mounts so that the components between these two mounts can be rotated as a whole. The Rotating Mount 9178-2 provides convenient rotation of both the beam
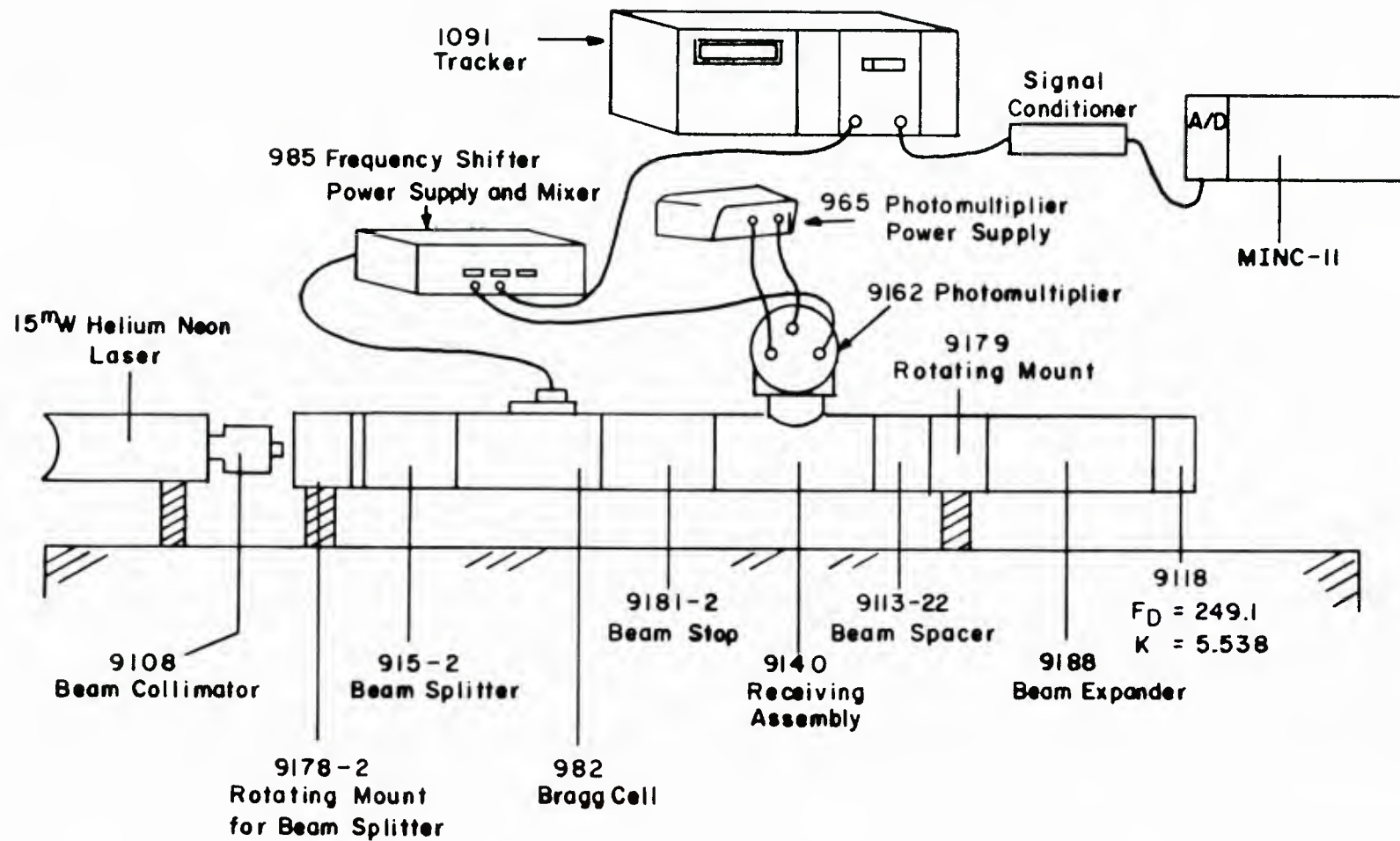
Fig. 5.4 Schematically plot of connection of LDA system, signal processing system and data processing system

polarity and the beamsplitter, which then rotates in the direction
of measurement. It has a scale which reads to an accuracy of 0.5°.
With a homemade level attached, it may read to 0.1'.

- Polarization Rotator: Is inside 9178-2. The light from the laser
  used in LDA is linearly polarized in the vertical direction. The
  polarization rotator is very crucial in order to make measurements
  in any other direction.

- Beam Splitter: Splits the incoming laser beam into two parallel
  beams: each 25 mm from the entering beam for Model 9115-2. The two
  beams are of equal intensity (dual beam mode) if the plane of
  polarity of the incoming beam is perpendicular to the plane of the
  two exiting beams. The beam intensity can be split 99.5% to 0.5%
  (reference beam mode) with a simple slide adjustment.

- Frequency Shifter (Bragg Cell, Power Supply, and Mixer): Shifts the
  zero flow signal by a specified frequency so that a reverse flow can
  be distinguished from the forward flow.

- Beam Stop: The Bragg cell produces several minor beams in addition
  to the strong diffracted beam to be used. The beam stop is used to
  block off those extra beams.

- Receiving Assembly: Focuses the collimated light from a collecting
  lens onto the photodetector aperture.

- Photomultiplier: Detects the scattered light through a 0.2 mm
  diameter aperture.

- Beam Spacer: Reduces the beam spacing from 50 mm to 22 mm
  (Model 9113-22) so that the Beam Expander 9188 can be used.

- Beam Expander: It increases the diameter of the incident laser beam entering the focusing lens by a factor of 2.27 (Model 9188). This will decrease the measuring volume diameter by a factor of 2.27, decrease the measuring volume length by a factor of 5, and increase the signal-to-noise ratio (power) by a factor of 5.

- Transmitting Lens 9118: Focal length, f, 249.1 mm; half angle, κ, 5.538°.

- 15 mW He-Ne Laser: λ = 632.8 nm.

A comparison of measuring volume and number of fringes using no beam expander and with the model 9188 beam expander is shown in Table 5.3.

	No Beam Expander	Model 9188 Beam Expander
Beam Separation Distance, d (mm)	50	22
Fringe Spacing, d_f (μm)	3.278	3.278
Measuring Volume Diameter, d_m (μm)	183	81
Measuring Volume Length, l_m (mm)	1.891	0.833
Number of Fringes, N_{FR}	58	25
Beam Diameter, D (mm)	1.1	2.5

Table 5.3 Comparison of System with Beam Expander to System with no Beam Expander

The formulas for Table 5.3 are

$$d_m = \frac{4\lambda f}{\pi D \cos \kappa}$$

$$l_m = \frac{4\lambda f}{\pi D \sin \kappa}$$

(5.1)

$$N_{FR} = \frac{1.27 \ d}{D}$$

$$d_f = \frac{d_m}{N_{FR}}$$

Notice that for the N_{FR} calculation d is the beam separation distance entering the transmitting lens and should be (22)(2.27) for the Beam Expander 9188. The d_f value is the same for the Beam Expander case and without the Beam Expander case, so the velocity measurement is not changed. This is because for the dual beam system the velocity is

$$u = f_D \ d_f = f_D \frac{\lambda}{2 \sin \kappa}$$

(5.2)

where f_D is the Doppler frequency.

5.5.2 Signal Processing System -- Tracker Type Processor

The output of the photodetector is a frequency that varies with particle velocity as in Equation (5.2). The tracker then converts this frequency to a voltage which is proportional to the input frequency.

The tracker has a bandpass filter and frequency discriminator which makes the tracker operate under circumstances of relatively poor signal-to-noise ratio. But, it may filter out "good" data if the "data density" is so low that the next good data has a frequency that lies outside the filter bandwidth. Then, the tracker holds the last reading until a frequency is in the range and is accepted by the tracker. The data density is referred to the time between successive, measurable signal bursts compared with the time scale of the velocity fluctuations. So, the data density is a quantity relative to the velocity fluctuation. For propeller flow measurements, the velocity fluctuation is very high when the measuring point is across the vortex sheet. A loss of data may be anticipated in this kind of measurement. If the bandwidth of the bandpass filter is increased, this problem can certainly be reduced, but this also reduces the ability of the tracker to distinguish signal from noise. The model 1090 tracker has three frequency ranges, each with a bandwidth of 10% of full scale, as shown in Table 5.4. The bandwidth vs. frequency in [TSI] has a log scale. A constant bandwidth in the log scale may give rise to a misunderstanding. It looks wider at the bottom (lower frequency) than at the top (higher frequency). Thus, it was pointed out incorrectly by Min [1978] that the "operation should be towards the bottom of the range for maximum capture bandwidth."

	Tracking Range (MHz)	Output (V/MHz)	Bandwidth (MHz)	Slew Rate (MHz/ms)
High Frequency	0.5 - 50	0.1	5	400
Mid Frequency	0.02 - 5	1.0	0.5	10
Low Frequency	0.002 - 0.5	10	0.05	0.1

Table 5.4 Tracker Characteristics

The slew rate (in Table 5.4) is the rate at which the tracker can slew up and down its full range in automatic mode. The slew rate is another limitation other than the bandwidth. These two limitations are different and should not be confused. The bandwidth is, as mentioned before, just a window (or a filter). Any data having a frequency difference with the previous data, over the window size, will be regarded as noise and be filtered out. If the flow acceleration is very high and if the data density is relatively low, "good data" may be filtered out because the bandwidth is too narrow. If, again, the flow acceleration is very high but the data density is very high also, then the tracker may track the signal very well until the acceleration is so high that the tracker could not slew with the flow. Usually, the bandwidth limitation, which depends on data rate, is reached sooner than the slew rate limitation.

5.5.3 Data Processing System -- MINC-11

MINC (Modular Instrument Computer) has one analog-to-digital converter which has an input range of -5.12 V to +5.12 V, with a resolution of one part in 4096, enabling it to detect differences as small as 2.5 mV.

The voltage output from the tracker is first sent to a Daytronics signal conditioner. One module of this signal conditioner is an Analog

Input Amplifier through which the tracker output can be amplified up to
±5.0 V. The amplified voltage is then sent to MINC to be converted to
digital. The advantage of this magnification is to increase the accuracy
of the voltage (therefore the velocity) measurement. An n-times
magnification sill give n-times greater accuracy. This is especially
useful for low-velocity measurement. But, care should be taken to ensure
that the amplified signal is not larger than 5 V.

The computer program used for data processing is an interactive
program. The user is asked to enter at the keyboard the coordinates of the
measuring point; the sampling frequency (or data points per one
revolution); the number of revolutions; whether to take new data, repeat
old data, or record the data; and so on. For each revolution, the computer
starts to take data when a Schmidtt trigger is fired and stops taking data
when the specified number of data points for one cycle have been taken.
Then, the computer waits for the next fire of the Schmidtt trigger to start
a new cycle of the data-taking process. The Schmidtt trigger is fired by a
magnetic pickup which can be inducted when the propeller shaft is at a
particular set angle. All of this setup is to guarantee that for each
cycle the data-taking process is starting at the same angular position. It
usually needs 200 cycles or more to have smooth averaged data, and needs
400 data points uniformly spaced in each cycle to give a resolution of less
than 1°. It is certainly necessary to record those data if a turbulent
analysis is required. Then, the total number of data points will be 80,000
or more, which exceeds the capacity of one floppy disk. Fortunately, only
the averaged (cycle average) data is needed for this thesis. Therefore,
the computer program replaces the old cycle data by the sum of old cycle
data and new cycle data, and the problem of storage does not occur.

5.6 Experiment Using Propeller 4660

5.6.1 Checking the Measured Velocities against Calculated Velocities

Before doing any measurements, it is always wise to check the reliability of the measuring system.

A direct comparison of the averaged unsteady velocities with theoretical predictions is ideal. If they match, then they are assumed to be correct.

The theoretical prediction has limitations from assumptions such as inviscid flow, and with its numerical model weaknesses such as a simplified, semi-empirical trailing vortex model. So, the prediction is usually not reliable in the trailing vortex region where the viscous vortex sheets with very complicated shape are embedded. The only region that is clear and thus reliable is upstream from the blades. But, if the measuring point is too far away from the blades, the velocities induced by the blades and the trailing wakes may be too weak to be seen. A point about 0.01 R ahead of the leading edge was chosen at r = 0.901 R, which is far away from the hub so that the hub effects may be neglected. The prediction has been done by PSF2 -- a computer program which ignores the hub effects. The averaged tangential velocity is zero as predicted by PSF2. It is certainly a good idea to check the computer program, because, theoretically, the averaged tangential velocity is zero ahead of the blades. All three components of the velocity are shown in Figure 5.5.

As for the measurements, the axial component and the radial component were taken in forward scatter mode, while the tangential component was taken in backscatter mode. The axial component can be measured at any

AXIAL   •——•——•——+

RADIAL   ■——■——■——■

TANGENTIAL   •——•——•——•

FIELD POINT POSITION

X=-0.194   R=0.901
ZERO ANGLE   0.00

————AXIAL————

	AMPL	PHASE
0	0.085	0.0
1	0.072	-126.6
2	0.027	-106.1
3	0.014	-74.1
5	0.006	-3.7

————RADIAL————

	AMPL	PHASE
0	-0.125	0.0
1	0.063	109.2
2	0.025	139.2
3	0.014	170.4
4	0.008	-157.9
5	0.004	-124.1

————TANGENTIAL————

	AMPL	PHASE
0	-0.001	0.0
1	0.056	-27.3
2	0.022	1.6
3	0.011	37.0
4	0.007	74.6
5	0.004	109.8

INDUCED VELOCITIES UA/VS,UR/VS,UT/VS

FIELD POINT ANGLE   DEGREES
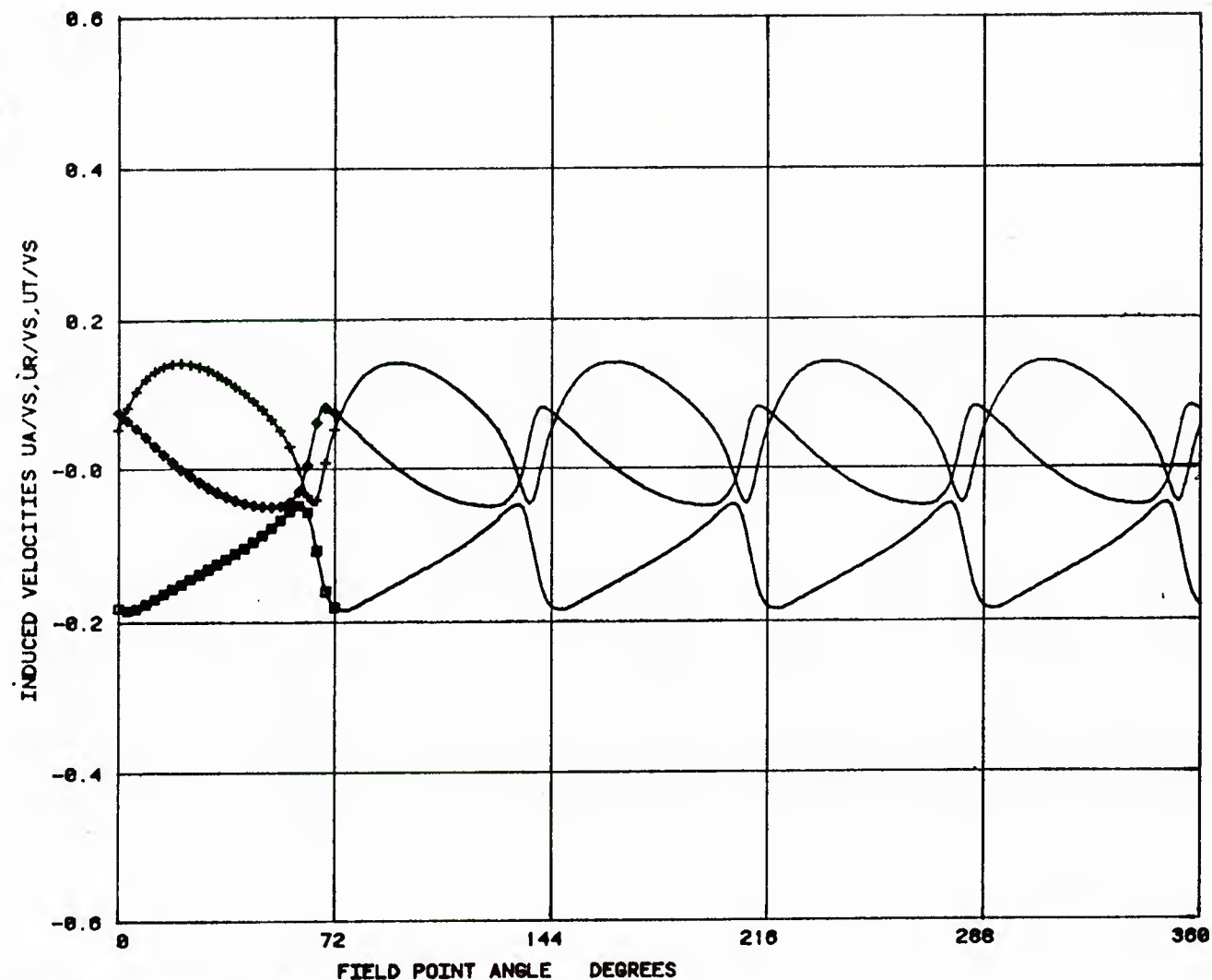
DTNSRDC 4660 (DD963) AT J=0.976 (DESIGN J=1.038)

FIG. 5.5 FIELD POINT VELOCITY PREDICTED BY PSF2

point when the laser beams were horizontal and the radial component can be obtained by measuring a vertical component in the center plane of the tunnel when the laser beams were vertical. The tangential component can be obtained by measuring a vertical component at the z-axis when the laser beams were vertical. This tangential component could only be measured in backscatter mode because of the existence of the propeller shaft which blocks the laser beams. Forward scatter mode can theoretically give 100 to 1000 times higher signal strength than backscatter mode [TSI, p.6]. In the author's experience, forward scatter mode has a sampling rate 5 to 10 times higher than backscatter mode. So, it is highly recommended that forward scatter mode be used whenever possible.

The comparison between measurement and calculation is shown in Figure 5.6, in which the induced velocities are plotted. The propeller speed was 1000 rpm, while the impeller speed was 248 rpm (so that $J = 0.976$). The hub diameter was 1.2" larger than the shaft diameter. There was an adaptor connected smoothly to both the shaft and the hub. Because the velocity was increased as the fluid flowed over this adaptor, the measured induced velocity should be subtracted from that increase. The resulting comparison was excellent. So, both the numerical model and the measuring system are reliable, at least for this "easy" point. The "hard" points for the numerical model may also be difficult to measure due to the existence of a rapid change in the flow field -- the trailing vortex sheets, which will be discussed in the next section.
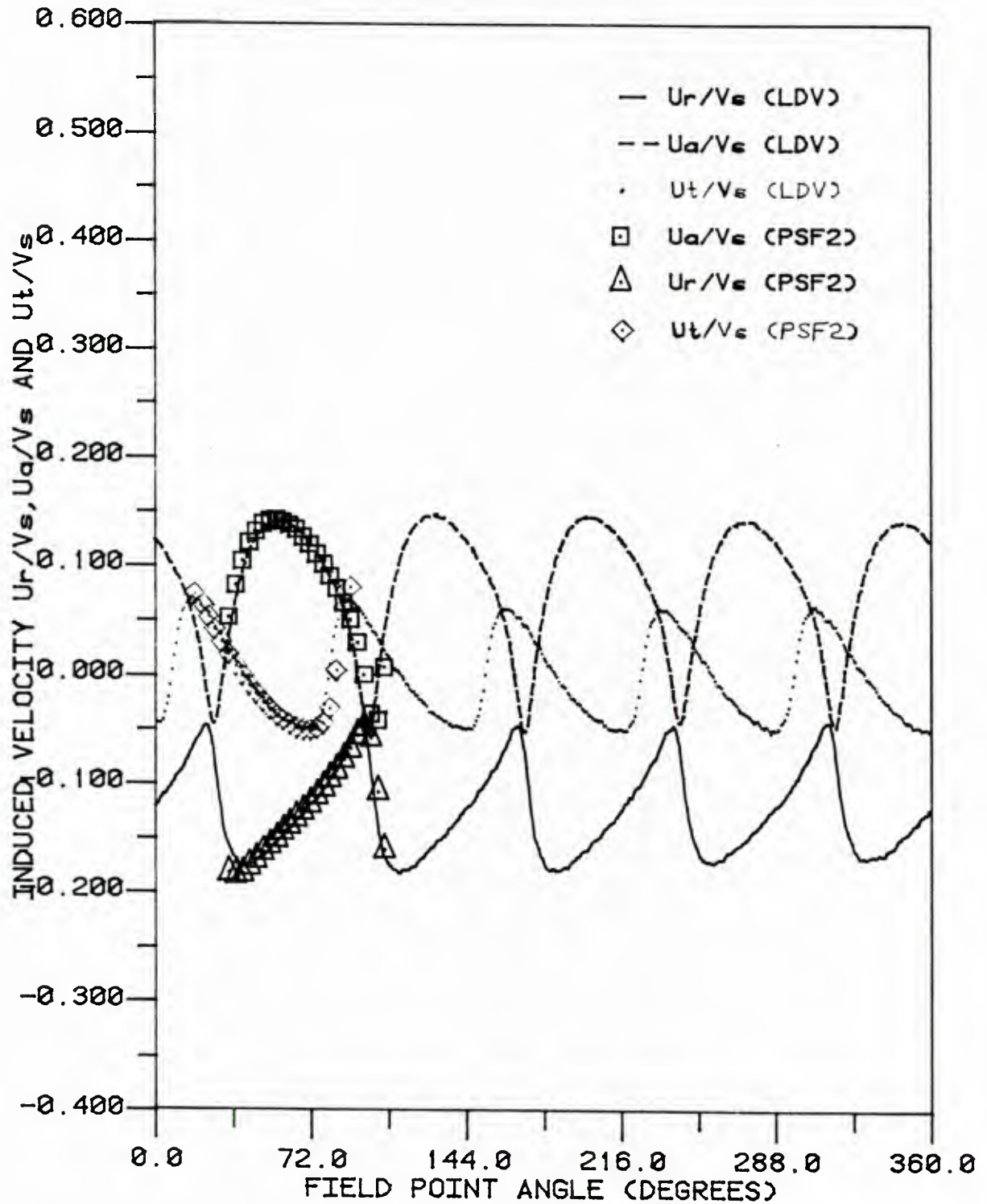
FIG. 5.6
COMPARE CALCULATED VEL. (PSF2) WITH
MEASURED(LDV);X=-.194R r=.901R;P4660

5.6.2 What was Wrong with the Radial Components?

As a continuation of the check of the measuring system, from the last section, a point in the trailing vortex region was examined. A negative radial component (an inward flow) is anticipated due to the flow contraction. But, the measured radial velocity was positive on the average which meant that the fluid was flowing out instead of flowing in!

The measurement was at $x = 0.281$ R, $r = 0.917$ R, and $\theta = 0°$ (upper half plane of tunnel), with the propeller and impeller at 1000 and 248 rpm respectively. When the measuring point was moved to $\theta = 180°$ (lower half plane) while the other conditions remained the same, the radial velocity remained outward, although this time the velocity was downward in contrast to the last time ($\theta = 0°$) when the velocity was upward.

In order to make sure that the measuring point was inside the slipstream, the tunnel pressure was reduced until the streamlines were visible from the cavity air bubble. From this, the measuring point was clearly shown to be inside the slipstream, although very close to it.

What was wrong? The same measuring system was working well in section 5.6.1. A so-called improved technique [Schoenberger, 1983, 1984] was tried. It was found that there had been an error in his software, or more specifically, the first argument in the subroutine MADC2 had been treated incorrectly. There also was an error in his hardware. The monostable, which was made by him, had only expanded the synch pulse to one microsecond, not 100 microseconds as intended. After the two errors had been fixed, the radial velocity was still wrong. A reduction of propeller and impeller speed with J constant was tried.[**] The change in averaged

---

[**]Suggested by Mr. Dean Lewis at MHL.

velocity was immediately seen to be in the right direction -- radial velocity changed from an outward direction to an inward direction.

A systematic study of the relationship between the propeller speed and the radial velocity was carried out. The results are shown in Figure 5.7, Figure 5.8, and Figure 5.9.

In Figure 5.7, eight different propeller speeds from 300 rpm to 1000 rpm were used while the J value was kept constant (0.976). The radial velocities are nondimensionalized with respect to the free stream; the abscissa is nondimensionalized to radians. Each curve representing the unsteady radial velocity consists of 400 data points each of which was an average of 200 revolutions. In addition to the unsteady velocity curves, the mean value of each curve is shown. The mean values decrease from 0.107 (outward) to -0.103 (inward) as the propeller speed decreases from 1000 to 300 rpm.

Most of the measurements were repeated by increasing the gain of the tracker as shown in Figure 5.8. Comparison of Figure 5.7 and Figure 5.8 indicates that the gain is another factor other than the speed influencing the measurement. It shows that a higher gain makes the velocity "converge" faster to the "true" value (mean = -0.102) at 500 rpm (compared to the lower gain case -- mean = -0.103 at 300 rpm).

The influence of position was investigated as well by changing the position from $\theta = 0°$ to $\theta = 180°$ (or $r = +0.917$ R in Figure 5.8 to $r = -0.917$ R in Figure 5.9 -- r should always be positive; by definition, a negative value is just shorthand for $\theta = 180°$). Under the same conditions (including approximately the same gain), the discrepancies between Figure 5.8 and Figure 5.9 show the sensitivity of the measuring position. Becuase of the errors in defining a center, the symmetry of the upper plane
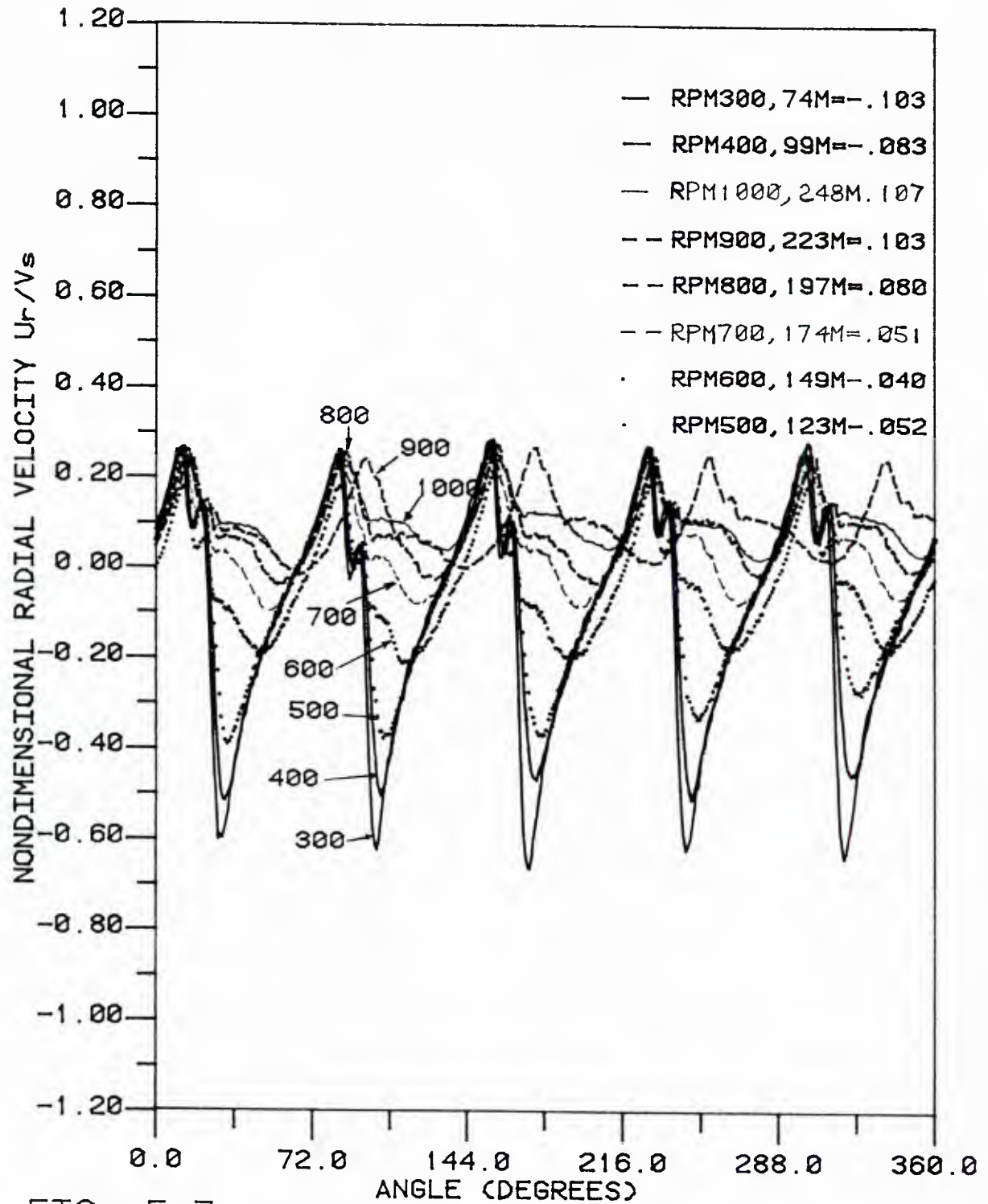
FIG. 5.7
COMPARISON OF UNSTEADY RADIAL VEL.
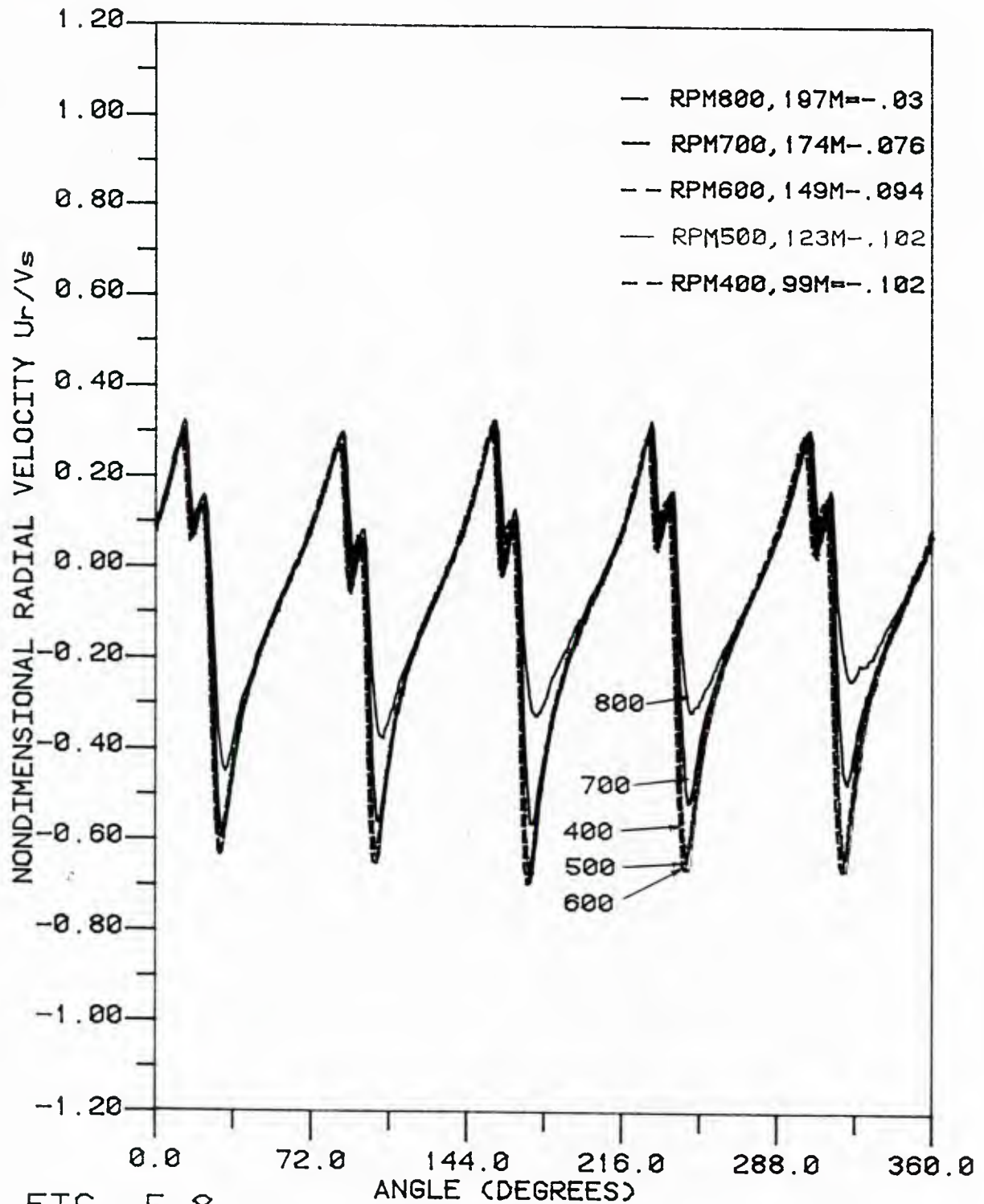X=.281R r=.917R P4660 J=.976; W/S.G.

FIG. 5.8
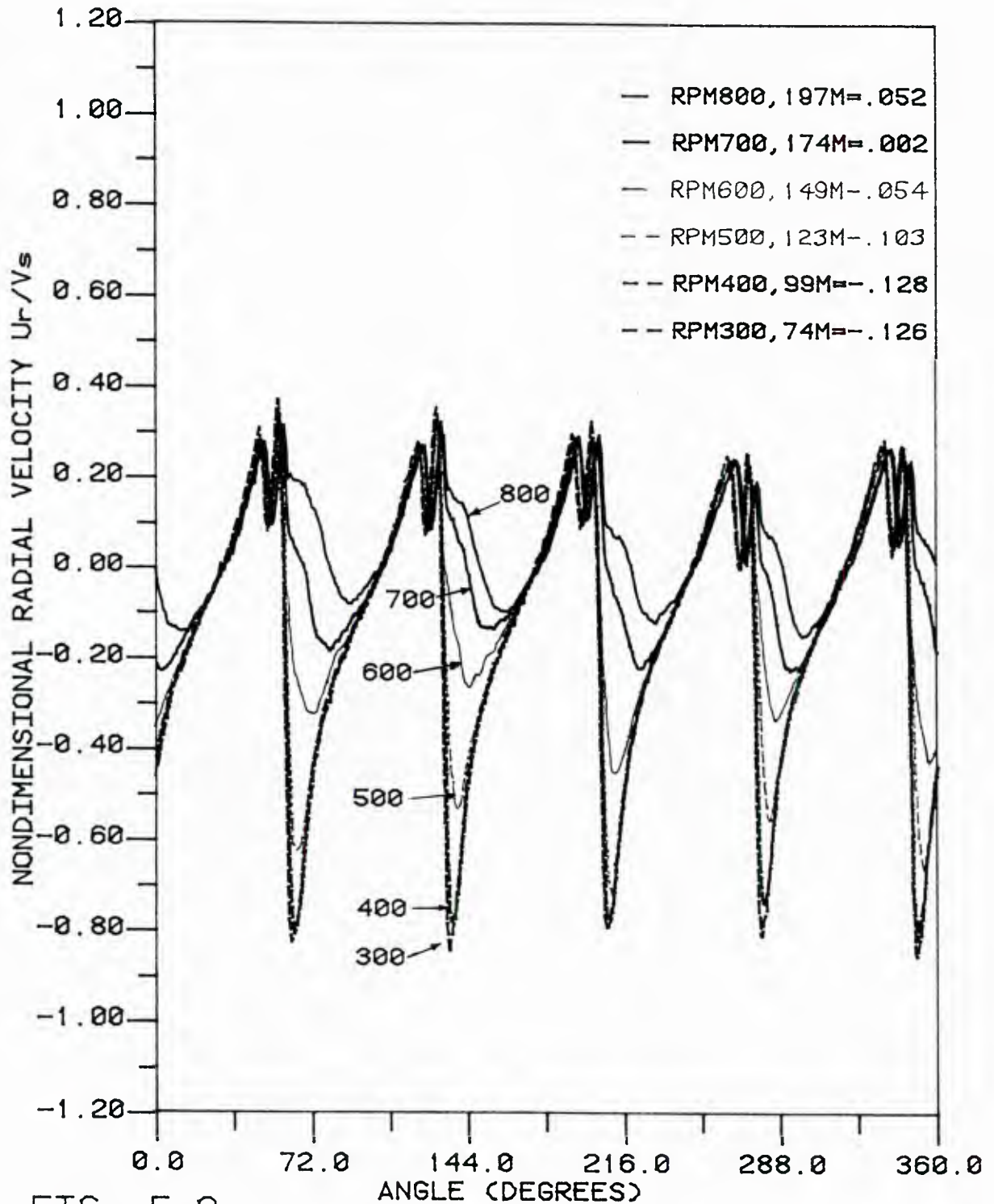COMPARISON OF UNSTEADY RADIAL VEL.
X=.281R r=.917R P4660 J=.976; W/L.G.

FIG. 5.9
COMPARISON OF UNSTEADY RADIAL VEL.
X=.281R r=.917R P4660 J=.976; W/L.G.

and the lower plane with respect to the center may not be strictly correct. An error of 0.1 in. may exist. The convergent mean radial velocity is -0.126 this time.

5.6.3 The Answers

The hint for answering the question which arose in the last section is in Figures 5.7, 5.8, and 5.9. That is, there are two things in common in all those curves: (1) There are two kinds of slope, one mild and the other steeper, for each curve; and (2) The data lost is always in the trough of the curve, not in the crest of the curve. Recall that those data were recorded immediately after the firing of the Schmidtt trigger which is at an angle of 0.0 in those curves. All of the above indicates that the tracker may lose tracking when the radial velocities are accelerated inward. This kind of loss of data is more serious when the propeller speed is faster.

The answer to the last question is that the measuring point was across a vortex sheet where the data density was too low and the data was lost because the tracker rejected new data beyond its bandwidth. Recall that the data density is a relative concept; it is low if the local velocity fluctuation is high. The most rapid change of velocity occurs when the measuring point is across a vortex sheet or a vortex tube. The radial velocities are almost tangent to the velocity jump across the trailing vortex sheet at most radii, while axial velocities and tangential velocities are almost perpendicular to it. So, the radial components are the most difficult of the three components to measure. When the propeller speed is reduced, the data density increases, the number of data points rejected decreases, and the results are better.

The influence of gain on measurement is such that the larger the gain the larger the signal and the larger the noise. A stronger signal makes the tracker easier to track, so the data density is higher. But, the noise may confuse the track if it is too large. Therefore, the gain can not be too large or too small. In the author's experience, the radial component measurment is optimum when the "Out of Range" light becomes all red and before the tracker loses its tracking.

As for the sensitivity of the position, it is a very interesting problem. From it, the structure of the trailing vortex (including the hub vortex, whose description is one of the purposes of the experiment) may be understood, as will be seen in the next section.

5.6.4 A Hypothesis

Suppose the radial velocities in Figures 5.7, 5.8, and 5.9 can be decomposed into two components: one is a rapidly changing component from a strong local trailing vortex sheet; the other is a mild component influenced by all the other velocities except the local vortex sheet. While the second component is not sensitive to the position, the first one is. The shape of the trailing vortex is a function of position. Although this function is not very sensitive to the position (for example, the pitch of the trailing vortex is not very sensitive), the velocities induced by these vortex sheets are sensitive to position. This is because the vortex sheet is very thin, and a point above a vortex sheet has a sign opposite in velocity to that of a point below the vortex sheet.

Suppose the mild component (which is not sensitive to position) has a shape as in Figure 5.10a and a steeper component (which is sensitive to position) has a shape as in Figure 5.10b. Then the superposition of

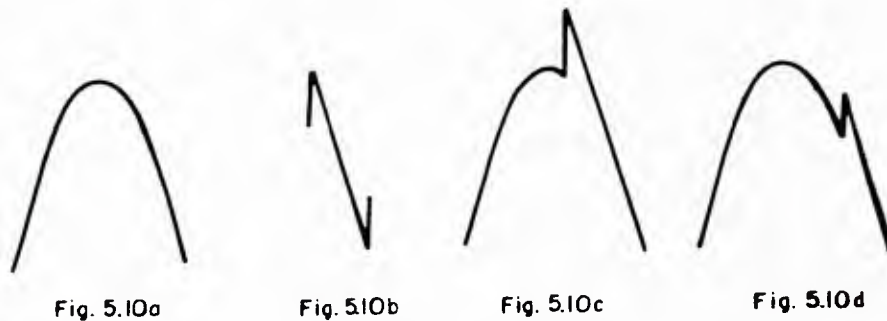Fig. 5.10a   Fig. 5.10b   Fig. 5.10c   Fig. 5.10d

Figure 5.10a and 5.10b may look like Figure 5.10c or Figure 5.10d, depending on the relative position of Figure 5.10a and Figure 5.10b.

From Figure 5.10c and Figure 5.10d, not only can the discrepancies between Figure 5.8 and Figure 5.9 be explained but the characteristics of the radial velocity will also be understood better. In short, the radial velocity (this may be extended to axial and tangential velocities as well) consists of two components: one from a local strong vortex sheet, and the other from all influences other than this vortex sheet. Second, the part with steeper slope is due to the local vortex sheet while the other part with mild slope is due to the other influences. The fact that a steep slope is evidence of a strong vortex sheet will be useful in identifying the existence of the "hub vortex sheet." Third, the dent in Figures 5.7, 5.8, and 5.9 is not a viscous dent but a result of superposition. A question thus arises: are all the "dents" found in [Min, 1977], [Kobayashi, 1981], and [Schoenberger, 1983] also just results of superposition, and not of viscosity? It may be necessary to collect more data to answer this

question (see next section). But, before doing so, it is a coincidence

that all the dents found are close to the tip region (r > 0.6 R, say) where

there are always strong vortex sheets. A dent in the axial component or in

the tangential component that is relatively smaller (or smoother) than the

radial component is just because the orientations of the radial components

are almost parallel to the jump velocity of the vortex sheet while the

other two are almost perpendicular to the jump velocity.

5.6.5 Some Evidence

A velocity survey at one station very close to the blade trailing edge

of propeller 4660 has been presented in Figures 5.11 to 5.13, parts a, b,

and c, a total of nine figures. This includes three components -- axial,

radial, and tangential. Each component has 12 curves representing 12

different radii. These are further grouped into three regions from those

12 radial positions, namely, the tip flow region, the mid-spin region, and

the near-hub region. Each region has its own characteristics which will be

seen next. All nine figures have the same scale so that the comparison

will be easier. The propeller speed was 300 rpm and the advance

coefficient was 0.976.

(A) Radial Components

(i) Tip Flow Region (Figure 5.11a)

It is seen that at r = 0.95 R the velocity curve is a

periodic function of angle with a single peak in each blade
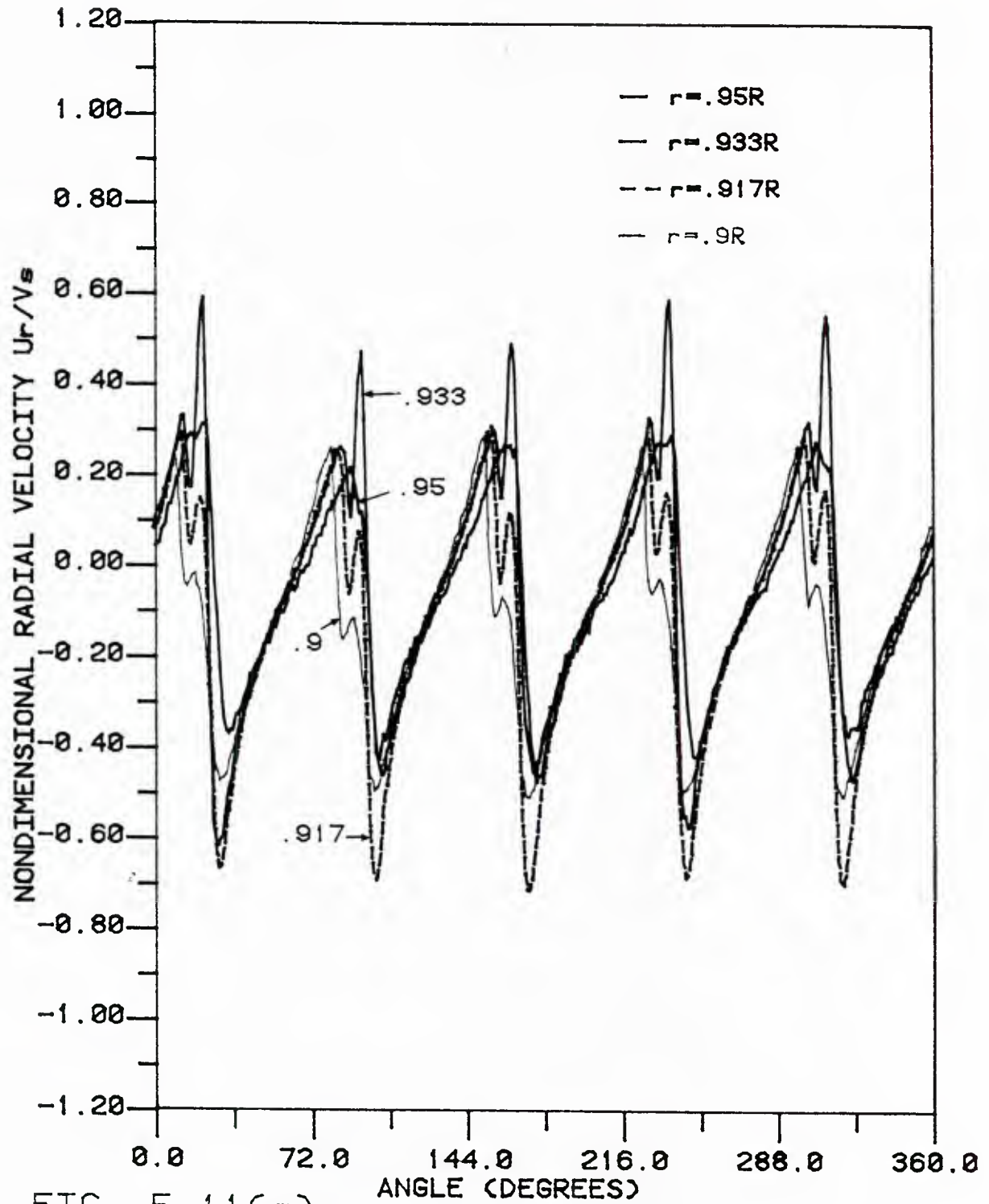
FIG. 5.11(a)

RADIAL VELOCITY AT TIP FLOW REGION
X=.281R (T.E.) PR4660 J=.976

period. When moving inward to r = 0.933 R, a sharp second peak appears. When moving further inward (r = 0.917 R or r = 0.9 R), this second peak gets smaller. To explain the behavior of those curves, the hypothesis in section 5.6.4 will be adopted. At r = 0.95 R, the measuring point was outside the slipstream and the velocity was induced there globally; in other words, there was no jump velocity for the local vortex sheet. At r = 0.933 R, the measuring point was inside the slipstream and was in a strong vortex sheet; the jump velocity due to this vortex sheet was superimposed to a global induced velocity curve which is not different (i.e., not sensitive to position) from the curve at r = 0.95 R. The fact that the jump velocities are getting weaker when r is further inward indicates that the vortex sheets are getting weaker as well. But meanwhile, the global part only changed a little (again, not sensitive to position). From the above, a tip vortex (near r = 0.933 R) can be defined as a rolled up vortex sheet. It is a part of the vortex sheet, not different from other parts except it is stronger. Notice that the loss of peak value and/or trough value is more serious at r = 0.933 R than at inner radii. This indicates that the data density/bandwidth problem still exists in the tip vortex region, even when the propeller speed was 300 rpm!

From the hypothesis of section 5.6.4, the dents in all these curves are just a result of superposition of a component which is sensitive to position with a component which is not sensitive to position. If this hypothesis is right, what about the concept of viscous dents? In fact, they both are correct. There are

viscous layers shedding from the surface of the blades. They are very thin boundary layers which are modeled as vortex sheets with zero thickness, in inviscid flow. The strength of the vortex sheet (thus the jump velocity) equals the derivative of the vortex bound to the blade, from potential theory. The thickness of the boundary layer (or the vortex sheet) can only be predicted by three-dimensional boundary layer theory, which is beyond the scope of this thesis. Also, recall that the thickness is a function of Reynolds number. The thickness measured from Figure 5.11a is only for a particular Reynolds number.

The hypothesis of superposition of two components may be right, but the application of it to the prediction of velocity is handicapped by the inability to predict the thickness of the vortex sheet from potential theory.

(ii) Mid-Span Region (Figure 5.11b)

Here, one thing is shown: the vortex sheet changes sign around the mid-span region. These four curves all have two parts with two kinds of slope -- one steeper and the other mild. The steeper side is recognized as the vortex sheet. In the region of outer radii (including the tip flow region in Figure 5.11a), the velocity induced in the upper half plane by a vortex sheet has a curve similar to that of Figure 5.10b, which has a steeper slope from left top to right bottom. If the vortex sheet has the opposite sign, the steeper slope part will change orientation,
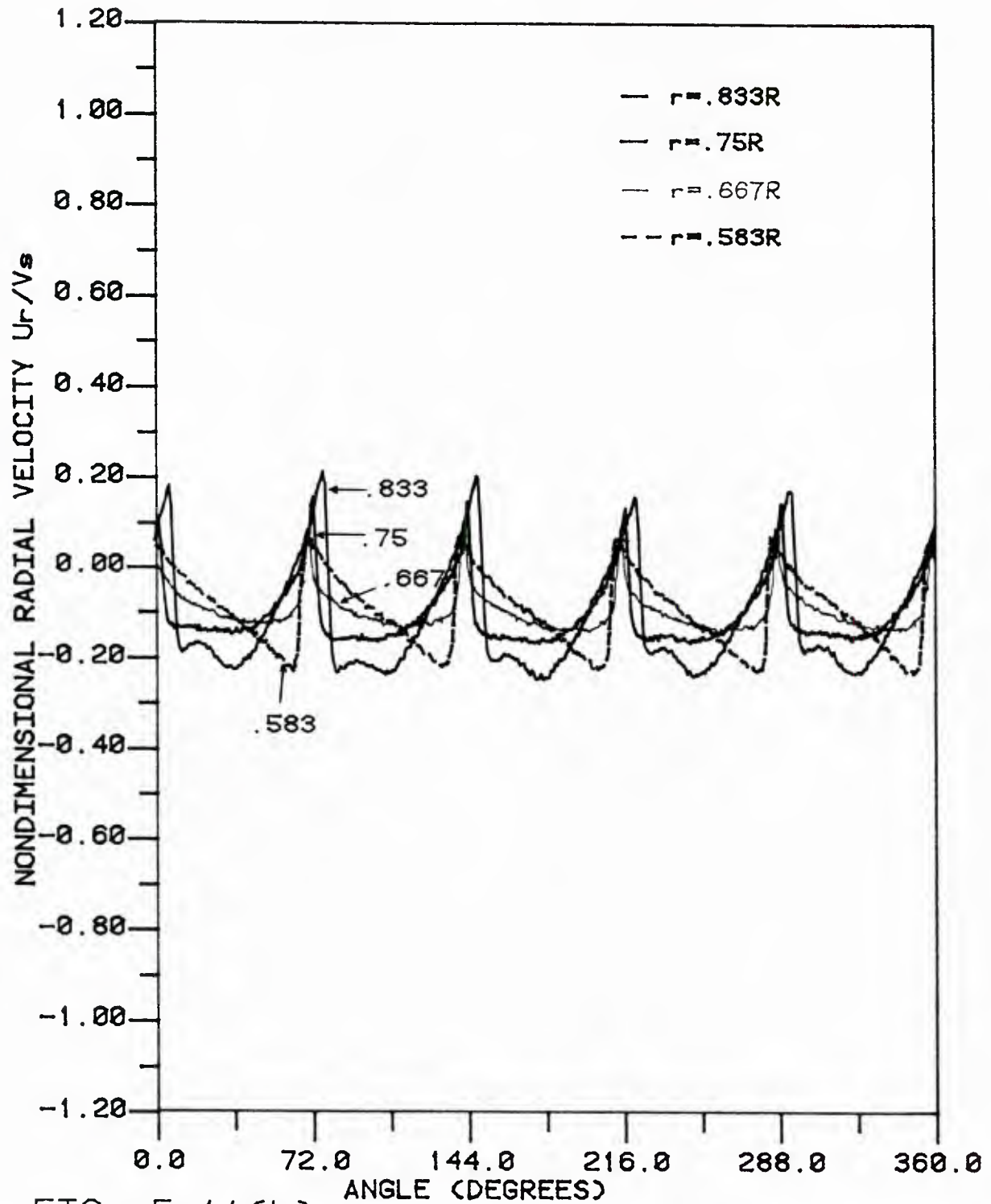
FIG. 5.11(b)
RADIAL VELOCITY IN MID-SPAN REGION
X=.281R (T.E.) PR4660 J=.976

becoming a line from right top to left bottom. This is exactly
what happened in the curve of r = 0.583 R.

(iii) Near-Hub Region (Figure 5.11c)

The fact that these four curves are different from those in
Figure 5.11a indicates that the vortex sheet structure is
different in these two regions. In short, there is no
concentrated (rolled-up) vortex in the hub region as there is in
the tip region. This provides evidence for the first theory for
the hub vortex instead of the second theory (see Chapter 1). The
nominal hub radius is about 0.288 R or less at this station. The
radial component at r = 0.3 R shows a vortex sheet of jumping
velocity ±0.1 of free stream velocity, while there is a jump
velocity of ±0.6 of free stream velocity in the tip vortex.

Though the application of the hypothesis of 5.6.4 is limited
by the unknown thickness of the vortex sheet, the determination
of the position of the vortex sheet from the measured radial
velocities is available. By measuring the angular position of
the midpoint of the steeper slope (in Figure 5.11) and the
angular position of the Schmidtt trigger relative to the
propeller blade, the angular position of the vortex sheet rel-
ative to the blade is just the summation of the above two angles.
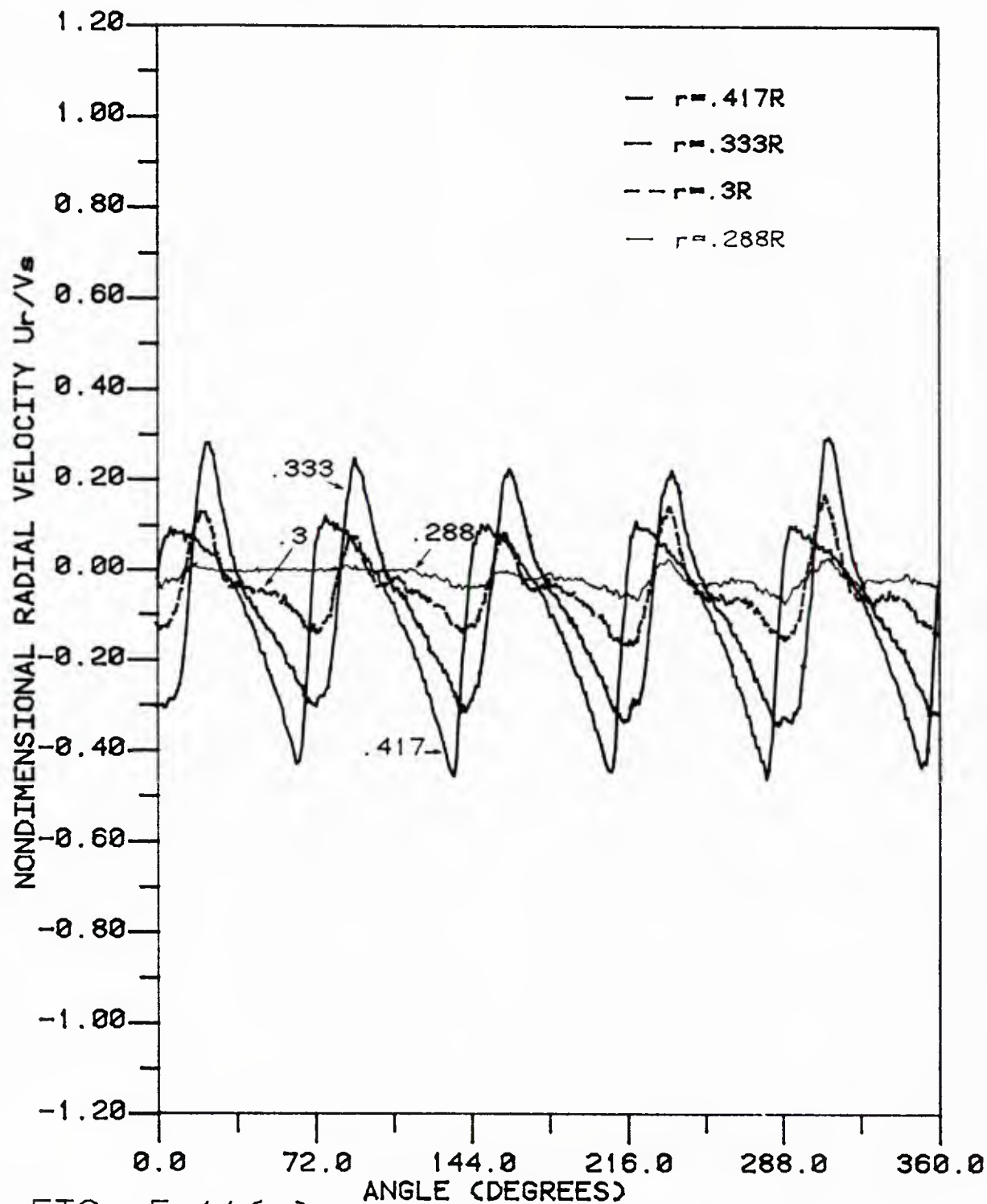
FIG. 5.11(c)
RADIAL VELOCITY NEAR HUB REGION
X=.281R (T.E.) PR4660 J=.976

(B) Axial Components

The axial components were measured at the same point that the radial components were measured. That means that there is no phase shift between the two. It is immediately found that the velocity induced by the local vortex sheet is at the same angular position as that for the radial component. But, the magnitudes of the jump velocities are relatively smaller than those of radial components, which was predicted.

The dents in the axial velocities in Figure 5.12 are all similar to those found in Min [1978], Kobayashi [1981], and Shoenberger [1983]. It is right to say these dents are viscous dents from boundary layer theory as well as to say these dents are jump velocities from the local vortex sheet, as was discussed in (A)(i).

(C) Tangential Components

The tangential components in Figure 5.13a can be used to determine the radial position of the tip vortex. The phase of peak value at $r = 0.933 R$ has shifted $180°$ from that at $r = 0.95 R$. A narrowing of the distance between those two radii can determine the tip vortex more accurately.

When it is approaching the hub region, the influence of potential flow is still very strong (Figure 5.13c), even at $r = 0.305 R$. The curve for $r = 0.283 R$ is a straight line, showing that the influence of potential flow has disappeared and the flow is dominated by a rotating hub boundary.
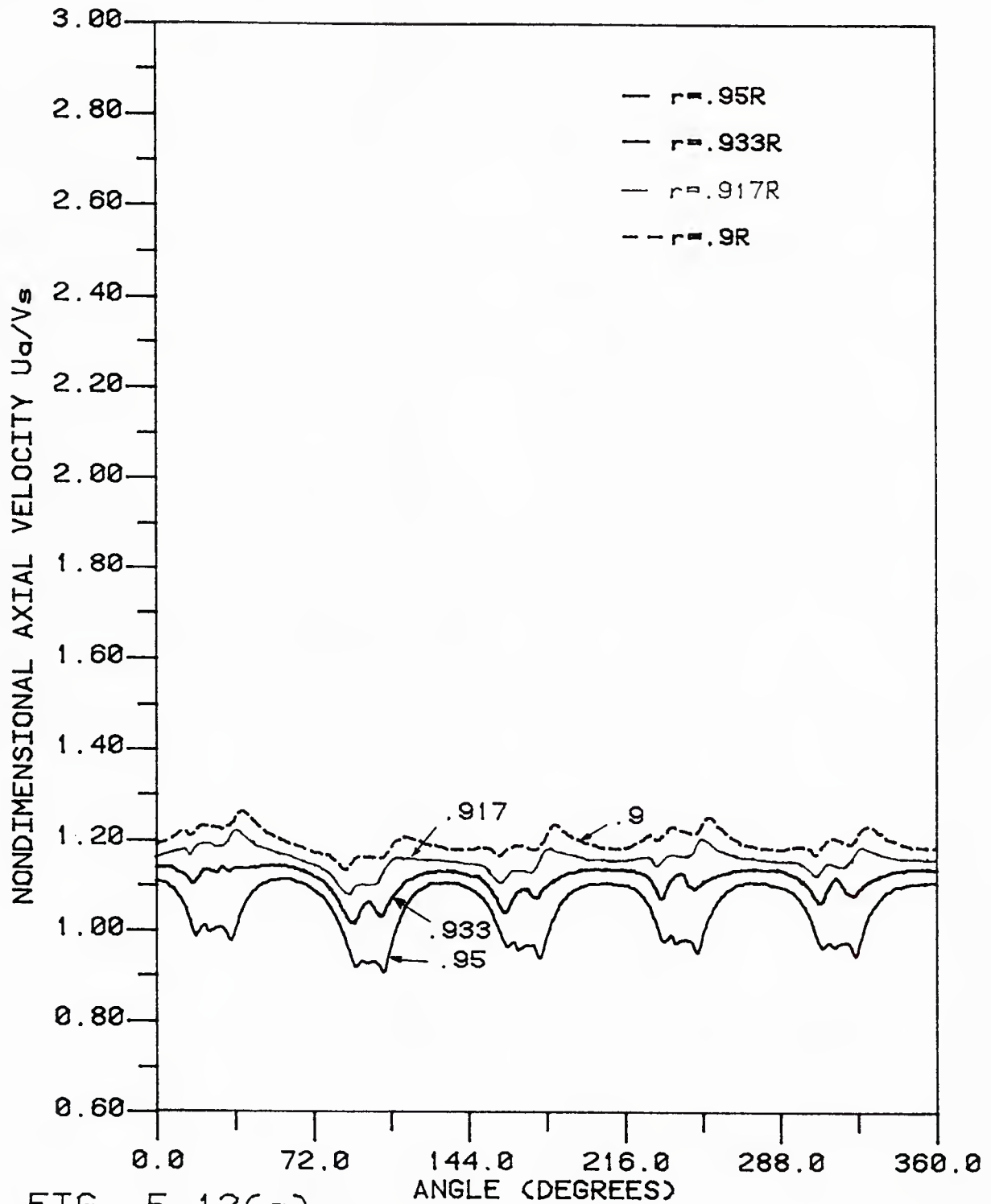
FIG. 5.12(a)

AXIAL VELOCITY IN TIP FLOW REGION
X=.281R (T.E.) PR4660 J=0.976
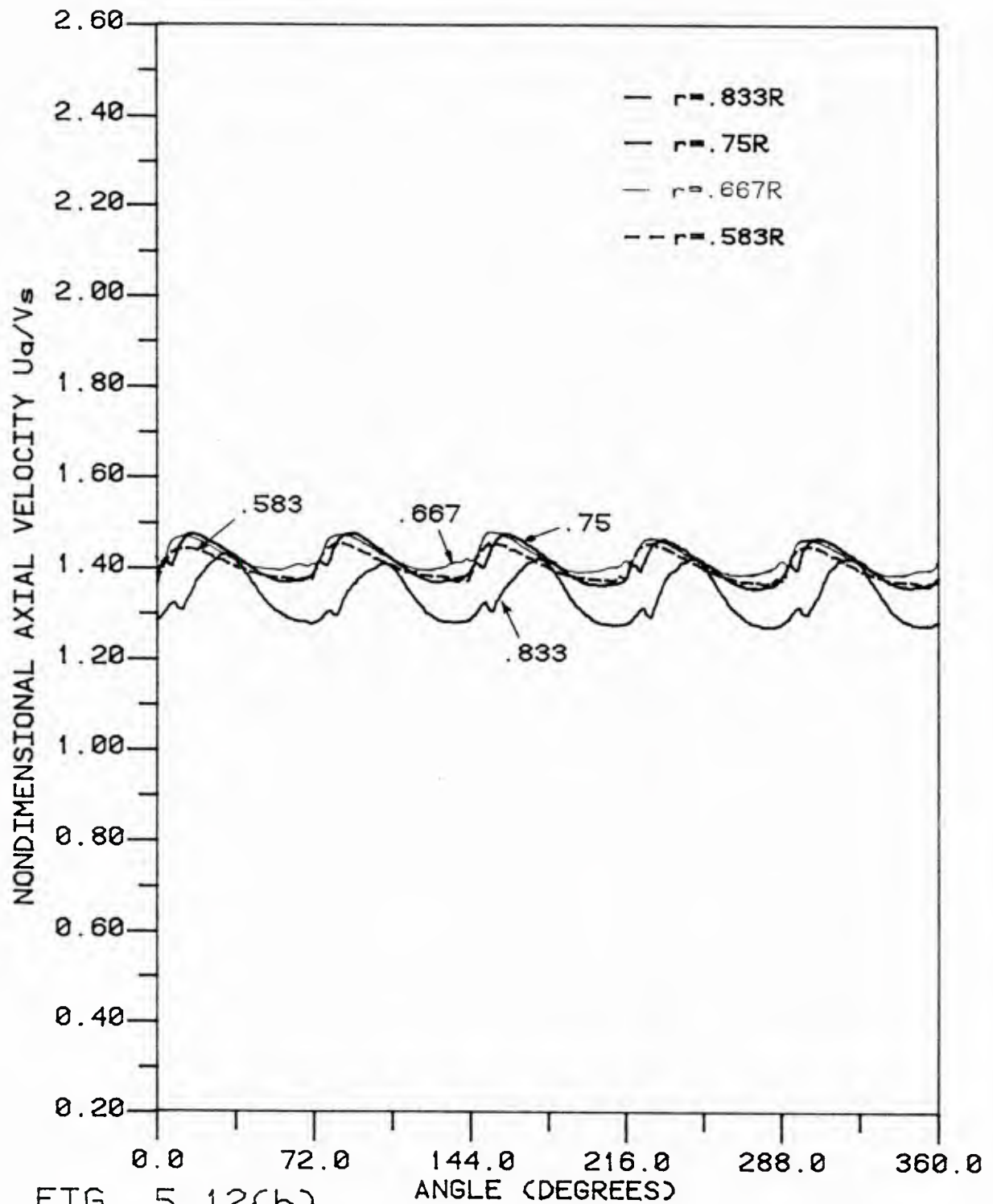
FIG. 5.12(b)

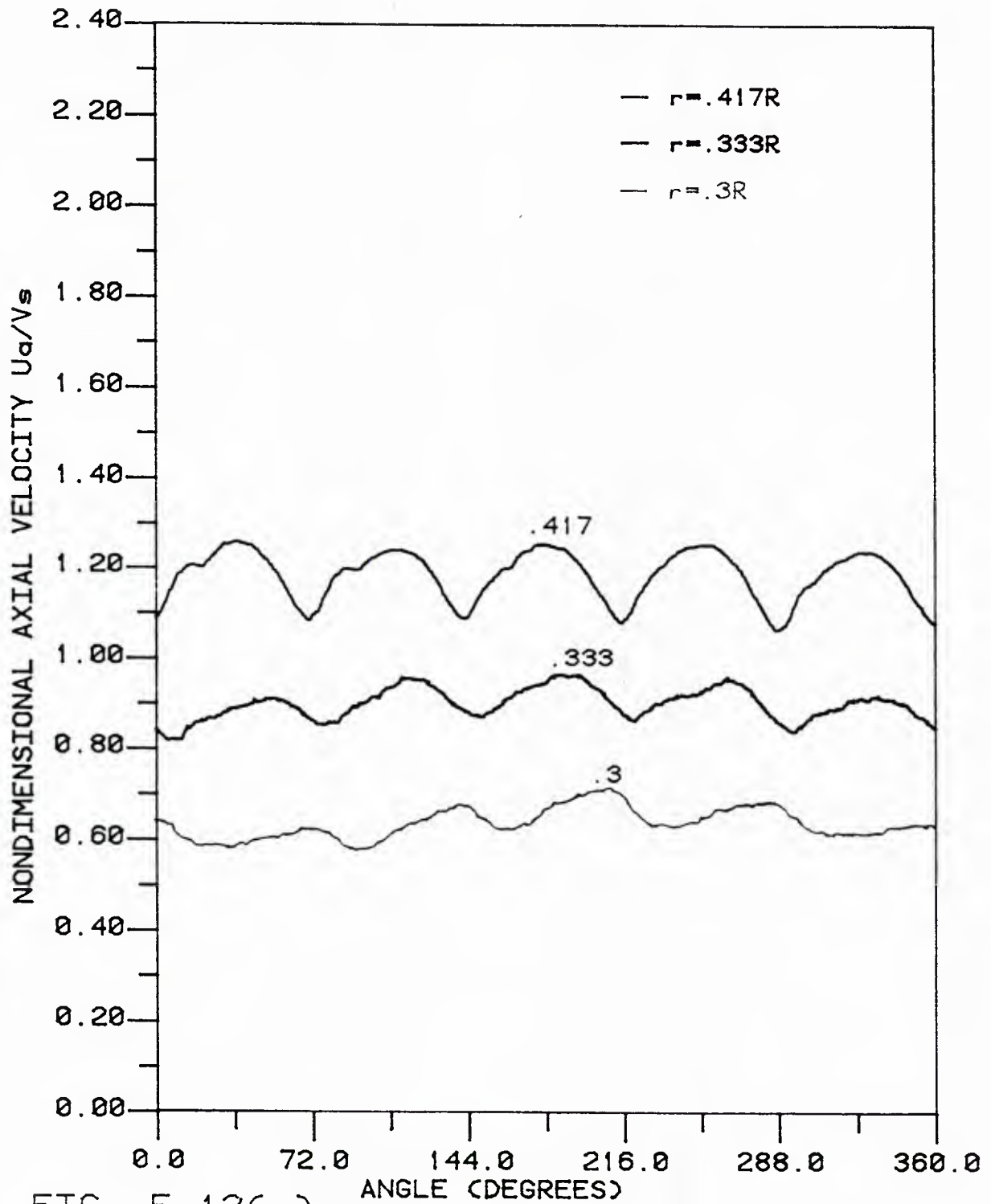AXIAL VELOCITY IN MID-SPAN REGION
X=.281R (T.E.) PR4660 J=0.976

FIG. 5.12(c)

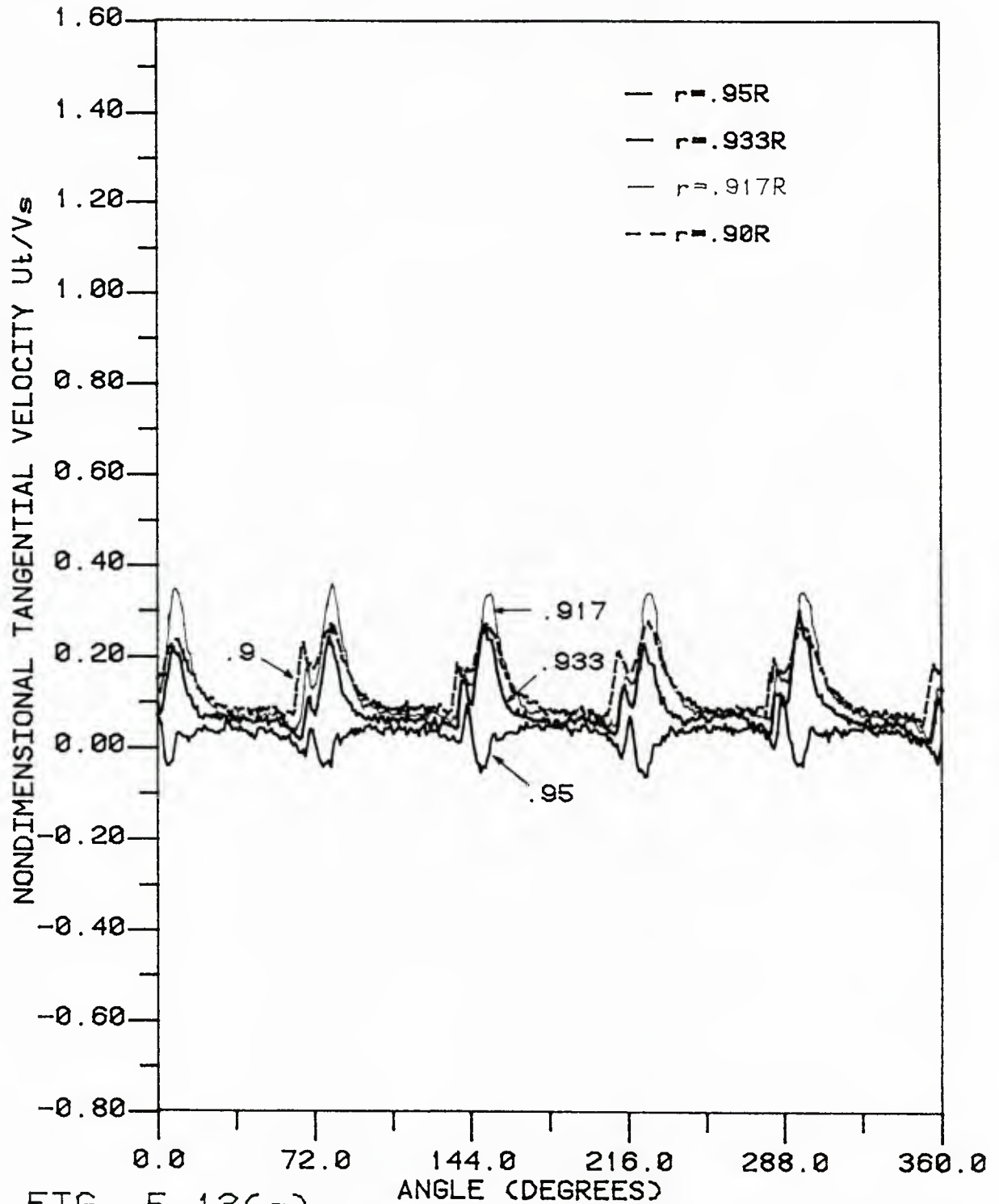AXIAL VELOCITY NEAR HUB REGION
X=.281R (T.E.) PR4660 J=0.976

FIG. 5.13(a)

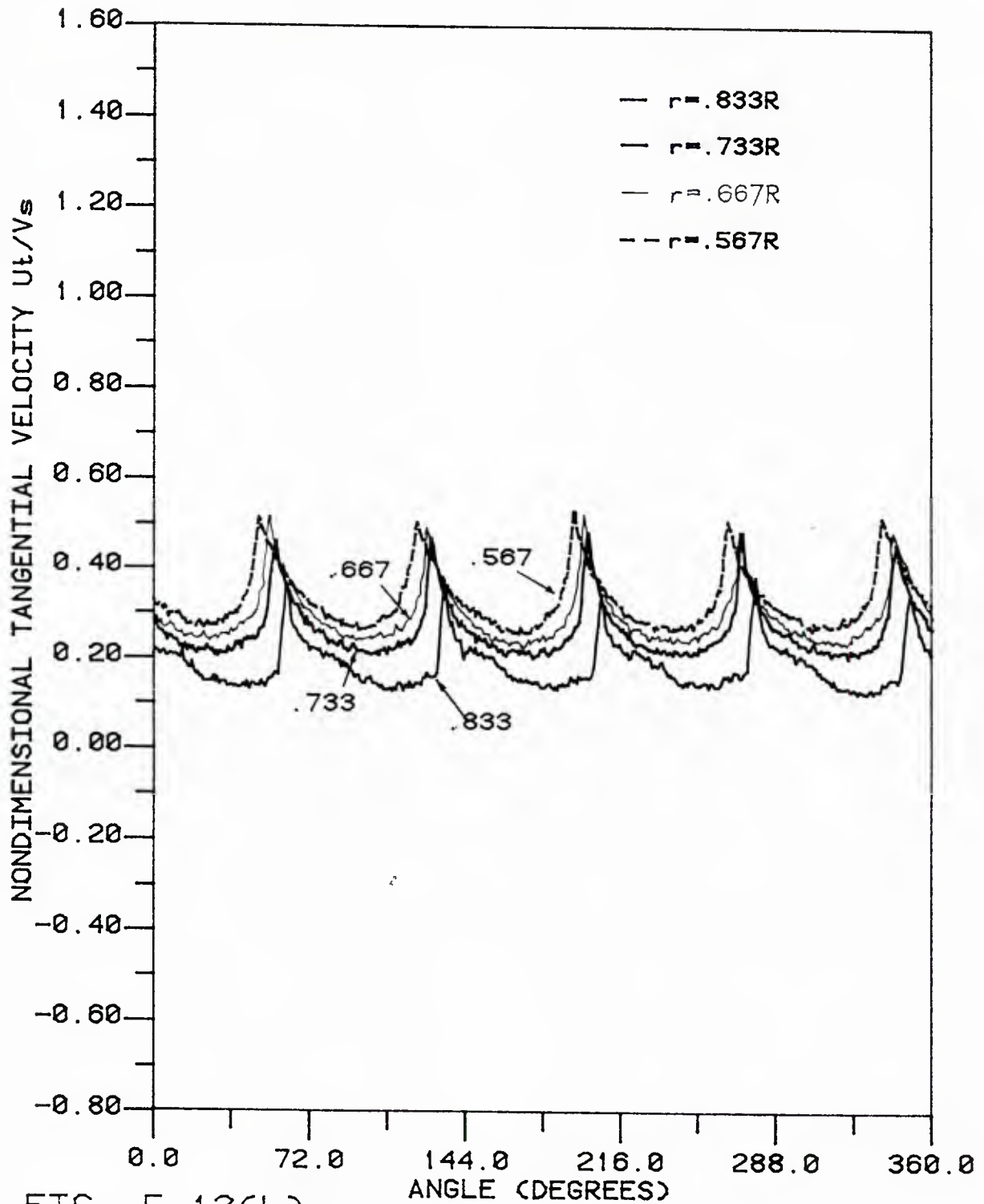TANGENTIAL VEL. IN TIP FLOW REGION
X=0.281R (T.E.) PR4660 J=0.976

FIG. 5.13(b)
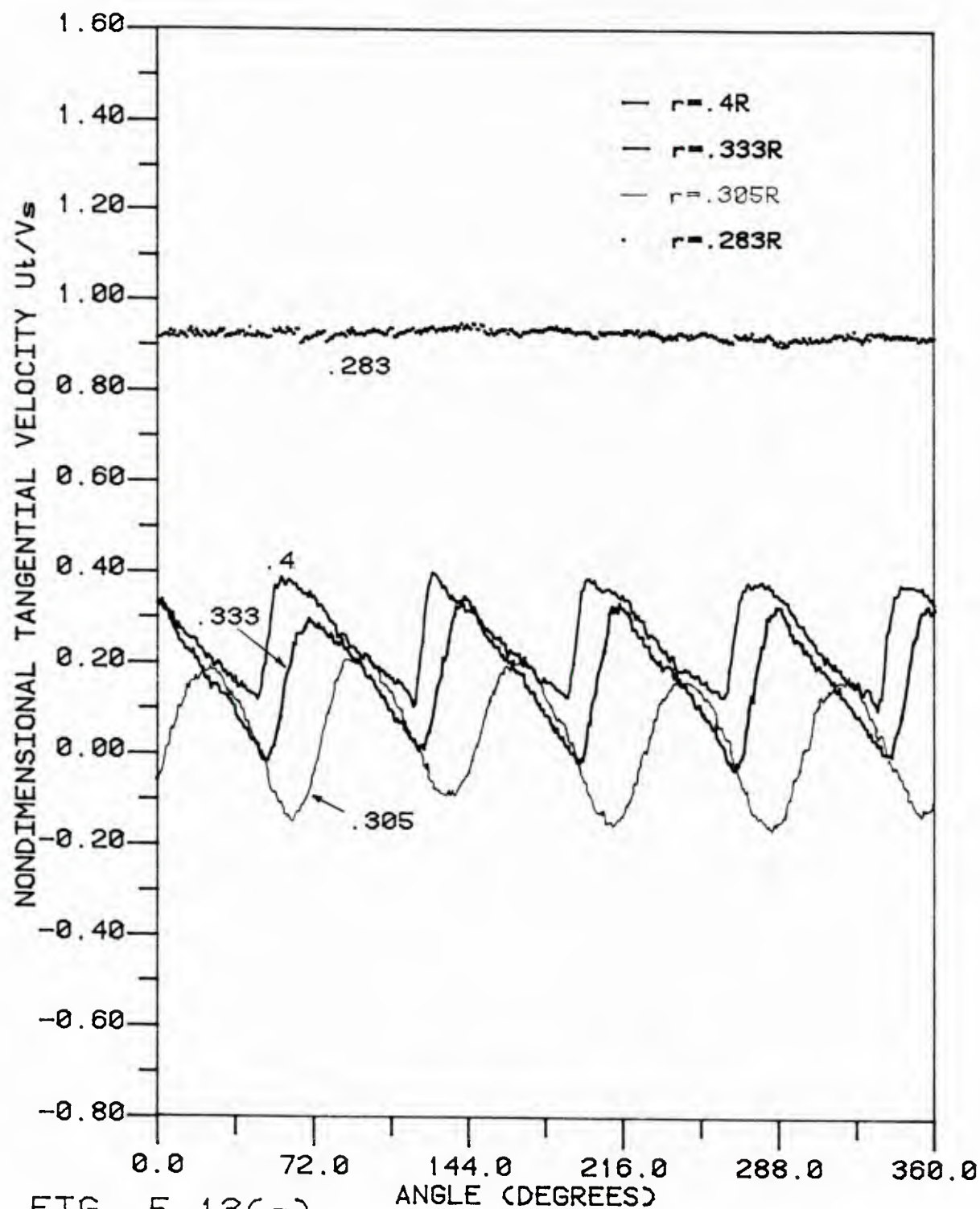TANGENTIAL VEL. IN MID-SPAN REGION
X=0.281R (T.E.) PR4660 J=0.976

FIG. 5.13(c)

TANGENTIAL VEL. NEAR HUB REGION
X=0.281R (T.E.) PR4660 J=0.976

Before closing this section, it may be interesting to look at the
deformation of the vortex sheet along the x-direction. Figure 5.14a shows
radial velocities in the tip flow region at x = 0.353 R (0.072 R downstream
from the last station). Basically, the curves in Figure 5.14a are similar
to those in Figure 5.11a. The tip vortex is still between r = 0.95 R and
r = 0.933 R. The angular position of the tip vortex has a difference of
about 14.4°. The average pitch diameter ratio of the tip vortex can be
approximately estimated as:

$$\left[\frac{P}{D}\right]_{avg.} = \frac{(360)(0.072)}{(14.4)(2)} = 0.9$$

The radial velocities further down (x = 1.053 R, which is in the hub
apex plane) are shown in Figure 5.14b. The shape of the velocity is
slightly different from that in Figure 5.14a or Figure 5.11a. That is
because the θ position of the jump component relative to the global
component changed. The tip vortex is between r = 0.917 R and r = 0.9 R,
which is closer to the propeller shaft than the last two stations, which
means that a contraction of tip vortex occurred. The average pitch
diameter ratio can only be estimated if the number of vortex sheets between
x = 1.053 R and x = 0.353 R is known. If we assume that there is one more
vortex sheet between these two stations, then the ratio will be:

$$\left[\frac{P}{D}\right]_{avg.} = \frac{(360)(1.053 - 0.353)}{(33.1 + 72)(2)} = 1.2$$

where 33.1° is the phase difference between Figure 5.14a and Figure 5.14b,
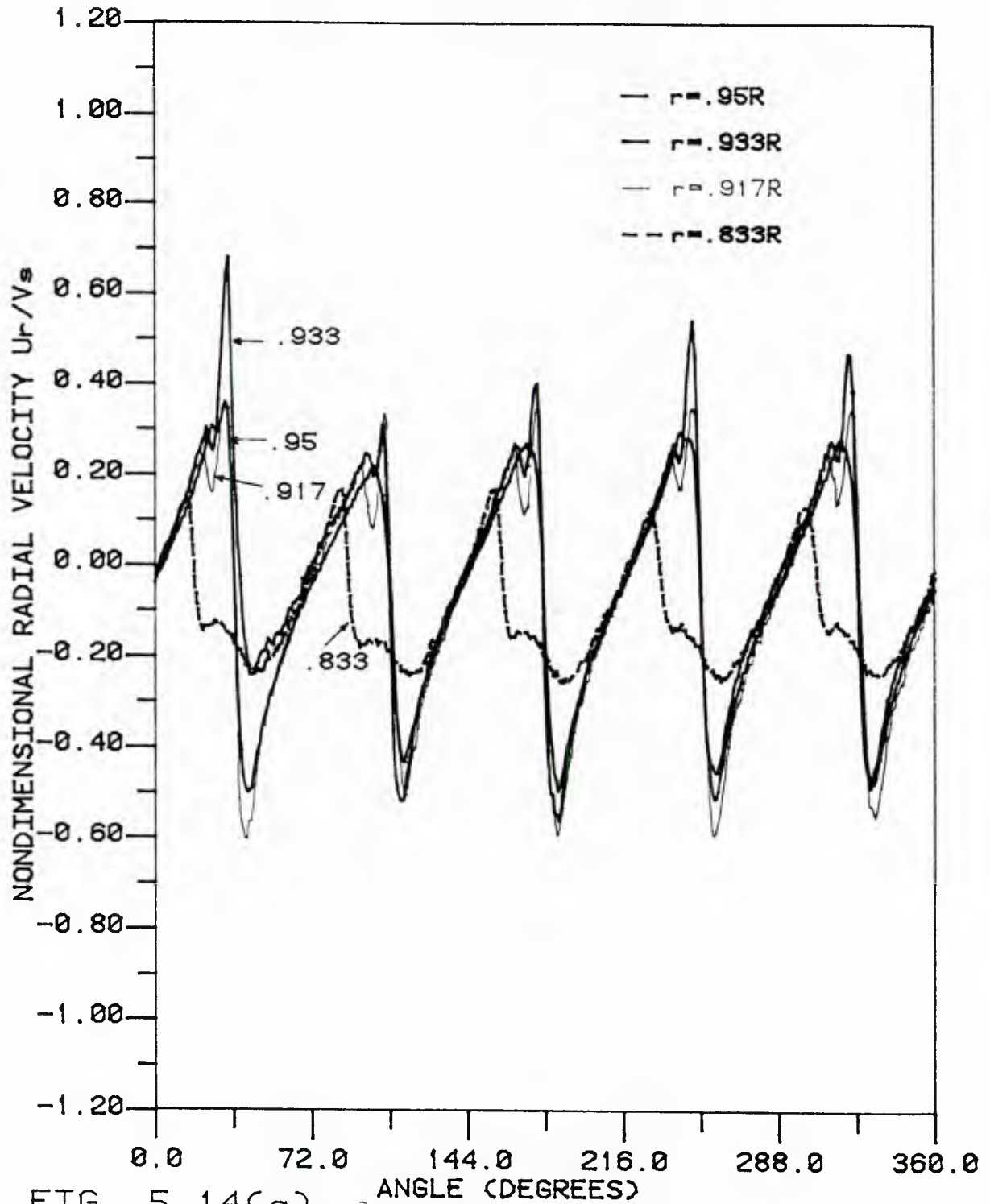and 72° is just the blade interval angle.

FIG. 5.14(a)
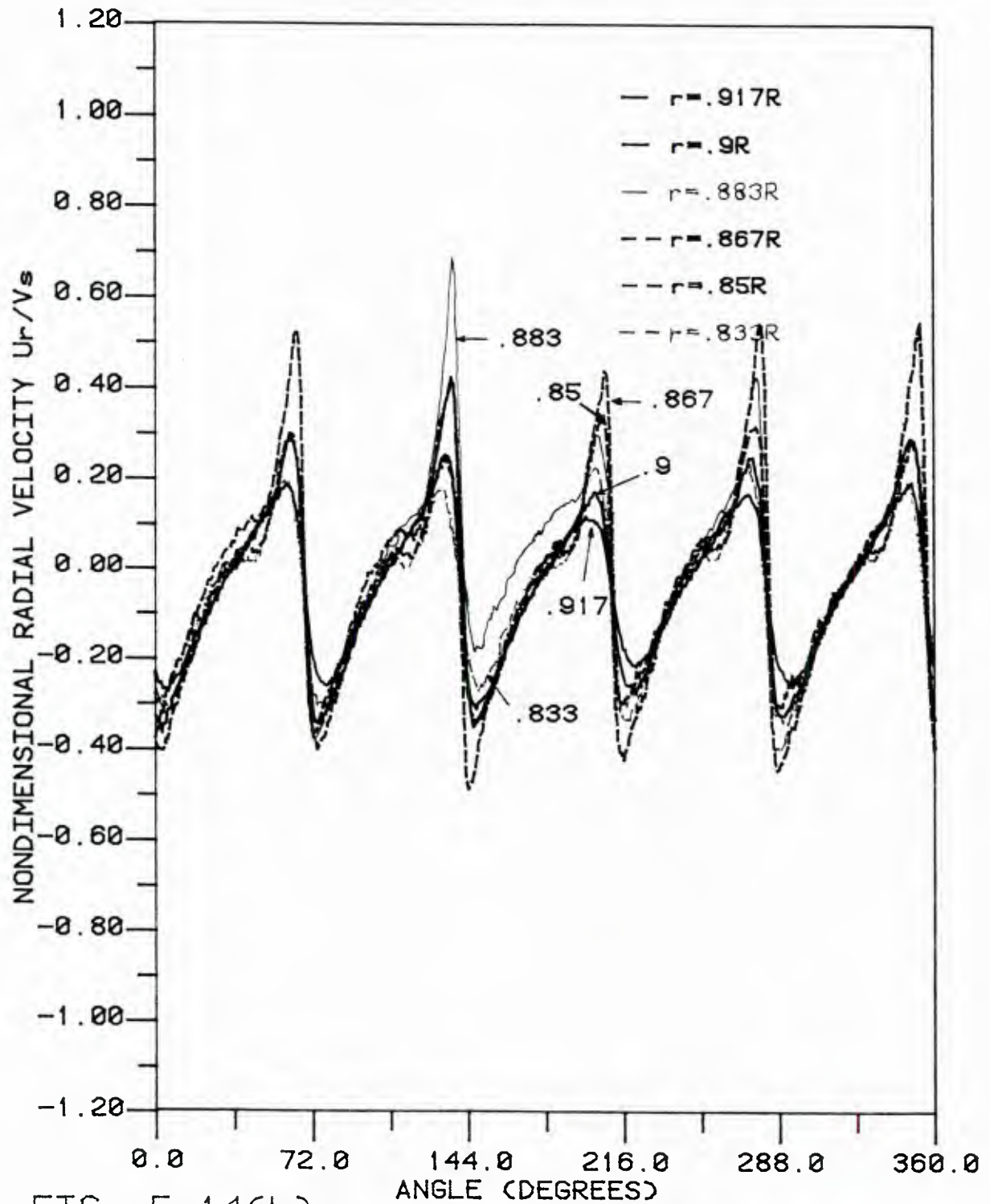
RADIAL VELOCITY IN TIP FLOW REGION
X=.353R PR4660 J=0.976

FIG. 5.14(b)
RADIAL VELOCITY IN TIP FLOW REGION
X=1.053R (HUB APEX) P4660 J=0.976

5.7 Circulation Conservation Law

In an inviscid fluid acted upon by conservative forces (e.g., gravity), the circulation Γ, defined as the integrated tangential velocity around any closed contour C in the fluid:

$$\Gamma = \oint_C \vec{V} \cdot d\vec{r},$$

(5.3)

is constant about any closed material contour moving with the fluid. This is Kelvin's theorem for the conservation of circulation:

$$\frac{D\Gamma}{Dt} = \frac{\partial \Gamma}{\partial t} + \vec{V} \cdot \nabla \Gamma = 0$$

(5.4)

In other words, once a certain amount of circulation is associated with a fluid, it will stay with that fluid forever. This is simply because the rotation rate of fluid particles is not changed when zero shear stresses act on the particles. Zero shear stress is a direct result of an inviscid fluid.

5.7.1 The Application of Kelvin's Theorem to a Propeller

By applying Kelvin's theorem to a propeller, a relationship between the circulation at the blades and the circulation in the trailing vortex wake can be established, as shown below.
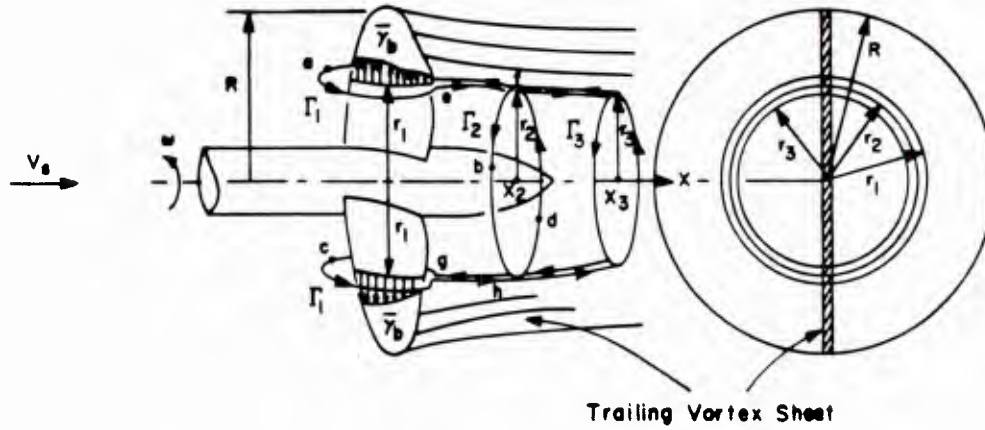
Figure 5.15 A Two-Bladed Propeller and Its Wake

For simplicity, a two-bladed propeller and its wake, shown in
Figure 5.15, will be demonstrated. A contour, abcda, is chosen in such a
manner that there is no contribution to the circulation from either the
path between e and f or the path between g and h, since these paths are
intentionally taken in the direction of the flow of the vortex sheets. The
trailing vortex shed from the blade section r_1 is deformed so that it has
radial distance r_2 at x_2 and r_3 at x_3. The circulation Γ_1 at r_1 is related
to the bound vortex $\gamma_b(r_1,\xi)$ by Stoke's theorem:

$$\Gamma_1 = \int_{\xi_1}^{\xi_t} \gamma_b d\xi \tag{5.5}$$

where ξ is a local chord coordinate, and ξ_1 and ξ_t correspond to the blade
leading edge and blade trailing edge respectively. Finally, the
circulation along the contour should be zero from Kelvin's theorem. Thus:

$$\Gamma_2(r_2) = -2\Gamma_1(r_1) \tag{5.6}$$

The same is true for $\Gamma_3(r_3)$, i.e.,

$$\Gamma_3(r_3) = -2\Gamma_1(r_1) \tag{5.7}$$

By measuring the tangential velocity along the path, bhdf, the circulation of Γ_2 can be calculated using (5.3). Thus, the circulation $\Gamma_1(r_1)$ will be:

$$\Gamma_1(r_1) = -\frac{1}{N} \int_{bhdf} \vec{V}(r_2) \cdot d\vec{r} \tag{5.8}$$

for an N-bladed propeller.

The only unknown is the relationship between r_2 and r_1. In other words, the way in which the trailing vortex sheet deforms is unknown although it is assumed to behave as a cubic function in the numerical model.

An assumption was made that the velocity of the trailing vortex equals the circumferential mean flow, which can be measured, as will be seen in the next section.

5.7.2 Circumferential Mean Streamlines

The circumferential mean axial velocities and the circumferential mean radial velocities for propeller 4660 with a short hub were measured at 14 stations -- from the blade trailing edge to far downstream. Both the axial component and the radial component were originally measured (using the

backscattering mode) at a propeller speed of 1000 rpm and an impeller speed
of 248 rpm, so that J = 0.976. Because of the data density/tracker
bandwidth problem (discussed in section 5.2), the measurements were
repeated (using the forward scattering mode) at lower speeds -- 300 rpm for
the propeller and 74 rpm for the impeller (so that J was still 0.976). The
mean radial velocities changed considerably, while the mean axial
velocities remained the same. This was because the only places where the
data density was too low for the tracker were the points which were across
vortex sheets. Also, the orientations of the jump velocities induced by
the vortex sheets were nearly in the radial direction. By reducing the
speed by a factor of 3.33, while keeping J constant, the time scale is
increased by a factor of 3.33 and the velocities will be decreased by the
same factor. Thus, the data density is increased by a factor of 11.11.

The circumferential mean axial velocities are shown in Figures 5.16a
through 5.16c, and the circumferential mean radial velocies are shown in
Figures 5.17a through 5.17c.

The radial velocity can only be measured in the center plane of the
tunnel, along a vertical line. Both the radial velocity and the axial
velocity were measured at the same points, which were along a vertical line
in the tunnel center plane. Dead corners for measuring either the axial
component or the radial component occurred when the measuring point was
very close to the body. A schematic plot of a dead corner for measuring
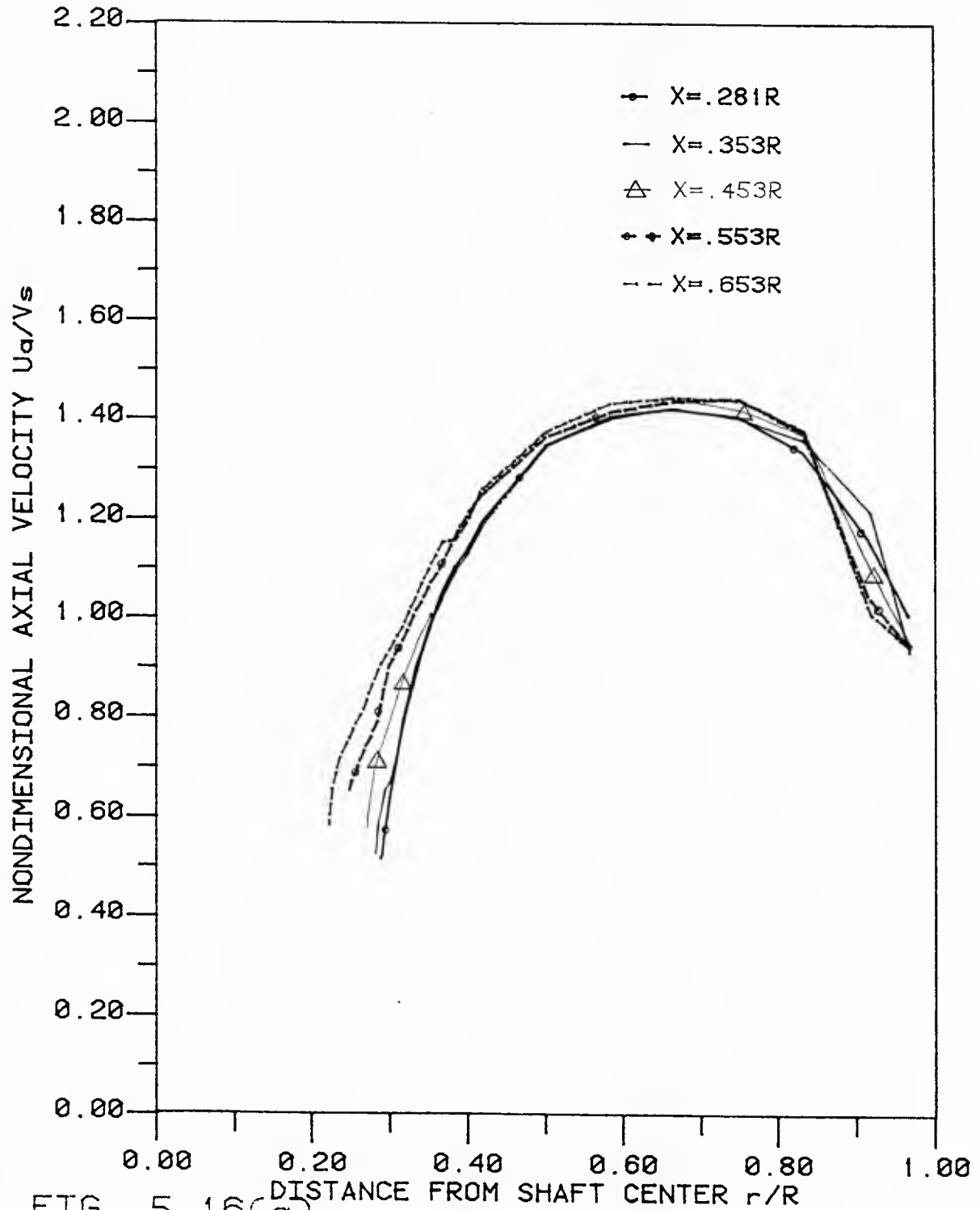the radial component is shown in Figure 5.18a.

FIG. 5.16(a)
CIRCUMFERENTIAL MEAN AXIAL VELOCITY
J=0.976 PROP.4660 WITH SHORT HUB

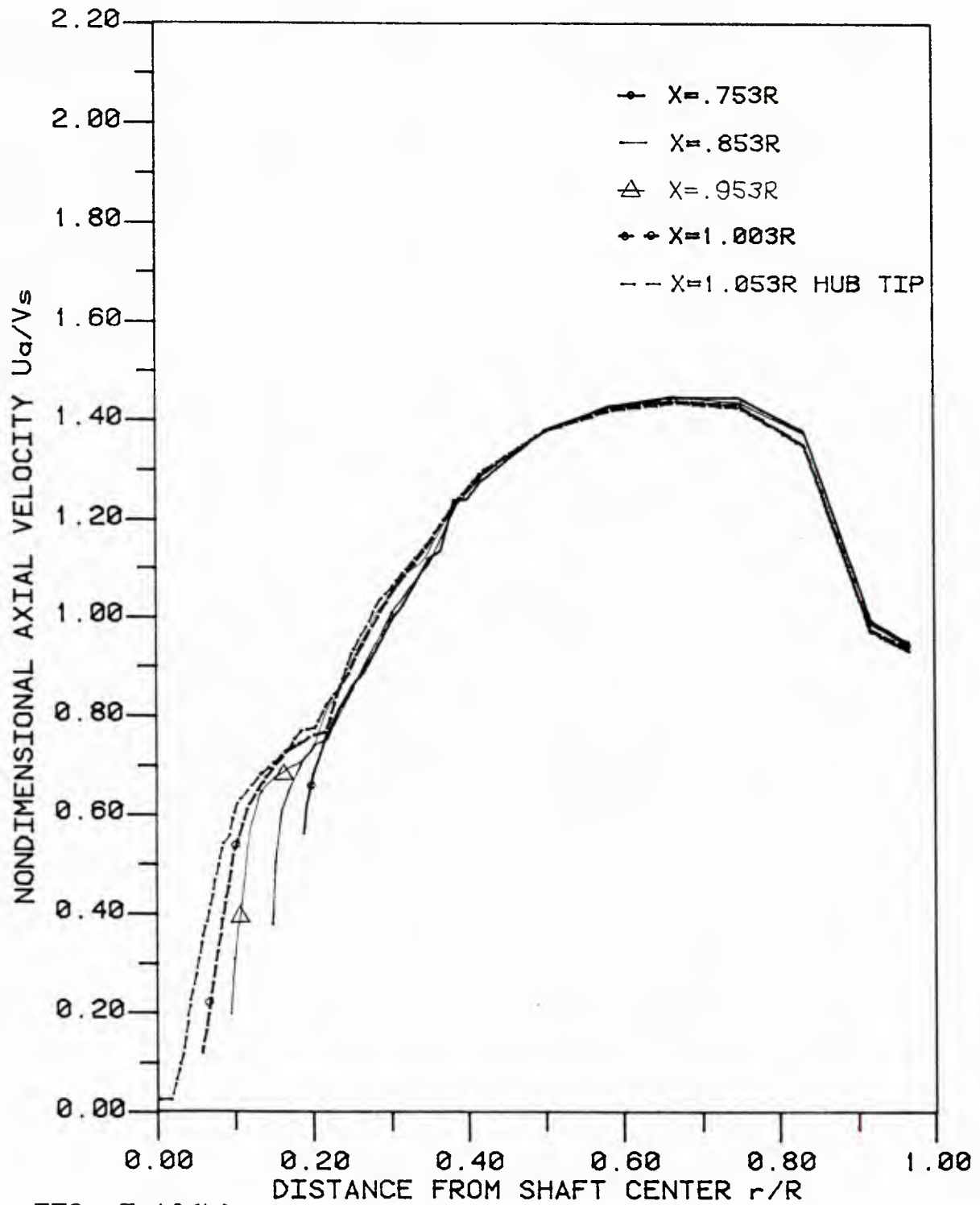FIG. 5.16(b)

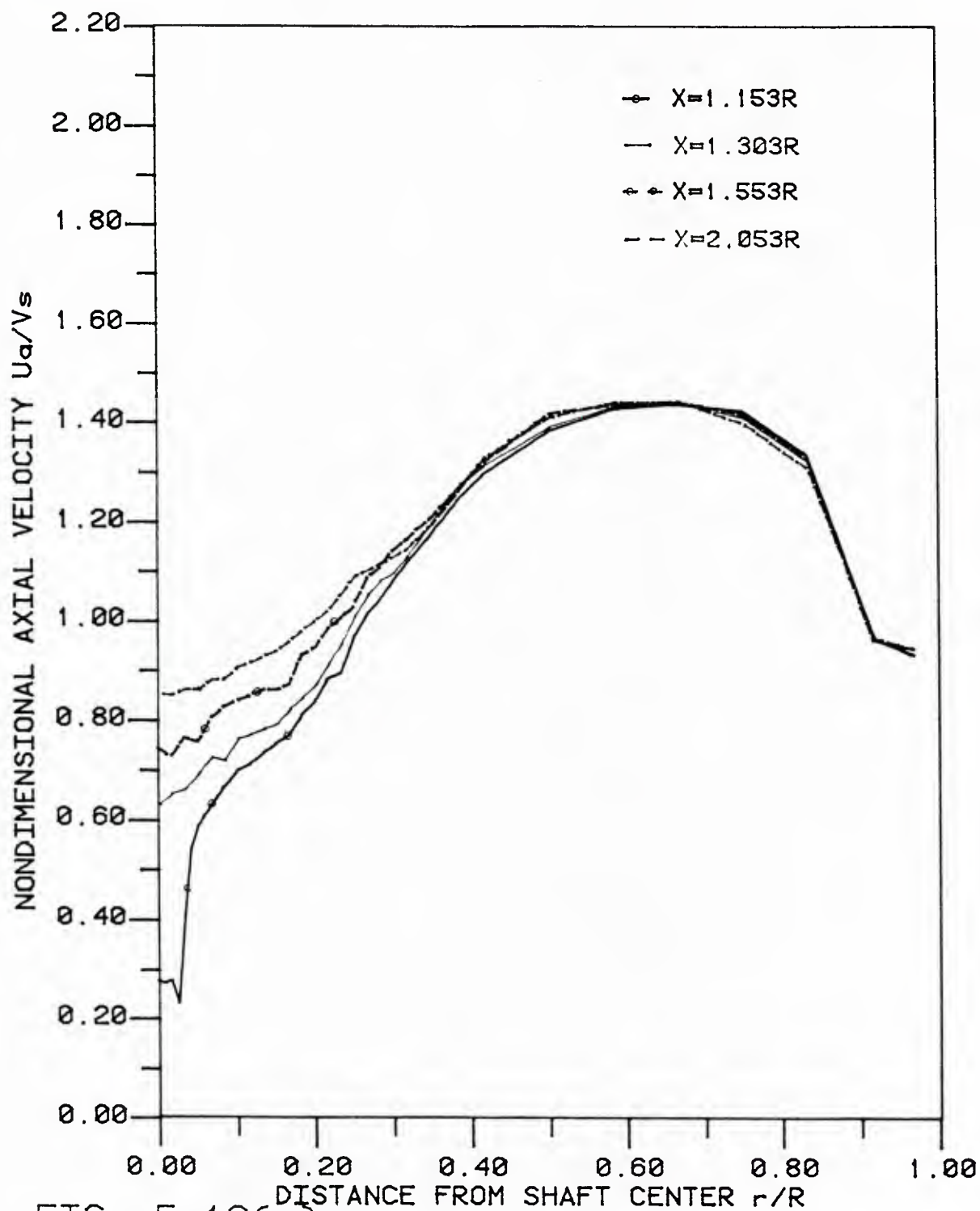CIRCUMFERENTIAL MEAN AXIAL VELOCITY
J=0.976 PROP.4660 WITH SHORT HUB

FIG. 5.16(c)
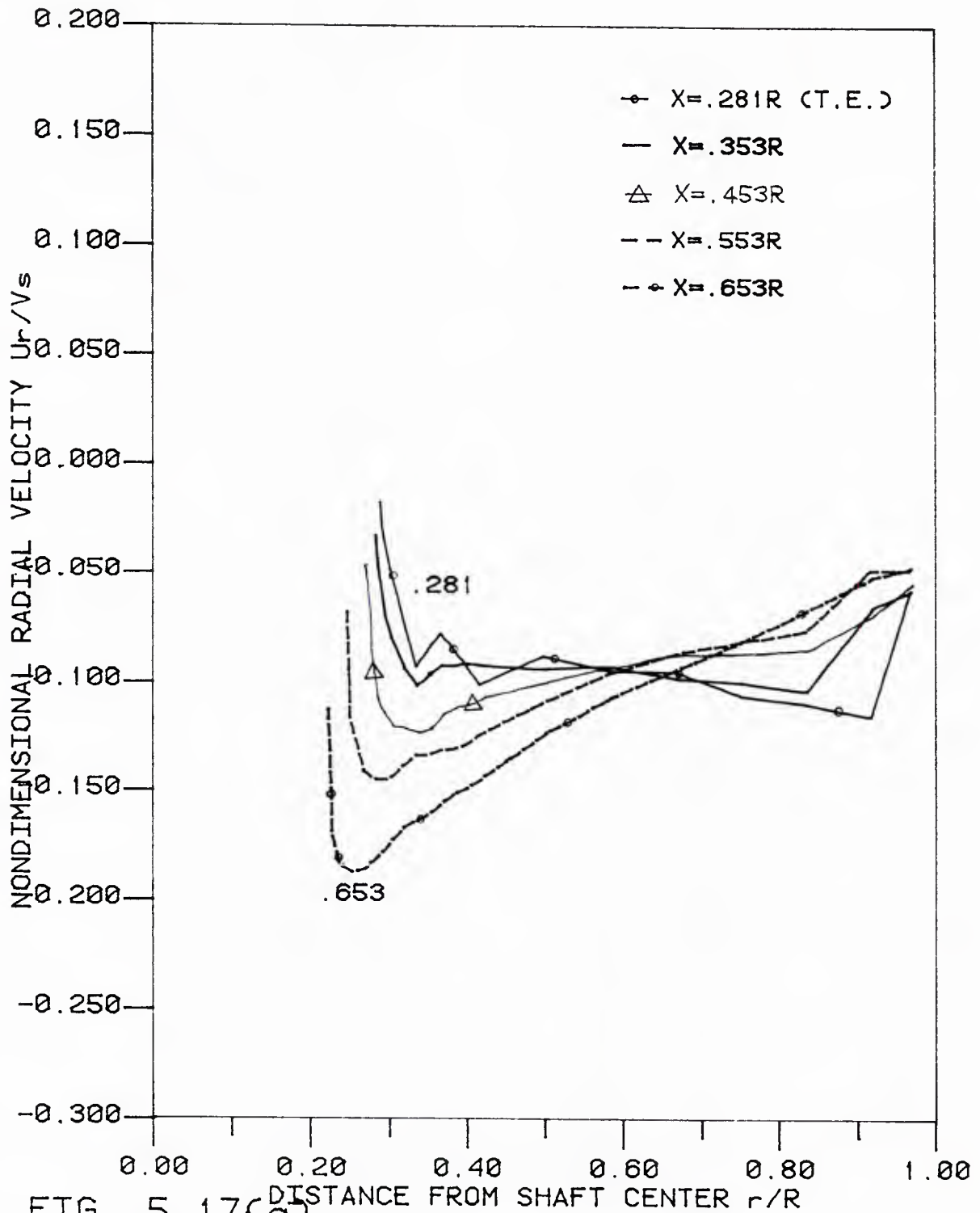CIRCUMFERENTIAL MEAN AXIAL VELOCITY
J=0.976 PROP.4660 WITH SHORT HUB

FIG. 5.17(a)
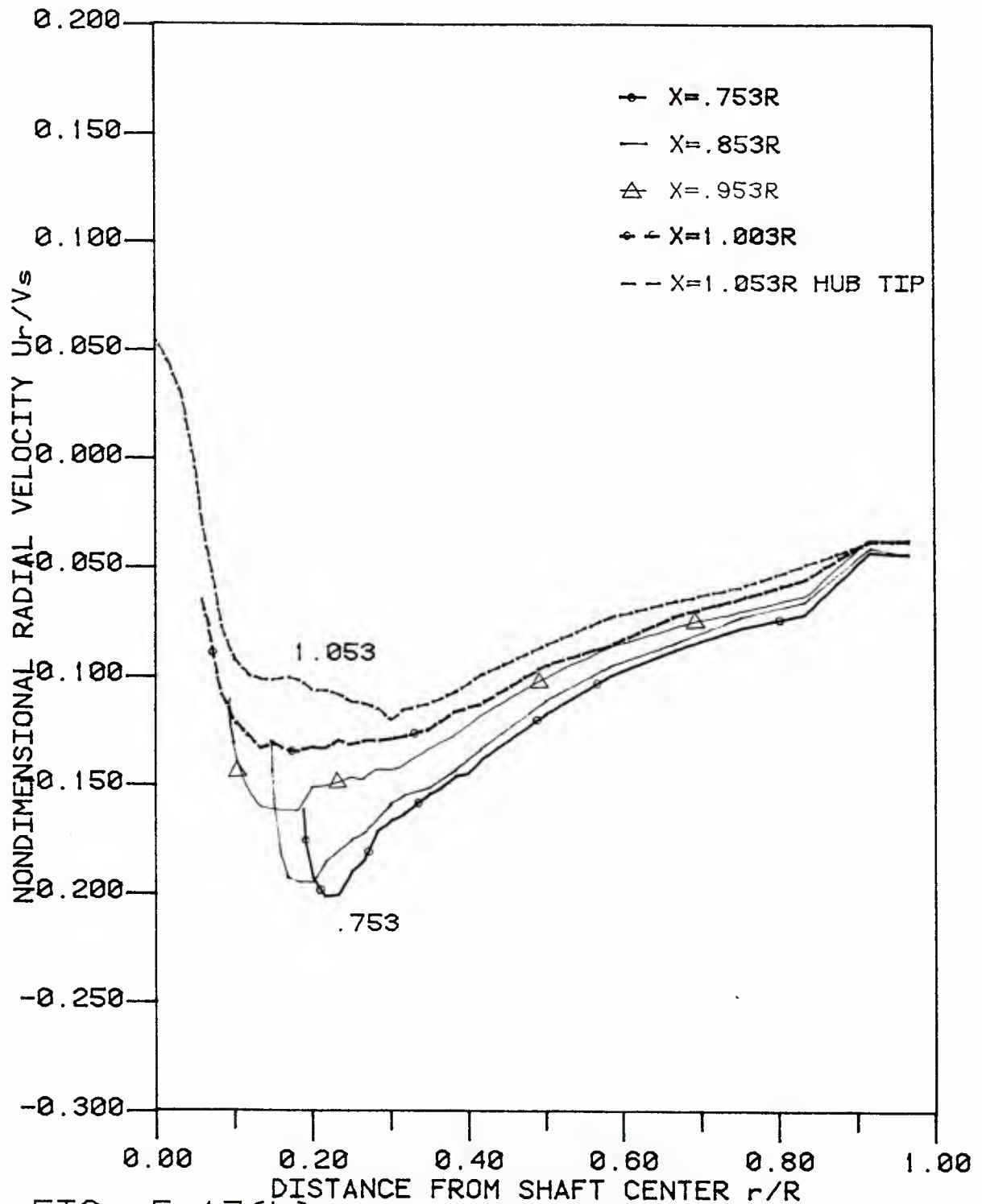CIRCUMFERENTIAL MEAN RADIAL VELOCITY
J=0.976; PROP.4660 WITH SHORT HUB

FIG. 5.17(b)
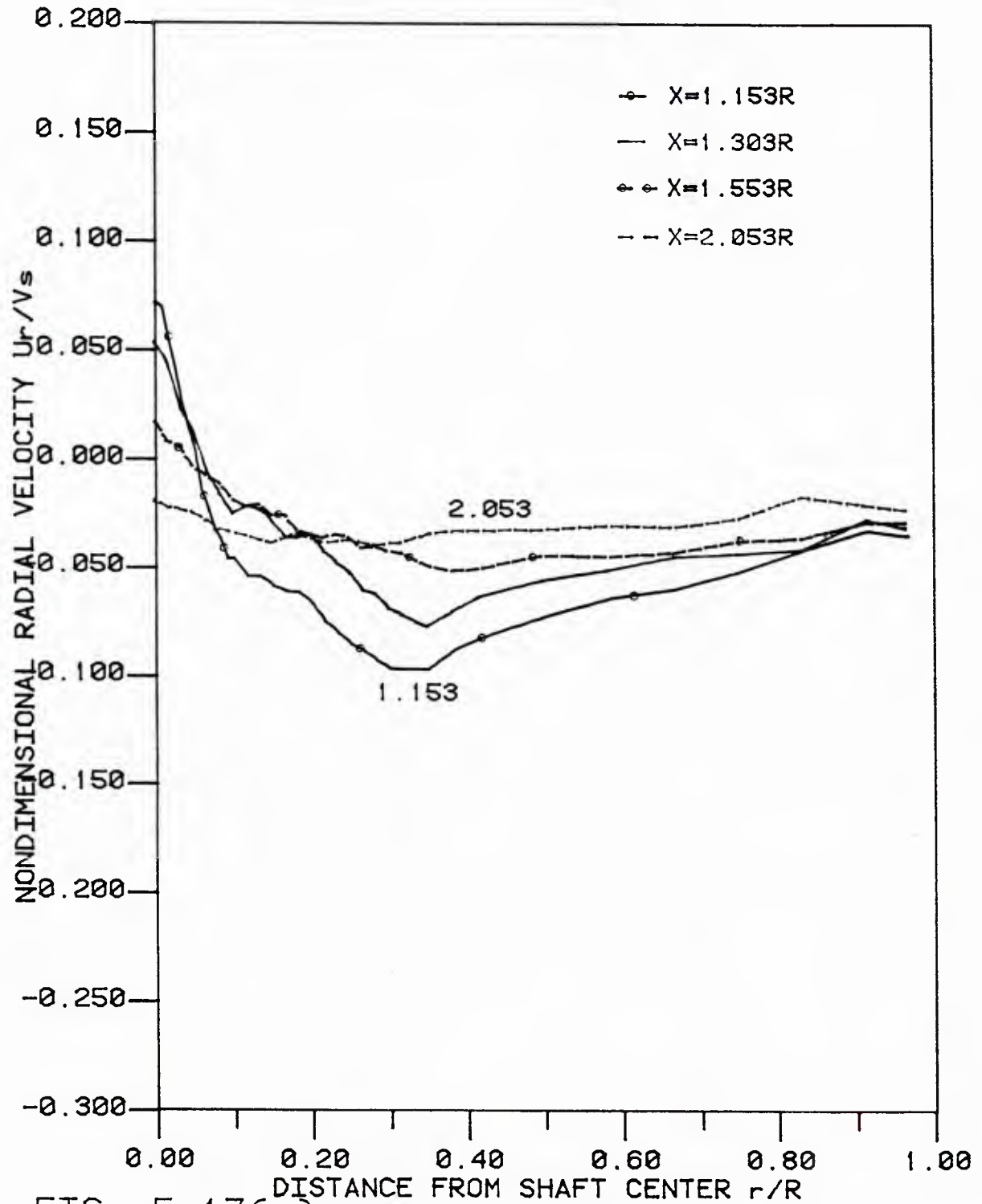CIRCUMFERENTIAL MEAN RADIAL VELOCITY
J=0.976 PROP.4660 WITH SHORT HUB

FIG. 5.17(c)
CIRCUMFERENTIAL MEAN RADIAL VELOCITY
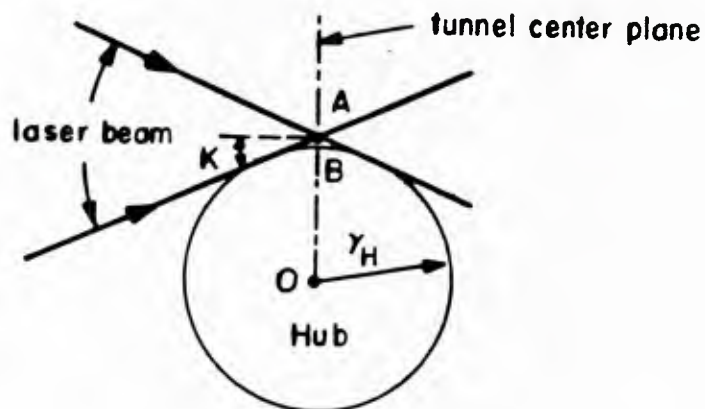J=0.976 PROP.4660 WITH SHORT HUB

Figure 5.18a Dead Corner for Measuring the Radial Velocities

The points on segment AB could not be measured because one of the two laser beams was blocked by the body. The length of AB is:

$$AB = AO - BO = \frac{r_H}{\cos \kappa} - r_H = r_H \left[\frac{1}{\cos \kappa} - 1 \right]$$

where κ is the half angle of the transmitting lens and r_H is the hub radius at this particular station. Notice that AB is proportional to r_H, so that AB is a maximum at the trailing edge station and is zero at the hub apex station. A typical value of AB is 0.0084 inch if κ is 5.538° (Lens 9118) and r_H = 1.8 inch. A typical value of the measuring volume diameter is 0.00032 inch. The calculation of the length of the dead corner for measuring the axial component is more difficult. A top view of this dead corner is shown schematically in Figure 5.18b.
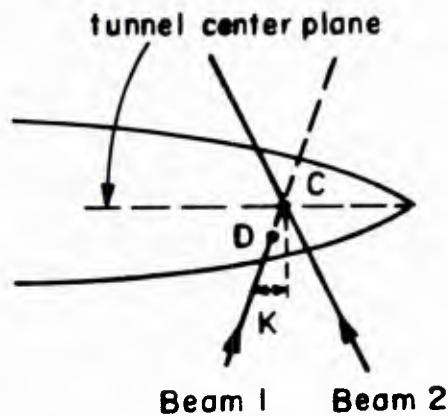
tunnel center plane

Beam 1   Beam 2

Figure 5.18b Dead Corner for Measuring the Axial Velocities

As seen in Figure 5.18b, laser beam 1 is blocked by the body at point D while beam 2 reaches the measuring point C. The length of the dead corner is related to r_H, κ, and the derivative of r_H with respect to x. The length of the dead corner for axial velocity is obviously smaller than that for radial velocity. Due to the existence of those dead corners, the velocities shown in Figures 5.16 and 5.17 could not reach zero, which is exactly the value for the velocities at the boundary. However, a vertical line (not shown) passing the last data point on each curve is almost correct, because the dead corners are so narrow that they are nearly zero at the scale of Figures 5.16 and 5.17.

The velocity vectors, constructed from measured axial and radial velocities, and the hub are plotted in Figure 5.19. The directions of those vectors, although for simplicity not shown, point in the downstream direction. The velocities, although not zero at the hub due to the measuring problem at the dead corner, are tangent to the hub -- this is a very good way to check the measurements. The dead corner in the measurement disappeared for the stations behind (and including) the station at the hub apex. It is seen that the velocities decrease to zero at the hub apex, which is a stagnation point.
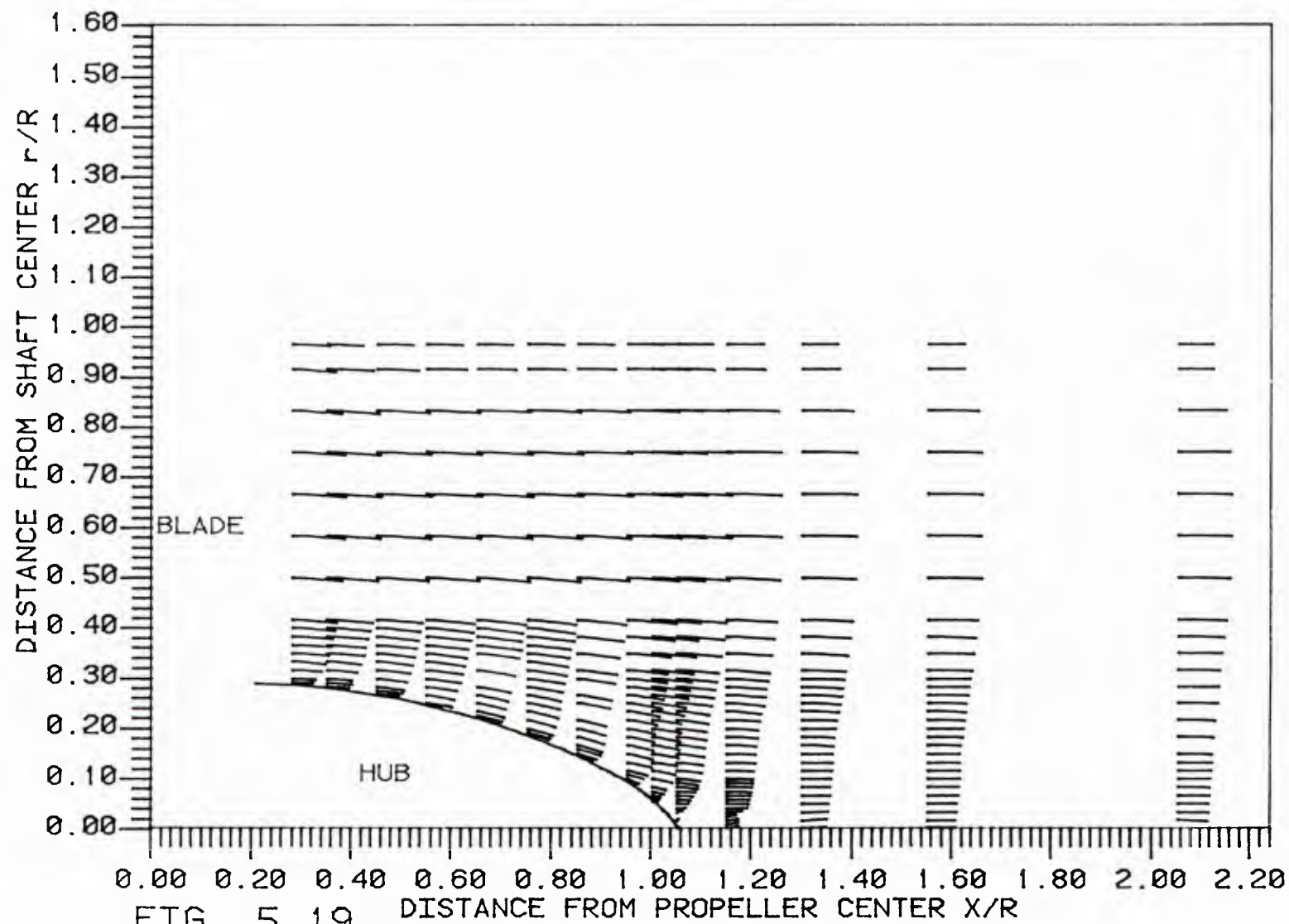
FIG. 5.19 CIRCUMFERENTIAL MEAN AXIAL & RADIAL
VELOCITY VECTORS; PROP.4660 J=0.976

The construction of circumferential mean streamlines from the mean velocity vectors is straightforward. Although there are many ways do this, only four of them will be investigated here. The first three methods construct the streamlines by integrating both the axial and radial velocities in the downstream direction. The fourth method constructs the streamlines by integrating only the axial velocity along the radial direction, from the dividing streamline to the top.

(i) Method 1 (see Figure 5.20a)

Each streamline starts with a point 1, say, along the vertical line at station 1, the station closest to the blade trailing edge. It then follows a straight line having a slope equal to the slope of the velocity vector at point 1, until it reaches the next station, station 2 at point 2. At point 2, the streamline changes slope. The new slope equals the slope of the velocity vector at point 2. The velocity at point 2 can be interpolated by fitting a spline curve to the velocity data along station 2. The streamlines were drawn by repeating the above procedures until the last station was reached. They were then extended a short distance further downstream, following the velocity at the last station.

(ii) Method 2 (see Figure 5.20b)

The location of point 2 and the velocity at point 2 were obtained in the same way as in method 1. Point 3, the
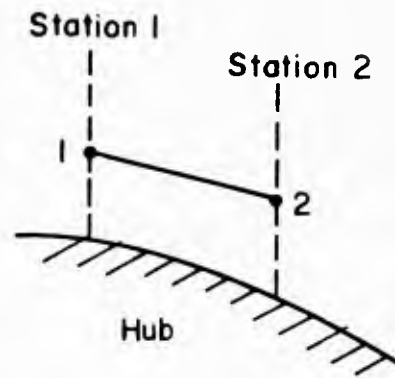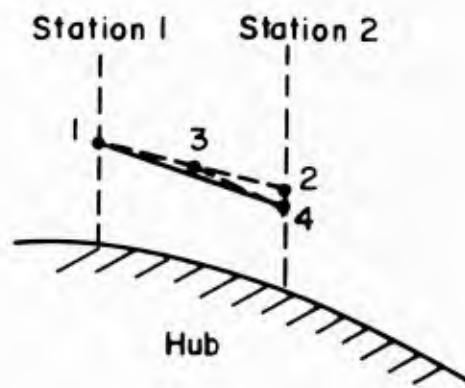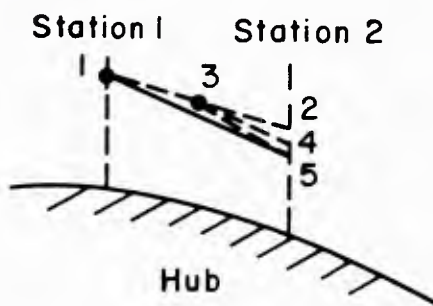
Fig. 5.20a Method 1

Fig. 5.20b Method 2

Fig. 5.20c Method 3

midpoint of segment $\overline{1\,2}$, was used as an auxiliary point from which a point 4, say, at station 2 can be determined. The slope of segment $\overline{3\,4}$ equals the slope of the average of the velocities at points 1 and 2. The segment $\overline{1\,4}$ is the streamline between station 1 and station 2.

(iii) Method 3 (see Figure 5.20c)

There were three auxiliary points -- points 2, 3, and 4 -- which were obtained using method 2. Point 5 at station 2 was determined in such a way that the slope of segment $\overline{3\,5}$ equals the slope of the average of the velocities at points 3 and 4. The segment $\overline{1\,5}$ will be the streamline between stations 1 and 2.

It was found that the differences for the streamlines among these three methods were very small. This is because the distance between any two consecutive stations is small enough that the slope of the streamlines is nearly constant. The streamlines are shown in Figure 5.21. It is seen that the streamline closest to the body retreats from the body as fluid flows downstream. This can be predicted from continuity; as the velocity of the flow decreases near the stagnation point, the space between adjacent streamlines gets wider. However, the question arises: was the flow separated from the body? The error in constructing the streamlines may accumulate in integrating from upstream to downstream. This kind of error-accumulation problem can be avoided using the fourth method.
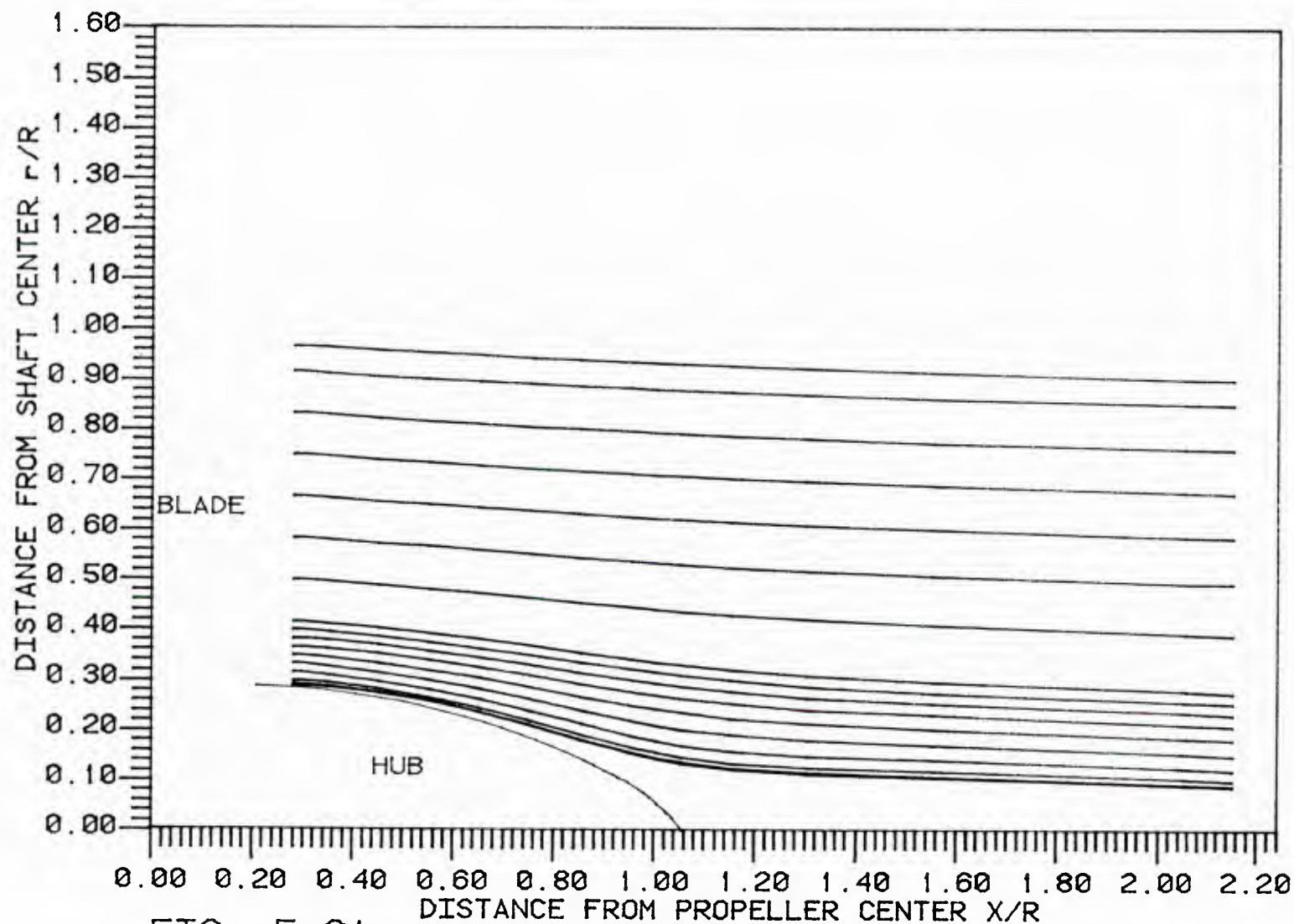
FIG. 5.21
CIRCUMFERENTIAL MEAN STREAM LINES
OF PROPELLER 4660 AT J=0.976. (METHOD 3)

(iv) Method 4

For axisymmetric flow, the stream function is defined by [Newman, 1977]:

$$2\pi\psi = Q = 2\pi \iint\limits_{s(r,x)} (u_x r\,dr - u_r r\,dx) \tag{5.8}$$

where ψ is the stream function and Q is the flux. For experimental data at any station $dx = 0$, Equation (5.8) simply becomes:

$$\psi = \int_{r_1}^{r_2} u_x r\,dr \tag{5.9}$$

The boundary condition for this integration is $\psi = 0$ at the dividing streamline, which is the combination of the hub surface and an array which starts at the hub apex and goes along the rotation axis. Notice that this method only requires axial components at each station. The integration was performed by first fitting $u_x r$ with a spline curve, and then integrating the spline curve. Spline curves are then fit to the constant stream functions at each station. The streamlines approach closer to the body than those in Figure 5.21, and separation does not occur. The streamlines become "wiggles" when they are far away from the dividing streamline. This may be due to the accumulating error of integration or the measurement error in the tip flow region. However, the streamlines in the tip flow region, constructed by the first three methods, seem to be smoother, which may indicate that the measurement error is acceptable.

Streamlines from a hybrid method which uses both methods

3 and 4 are shown in Figure 5.22. The top four streamlines

are obtained from method 3 and the rest from method 4. The

stream function is only known for the streamlines from

method 4. A nondimensional stream function is defined by:

$$\bar{\psi} = \frac{800 \ \psi}{R^2 V_S} \tag{5.10}$$

The $\bar{\psi}$'s for the first 14 streamlines are 0.0625, 0.25, 1, 4,

9, 16, 25, 36, 49, 64, 81, 100, 121, and 144. $\bar{\psi}$ for the

topmost streamline shown in Figure 5.22 approximately

coincides with the streamline from method 4, with a $\bar{\psi}$ of 400.

This means that $\psi = 0.5 \ R^2 V_S$ or $Q = \pi R^2 V_S$. Figure 5.19 shows

that the radial velocities at the station immediately

downstream of the hub apex and near the x-axis are directed

outwards. However, Figure 5.22 indicates that these radial

velocities should be directed inwards. This conflict may be

due to the error in the measurement of the radial velocities.

5.7.3 Tangential Velocity and Circulation

The influence of propeller speed and measuring mode on the tangential

velocities at the hub apex station was studied (see Figure 5.23) using

different speed/mode combinations. The velocities can be divided into two

regions. The inner region is closer to the hub apex where the tangential

velocities have a Rankine vortex structure. In the outer region, the

tangential velocities arise purely by blade rotation. The outer region has

a one-peak curve, except when the propeller speed is 1000 rpm and the
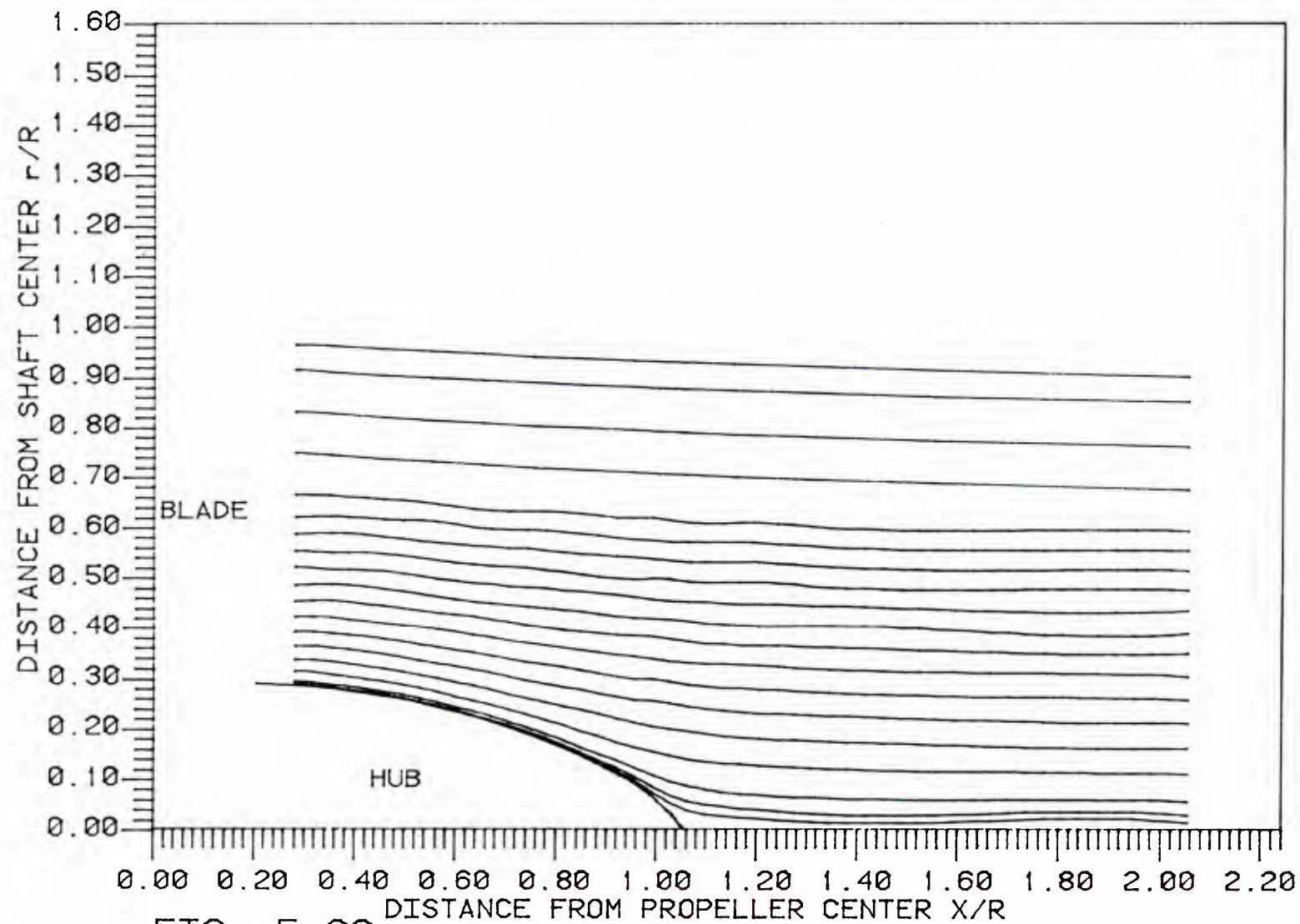
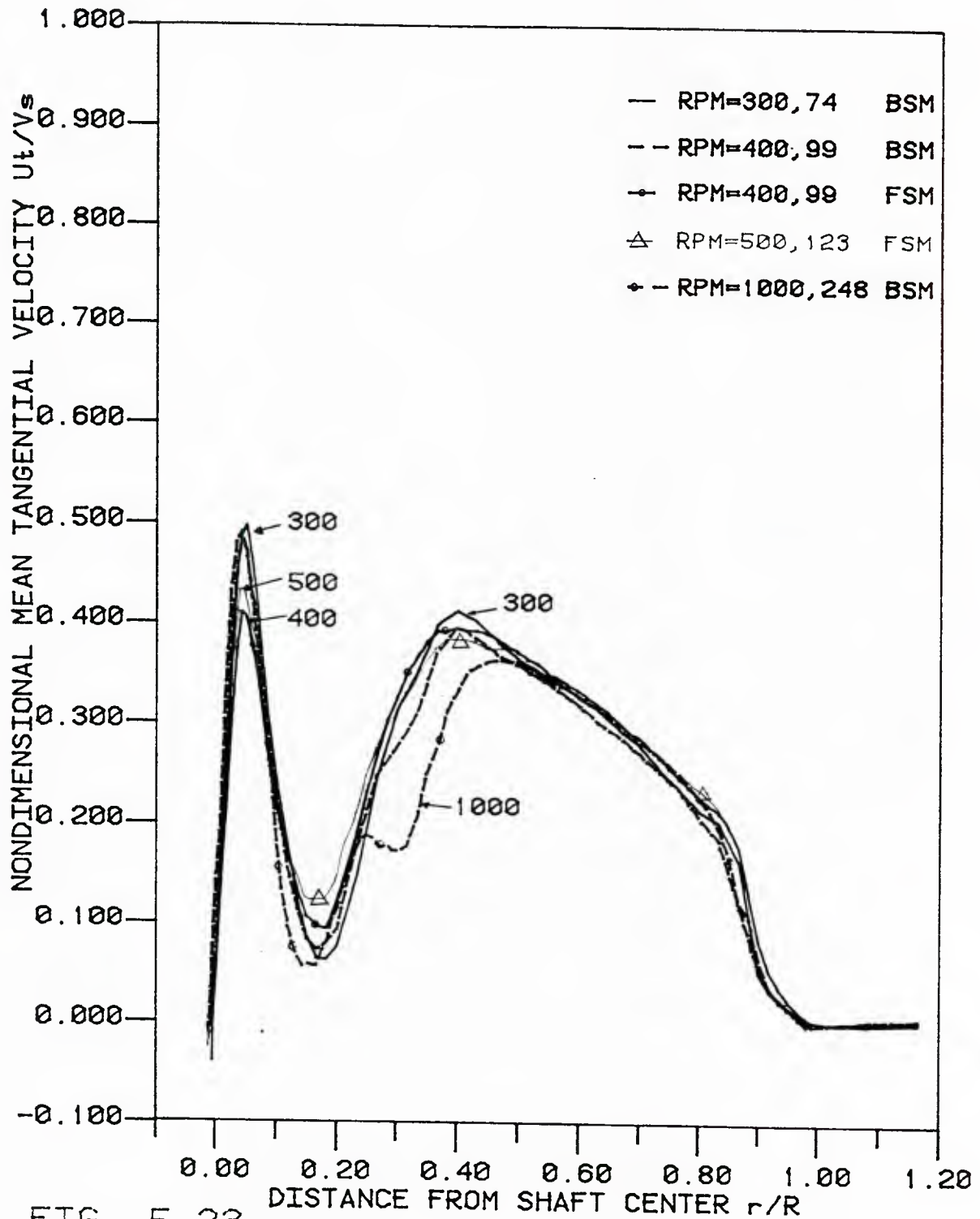FIG. 5.22 CIRCUMFERENTIAL MEAN STREAMLINES
OF PROPELLER 4660 AT J=0.976

FIG. 5.23
COMPARISON OF MEAN TANGENTIAL VEL.
X=1.053R (HUB APEX) PR4660 J=0.976

backscatter mode is used, in which case a two-peak curve results. This is due to the problem of measurement at high speed, as discussed in section 5.6.2. The forward scatter mode has a higher data acquisition rate than the backscatter mode, so it is theoretically more accurate. When the propeller velocity is 400 rpm, the tangential velocities measured using the forward scatter mode are larger than those measured using the backscatter mode in the outer region. This trend is opposite in the inner region. The reason for this is not yet known. An averaged discrepancy of 10% or more is seen among these curves, except the case of 1000 rpm which should definitely be discarded.

The tangential velocities were all measured at 300 rpm at five stations (shown in Figure 5.24). Three of them were in the hub region where only the backscatter mode can be used. The nearly vertical lines are the surface velocities of the hub. One station was at the hub apex and one was further downstream. The velocities at the hub station were measured using the backscatter mode, whereas the velocities further downstream were measured using the forward scatter mode in order to obtain better accuracy. The circulation calculated using Equation (5.8) and the measured tangential velocities are shown in Figure 5.25.

5.7.4 Conservation of Circulation

Figure 5.26a shows the result of combining streamlines (Figure 5.22) and tangential velocities (Figure 5.24). Figure 5.26b shows the result of combining streamlines (Figure 5.22) and the circulation distribution curves (Figure 5.25). In Figure 5.26b, conservation of circulation can be roughly checked by following any streamline. The circulation curves and the
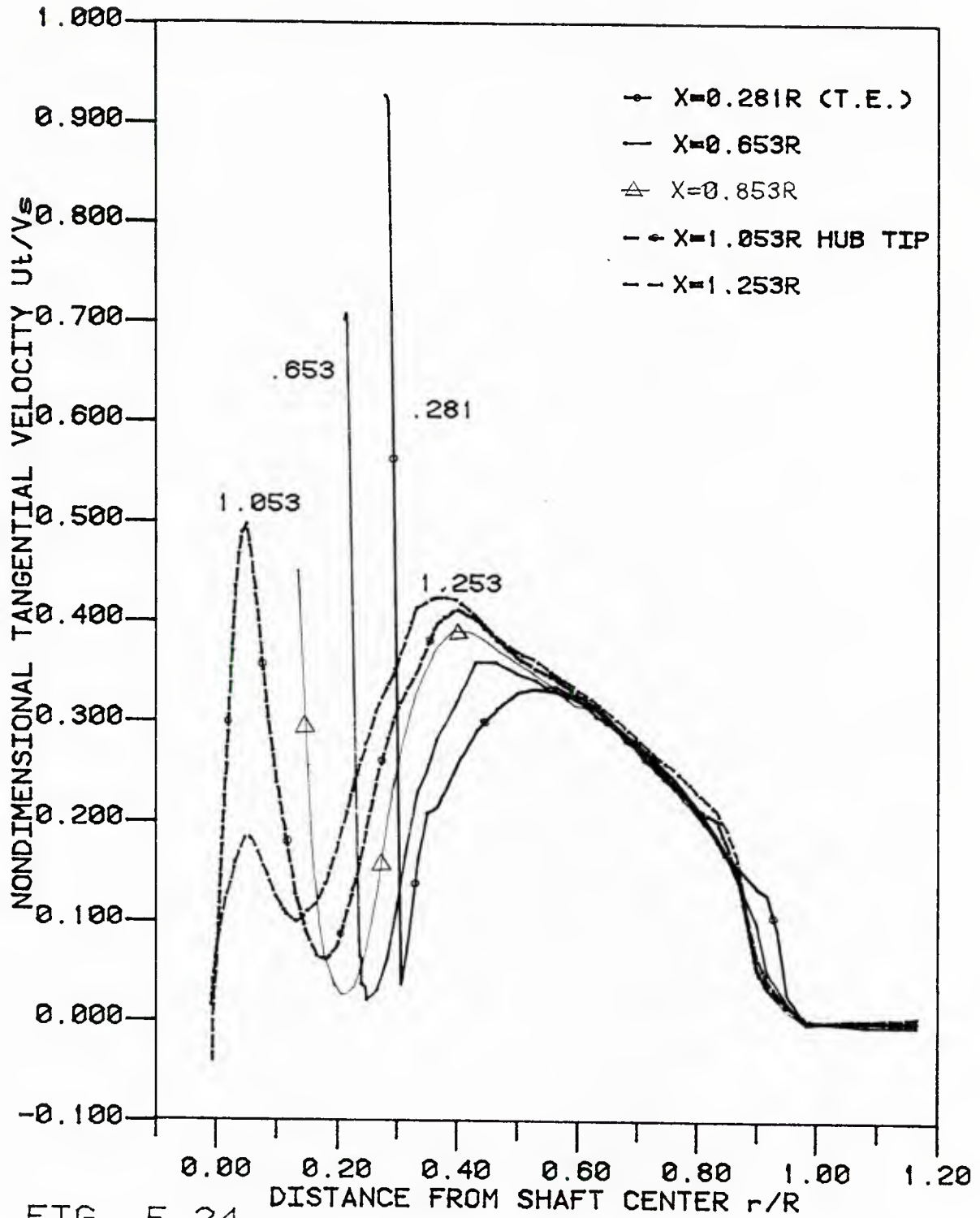
FIG. 5.24
CIRCUMFERENTIAL MEAN TANGENTIAL VEL.
IN RADIAL DISTRIBUTION PR4660 J=.976
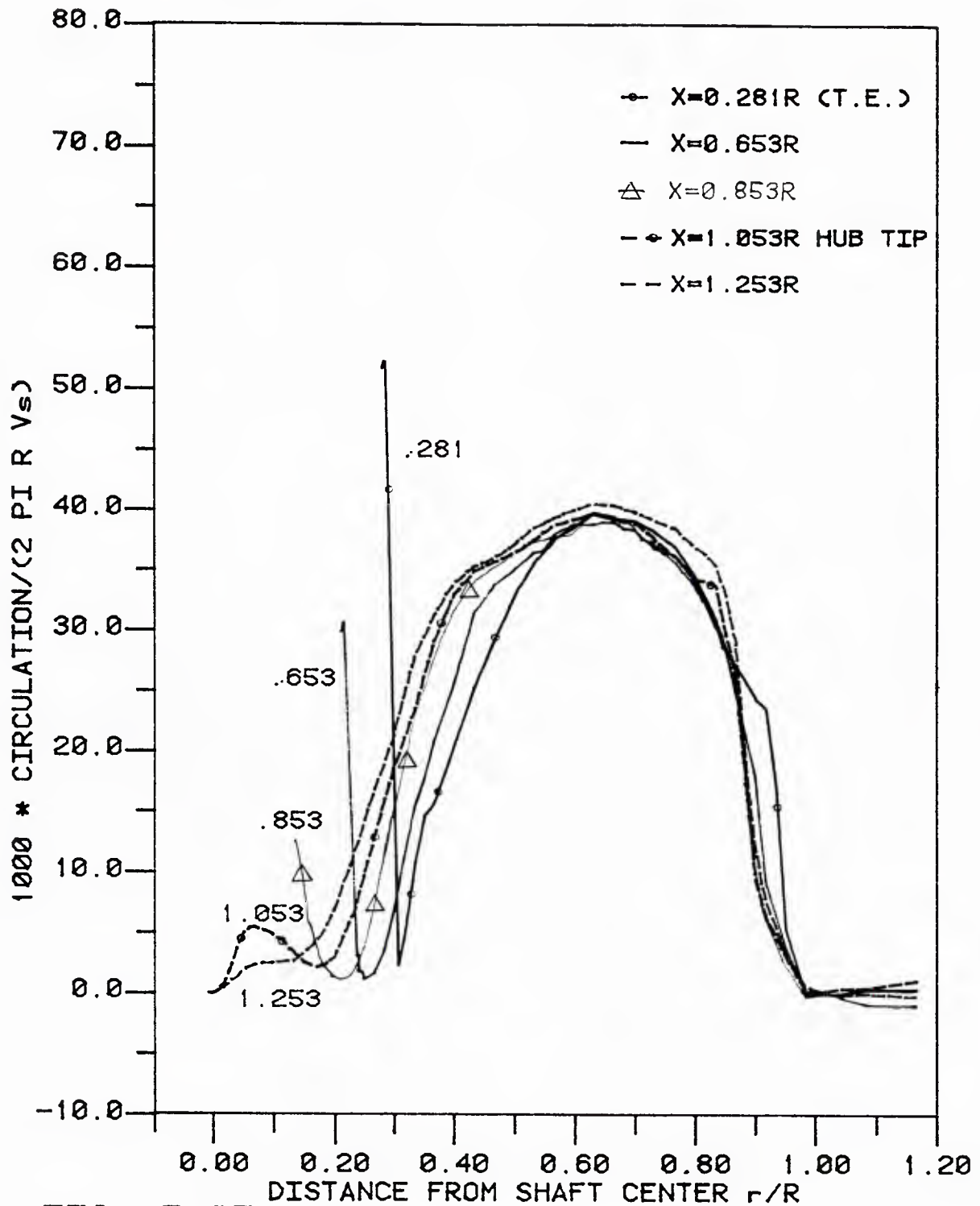
FIG. 5.25
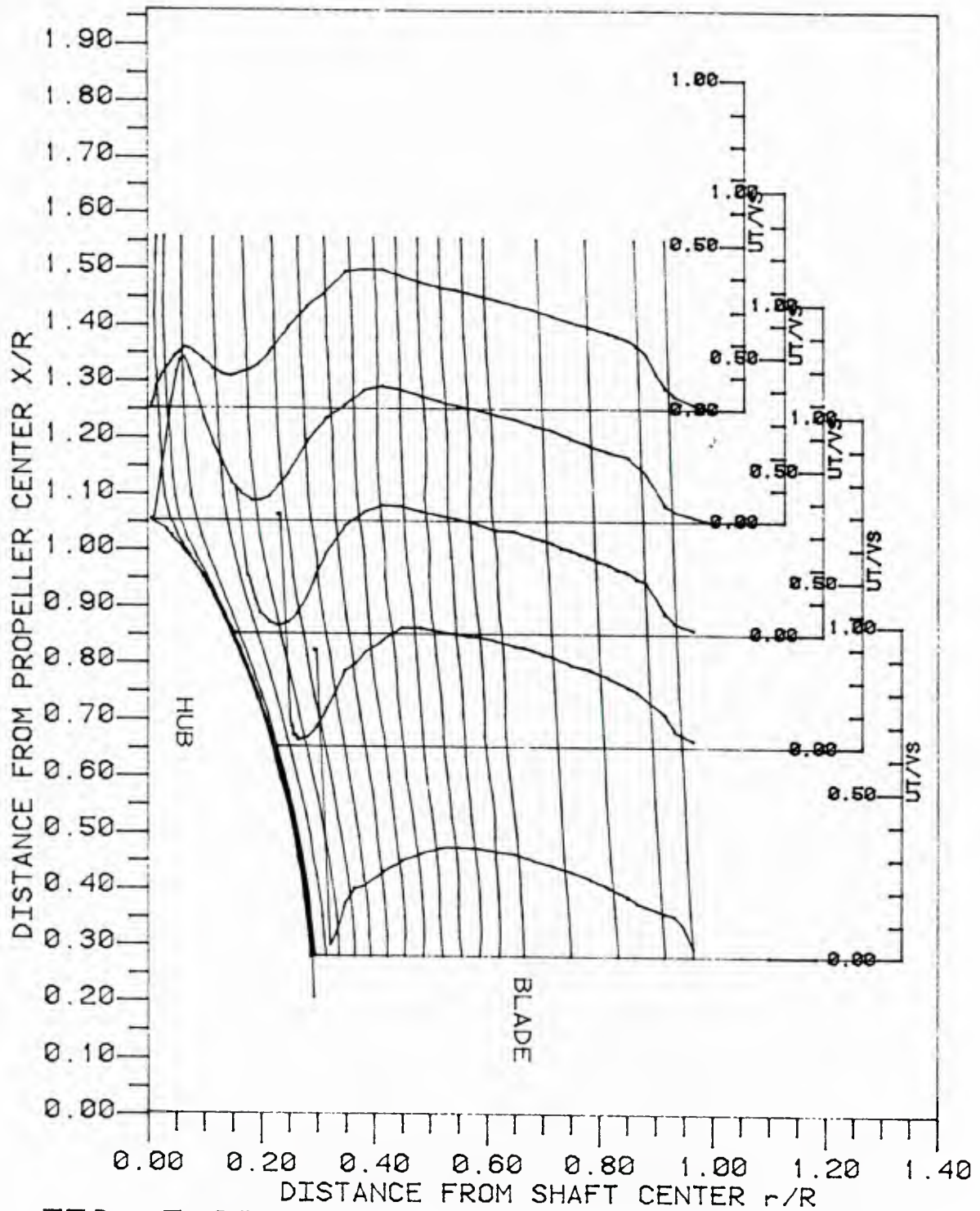CIRCULATION DISTRIBUTION OF
PROPELLER 4660 AT DESIGN J=.976

FIG. 5.26(a)
CIRCUMFERENTIAL MEAN STREAMLINES &
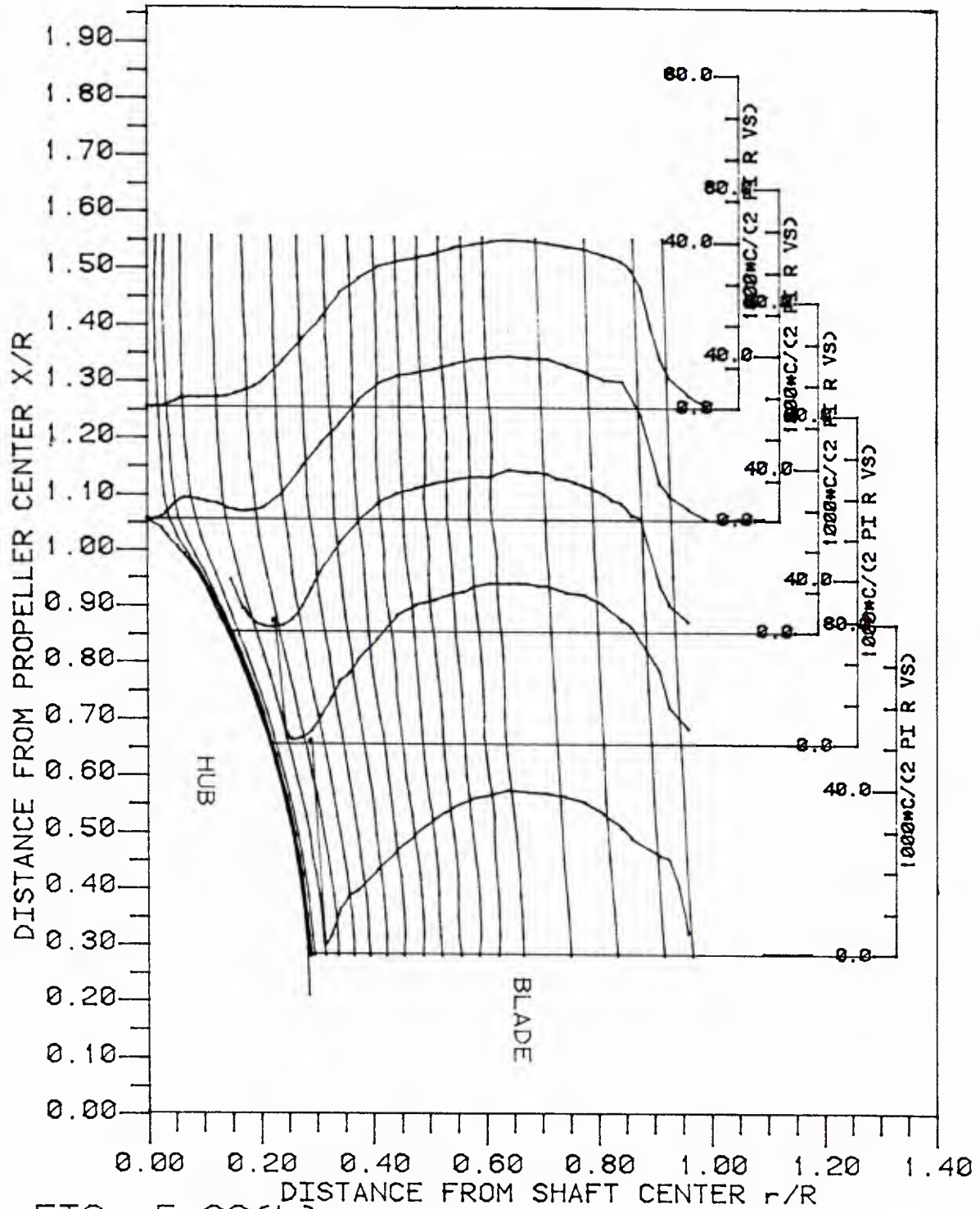TANGENTIAL VELOCITY. P4660,J=0.976

FIG. 5.26(b)
CIRCUMFERENTIAL MEAN STREAMLINES &
CIRCULATION DEFORMATION P4660 J=.976

streamlines in Figure 5.26b were compressed in Figure 5.27 so that the circulation conservation law could be checked more easily. The dotted and dashed lines represent the circulation, while the short solid line represents the change in circulation along the streamlines. The solid line runs from a station near the trailing edge (x = 0.281 R) to a station in the wake (x = 1.253 R). The solid lines were constructed by connecting the raw data without any curve fitting. Circulation is conserved if these solid lines are horizontal. An increase in circulation is seen in the region from r = 0.4 R to r = 0.9 R. A decrease in circulation is seen when r = 0.95 R is reached. An decrease and then increase in circulation is seen in the region between the hub surface and r = 0.4 R. Notice that the velocities at the last station (x = 1.253 R) were the only ones measured using the forward scatter mode, which usually gives larger velocities (see Figure 5.23). Thus, the increase in circulation probably is due to measurement error. Another error may come from the assumption that the vortex sheet follows the mean streamlines. This assumption may be true near the hub region but not in the tip region where the tip vortex contracts more than the mean streamlines. Nevertheless, circulation is, roughly speaking, conserved.

5.7.5 The Circulation of the Hub Vortex

It was determined in the last section that circulation is, roughly speaking, conserved along the mean streamlines. Here, an emphasis will be put on the circulation of the hub vortex and its relationship with the circulation at the hub near the trailing edge. The circulation of the hub vortex is very important in calculating the force on the hub. This will be discussed in Chapter 6.
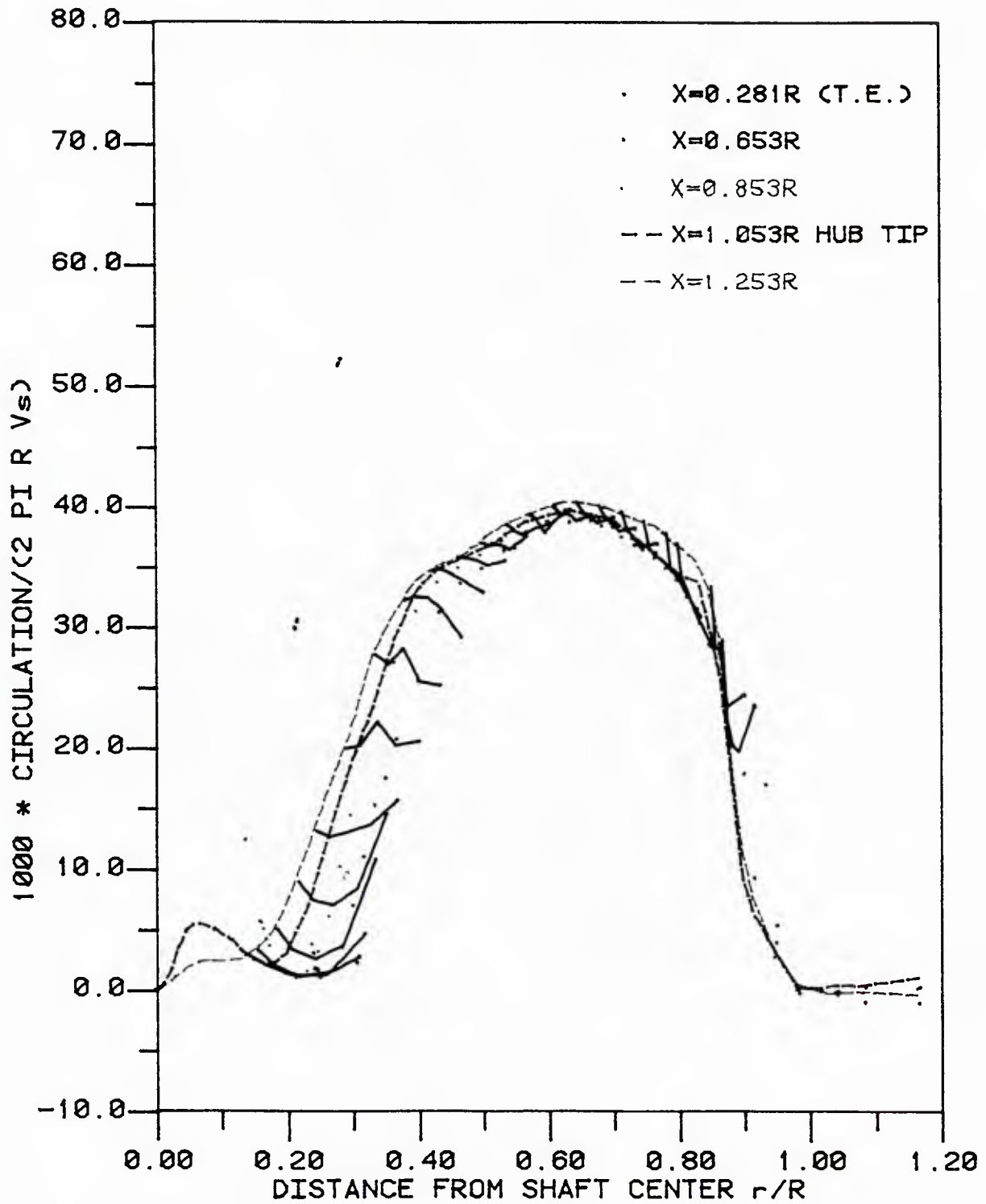
FIG. 5.27
CIRCULATION DEFORMATION OF
PROPELLER 4660 J=0.976

The circulation of the hub vortex depends on the blade geometry, the hub geometry, and the advance coefficient. There were two propellers involved in this study, propellers 4660 and 4498. Propeller 4660 has a lower pitch and lower camber at the root and a larger hub-diameter ratio than propeller 4498. Propeller 4660 has three different fairing lengths, whereas propeller 4498 has only one (see Figures 5.1, 5.2, and 5.3). For propeller 4660, there were two advance coefficients for each of the three different fairings. There were four advance coefficients for propeller 4498. In each case above, there were two tangential velocity measurements along two radial lines. One radial line was in a plane very close to the trailing edge, and the other was in a plane through the hub apex.

In addition, the tangential velocities at 11 stations for propeller 4498, with $J = 0.865$, were measured in order to understand the circulation of a propeller with a heavy load at the root.

Finally, the case of a dummy hub was studied for both propellers. The tangential velocities were measured in the dummy hub apex plane, using the same impeller speeds and the same propeller shaft speeds as in the case of propellers with blades.

5.7.5.A   The Hub Vortex of Propeller 4498

The tangential velocities for propeller 4498, with $J = 0.865$, are shown for 11 stations in Figures 5.28a and 5.28b. The corresponding circulation distributions are shown in Figures 5.29a and 5.29b. It was found that the tangential velocity can again be divided into two regions (recall that the same phenomenon was found for propeller 4660; see section 5.7.3). One region was a potential flow region, and the other was a
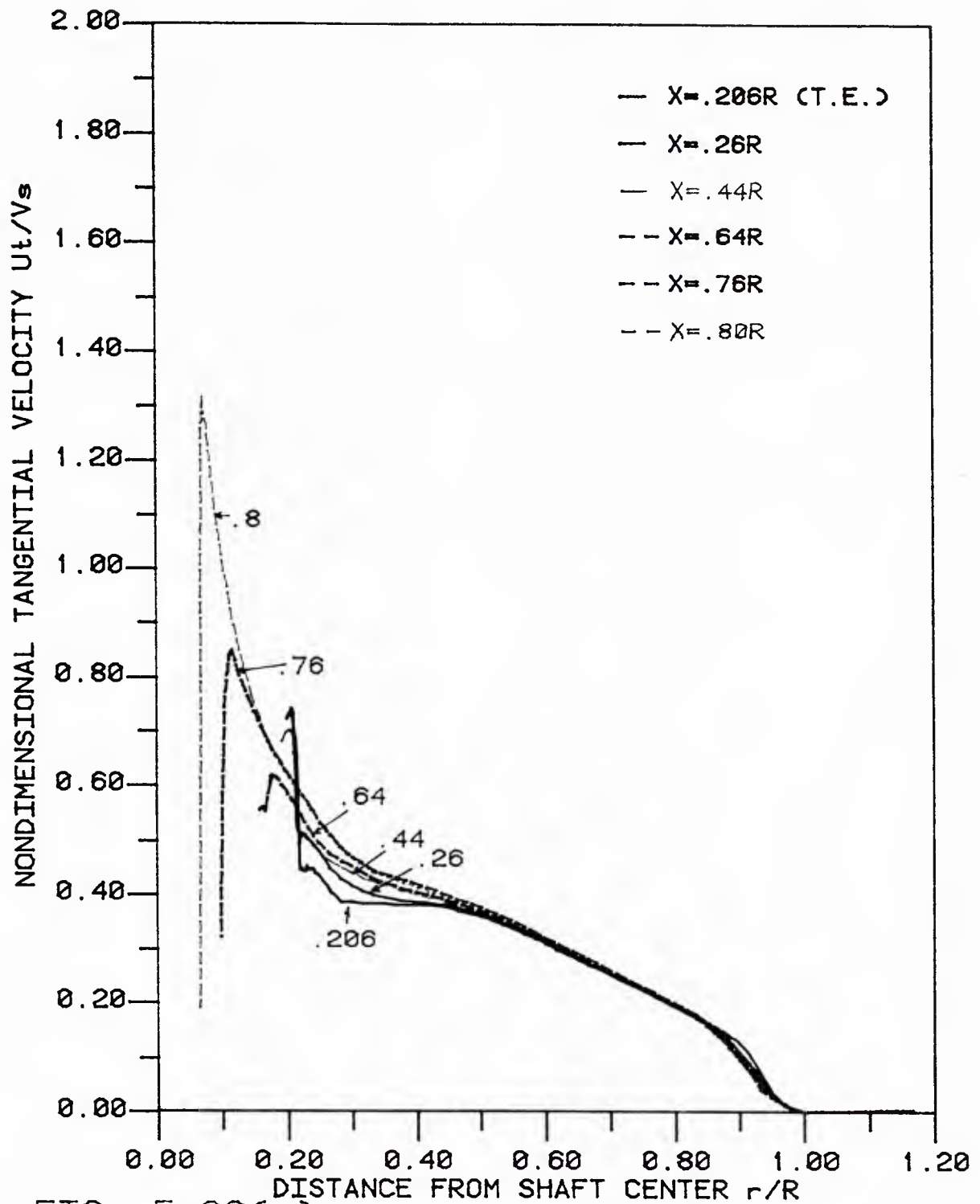
FIG. 5.28(a)
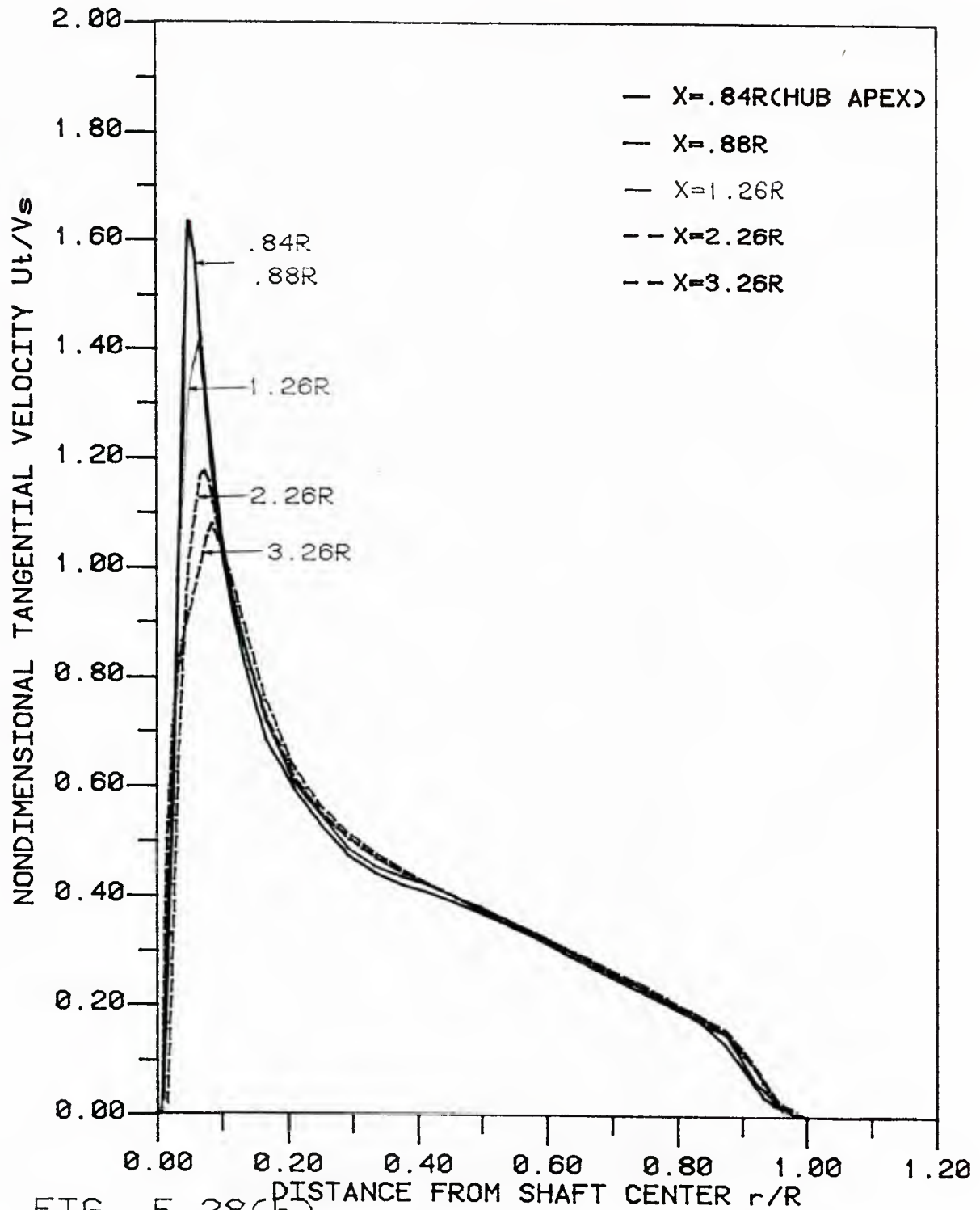CIRCUMFERENTIAL MEAN TANGENTIAL VEL.
IN RADIAL DISTRIBUTION; P4498 J=.865

FIG. 5.28(b)
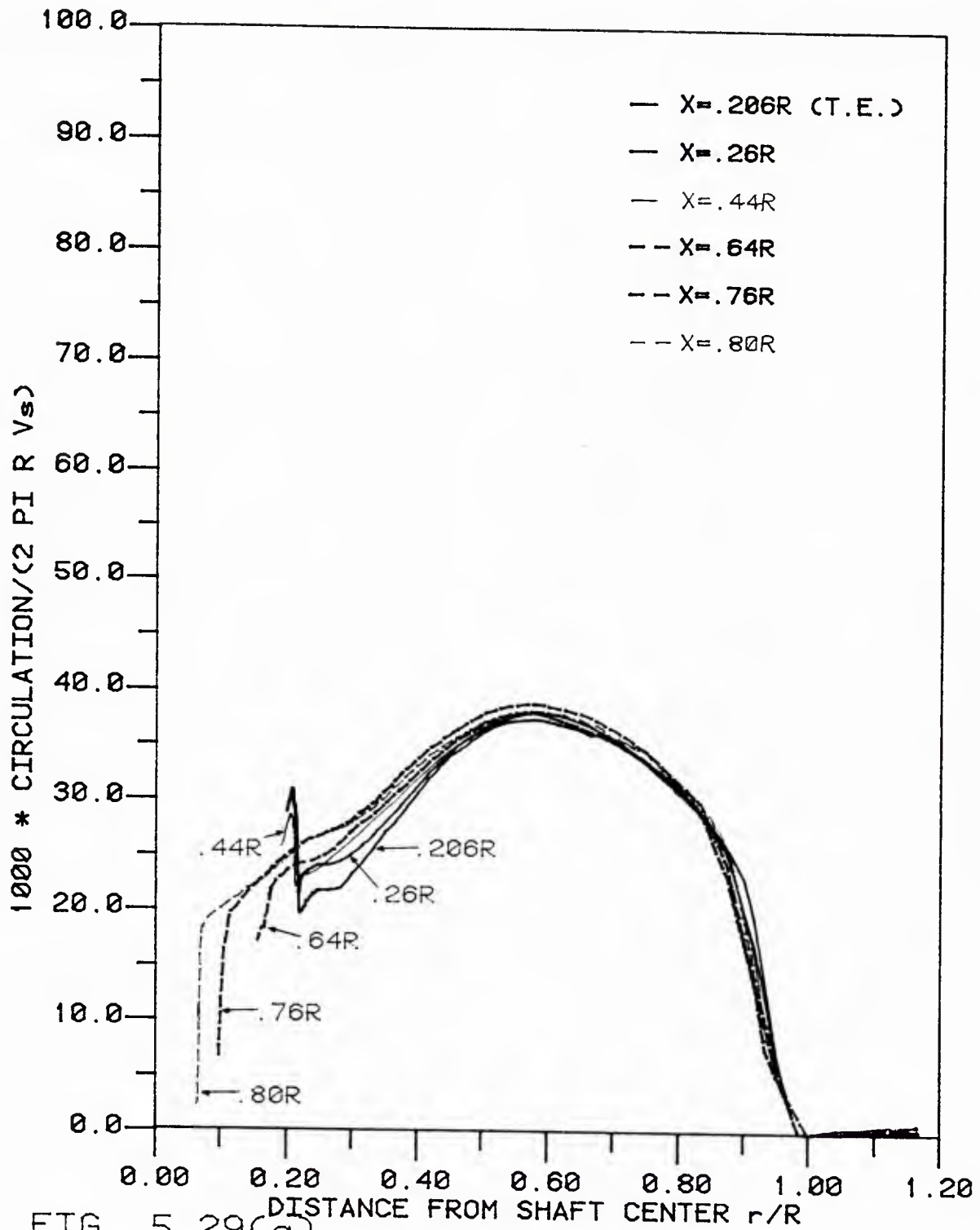CIRCUMFERENTIAL MEAN TANGENTIAL VEL.
IN RADIAL DISTRIBUTION; P4498 J=.865

FIG. 5.29(a)

CIRCULATION DISTRIBUTION OF
PROPELLER 4498 AT J=0.865
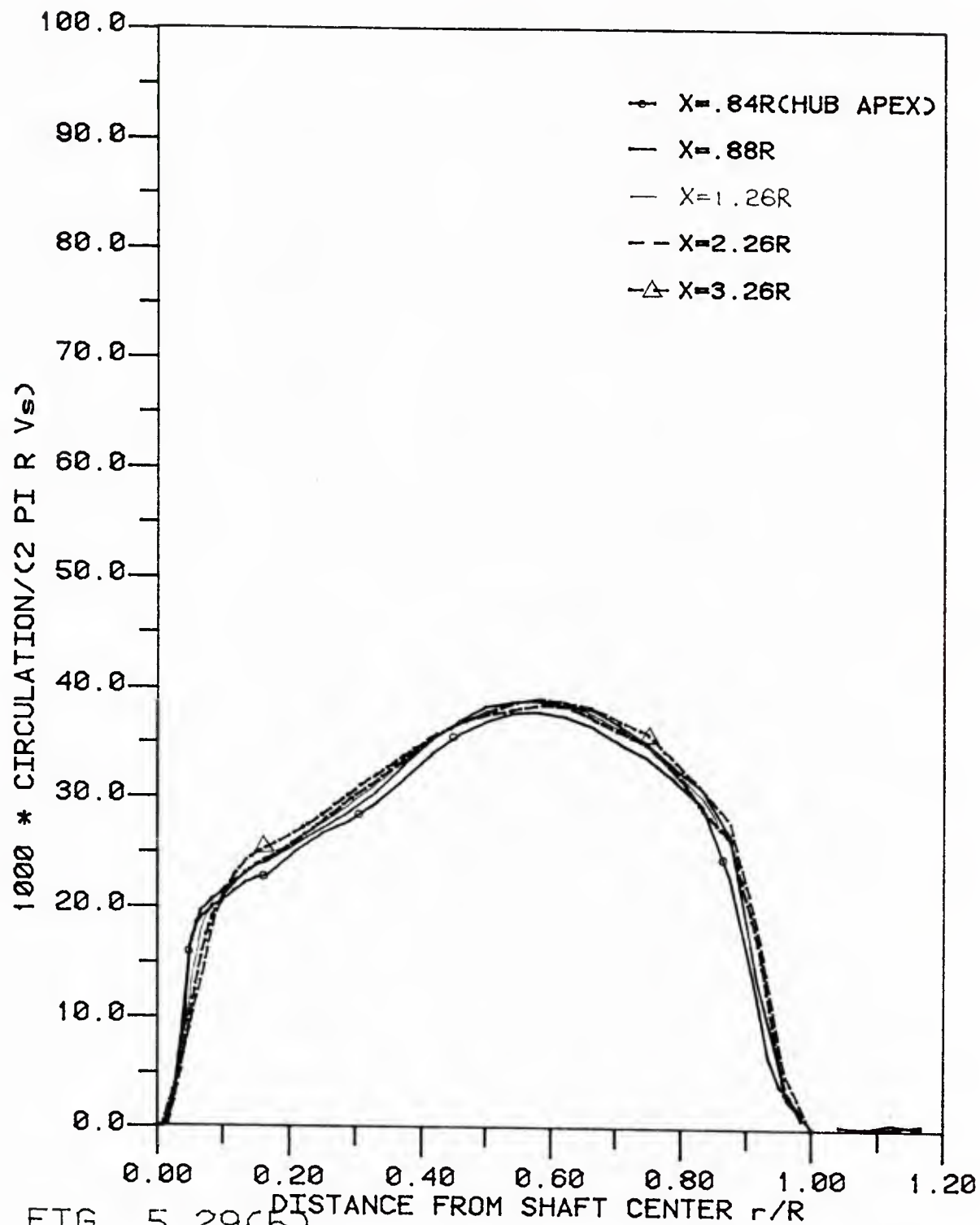
FIG. 5.29(b)
CIRCULATION DISTRIBUTION OF
PROPELLER 4498 AT J=0.865

viscous flow region. The potential flow arose purely due to the blade

loading, whereas the viscous flow was due to the rotating hub. At the

first station, the one closest to the trailing edge, the velocity of

potential flow was lower than the hub surface speed. An acceleration of

tangential velocity by the body was anticipated. This acceleration

continued as the flow moved downstream until the tangential velocity of the

flow equaled the hub surface speed. This may happen because the hub

surface speed decreases linearly with hub radius, whereas the speed of the

fluid particles increases approximately parabolically with hub radius if

the law of conservation of angular momentum holds (see Figure 5.28a).

Beyond the equilibrium station (the one where the tangential velocity of

the flow equals the hub tangential surface speed), the fluid particles were

decelerated by the body until they were beyond the hub apex. Beyond the

hub apex, a strong hub vortex was formed and another effect, which may have

existed weakly upstream, became stronger. This effect was due to the

rolling-up of the vortex sheet into the hub vortex, so that, depending on

how quickly the rolling-up took place, the circulation of the hub vortex

was again increased. The size of the hub vortex became larger, while the

maximum velocity became smaller as the fluid particles moved further

downstream (see Figure 5.28b), although the product of the two (i.e., the

circulation) was still growing because of the rolling-up. It would

eventually decay very far downstream because of viscous dissipation (not

shown in Figure 5.28b).

Table 5.4 shows the tangential velocity v_1 at r_1 and the deformation

of circulation for the 11 stations. A definition of v_1 and r_1 is shown in

Figure 5.30.

Station	x/R	v_1 (ft/sec)	r_1 (in.)	$2\pi v_1 r_1$ (ft²/sec)	
1	0.206*	6.071	1.31	4.164	acceleration
2	0.26	6.501	1.31	4.459	region
3	0.44	7.102	1.26	4.685	
4	0.64	7.951	1.1	4.579	deceleration
5	0.76	11.177	0.7	4.097	region
6	0.80**	17.369	0.42	3.820	
7	0.84**	21.325	0.31	3.461	
8	0.88	21.342	0.31	3.464	rolling-up
9	1.26	18.555	0.37	3.595	region
10	2.26	15.470	0.445	3.605	(increase
11	3.26	14.149	0.51	3.778	again)

Table 5.4   Deformation of the Circulation of Propeller 4498

*Trailing Edge
**Hub Apex
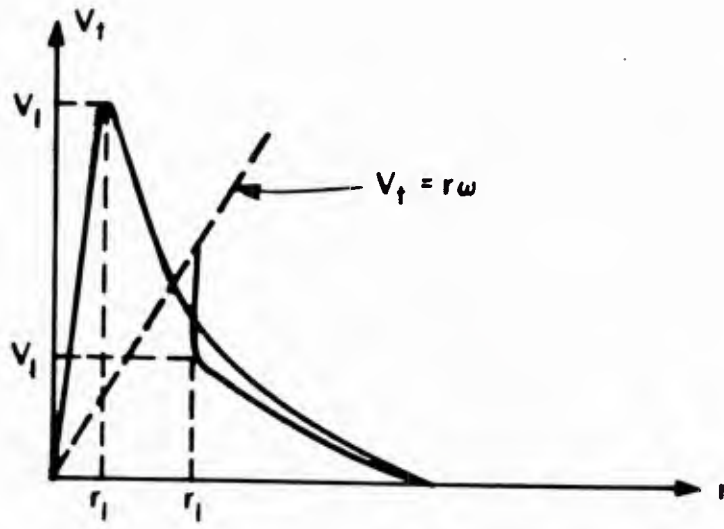
Figure 5.30   Definition of v_1 and r_1

A study of the relationship between the circulation upstream and near the

trailing edge and the circulation in the hub apex plane was carried out for

different advance coefficients.   The results are shown in Figures 5.31a and

5.31b.   The corresponding circulation distributions are shown in Figures

5.32a and 5.32b.   In Figure 5.31b, two curves are missing the peak value of
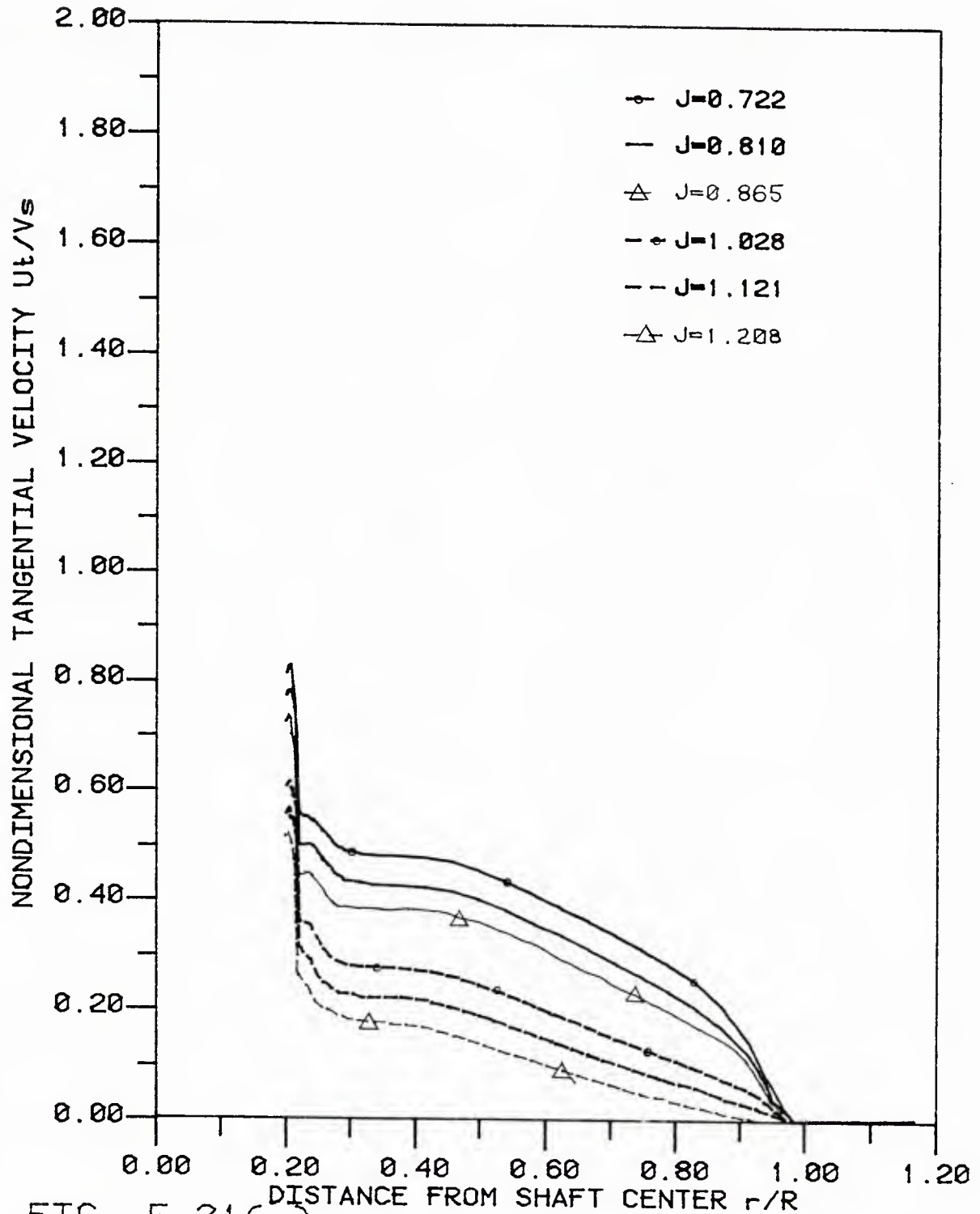
FIG. 5.31(a)
CIRCUMFERENTIAL MEAN TANGENTIAL VEL.
AT DIFFERENT J'S; X=.208R(TE); P4498
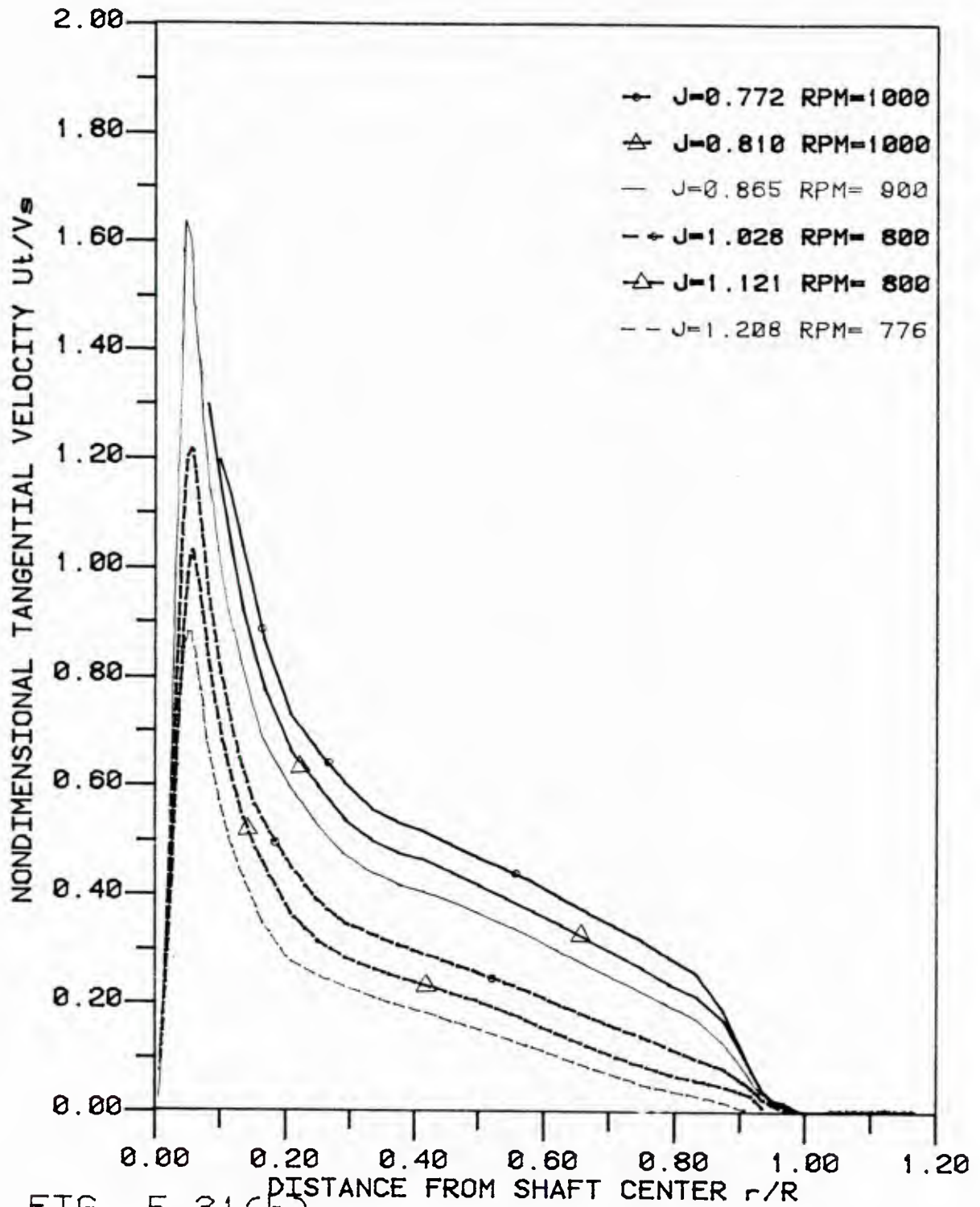
FIG. 5.31(b)
CIRCUMFERENTIAL MEAN TANGENTIAL VEL.
AT DIFFERENT J'S;X=.84R(H.APEX)P4498
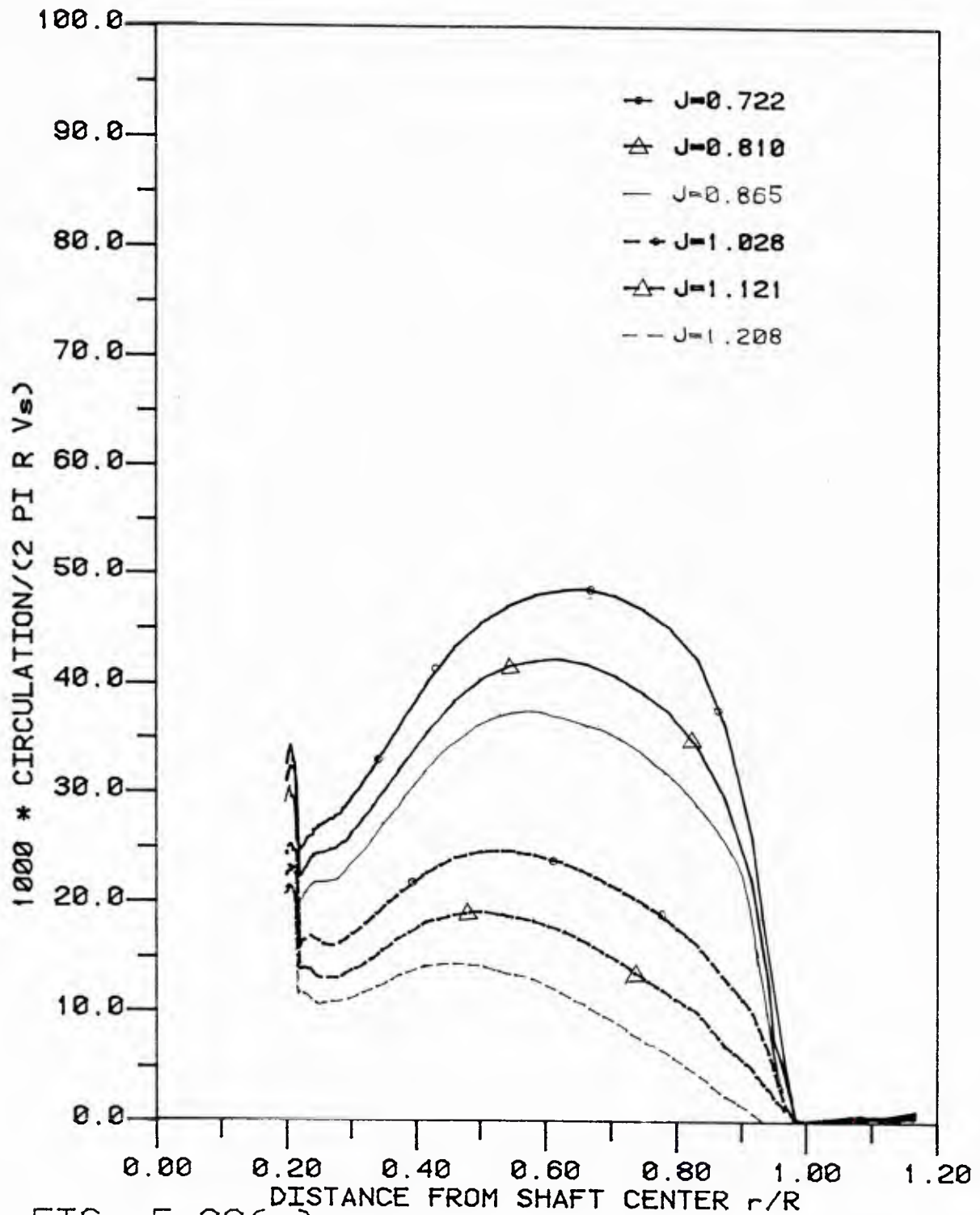
FIG. 5.32(a)
CIRCULATION DISTRIBUTION OF PR4498
AT DIFFERENTIAL J'S; X=.206R (T.E.)
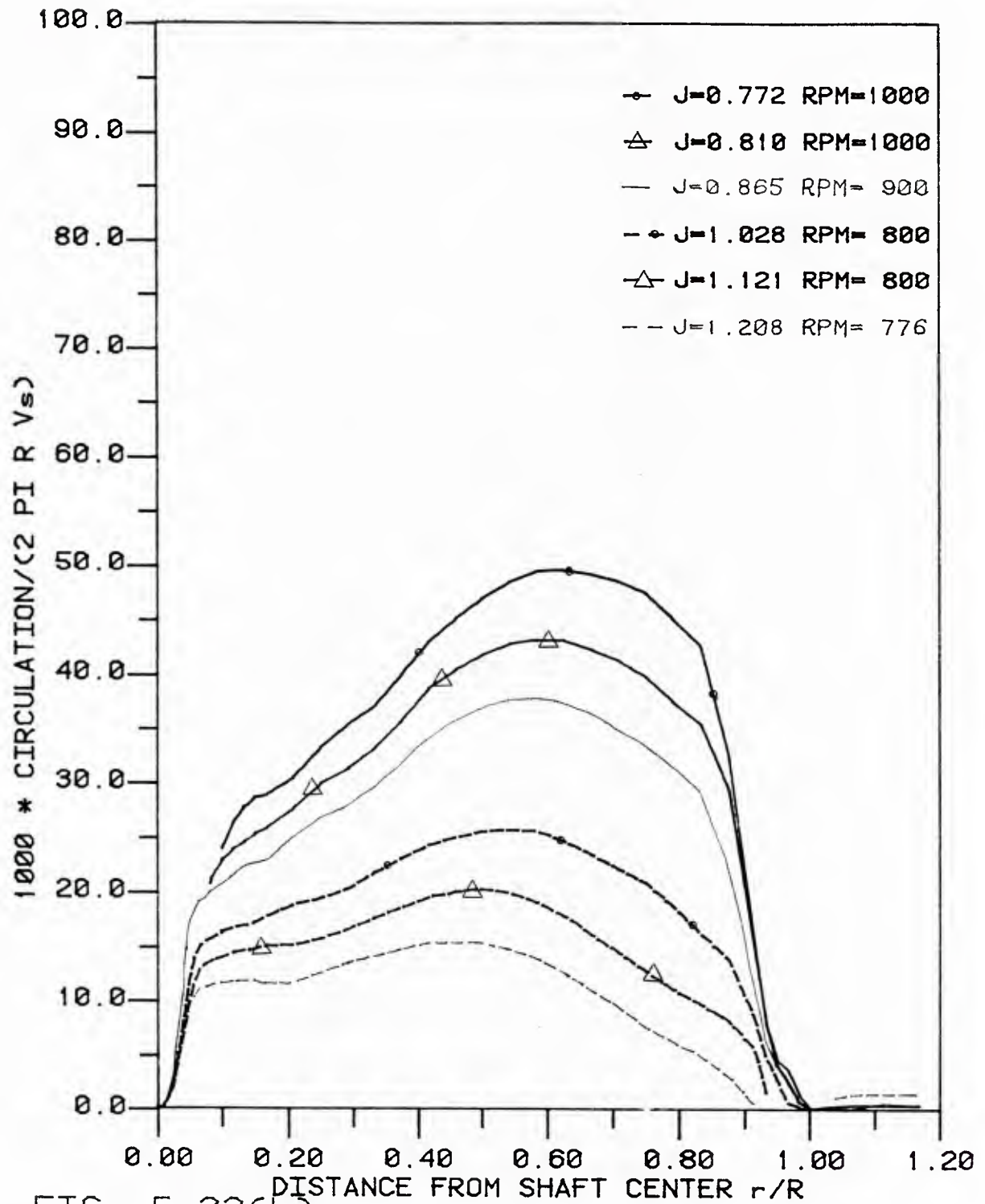
FIG. 5.32(b)
CIRCULATION DISTRIBUTION OF PR4498
AT DIFERENT J'S; X=.84R (HUB APEX)

tangential velocity, because the hub vortex cavity made the LDA measurement impossible. Those two curves were measured at very low advance coefficients. The tangential velocity v_1 at r_1 and the circulation are shown in Table 5.5. The loss of circulation was less than 16%.

| J	Position	v_1/v_s	r_1/R	$\bar{\Gamma}_T{}^*$	Loss of $\bar{\Gamma}_T$	%
1.208	T.E.	0.267	0.223	59.5	6.5	10.9
	Hub Apex	0.930	0.057	53.0		
1.121	T.E.	0.315	0.220	69.3	10.5	15.2
	Hub Apex	1.031	0.057	58.8		
1.028	T.E.	0.366	0.223	81.6	12.2	15.0
	Hub Apex	1.218	0.057	69.4		
0.865	T.E.	0.446	0.218	97.2	14.5	14.9
	Hub Apex	1.590	0.052	82.7		

Table 5.5   Loss of Circulation of the Hub Vortex of Propeller
4498 at Four Different Advance Coefficients
$$* \quad \bar{\Gamma}_T = \frac{1000 \ \Gamma_T}{2\pi R v_s}; \ \Gamma_T \text{ is the total circulation of}$$
all five blades $= 2\pi r_1 v_1$.

The loss of circulation may come from the deceleration of the hub; therefore the tangential velocities for a dummy hub were measured. The tangential velocities at four stations are shown in Figure 5.33. It is seen that a "hub vortex" is generated by a dummy hub at $J = 0.865$. Five additional measurements at different J's were performed and are shown in Figure 5.34. The v_1 and r_1 values as well as the corresponding circulations are shown in Table 5.6.
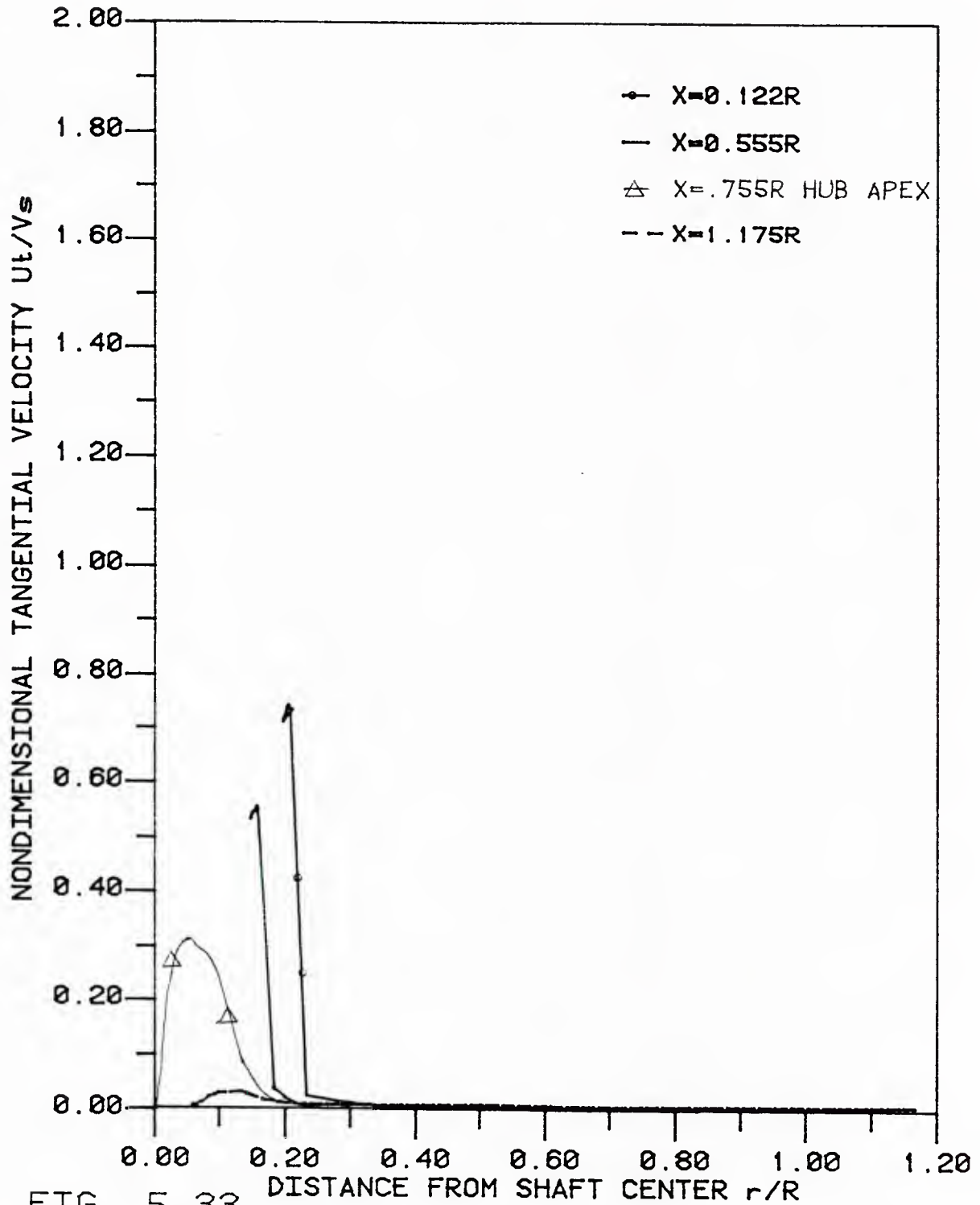
FIG. 5.33
CIRCUMFERENTIAL MEAN TANGENTIAL VEL.
AT DIFFERENT X; DUMMY P4498; J=0.865
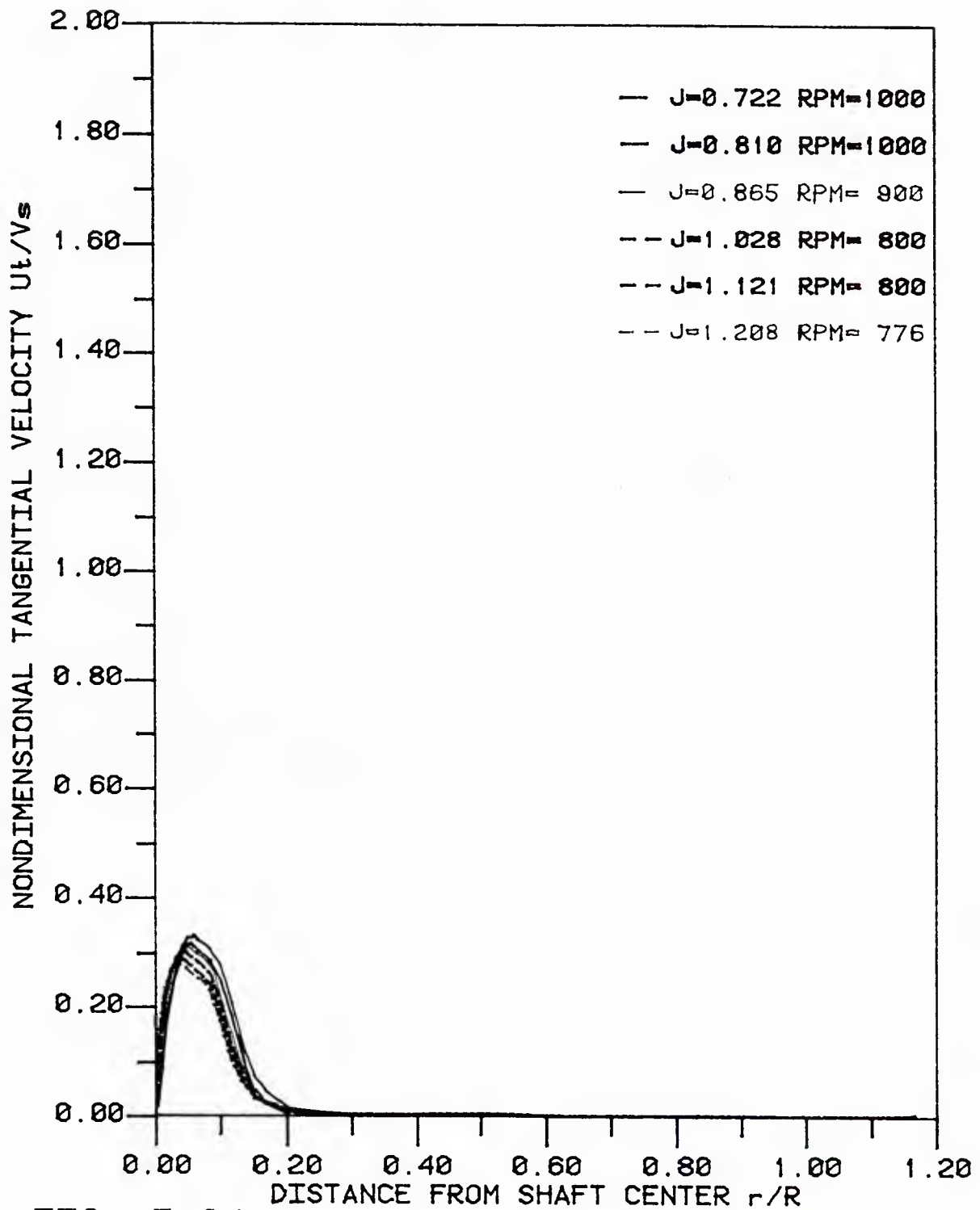
FIG. 5.34
MEAN TANGENTIAL VEL. AT DIFFERENT J;
IN P4498 DUMMY HUB APEX PL. X=.755R

J	v_1/v_s	r_1/R	$\bar{\Gamma}_T$
1.208	0.282	0.037	10.4
1.121	0.290	0.04	11.6
1.028	0.303	0.047	14.2
0.865	0.315	0.05	15.8

Table 5.6 Tangential Velocity and Circulation of the
Dummy Hub of Propeller 4498 in the Hub Apex
Plane for Four Advance Coefficients

It was discovered (see Tables 5.5 and 5.6) that the loss of circulation
going from upstream to downstream was almost identical to the circulation
generated by a dummy hub. This can be explained simply by the concept of
relative motion. In the case of the propeller, the "outer flow" was faster
than the hub surface speed, and the flow speed was reduced by the hub. In
the case of the dummy hub, the "outer flow" had zero tangential velocity,
and the flow speed was accelerated by the surface of the body by almost the
same amount as the reduction in the case of the propeller. More data is
needed to support this explanation; hence, further study of the circulation
deformation using propeller 4660 will be discussed next.

5.7.5.B The Hub Vortex of Propeller 4660

From the previous experiment of section 5.7.3, we know that the
circulation at the root section of propeller 4660 was nearly zero. This
was because the pitch-diameter ratio and the advance coefficient were
nearly identical and the camber was zero, that is, there was almost zero
loading at the root section. If we reduce the advance coefficient, then
the loading will increase and a finite circulation may appear at the root
section, as was the case for propeller 4498. The length effects of

fairings on the hub vortex were also investigated. Three fairings with different lengths, introduced in section 5.3, in combination with two advance coefficients, gave a total of six different cases. For each case, the tangential velocities at the station close to the trailing edge and at the hub apex station were measured. Figure 5.35a shows the tangential velocities near the trailing edge, and Figure 5.35b shows the tangential velocies at the hub apex. The calculation of the change in circulation at the hub, from the trailing edge to the hub apex, is shown in Table 5.7.

J	Hub	Position	v_1/v_s	r_1/R	$\bar{\Gamma}_T$	Change in $\bar{\Gamma}_T$
0.976	Long	T.E.	0.002	0.308	0.6	+ 21
		Hub Apex	0.813	0.027	22	
	Medium	T.E.	0.079	0.308	24	+ 3
		Hub Apex	0.739	0.037	27	
	Short	T.E.	0.038	0.305	12	+ 13
		Hub Apex	0.500	0.05	25	
0.525	Long	T.E.	0.460	0.317	146	- 39
		Hub Apex	2.148	0.05	107	
	Medium	T.E.	0.502	0.317	159	- 31
		Hub Apex	2.557	0.05	128	
	Short	T.E.	0.469	0.325	152	- 39
		Hub Apex	2.629	0.043	113	

Table 5.7 Change in the Circulation of the Hub Vortex of Propeller 4660 with Three Different Hub Lengths and Two Advance Coefficients

The tangential velocity at the hub apex for the dummy hubs of propeller 4660 was measured (Figure 5.36) and the circulation is shown in Table 5.8.
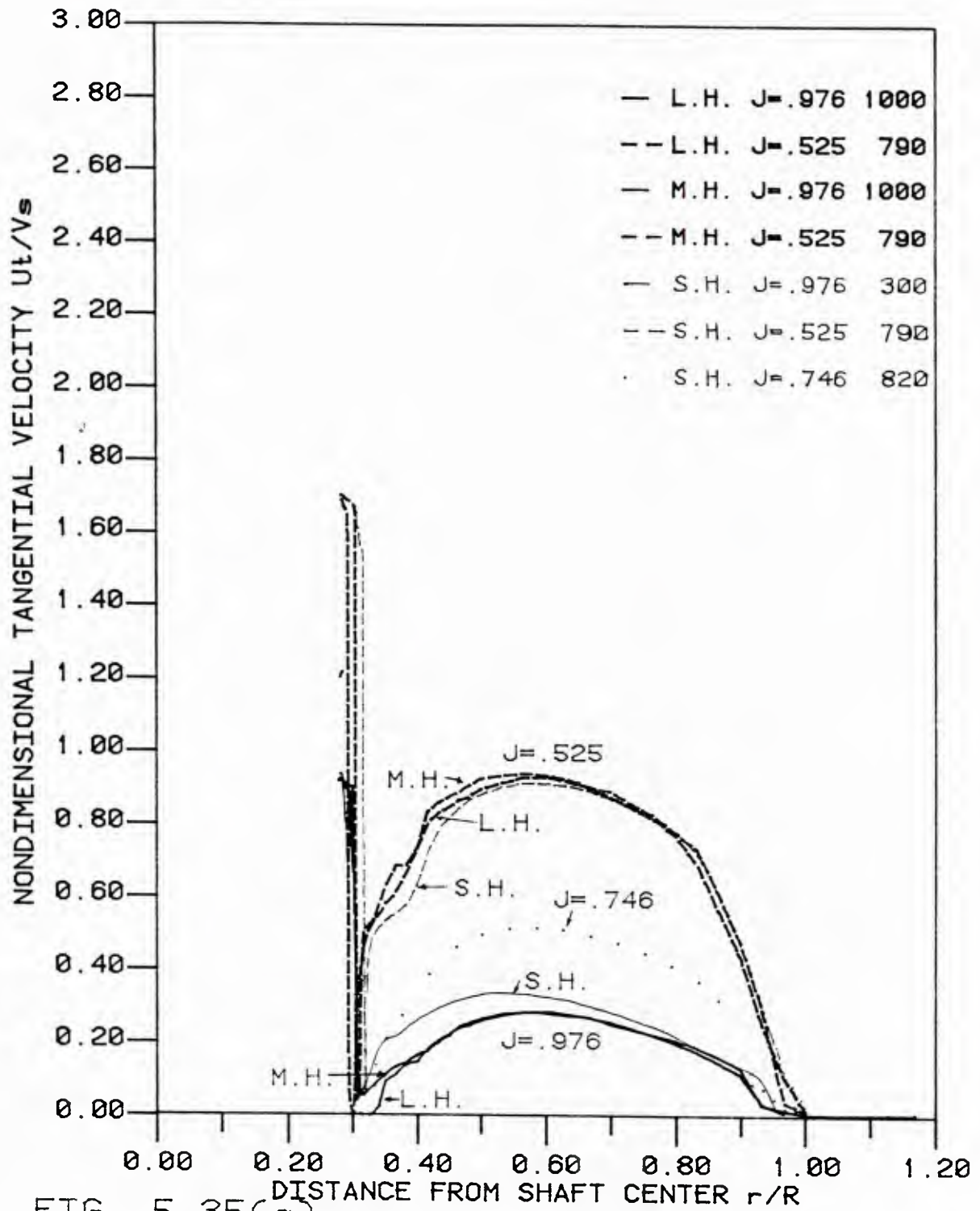
FIG. 5.35(a)
TANGENTIAL VELOCITY NEAR TE. X=.281R
P4660 WITH 2-3 J'S AND 3 HUBS
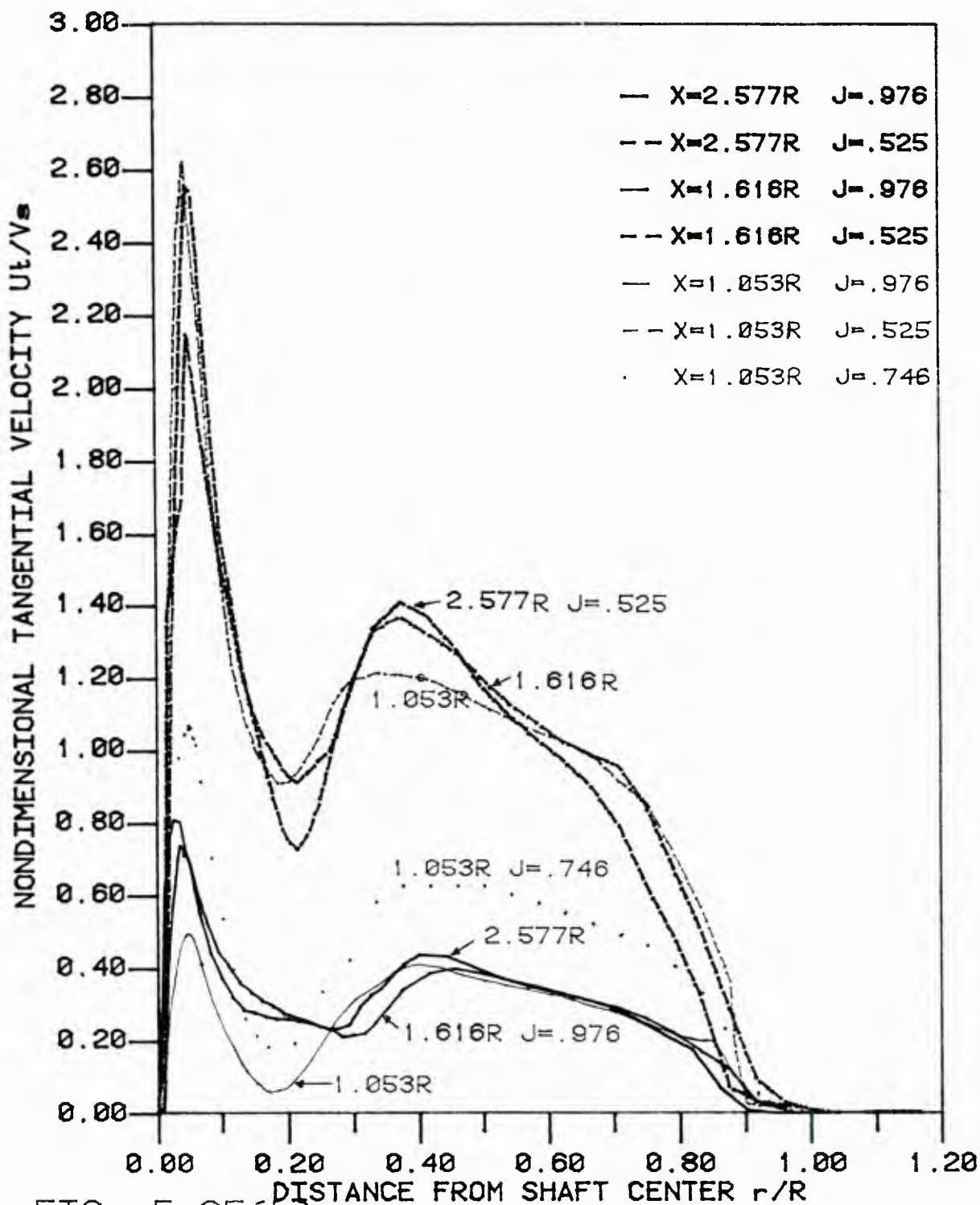
FIG. 5.35(b)
TANGENTIAL VELOCITY AT HUB APEX PL.
P4660 WITH 2-3 J'S AND 3 HUBS
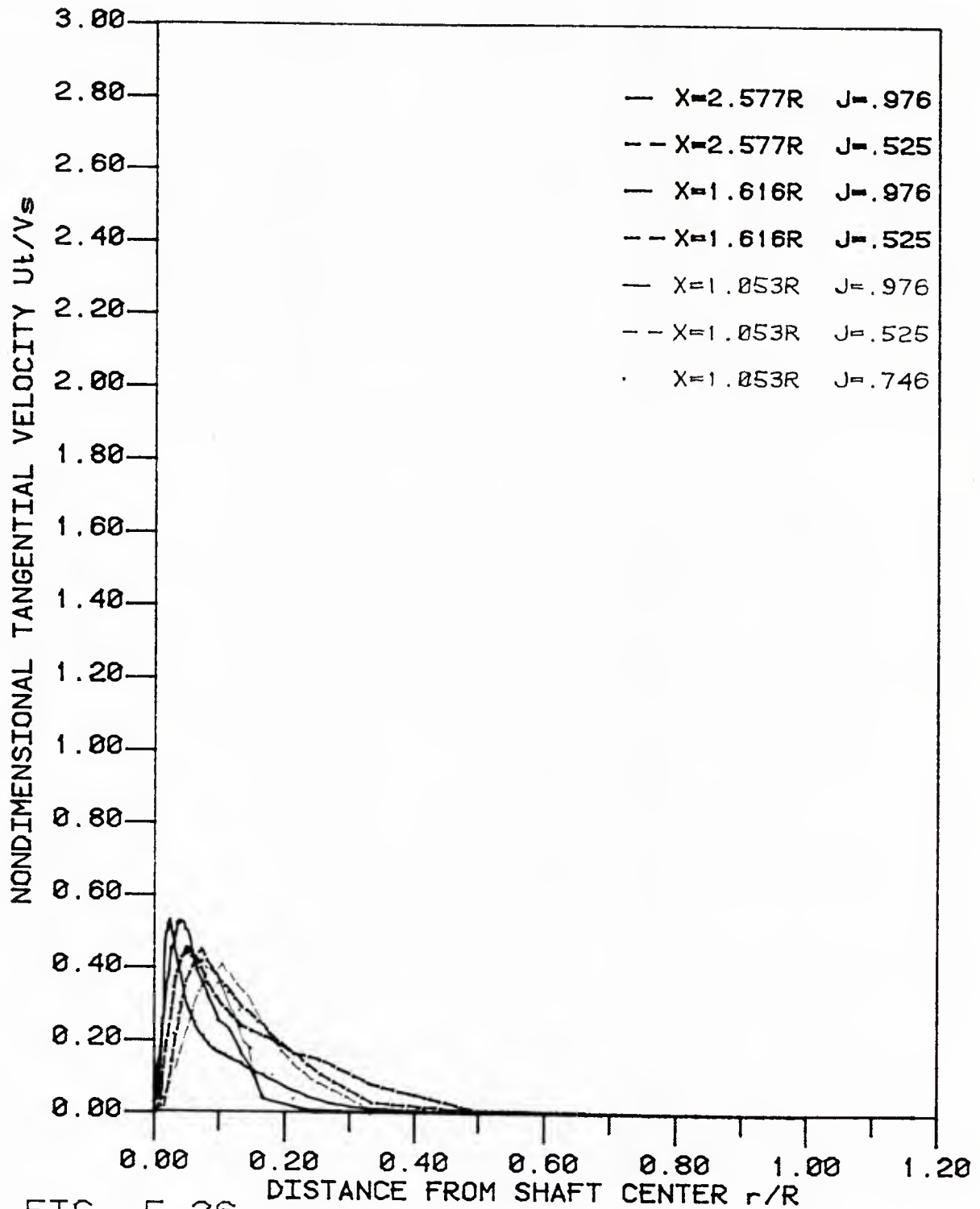
FIG. 5.36
TANGENTIAL VELOCITY AT P4660 DUMMY
HUB APEX PL. ; 2-3 J'S AND 3 HUBS

J	Hub	v_1/v_S	r_1/R	$\bar{\Gamma}_T$
0.976	Long	0.531	0.025	13
	Medium	0.533	0.04	21
	Short	0.459	0.055	25
0.525	Long	0.458	0.05	23
	Medium	0.454	0.073	33
	Short	0.414	0.108	45

Table 5.8   Tangential Velocities and Circulation of
the Dummy Hubs of Propeller 4660 at the Hub
Apex Plane for Two Advance Coefficients

It was found, from Tables 5.7 and 5.8, that the increase in circulation, for the case where J = 0.976, was comparable to the circulation generated by the rotating dummy hubs. This was because the outer flow had almost zero tangential velocity near the hub. Thus, as far as the boundary layer was concerned, it was almost identical to the rotating dummy hub case. In the case where J = 0.525, the situation was opposite. The outer flow had a larger tangential velocity somewhere ahead of the hub apex, so that the flow was decelerated and the circulation was reduced. The reduced amount was almost identical to the circulation generated by the dummy hubs.

5.7.5.C   The Hub Vortex of Propeller 4498 without Fairing

All previous study of the hub vortex has been done using propellers with fairings. Here, a study of propeller 4498 without a fairing is carried out, and special consideration is made of how much loss in the circulation of the hub vortex is due to a blunt hub.

The tangential velocities were measured at three stations: the first very close to the trailing edge, the second at the end of a screw (which

tightens the hub to the shaft) at the hub end on the blunt hub, and the third in the plane where the fairing apex was located. Figure 5.37 shows the tangential velocity distribution. Figure 5.38 shows the corresponding circulation distribution. It shows in Figure 5.37 that the tangential velocities in the trailing edge plane are almost identical to the tangential velocities in the same place when there was a fairing (see Figure 5.28a). The hub vortex at $x = 0.84$ R in Figure 5.37 has a smaller tangential velocity but wider hub vortex core than the hub vortex had when there was a fairing. The circulation of the hub vortex can be calculated and is shown in Table 5.5, as before. It turns out that for the station $x = 0.353$ R (blunt hub end), $v_1/V_S = 1.157$ and $r_1/R = 0.033$; hence $\bar{\Gamma}_T = 38.2$ and there is a 61% loss of circulation. For the station $x = 0.84$ R, $v_1/v_S = 0.841$ and $r_1/R = 0.075$; hence, $\bar{\Gamma}_T = 63.1$ and there is a 35% loss of circulation. The circulation of the hub vortex grows from $x = 0.353$ R to $x = 0.84$ R. This is because at the end of the blunt hub the flow separates and there are two small peaks in addition to a large peak in the tangential velocity distribution. Hence, the circulation contained in the largest peak (the hub vortex) is smaller than the circulation of the hub vortex downstream where the largest peak absorbs the other two small peaks through turbulence.

5.8 Summary

The circulation is, roughly speaking, conserved along the circumferential mean streamlines. The circulation at the hub will increase when the velocity of the outer flow is greater than the hub surface rotation speed, and decrease when it is less. The length of the fairings is relatively unimportant, since the effect of viscosity is relatively small (see Table 5.7).
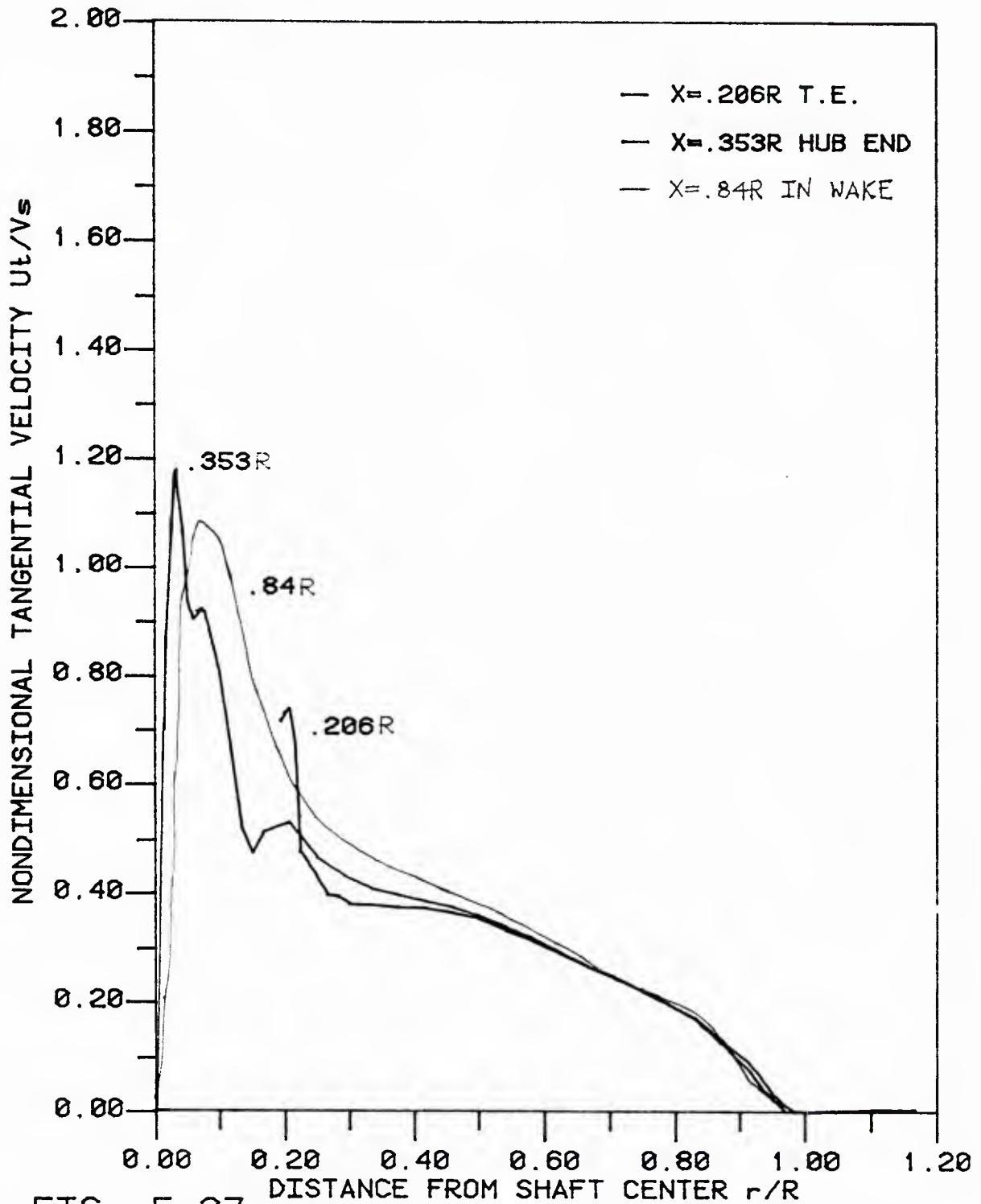
FIG. 5.37
CIRCUMFERENTIAL MEAN TANGENTIAL VEL.
P4498 WITHOUT FAIRWATER; J=0.865
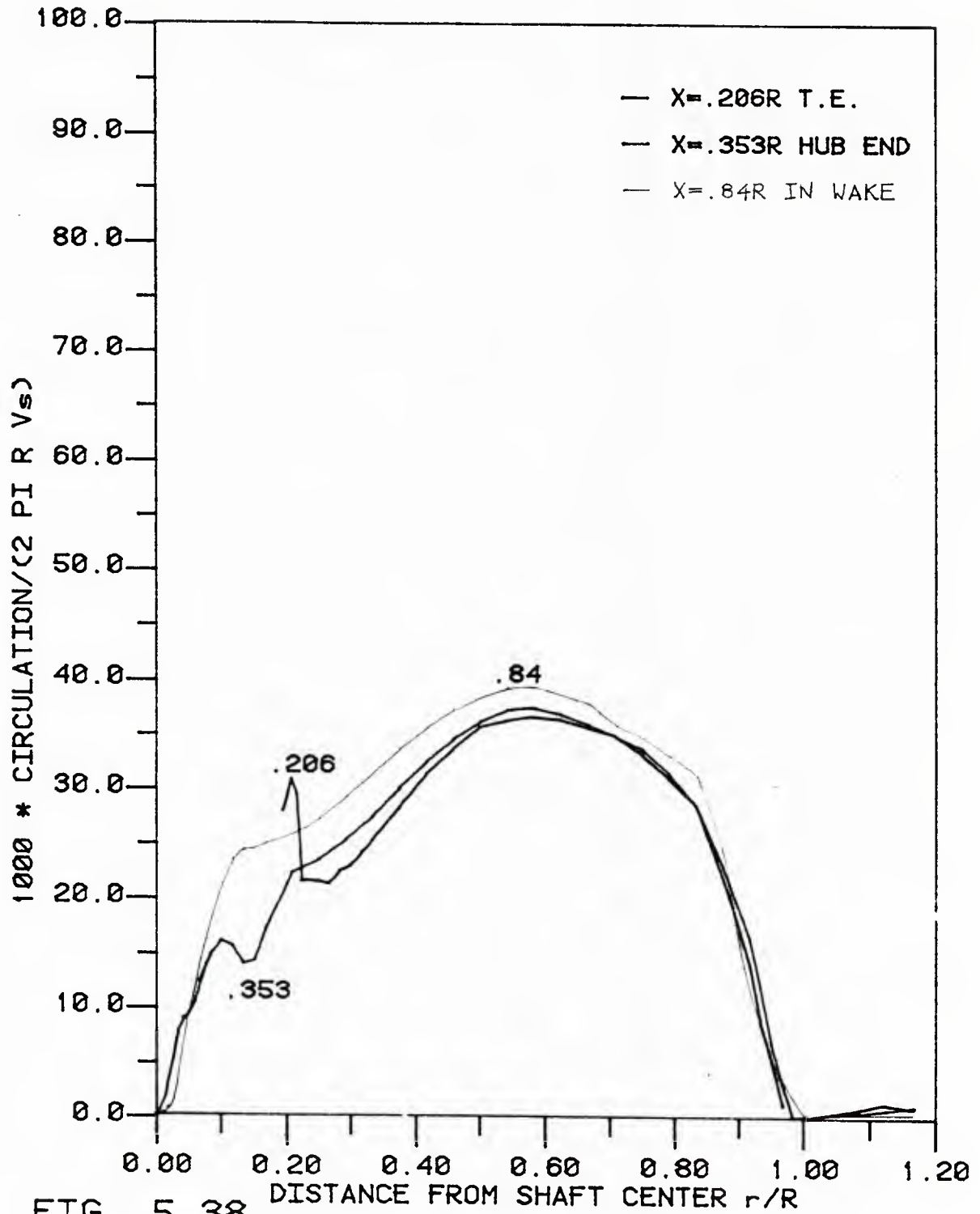
FIG. 5.38

CIRCULATION DISTRIBUTION OF P4498
WITHOUT FAIRWATER; J=0.865

The hub vortex is a Rankine vortex. It is formed in a different way from the tip vortex. The tip vortex is formed by the flow rolling over the blade tip from the high pressure side to the low pressure side, whereas in the root section this rolling-up is prohibited by a solid boundary -- the hub. However, a secondary flow is formed so that the fluid flows from the high pressure side of one blade to the low pressure side of the adjacent blade. Thus, there is not a concentrated hub vortex along the hub surface, only strong trailing vortex sheets (see section 5.6.5). The hub vortex forms when these strong sheets join each other at the hub apex. The size of the hub vortex depends on the viscosity, which is beyond the scope of this thesis. However, the strength of the hub vortex can be estimated. It is related to the circulation at the root section through the circulation conservation law, with a modification due to the concept of relative motion. The circulation at the root is known for the design problem and has been determined in Chapter 4 for the analysis problem. In order to calculate the force on the hub, only the strength of the hub vortex is important. This will be discussed in Chapter 6.

CHAPTER 6

COMPARISON OF NUMERICAL SOLUTIONS WITH EXPERIMENTAL RESULTS

So far, the analysis problem has been solved in Chapter 4 and the results of the experiments have been shown in Chapter 5. Now, a comparison between the numerical solution and the experimental results is possible -- each is necessary in order to verify the other.

There will be two bases for comparison: the circulation distribution and the force. The circulation comparison will be presented in section 6.1, and the force comparison in section 6.2. The two propellers involved in these comparisons are 4498 and 4660.

6.1 Comparison of Circulation Distribution

The analysis problem of propeller 4498 was solved first with a coarse grid on the blades, 8 spanwise and 8 chordwise segments on the key blade, and 8 spanwise and 4 chordwise segments on the other 4 blades. The afterbody of the hub was fitted with a cubic function. The artificial forebody had a length of one propeller radius.

The uniform flow was modified in the same way as in Chapter 3. The advance coefficient was 0.889. The wake alignment was involved in this coarse grid run.

The solution converged in two and a half iterations -- three times for the blade analysis, two times for the wake alignment, and two times for the hub analysis.

Next, a finer grid case was run with 18 spanwise segments and 9 chordwise segments on the key blade, while the other blade retained 8 × 4 grids. The wake geometry was fixed and was the same as the converged wake for the coarser grids. Convergence occurred in four and a half iterations. The forces on the blade and on the hub were calculated afterwards.

In order to see the hub effects, a run without the hub was also carried out by PSF2. The circulation distribution from the present method (PSF2-HUB) and from PSF2 and the actual measurement are presented in Figure 6.1. The predictions by these programs were very close for the outer radii -- the discrepancy between numerical and experimental solutions for any given point could result from experimental error. The circulation predicted by PSF2-HUB was finite at the hub, which agreed with the experimental results, whereas the circulation predicted by PSF2 had a tendency to drop to zero as it approached the hub. This is reasonable, as we expect the circulation to go to zero at the endpoints where there are no solid boundaries. So, for a propeller without a hub the circulation drops to zero at both the tip and the hub. For a propeller with a hub, the circulation may be finite at the hub and zero again at the tip.

The CP propeller 4660, with the short hub, was observed at two advance coefficients. A comparison of the circulation distribution for the two analytical solutions (one with a hub and one without) and the experimental results are shown in Figure 6.2 for $J = 0.976$ and in Figure 6.3 for $J = 0.529$. In the experiment, the propeller speed was 300 rpm and the impeller speed 74 rpm for $J = 0.976$, and 790 rpm and 80 rpm respectively for $J = 0.529$. In the physical model, the inflow was not uniform at the propeller disk because the hub radius was about 0.6" (or 10% of propeller radius) larger than the shaft radius. So, a wake survey was made for the
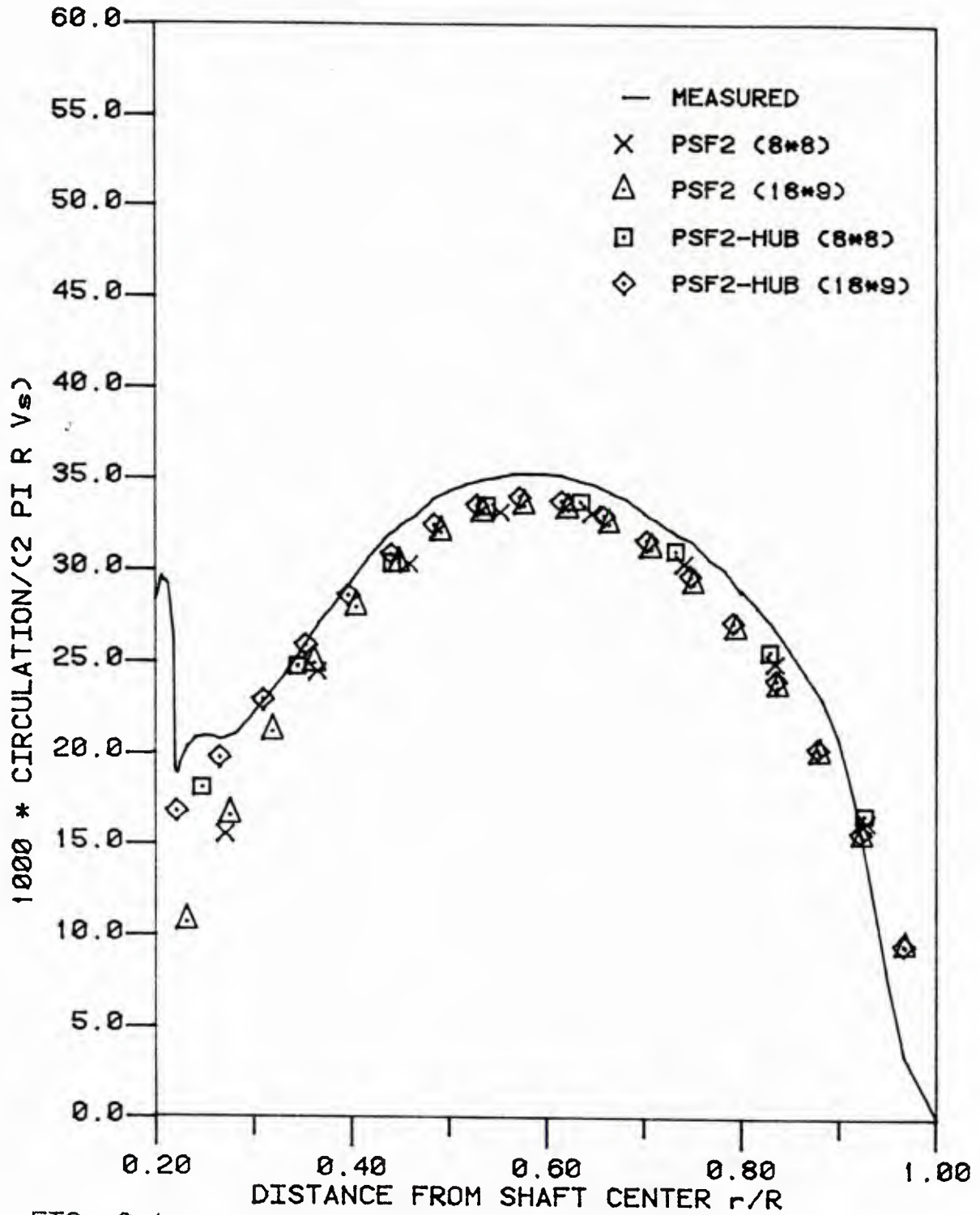
FIG. 6.1
MEASURED AND CALCULATED CIRCULATION
OF PROPELLER 4498 AT DESIGN J=0.889
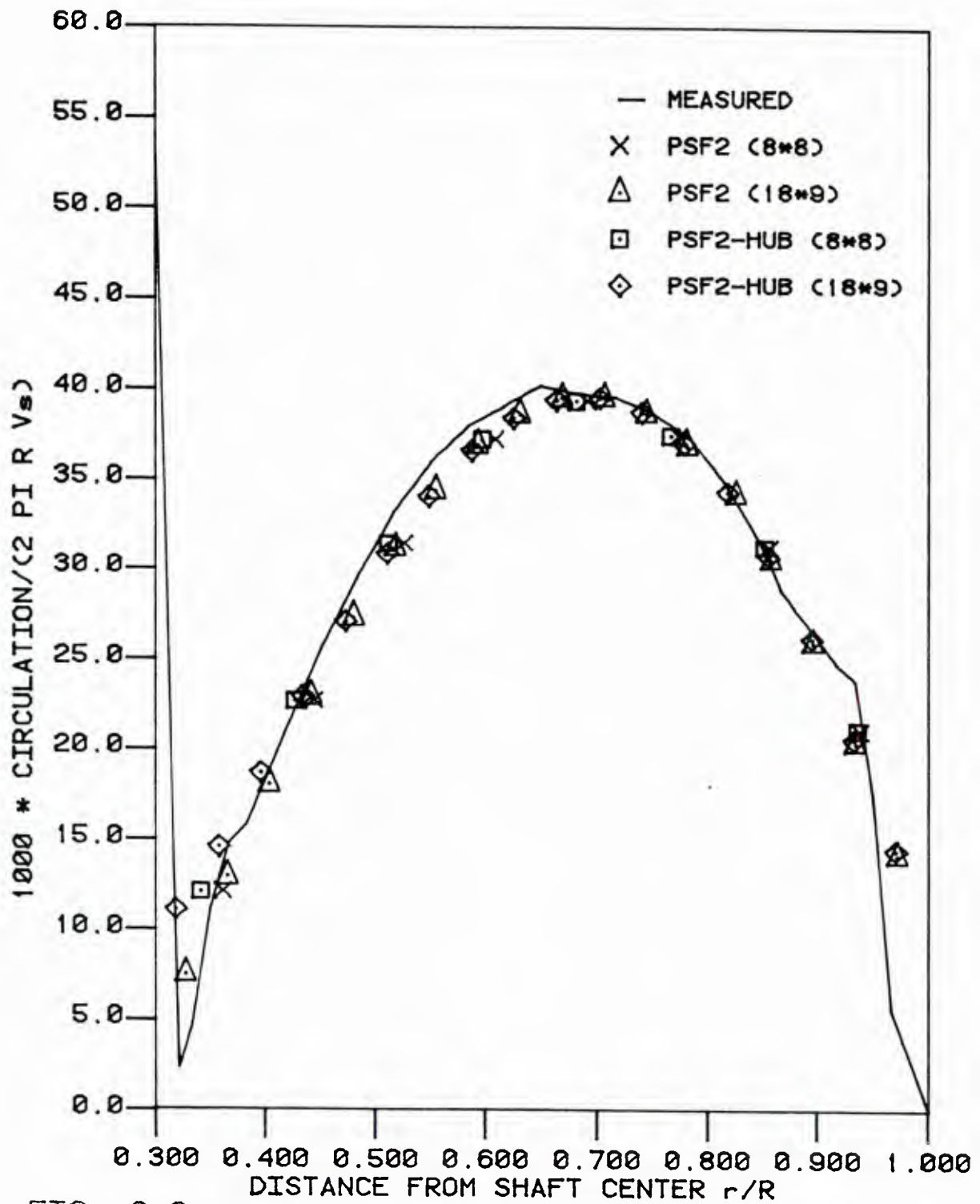
FIG. 6.2
MEASURED AND CALCULATED CIRCULATION
OF PROPELLER 4660 AT J=0.976
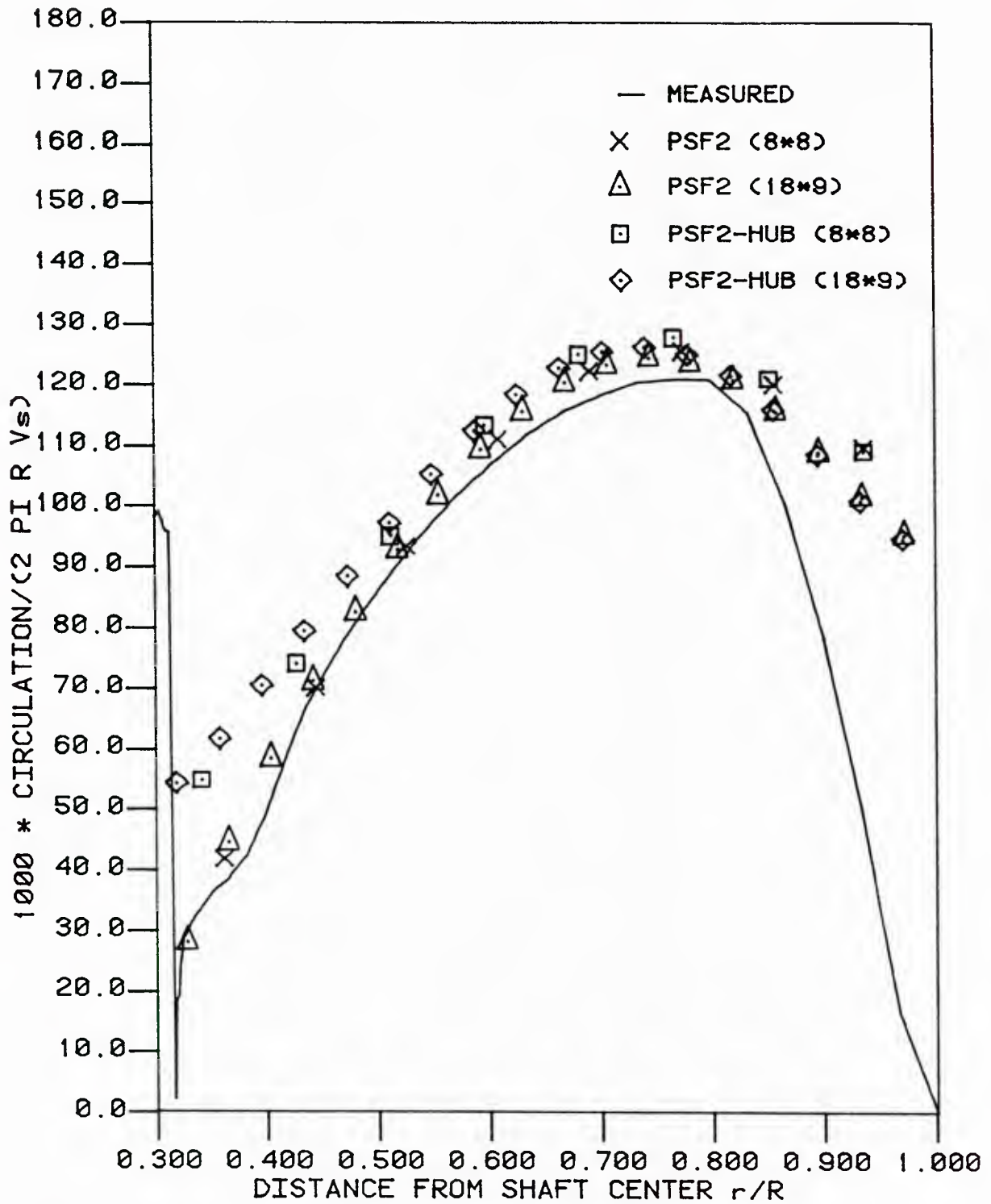
FIG. 6.3
MEASURED AND CALCULATED CIRCULATION
OF PROPELLER 4660 AT J=0.529

dummy hub, and the measured inflow was put into the program PSF2. The measured inflow was further modified before being put into program PSF2-HUB. In Figure 6.2, it can be seen that both analytical solutions are very close to the experimental results except at the hub. Once again, the circulation predicted by PSF2 had a tendency of dropping to zero at the hub. The measured circulation at the hub was finite, although smaller than the prediction by PSF2-HUB.

A question arises: Why did the prediction of PSF2-HUB become less accurate when the propeller was changed from 4498 to 4660? What is the difference between these two propellers? A closer look gives the answer (see photographs of the two propellers in Figures 6.4a and 6.4b). Propeller 4498 is a conventional propeller and has a smaller and simpler fillets than a CP propeller, such as propeller 4660. The blades of propeller 4660 were bolted onto the hub. There was a cutoff at the trailing edge of each blade. These cutoffs were about one fifth of the chord length and allowed fluid to go through from the pressure side to the suction side, just as it does in the tip region. Thus, the circulation, as well as the load, was reduced because of the pressure balance from this leakage. The leakage depended on the details of the attachment between the blades and the hub. The geometry of the hub was simplified for the numerical model. Details, such as bolts, cutoffs, and fillets, were ignored in the numerical model. The blades were modeled as a discretized vortex lattice and source segments over the camber surfaces. This simple model becomes insufficient when dealing with a complicated geometry as in

FIG. 6.4.a A CONVENTIONAL PROPELLER, PROPELLER 4498.

FIG. 6.4.b A CONTROLLABLE PITCH PROPELLER, PROPELLER 4660.

the case of propeller 4660, and high accuracy is not possible. The influence of fillets on wings is important for accuracy [Klein, 1934].

When the advance coefficient was reduced to 0.529, the load was increased, as was the strength of the trailing vortex sheets. Errors may occur in measured data in this flow condition, because the data density was relatively low. This explains the discrepancy between the experimental results and the analytical results in Figure 6.3 It was found that the thrust and torque measured directly by the load cell were almost equal to those given by the analytical solutions (see next section). This meant that the measured circulation was innacurate. If the measured circulation was increased uniformly so that it matched the circulation of the analytical solution at mid-span, then we would find that the circulation measured at the hub was just midway between the two predicted circulations. The overprediction at the root by PSF2-HUB was, once again, due to over-solidity at the hub by the model. The underprediction of the circulation at the root by PSF2 was due to the under-solidity at the hub by PSF2.

6.2 Comparison of Forces

The force on an isolated blades-hub configuration can be divided into two parts, the force on the blades and the force on the hub. Because of the existence of a hub vortex at the hub apex, the force on the hub can be further divided into two parts: the force in the area inside the hub vortex core and the force in the area outside the the hub vortex core. The force on the blades and on the hub outside the hub vortex was calculated in section 3.7.7. The calculation of the force in the area inside the hub vortex core was put off until now because little was known of the structure

of the hub vortex in section 3.7.7. Now, we know from the experiments in Chapter 5 that the hub vortex has a universal structure -- a Rankine type vortex. The force in the area inside this hub vortex can be calculated as follows.

Suppose there is a hub vortex core with strength Γ_0 and radius r_0 at the hub apex and extending an infinite distance in the downstream direction, as shown in Figure 6.5a. Also, assume that the vortex is a Rankine vortex.
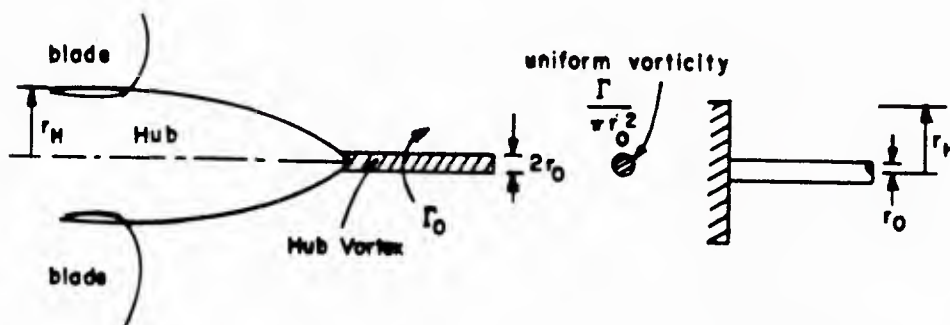
Fig. 6.5a Hub and Semi-Infinite. Long Hub Vortex

Fig. 6.5b Simplied Hub and Semi-Infinite Long Hub Vortex

For an infinitely long Rankine vortex, the velocity distribution $v_t(r)$ is [Milne-Thomson, 1969]:

$$v_t(r) = \begin{cases} \dfrac{\Gamma_0}{2\pi r_0^2}\, r & r \leq r_0 \qquad\qquad (6.1.a) \\[3ex] \dfrac{\Gamma_0}{2\pi}\,\dfrac{1}{r} & r \geq r_0 \qquad\qquad (6.1.b) \end{cases}$$

And the circulation distribution $\Gamma(r)$ is:

$$\Gamma(r) = \begin{cases} \dfrac{\Gamma_0}{r_0^2}\, r^2 & r \leq r_0 \\[2em] \Gamma_0 & r \geq r_0 \end{cases} \qquad (6.2)$$

The equation of motion [Batchelor, 1967] is:

$$\frac{1}{\rho}\frac{dp}{dr} = \frac{v_t^2}{r} \qquad (6.3)$$

The dynamic boundary condition is:

$$p \to p_\infty \quad \text{as} \quad r \to \infty \qquad (6.4)$$

and the pressure is continuous at $r = r_0$.

Integrate (6.3) with v_t replaced by (6.1.a), obtaining:

$$p = \frac{\rho\Gamma_0^2}{8\pi^2 r_0^4}\, r^2 + p_0 \qquad r \leq r_0 \qquad (6.5)$$

where p_0 is the pressure at $r = 0$.

Integrate (6.3) again, with v_t replaced by (6.1.b), and invoke (6.4), obtaining:

$$p = p_\infty - \frac{\rho\Gamma_0^2}{8\pi^2}\frac{1}{r^2} \qquad r \geq r_0 \qquad (6.6)$$

The pressure is continuous at $r = r_0$ -- thus, from (6.5) and (6.6):

$$p_0 = p_\infty - \frac{\rho \Gamma_0^2}{4\pi^2 r_0^2} \tag{6.7}$$

This is the minimum pressure. The pressure coefficient C_p is:

$$C_p \equiv \frac{p - p_\infty}{\frac{1}{2}\rho v_\infty^2} = \begin{cases} - \left[\dfrac{\Gamma_0}{2\pi r v_\infty} \right]^2 & r \geq r_0 \\[2em] \left[\dfrac{\Gamma_0}{2\pi r_0 v_\infty} \right]^2 \left[\left[\dfrac{r}{r_0} \right]^2 - 2 \right] & r \leq r_0 \end{cases} \tag{6.8}$$

where v_∞ is the velocity at $r = \infty$. v_t, Γ, and C_p are plotted in Figure 6.6. Cavitation begins when p_0 equals p_v, the vapor pressure, and:

$$r_0 = \frac{\Gamma_0}{2\pi} \left[\frac{\rho}{p_\infty - p_v} \right]^{1/2} \tag{6.9}$$

Now the force, F_I, inside the hub vortex core is:

$$F_I = \int_0^{r_0} 2\pi(p - p_\infty) r\, dr \tag{6.10}$$

Substituting (6.5) and (6.7) into (6.10), we obtain:

$$F_I = - \frac{3}{16} \frac{\rho}{\pi} \Gamma_0^2 \tag{6.11}$$

Rankine Vortex

$$\Gamma_0 = 2\pi r_0 V_0$$

$$-\frac{1}{2}\left(\frac{\Gamma_0}{\pi r_0 V_\infty}\right)^2$$
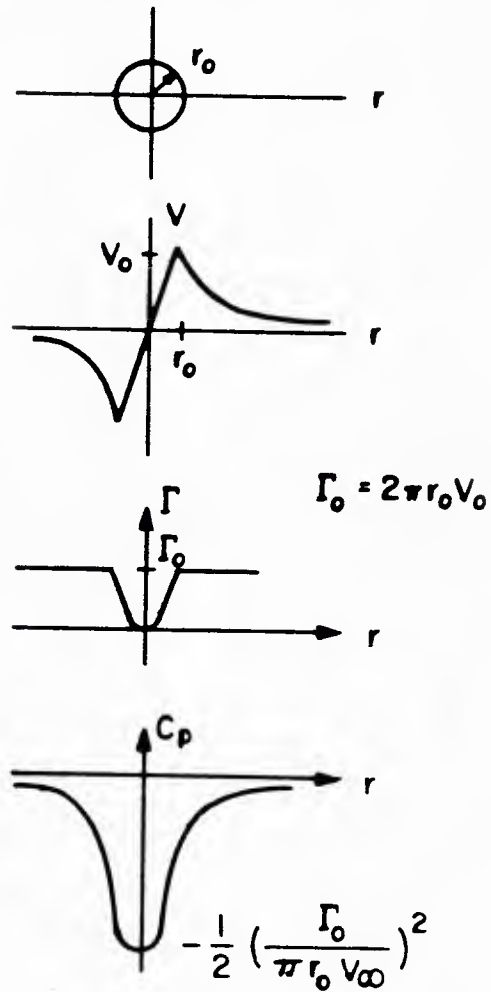
FIG. 6.6 VELOCITY, CIRCULATION AND PRESSURE
COEFFICIENT DISTRIBUTION OF A RANKINE VORTEX.

Notice that the force inside the hub vortex core only depends on Γ_0. The force on the hub, induced by a semi-infinite hub vortex, in the area outside the hub vortex core is bounded by the force F_e on an annulus between r_H, the hub radius, and r_0 (see Figure 6.5.b):

$$F_e = \int_{r_0}^{r_H} 2\pi(p - p_\infty)r\,dr \qquad (6.12)$$

The velocity induced by a semi-infinite vortex is one-half of (6.1.b) and the pressure becomes:

$$p = p_\infty - \frac{\rho\Gamma_0^2}{32\pi^2}\frac{1}{r^2} \qquad r \geq r_0 \qquad (6.13)$$

From (6.12) and (6.13):

$$F_e = -\frac{\rho\Gamma_0^2}{16\pi}\ln\frac{r_H}{r_0} \qquad (6.14)$$

The ratio of F_e to F_I is:

$$\frac{F_e}{F_I} = \frac{1}{3}\ln\frac{r_H}{r_0} \qquad (6.15)$$

So, Fe will be smaller than F_I if r_0 is greater than e^{-3} r_H, or 0.05 r_H. In other words, F_e will be smaller than F_I if r_0 is smaller than 0.015 R of a propeller of 30% hub and 0.01 R of a propeller of 20% hub. These upper bound limits are useful. In the numerical model, the last control point is

at the middle of the last vortex ring and the hub apex. The position of the vortex ring is controlled by the trailing vortex sheet. In other words, there is no freedom to choose the last control point arbitrarily close to the hub vortex. This may underestimate the force outside the hub vortex core. However, the upper bound value of F_e tells us the error from this model would be on the order of F_I, because the size of r_0 is usually greater than two percent of the propeller radius, from experimental data (see section 5.7.5).

In order to compare the force on the hub with the force on the blades, several nondimensional force coefficients are defined. F_I and F_e are nondimensionalized with respect to $\rho n^2 D^4$ just as the thrust T was:

$$K_{F_I} \equiv \frac{F_I}{\rho n^2 D^4} = -\frac{3}{64\pi} \left[\frac{J\Gamma_0}{RV_s} \right]^2 \tag{6.16}$$

$$K_{F_e} \equiv \frac{F_e}{\rho n^2 D^4} = -\frac{1}{64\pi} \left[\frac{J\Gamma_0}{RV_s} \right]^2 \ln \frac{r_H}{r_0} \tag{6.17}$$

The force on the hub calculated by the program PSF2-HUB is called F_E, which is also nondimensionalized with respect to $\rho n^2 D^4$ and is called K_{F_E}.

The force coefficients calculated by the program PSF2, PSF2-HUB, and measured from experiment are shown in Table 6.1.

In Table 6.1, K_T is the force on the blades, K_{F_E} is the force on the hub outside the hub vortex core. K_{F_e} is the upper bound force by (6.17), and K_{F_I} is the force inside the hub vortex core by (6.16). The values of Γ_0 and r_0 are measured. $(K_T)_{net}$ is the summation of K_T, K_{F_E}, and K_{F_I}.

Propeller	J	Method	K_T	K_{F_E}	K_{F_e}	K_{F_I}	$(K_T)_{net}$	K_Q
4498	0.889	PSF2-HUB	0.245	-0.001	-0.001	-0.003	0.241	0.687
		PSF2	0.240				0.240	0.691
		experiment	0.242				0.242	0.659
4660	0.976	PSF2-HUB	0.283	-0.005	-0.000	-0.000	0.278	0.660
		PSF2	0.280				0.280	0.674
		experiment	0.279				0.279	0.647
	0.529	PSF2-HUB	0.546	-0.009	-0.001	-0.002	0.535	0.396
		PSF2	0.525				0.525	0.413
		experiment	0.522				0.522	0.391

Table 6.1 Comparison of force coefficients of theretical predictions
with those of experimental measurements

The thrust on the blades of propellor 4498 was increased by about 2%
due to the effects of the hub. But, the drag on the hub was about 1.5% of
the total thrust. So, the net force is almost the same as in the case of
ignoring the hub totally. The drag inside the hub vortex core is about 1%
of the total thrust and the force ouside the hub vortex is about 0.5%. As
for a larger hub (propeller 4660), the drag outside the hub vortex is
larger (look at K_{F_E} values). The drag inside the hub vortex core is
proportional to the square of $J\Gamma_0/(RV_S)$. At lower J, the Γ_0 is much larger
than the high J. So the drag inside the hub vortex is larger for J = 0.529
than for J = 0.976 for the same propeller. The torque coefficients
predicted by PSF2-HUB are better than those predicted by PSF2.

6.3 What Was Wrong with the Torpedo Propeller?

As mentioned in Chapter 1, a model test of a torpedo propeller
No. 1010 had a reduction of thrust of 45 percent because of the existence
of a strong hub vortex. This propeller was designed to be heavily loaded

at the hub. The pitch diameter ratio was 2.305 uniformly from hub to tip, and the inflow was decreasing from 0.971 of free stream at the tip to 0.4 at the hub. The advance coefficient was 2.305. The design value of $\Gamma/(RV_s)$ at the hub was 0.1377. The number of blades was 8. In order to estimate the circulation of the hub vortex, the loss of circulation from upstream to the after face of the hub should be estimated first. The experimental data in 5.7.5 shows that the loss of circulation was 15% for propeller 4498 at design J (0.889) and 25% for propeller 4660 at off-design J (0.525). These two propellers had a rotating fairing, while propeller 1010 had a stationary fairing, which may lose more circulation due to the concept of relative motion. Also, the fairing of the propeller 1010 had a blunt face which meant even more loss of circulation due to turbulence. A loss of 61% of the circulation was observed in the experiment with propeller 4498 without a fairing (see section 5.7.5.C). An estimate of 50% loss may be reasonable. We define a thrust load coefficient as:

$$C_T = \frac{T}{\frac{1}{2}\rho V_s^2 \pi R^2} \tag{6.18}$$

and define the nondimensional drag coefficients:

$$C_{F_I} \equiv \frac{F_I}{\frac{1}{2}\rho V_s^2 \pi R^2} = -\frac{3}{8}\left[\frac{\Gamma_0}{\pi R V_s}\right]^2 \tag{6.19}$$

$$C_{F_e} \equiv \frac{F_e}{\frac{1}{2}\rho V_s^2 \pi R^2} = -\frac{1}{8}\left[\frac{\Gamma_0}{\pi R V_s}\right]^2 \ln\frac{r_H}{r_0} \tag{6.20}$$

where (6.11) and (6.14) are applied. Γ_0 is estimated as:

$$\frac{\Gamma_0}{RV_S} = (8)(0.1377)(0.5) = 0.55$$

A measurement from Figure 5.1 of [McCormick et al., 1956] shows r_H/r_0 = 3.68. Then, the total reduction of thrust coefficient may be estimated as:

$$C_{F_I} + C_{F_e} = -\frac{3}{8}\left[\frac{0.55}{\pi}\right]^2 - \frac{1}{8}\left[\frac{0.55}{\pi}\right]^2 \ln 3.68 = 0.016$$

The measured value of reduction of thrust coefficient was 0.018. So the results are very encouraging.

CHAPTER 7

CONCLUSIONS AND RECOMMENDATIONS

7.1 Conclusions

A numerical lifting surface theory which takes account of hub effects has been developed for the design of propeller blades. An example with zero circulation at both ends of the blades is given in Chapter 3. The design which incorporates hub effects has lower values of pitch and camber at the root section than the hubless design.

The same theory has been applied to the analysis problem. Two examples are given in Chapter 5, along with comparisons to the experimental data. The examples show that, for a conventional propeller with relatively large pitch and camber at the root, the predictions with hub effects considered are much more accurate than the predictions with hub effects ignored. For a CP propeller, with relatively small pitch and camber at the root, the theory overpredicts the circulation when hub effects are considered. This overprediction occurs for two different advance coefficients, and is believed to be due to the complicated geometry of the blade fillets, bolts, cutoffs, etc. The leakage of pressure through the cutoffs makes the hub less solid. The fillets and bolts may generate complicated flow patterns which reduce the circulation.

An experiment was performed to demonstrate that the circulation is, roughly speaking, conserved along circumferential mean streamlines. This is based on the assumption that the vortex sheet follows the mean streamlines. The circulation at the blade root decreases 15 to 25% by the

time it reaches the hub apex, depending on the tangential speed of water particles relative to the hub surface. The circulation may increase due to the motion of the hub surface relative to water particles, if the circulation is essentially zero at the hub in the propeller plane.

The estimated force on the hub has two components. The force outside the hub vortex core was calculated numerically. The force inside the hub vortex was calculated based on the experimental data. It was confirmed that the hub vortex has a Rankine-type structure. The strength of the hub vortex was measured, enabling the force to be calculated by Equation (6.11). In general, the thrust on blades is increased by the hub effect due to a higher circulation maintained at the root section. However, drag on the hub will reduce the thrust by almost the same amount that it is increased. This is only true for propellers with a light load at the root. For propellers which are heavily loaded at the root, e.g., the torpedo propeller mentioned in Chapter 6, the gain in thrust due to the hub may be less than the loss due to the hub vortex. The estimate of the thrust reduction due to the hub vortex is very close to the experimental result for the torpedo propeller, although the accuracy of this estimate depends on the accuracy of the estimated loss of circulation. Experimental data are needed to establish an empirical formula for a hub with a blunt end, or to solve the axisymmetric flow boundary layer problem (e.g., Wilcox, 1979).

The bound circulation may be kept finite at the root due to the hub effects. The slope of the bound circulation must be zero at the root for a potential flow in order to satisfy the normal boundary conditions at the hub (e.g., McCormick, 1955, Figures 1 and 2). This is because a non-zero slope for the circulation gives a non-zero strength for the trailing vortex sheet at the hub, which in turn violates the boundary conditions at the

hub. In formulating the boundary value problem for velocity potential, the condition of zero slope for the circulation at the hub is not necessary. It is automatically satisfied if the normal boundary condition is satisfied at the hub.

If distributed singularities are used in place of the velocity potential, then there are two ways to treat the zero slope for the circulation. The first is to use an image at the hub to "carry over" the lift (see Chapter 1). The second is to use the method presented in this thesis. The condition of zero slope is not explicitly given in the problem formulation (see section 3.5). However, the boundary conditions at the hub control point will cause the net strength of the helical vortex, at the intersection of the trailing vortex sheet and the hub, to be equal to zero. The numerical result confirms this. Basically, both methods are correct, as long as the boundary conditions at the control points are satisfied.

In measuring the velocity field of a propeller using an LDA and a tracker, care should be taken with the data density, especially for the radial components of velocity, which have an orientation parallel to the jump velocity of the trailing vortex sheet. The bandwidth limitation of the tracker was not well known by the researchers who used the LDA and the tracker. Kobayashi [1981] found that there was a discrepancy in the velocity measurement at different propeller speeds, while J was constant. However, there was no explanation for the discrepancy. Okamura [1983] measured an outward radial velocity, in the tip vortex flow region, which was as large as 1.5 times the free stream velocity. This conflicts with the fact that the flow contracted inwards.

The problem with data density using a tracker can be solved by reducing the propeller speed. However, this may reduce the Reynolds number

below a critical point, thus altering the viscous drag. An alternative
method uses a counter which accepts all the signal and noise. A counter is
usually good for flow with a low data density. However, the counter has to
filter out the noise. The data density is inversely proportional to the
local velocity, which changes periodically in time for a propeller flow. A
filter which allows the bandwidth and central frequency to be changed may
be needed.

7.2 Recommendations

1. The input circulation for the propeller blade design is somewhat
   arbitrary, although it usually results from a lifting line calculation.
   It has zero circulation at the hub, which usually results in a very low
   pitch, and small and even negative camber at the root section. This
   brings up the problem of manufacture. It may mean that a slight
   increase in the circulation at the root is necessary, although this
   increase should not be too large or else a strong hub vortex cavity and
   a thrust reduction may occur. The estimatation of drag due to the hub
   vortex can be made using the approach of this thesis.

2. In order to avoid guessing blindly in modifying the circulation, a new
   design concept may be used. First, design the blade without considering
   the hub effect -- this blade usually has a higher pitch and camber at
   the root and is easier to manufacture. Then, carefully analyze the
   blade loading considering hub effects. Modify the blade geometry so
   that there is a more uniform loading over the chord of the blade.

3. In order to make the analysis of blade loading more accurate, it would be desirable to replace the camber surface singularity distribution with a surface singularity distribution over the blade.

4. An image method may be adopted for the blade singularities and trailers (e.g., Kerwin and Leopold, 1964). This will reduce the strength of the surface singularities over the hub, thus increasing the accuracy of the pressure calculation.

5. Research may be necessary to investigate the instability in the stream function at outer radii, as found in section 5.7.2. The mean streamlines were found to be wiggling at outer radii when the stream function method was used. The reasons for this should be determined.

REFERENCES

Andrews, J.B. and Cummings, D.E., "A Design Procedure for Large-Hub Propellers," *Journal of Ship Research*, Sep. 1972.

Batchelor, G.K., *An Introduction to Fluid Dynamics*, Cambridge University Press, 1967.

Breslin, J.P., "Propeller-Induced Hull Forces," Seventy-Fifth Diamond Jubilee Symposium, Versuchsanstalt für Wasserbau und Schiffbau, Berlin, West Germany, Nov. 21-22, 1978.

Breslin, J.P., Van Houten, R.J., Kerwin, J.E., and Johnsson, C-A., "Theoretical and Experimental Propeller-Induced Hull Pressures Arising from Intermittent Blade Cavitation, Loading, and Thickness," Trans. SNAME, Vol. 90, 1982.

Brockett, T., Boswell, R., Jessup, S., and Cox, B., *Design Theory for Marine Propellers*, 1981.

Eckhardt, M.K. and Morgan, W.B., "A Propeller Design Method," Trans. SNAME, Vol. 63, 1955.

Goldstein, S., "On the Vortex Theory of Screw Propellers," Proceedings of the Royal Society (A), Vol. 123, 1929, pp. 440-465.

Greeley, D.S. and Kerwin, J.E., "Numerical Methods for Propeller Design and Analysis in Steady Flow," Annual Meeting, New York, NY, Nov. 17-20, 1982, *SNAME*.

Hess, J.L., "Calculation of Potential Flow about Arbitrary Three-Dimensional Lifting Bodies," Final Technical Report, October 1972, Report No. MDC J5679-01, Douglas Aircraft Company, McDonnel Douglas Corporation, Long Beach, California.

Hess, J.L. and Valerezo, W.O., "Calculation of Steady Flow about Propellers by Means of a Surface Panel Method," AIAA-85-0283.

Huang, T.T. and Cox, B.D., "Interaction of Afterbody Boundary Layer and Propeller," Symposium on Hydrodynamics of Ship and Offshore Propulsion Systems, Høvik outside Oslo, Norway, Mar. 20-25, 1977.

Jessup, S.D., Boswell, R.J., and Nelka, J.J., "Experimental Unsteady and Time Average Loads on the Blades of the CP Propeller on a Model of the DD-963 Class Destroyer for Simulated Modes of Operation," DTNSRDC Report 77-0110, 1977.

Kerwin, J.E. and Lee, C.S., "Prediction of Steady and Unsteady Marine Propeller Performance by Numerical Lifting-Surface Theory," Trans. SNAME, Vol. 86, 1978.

Kerwin, J.E. and Leopold, R., "A Design Theory for Subcavitating Propellers," Annual Meeting, New York, NY, Nov. 12-13, 1964, <u>SNAME</u>

Kim, K.H. and Kobayashi, S., "Pressure Distribution on Propeller Blade Surface Using Numerical Lifting Surface Theory," Trans. SNAME, Vol. 92, 1984.

Klein, A.L., "Effect of Fillets on Wing-Fuselage Interference," Trans. ASME, Vol. 56, No. 1, 1934.

Kobayashi, S., "Experimental Methods for the Prediction of the Effect of Viscosity on Propeller Performance," Ph.D. Thesis, MIT, 1981.

Küchemann and Weber, <u>Aerodynamics of Propulsion</u>, McGraw-Hill Book Company, Inc., 1953.

Lerbs, H.W., "Moderately Loaded Propellers with a Finite Number of Blades and an Arbitrary Distribution of Circulation," Annual Meeting, New York, NY. Nov. 13-14, 1952, <u>SNAME</u>.

Ludolph, K., "Propeller-Hub Interference Effects Using an Approximate Lifting Surface Theory," Technical Memorandum, File No. TM 77-198, Applied Research Laboratory, The Pennsylvania State University, June 15, 1977.

McCormick, B.W., "The Effect of a Finite Hub on the Optimum Propeller," Journal of the Aeronautical Sciences, Vol. 22, No. 9, Sep. 1955.

McCormick, B.W., Eisenhuth, J.J., and Lynn, J.E., "A Study of Torpedo Propellers -- Part I," Ordnance Research Laboratory, Pennsylvania State University, NORD 16597-5, Mar. 1956.

Milne-Thomson, L.M., Theoretical Hydrodynamics. 5th ed, Academic Press, New York, 1968.

Min, K.S., "Numerical and Experimental Methods for the Prediction of Field Point Velocities around Propeller Blades," Ph.D. Thesis, MIT, 1978.

Morgan, W.B. and Wrench, J.W., "Some Computational Aspects of Propeller Design," <u>Methods in Computational Physics</u>, Academic Press, Inc., New York, NY, Vol. 4, 1965.

Newman, J.N., <u>Marine Hydrodynamics</u>, The MIT Press, Cambridge, MA, 1977.

Okamura, N., "Experimental Analysis of the Flow Field around a Screw Propeller," <u>IHI Engineering Review</u>, Vol. 16, No. 4, Oct. 1983.

Prandtl, L. and Tietjens, O.G., <u>Applied Hydro- and Aeromechanics</u>, Dover Publications, Inc., 1934.

Saunders, H.e., <u>Hydrodynamics in Ship Design</u>, 1957.

Schoenberger, R.B., "Experimental Determination of Propeller Field Point Velocities Using Laser Doppler Anemometry," Master Thesis, MIT, 1983.

Shoenberger, R.B., "Improved Techniques for the Experimental Determination of Propeller Field Point Velocities Using Laser Doppler Anemometry," Trans. SNAME, Vol. 92, 1984.

Tachmindji, A.J., "The Potential Problem of the Optimum Propeller with Finite Hub," International Shipbuilding Progress, Vol. 3, 27, November 1956.

Tachmindji, A.J. and Milam, A.B., "The Calculation of the Circulation Distribution for Propellers with Finite Hub Having Three, Four, Five and Six Blades," David Tayor Model Basin Report 1141, June 1957.

Thorsen, T.L., "Approximate Theory for the Optimum Circulation Distribution for Propellers with Very Large Hubs," Hydronautics, T.R. 127-2, July 1962.

TSI, "Laser Velocimetry Systems."

Vorus, W.S., "Calculation of Propeller-Induced Vibratory Hull Forces, Force Distributions, and Pressures; Free-Surface Effects," Journal of Ship Research, Vol. 20, 1976.

Wald, Q.R., "The Distribution of Circulation on Propellers with Finite Hubs," ASME paper 64-WA/UNT-4, Nov. 1964.

Wilcox, D.C., "Recent Improvements to the Spinning Body Version of the "EDDYBL" Computer Program," Report DCW-R-24-01, NASA, 1979.

Wind, J., "Hub Size Selection Criteria for Controllable Pitch Propellers as a Means to Ensure Systems Integrity," Naval Engineers Journal, Dec. 1978.

APPENDIX

This appendix will illustrate the reduction in the number of unknown strengths on the hub, using the concept of key hub.

Suppose there is a set of linear algebraic equations in matrix form:

$$
\begin{bmatrix}
a_{11} & a_{12} & a_{13} & a_{14} & a_{15} & a_{16} \\
a_{21} & a_{22} & a_{23} & a_{24} & a_{25} & a_{26} \\
a_{31} & a_{32} & a_{33} & a_{34} & a_{35} & a_{36} \\
a_{41} & a_{42} & a_{43} & a_{44} & a_{45} & a_{46} \\
a_{51} & a_{52} & a_{53} & a_{54} & a_{55} & a_{56} \\
a_{61} & a_{62} & a_{63} & a_{64} & a_{65} & a_{66}
\end{bmatrix}
\begin{bmatrix}
y_1 \\ y_2 \\ y_3 \\ y_4 \\ y_5 \\ y_6
\end{bmatrix}
=
\begin{bmatrix}
C_1 \\ C_2 \\ C_3 \\ C_4 \\ C_5 \\ C_6
\end{bmatrix}
\tag{A-1}
$$

which has the following properties:

$$
\begin{aligned}
y_1 &= y_3 = y_5 & C_1 &= C_3 = C_5 \\
y_2 &= y_4 = y_6 & C_2 &= C_4 = C_6
\end{aligned}
$$

Then (A-1) becomes three sets of equations:

$$
\begin{bmatrix}
(a_{11} + a_{13} + a_{15}) & (a_{12} + a_{14} + a_{16}) \\
(a_{21} + a_{23} + a_{25}) & (a_{22} + a_{24} + a_{26})
\end{bmatrix}
\begin{bmatrix}
y_1 \\ y_2
\end{bmatrix}
=
\begin{bmatrix}
C_1 \\ C_2
\end{bmatrix}
\tag{A-2}
$$

$$
\begin{bmatrix}
(a_{31} + a_{33} + a_{35}) & (a_{32} + a_{34} + a_{36}) \\
(a_{41} + a_{43} + a_{45}) & (a_{42} + a_{44} + a_{46})
\end{bmatrix}
\begin{bmatrix}
y_3 \\ y_4
\end{bmatrix}
=
\begin{bmatrix}
C_3 \\ C_4
\end{bmatrix}
\tag{A-3}
$$

$$\begin{bmatrix} (a_{51} + a_{53} + a_{55}) & (a_{52} + a_{54} + a_{56}) \\ (a_{61} + a_{63} + a_{65}) & (a_{62} + a_{64} + a_{66}) \end{bmatrix} \begin{bmatrix} y_5 \\ y_6 \end{bmatrix} = \begin{bmatrix} C_5 \\ C_6 \end{bmatrix} \qquad (A-4)$$

Suppose further that we assume that

$$a_{11} = a_{33} = a_{55} \qquad a_{13} = a_{35} = a_{51} \qquad a_{15} = a_{31} = a_{53}$$

$$a_{12} = a_{34} = a_{56} \qquad a_{14} = a_{36} = a_{52} \qquad a_{16} = a_{32} = a_{54} \qquad (A-5)$$

$$a_{21} = a_{43} = a_{65} \qquad a_{23} = a_{45} = a_{61} \qquad a_{25} = a_{41} = a_{63}$$

$$a_{22} = a_{44} = a_{66} \qquad a_{24} = a_{46} = a_{62} \qquad a_{26} = a_{42} = a_{64}$$

Then, (A-3) and (A-4) become redundant to (A-2) and only equation (A-2) needs to be solved. Thus, the unknowns are reduced by a factor of three.

Suppose we have exactly six helical vortices on the whole hub surface and only two helical vortices in the key blades of a three-bladed propeller. Six vortices numbered from one to six are spread over the whole hub surface at equal angular spacings, and six control points numbered from 1' to 6' are located in the middle of vortices as shown in Figure A.1.

Then the influence coefficients have exactly the same relationships as in (A-5), if i, the first index of a_{ij}, is replaced by i' (for example, if 1 is replaced by 1', $a_{1'5}$ means the velocity induced at 1' by a unit vortex at 5).

In order to save the storage, only the key hub information is stored, namely, the grid points, control points, and normal vectors. The lack of information about control points is easier to generate than grid points. So, a_{15} in (A-2) is replaced by a_{31} from (A-5) and the control point at 3' is generated from the control point at 1' by shifting an angle of blade interval $2\pi/K$. One thing to be careful of is that the induced velocity $\vec{v}_{15}$
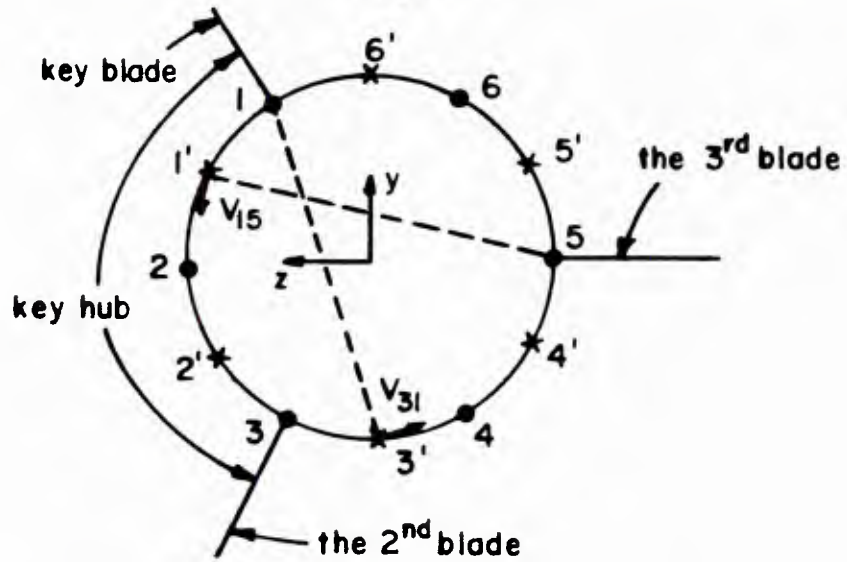
Figure A.1   Vortex Points and Control Points on Hub Section

is recovered by shifting the velocity $\vec{v}_{31}$ back an angle $2\pi/K$.   Certainly

this shift only affects the v and w components, not the u component.   After

treating the other coefficients in (A-2) the same way as a_{15}, we obtain

$$
\begin{bmatrix} (a_{11} + a_{51} + a_{31}) & (a_{12} + a_{52} + a_{32}) \\ (a_{21} + a_{61} + a_{41}) & (a_{22} + a_{62} + a_{42}) \end{bmatrix} \begin{bmatrix} y_1 \\ y_2 \end{bmatrix} = \begin{bmatrix} c_1 \\ c_2 \end{bmatrix} \tag{A-6}
$$

which has three times fewer unknowns.